Laser cooling of BaH molecules, and new ideas for the detection of dark matter

Rees McNally

Submitted in partial fulfillment of the
requirements for the degree of
Doctor of Philosophy
under the Executive Committee
of the Graduate School of Arts and Sciences

COLUMBIA UNIVERSITY

2021

Abstract

Laser cooling of BaH molecules, and new ideas for the detection of dark matter

Rees McNally

The advent of laser cooling and optical manipulation for atomic samples revolutionized atomic physics in 1990's, allowing the creation of new phases of matter, more accurate atomic clocks, and enabling leading candidates for the first functional quantum computer. This could not have been predicted at the time, and is a testament to the value of fundamental research for its own sake. These same laser cooling techniques are now being applied to simple molecular systems with the same revolutionary potential. In this thesis, I will present a range of experiments exploring these schemes in a new class of molecules, the diatomic alkaline earth hydrides. We present the creation and characterization of a bright beam of cold barium hydride molecules, high precision spectroscopy of these samples, as well as optical deflection and transverse cooling. This represents the first laser cooling of a Hydride molecule. This is a crucial step towards the creation of new cold molecular samples for a variety of scientific applications.

In the final chapter, I will change gears, and introduce new ideas for the detection of scalar field dark matter. While this variety of dark matter is typically searched for using atomic clocks, I will show that the same coupling also leads to anomalous acceleration of test masses. This acceleration would be detectable using both a network of precision acceleration sensors known as the IGETS network, and by the LIGO observatory. This new technique will compliment existing search strategies, and has higher sensitivity for a wide region of parameter space.

Table of Contents

List of Tables

List of Figures

Acknowledgements

The best part of my time at Columbia, was the chance to work with some of the brightest people I have ever met. Late night problem sessions, spirited disagreements, and constantly checking with Albert Law to see who was actually correct (because he always knew) dominated my first two years. It is a very special feeling to be surrounded by such intelligent people, all working hard on such different problems, and all of them willing to share and help out in any way they can. I want to make a special shout out to the Paddy's pub trivia team (Joey, Steve, Konrad, Albert, Giuliano, and Alex, among many others) for coming in second place behind the law school students every single week, and winning the wake-board anyway. I also want to thank Steve and Konrad for being groomsmen in my wedding, which is currently in a superposition state between happening and canceled thanks to COVID-19.

When I started to make the transition from school work to lab work, I came at a great time to help start a new experiment. The senior student on the molecule cooling project when I joined, Geoff Iwata, was an excellent mentor and helped me tremendously through those early years. He is a very talented and very kind scientist, and we shared an enthusiasm for somewhat zany side projects. Geoff and the other senior lab members of the lab at the time (Bart McGuyer, Mickey McDonald, and Chih-Hsi Lee) did an excellent job building a stimulating environment, not singularly focused on our own research, but actively discussing and thinking about many other fields. This general interest made me think hard about a lot of different issues, and I think it made me a better scientist. Later in my PhD the Zlab had the good fortune to gain two excellent post-docs; Stanimir Kondov, and Ivan Kozyrev. Stan was an invaluable resource for hard technical problems, and a true expert at all things quantum in cold atom systems. I learned an enormous amount from him, and he was a great resource to bounce ideas of off. Ivan Kozyrev joined my experiment 2018, and his impact was immediate. Ivan was an excellent mentor, and really drove the progress on the experiment forward. He was tremendously helpful in developing several side projects, and has the strongest vision for the future of the field of anyone I have worked with. Talking with him always felt like you could see a clear path forward, regardless of the difficulties you were facing. I am confident that this progress will continue after our departure thanks to the junior scientists taking over this work. Sebastian Vazquez-Carson is a very passionate scientist, who is not afraid of unorthodox ideas, and I think that will serve him well in the future. Qi Sun is meticulous, enthusiastic, and far more patient than I am when faced with a difficult problems. These traits will serve them well on this experiment, and I cannot wait to see what exciting results will come in the next few years.

Behind all of this work was the consistent mentoring of my advisor, Professor Tanya Zelevinsky. I am very thankful for the trust that Tanya had in me, even early in my time working with her. She always provided clear high level guidance, but allowed me to lead the cooling experiment how I saw fit, even though this was uncharted territory for both of us. This trust helped me gain confidence in my own abilities, and I never felt like I was simply completing tasks, I always felt like a scientist. This can be rare for a graduate student, and I am very grateful for it.

Outside the lab, none of this work would have been possible without the consistent love and support of my family. Much of my childhood was spent in the garage with my dad trying to make a wide range of ill conceived projects (catapults, go-carts, a propane forge, and on and on). It was was not until I was much older that I realized most kids did not spend their weekends living out mad scientist fantasies, but I would not have had it any other way. I am grateful to my parents for the environment of discovery they created. Every-time I visited my grandparents my grandpa always had a new biology experiment waiting for me, to teach me something new about insects, or plants, but mainly about fish. Both my grandma and grandpa were educators for their entire career, and their love of teaching is something they certainly passed on to me. In hindsight, there was never any chance I would be anything but a scientist, the only question was what field.

Finally, I would like to thank my wife Kaitlin (and to a lesser extent our cat Pixel). There were many hard-times in graduate school where I did not feel like things were working out. It was an enormous comfort to know that throughout those times, no matter how lost I felt, I already had the most important part of my life figured out. She has been my anchor through all of this, and I am excited to find out whats next.

At least I know I'm bewildered about the really fundamental and important facts of the universse. They both savoured the strange warm glow of being much more ignorant than ordinary people, who were only ignorant of ordinary things.

- Terry Pratchett

Chapter 1: Why Molecules

The study of atomic and molecular systems is one of the oldest fields in physics, and early experiments lead directly to the quantum revolution of the 1920's. Continued progress since those early days has lead to a transition in how we think about atomic systems. It is becoming increasingly common that the field of AMO no longer studies atoms for atoms sake. Instead, we use them to study some other process. These simple quantum systems are now used to test the fundamental symmetries of nature [1, 2, 3], to simulate condensed matter systems [4, 5], and to build increasingly accurate measurement and metrological tools [6, 7, 8, 9]. However this new paradigm has been hard fought, and requires precise knowledge of the atom/system you want to exploit. To use the properties of these systems you must be able to control it, and to control it you must understand it. This thesis will present work for a new quantum system, the diatomic barium monohydride (BaH) molecule. We will start with measurements of the molecule so we can understand it, and end with demonstrations that this knowledge allows us to control and cool these molecules using laser light. This is the first demonstration of laser cooling for hydride molecule, and the first steps towards using these systems to explore new opportunities. To motivate this work, I will introduce a range of applications for diatomic molecules, and discuss why the additional complication of a molecule are worth the extra effort. I will also present why we need new molecular systems to study, and why BaH and the hydrides more generally, are worth particular attention.

1.1 Applications

The additional degrees of freedom in a diatomic molecule require new control techniques, but also form the basis for why molecules interesting. This additional complexity enables unique scientific opportunities for precision measurements, quantum simulation, and cold/ultracold chemistry which has no analog in simple atomic systems. For each of these applications I will discuss why laser cooling and control can be of great benefit, or is critically important. This list is by no means exhaustive, but includes the applications I find most exciting.

1.1.1 Precision Tests of Fundamental Physics

The standard model is the crowning jewel of modern physics. It has successfully explained a huge variety of observations, and has been used to make theoretical predictions that match experimental data to an incredible fractional accuracy of 10^{-12} [10, 11]. This level of theory and experimental agreement is unparalleled in any other branch of science. However, we know that it cannot be complete. There is no place in the framework for Dark Matter (DM) which makes up some 30% of our universe [12], and there are tantalizing numerical coincidences that hint at additional particles [13]. Because the next generation of particle accelerators may be prohibitively expensive, and searches for some of the currently favored DM candidates are approaching fundamental limits [14], its now more important then ever to consider a wide variety of ways to test the standard model. One type of test that I find especially beautiful, are precision measurements at low energies using atomic and molecular systems. Though it is not related to molecules, I will also discuss a new low energy dark matter search technique in Chapter 8. In general, a precision measurement has a few requirements. You must choose a physical system, which is as sensitive as possible to the effect you want to measure, and as insensitive as possible to everything else. An example would be making a magnetometer based on the energy levels of atom trapped in a vacuum chamber [9]. If properly built this system will be sensitive to applied magnetic fields, and not the temperature in the lab. Laser cooling helps enable this pristine isolation, and decouple the system of interest from the environment as much as we can. Moving from atoms to molecules, we also gain access to new systems which are sensitive to new types of effects, or that have greatly enhanced sensitivity [15].

To take a specific example, there is large body of work focused on the use of atomic clocks to study temporal or spatial variation in fundamental constants. These searches operate by monitoring energy levels in an atom, and seeing if they change over time [16, 17]. Because atomic energy levels are primarily determined by the Rydberg constant (or equivalently the fine structure constant) this means atomic clocks are most sensitive to changes in the fine structure constant α and less sensitive to changes in other fundamental constants [18]. Moving to molecular samples we have new degrees of freedom such as vibration and rotation, with associated energy levels that are determined by the electron proton mass ratio μ and the relative mass of the atomic constituents. This means using rotational/vibrational levels instead of atomic levels to perform these searches measures an entirely different parameter space [19]. The concept for the two experiments is the same, but we are sensitive to new physical effects when we switch to molecules.

Another example, is the search for permanent electric dipole moments (EDM) of fundamental particles. While atoms can be used for EDM searches [20, 21], diatomic[22, 23] or poly atomic molecules [24, 25] have a substantially larger sensitivity thanks to the large electric field present inside a molecule [26]. This means for the price of the additional complexity, we can search for substantially smaller effects. This has been experimentally demonstrated, and modern EDM searches using molecules are now searching for new physics beyond the reach of even the LHC [27]. However, in order to take full advantage of these new systems we need to make as accurate a measurement of possible. In general these searches come down to the precise measurement of a frequency difference caused by the presence on an EDM. A frequency measurement, in the absence of additional noise or decoherence, has an accuracy $\Delta\omega$ which scales as

$$\Delta\omega = \frac{1/\tau}{\sqrt{N}}, \tag{1.1}$$

where τ is the measurement time, and N is the number of atom/molecules. One type of molecular EDM experiment is done using a molecular beam [22, 28], which leads to large N by using bright molecular beams, but the finite beam length and forward beam velocity limits τ. Another type is done with trapped molecular ions [23] which have very long τ but finite trap volume limits you to relatively small N. Both techniques currently have similar sensitivity to new physics. If we are able to use laser cooling/trapping to obtain large samples of trapped EDM sensitive molecules, this would allow large N and large τ simultaneously. This could lead to an orders of magnitude improvements in sensitivity, and early experiment towards this goal are underway [29, 30]. However, the techniques to trap laser cooled molecules are relatively new, and have so far only been demonstrated using a handful of specially chosen molecules (CaF[31, 32], SrF [33], and YO[34]). If we wish to extend these techniques to EDM sensitive molecules we need to learn more about these systems, and improve our techniques for molecules that are sub-optimal for laser cooling. The large atomic mass, and low applied force, make BaH an example of a “harder" to cool molecule, and I hope lessons we have learned can be applied to these EDM experiments.

1.1.2 Quantum Simulation

Another fascinating emerging field is the use of simple quantum systems (individual atoms/molecules) laser cooled, and used simulate much more complex systems. This can be broken down into two different categories, the direct simulation experiments [35, 36], and generalized gate based quantum computation [37, 38, 39]. For direct simulations the idea is that some relatively simple quantum models for real world materials cannot be solved analytically, or even computationally, in an efficient way [40]. However atoms are quantum objects so if we can control them sufficiently well we can engineer the model we want to study, and simulate it directly using the atoms. This idea was originally proposed by Richard Feynman in the 1980’s [41]. An example of such a model is the 2D Fermi-Hubbard model, which describes Fermions with onsite interactions hopping on a 2D lattice [42]. Even this relatively simple model, with no long range interactions, leads to a rich phase diagram and is thought potentially explain high temperature super conductivity. A recent experiment in the group of Waseem Bakr was able to simulate this system experimentally, and show that this model contains one of the key experimental signatures of high temperature superconductivity known as T-Linear resitivity [43]. This was an exciting example where they were able to use an engineer a quantum system made of individual atoms, use it to simulate a model that is right at the edge of what can be studied using computational techniques, and gain insight into a very important open problem in condensed matter physics.

While this is a very fruitful idea for atoms, they are limited to models which rely on short range interactions because, in general, ultracold atoms only experience 'hard-sphere' scattering (though some highly magnetic do have appreciable dipolar interactions [44]. By contrast molecules have preferred axis and can be easily polarized, leading to large long range dipole-dipole type interactions. This additional interaction would allow you to simulate a wide variety of new models that are challenging or not feasible with atoms alone [45, 46]. However, these experiments require extremely low temperatures and high densities making them very challenging for existing direct molecule laser cooling techniques. Personally, I think a better route for these sort of studies is to assembly molecules from ultracold atoms [47, 48], and avoid the need to directly cool the molecules to the incredibly low temperatures required. This alternative technique is well developed, and simulations with these systems is being pursued by a number of groups. While a fascinating application, this was not the focus of my work, because BaH is not a good candidate for a variety of reasons that will be discussed in this thesis.

Generalized quantum computing, also serves as an excellent opportunity for ultracold molecules. Large arrays of atoms trapped in micro-traps have already demonstrated some of the highest fidelity gate operation [49], and scalability to thousands of qubits should be possible. Compared to atoms, molecules offer additional challenges (due to the new degrees of freedom) but also unique opportunities. The additional degrees of freedom mean molecules have a much larger number of states, that can be used to store quantum information using special robust techniques [50]. Additionally, the long range dipole-dipole interactions discussed previously could enable more efficient 2 qubit gates, but this is an open question. The use of optical tweezers traps also relaxes the temperature requirements (compared to quantum gas microscopes), and has been experimentally demonstrated for directly laser cooled molecules [51, 52]. This a relatively unexplored parameter space, that I am sure will lead to some exciting results in the near term.

1.1.3 Cold and Ultracold Chemistry

In a similar spirit, we can also use the unique control enabled by laser cooling/trapping to study chemical reactions in new regimes. This can do done using an atom first picture where we can build molecules from individual atoms, or using samples of laser cooled molecules. Cold collisions between molecules are a deceptively complicated interaction, especially considering cold atom collisions are so well understood. In fact, there is a recent evidence that in the ultracold regime, molecular collision lead to formation of new bound states, with extraordinarily long lifetimes. To discuss this more quantitatively, in a typical chemical reaction $A + BC \rightarrow AB + C$ there will exist an intermediate state $[ABC]$ that forms while the chemical reaction is progressing. These intermediate states very unstable, with a typical lifetime on the order of a picosecond (10^{-12} s)[53] but the chemical reaction must go through this intermediate step in order for it to occur. It is now believed that when two cold diatomic molecules collide ($AB + AB \rightarrow AB + AB$) an intermediate 4 body state ($[AABB]$) is formed, making the collision almost like a chemical reaction. This was first observed because if one shines laser light onto two cold molecules as they collide, the molecules are lost after a collision [54, 55, 56, 57], and mass spectrometry shows fragments of this 4 body bound state are produced [58]. It is thought that the laser excites this transient 4 body bound state and breaks it apart. By modulating this laser several groups have now measured the lifetime of this 4 body state, and instead of picoseconds, they have found the low temperature leads to extremely long lived intermediate state lifetimes of up to $500\mu s$ [59, 60]. This opens up very exciting opportunities to study the intermediate states, and allows unprecedented insights into how chemical reactions proceed. These experiments are excellent opportunities for the direct laser cooling because quantum degeneracy is not needed, and these collisional losses have already been seen in several experiments.

There are many open questions about how these reactions take place, how they depend what state the molecules are in, and performing these measurements for a variety of different molecular species will be important to gaining insight. Hydrides are also computationally simpler than many other classes of molecules thanks hydrogen only possessing a single electron, and could be uniquely suited for comparisons with theory. So far these experiment have been done using directly laser cooled diatomic molecules, and diatomic molecules that have been assembled from cold atoms. If one wishes to study collisions with larger polyatomic molecules, direct laser cooling shows great promise for molecules of up to 5 atoms, or more [61, 62, 63]. By comparison there are no clear prospects for how to scale atomic assembly to this large of a molecule. Because of this I think cold and ultracold chemistry are an especially important application for direct molecular cooling experiments. Improving our understanding for how these intermediate complexes form, and how chemistry occurs in the cold and ultracold regimes has the potential to provide insights into how some complex molecules form in interstellar space [64]. This is a large open question that will take lots of experimental work, and has potential to improve our understanding of the origin of life, and I hope that laser cooling can help.

1.2 New Molecules and New possibilities

Each of the the applications I have discussed above have different, and sometimes competing requirements. For simulations we want strong dipolar interactions between molecules, and the ability to get to ultracold temperatures. For direct quantum computing experimental control in king, and we want to select a system which is easy to handle, and has extremely weak coupling to its environment (as well as a strong dipole interaction for two qubit gates). For precision measurements the size of the signature of new physics typically scales quite strongly with the atomic number of the heavy nuclei in the molecule, so we want heavy molecules. Lastly, for cold chemistry, we want everything, but are particularly interested in more. This means any particular molecular species we chose will not be able to study all the physics we want. We need a diverse set of molecules to study, so expanding this set of laser cooled candidates is very important.

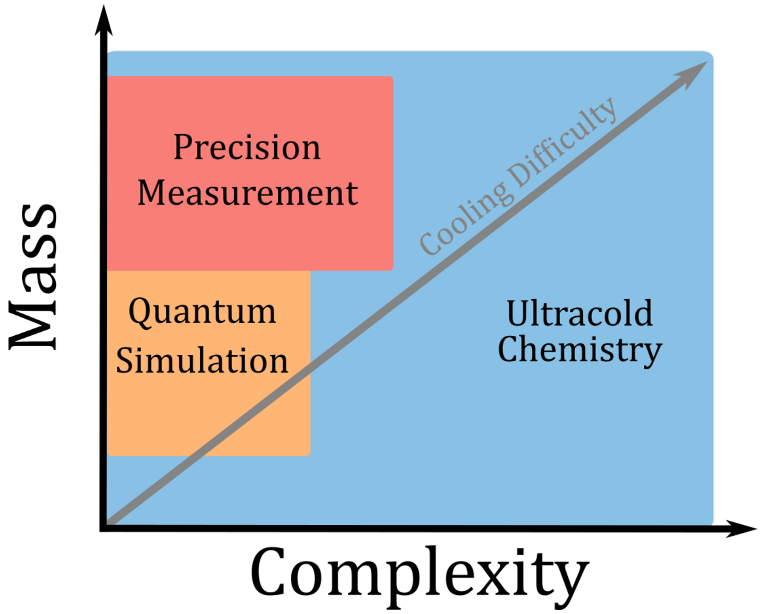

Figure 1.1: Rough scaling of potential applications for the direct laser cooling of molecules. Atom-Atom assembly is currently limited to diatomic molecules, and how to scale to more complex polyatomics molecules is not obvious. By contrast laser cooling as the potential to work for large polyatomic species.

Slowing/Cooling higher mass molecules is typically more challenging because it requires a larger transfer of momentum, but the scaling along this axis is relatively straightforward. As we increase the complexity of the molecules from diatomic, to large polyatomic molecules, the scaling is less than obvious. As the number of vibrational modes (which scales linearly with the number of atoms in a molecules) increase there are more decay paths available, and vibrational closure becomes harder to achieve. In addition to this, the higher density of states can lead to more perturbations, and can potentially break rotational closure through mixing in the excited state. However, it has recently been shown that this can be experimentally overcome for triatomic molecules, and theoretical studies and spectroscopic studies show that some larger linear, symmetric-top, and even non-linear, molecules could be laser cooled [61, 62, 63]. This is a very exciting opportunity, because the generation of ultracold polyatomic molecules through other means will be extremely challenging, and I believe laser cooling is currently the best route. Lessons learned with simpler diatomic such as BaH will help pave the way for this next generation of experiments.

1.3 Hydrides: An interesting stepping stone

With many exciting new molecular species to chose from, why choose the hydrides, and BaH specifically. Beyond the interest in showing a new species can be laser cooled, hydrides can potentially be used for precision measurement applications in the novel way. What we are interested in is using a laser cooled sample of BaH, as a new way to generate cold samples of atomic hydrogen. This concept is based on a proposal from Ian Lane [65], and on the low energy photo-dissociation work carried out by the our sister experiment in the ZLab. Consider a trapped gas of some diatomic molecule in thermal equilibrium. In this case the velocity distribution of the molecules will be given by a Maxwell-Boltzmann distribution defined by the mass of the molecule and the temperature T. In the limit where photo-dissociation adds no additional energy (and excess energy on the order of 100 nK has been experimentally achieved using strontium dimers) the molecule's atomic continents after photo-dissociation will have the same velocity distribution as the original molecule. This means the velocity distribution of the molecules, and the velocity distribution of each of the atomic constituents will be essentially the same. However, temperature and velocity are related in a Boltzmann distribution by the mass of the particle

$$T = \frac{Mv_p^2}{2K_b}, \tag{1.2}$$

where k_b is the Boltzman constant, and v_p is the most probable velocity. Because both the initial molecule and atomic constituents have the same velocity in this low energy limit we can relate the atomic temperature to the molecular temperature

$$T_A = \frac{T_{AB}}{M_{AB}/M_A}. \tag{1.3}$$

This means the lighter atom will be cooled relative to the original temperature, by the mass fraction M_{AB}/M_A. For BaH this results in a reduction of temperature of 138, which is a large factor. This effective cooling is why we chose BaH, instead of a lighter hydride molecule. However recent experiments have achieved extremely cold temperatures for molecular laser cooling (as low as 5.4 μK) so this cooling factor may not be needed, and we are currently exploring lighter hydrides as alternatives.

So why do we need new ways to generate cold hydrogen? I think there are two very compelling reasons. The first, is that while hydrogen has been cooled to degeneracy in the past [66], these experiments were based on evaporative cooling and had extremely high densities. These high densities lead to collisional shifts that made the samples challenging for precision measurements [67, 68]. Instead, precision measurements in atomic hydrogen are performed in sophisticated beam experiments which have been steadily improving for many decades. The most accurate transition these experiments have measured is the $1S \to 2S$ transition, to an incredible accuracy on the order of 10^{-15} fractional uncertainty [69]. Currently the largest systematic uncertainty in these experiments come from residual Doppler shifts, and a line-shape model that depends on the beams forward velocity. Modern atomic clocks where able to avoid these systematic limitations for other atoms by moving away from beam experiments, and into magic-wavelength traps. The magic wavelength for this $1S \to 2S$ transition has been calculated, and samples generated via this photo-dissociation technique would be cold enough to be directly loaded into these traps. This could enable a magic-wavelength optical clock for hydrogen, and potentially allow substantial improvements in the measurement of this transition. This would be a very technically challenging experiment, and would likely require a collaboration between several groups, but hydrogen is the gold standard for precision measurements, and any improvements to the current state of the art are worth the effort, and help settle discrepancies in current measurements [70].

The other reason I find low energy dissociation an extremely exciting idea to work on, is because this idea is potentially scalable, and hydrides would be an excellent place to start. There is an ever increasing catalog of molecules that have been laser cooled, including hydrides, oxides, fluorides, and hydroxides. Going even larger there are strong prospects for even more complicated molecules, as has been previously discussed. If this idea of dissociation works, and can be extended to these other systems, we could generate a wide variety of cold samples that can not currently be generated using other techniques. These new samples would offer new opportunities to explore each application I have discussed, and will be particularly interesting to study cold collisions. As with any new technology it is impossible to know what applications will be found for cold molecules, but I think there is a bright future for these techniques. In this thesis I will discuss our contributions to this emerging field, and the details required to take BaH from a system we want to study, to a system we can control.

1.4 BaH: A unique opportunity

Typically, laser cooling techniques rely on spontaneous emission of some excited state as a part of the cycle. You engineer a situation where absorption occurs for certain velocity classes, and not for others, then the molecule decays back to the ground state and we can repeat the process. This style of manipulation is fundamentally limited by the lifetime of the excited state. If it is long lived the molecule will not decay for some time and this limits how quickly we can scatter light, and the maximum force we can apply. However with some creativity you can find a way to beat this seemingly fundamental limit. Consider a molecule at rest in its ground state. If we apply a short laser pulse with the correct intensity and duration, we can transfer this molecule to it's excited state, and give it a $\hbar k$ momentum kick in the direction of the laser pulses propagation. Now, before it has a chance to decay, we apply a second pulse of laser light travelling in the opposite direction of the first. This second pulse takes the excited state molecule, transfers it back to the ground state, and gives it a second $\hbar k$ momentum kick in the same direction as the first. This leads to a net momentum transfer of $2\hbar k$. Because spontaneous decay is not needed anywhere in this cycle there is no fundamental limit to how quickly this process can repeat and only technical limitations such as laser power will apply. This type of optical forces are generally known as coherent forces, and has a variety of different implementations [71, 72].

BaH is an excellent molecule to explore these schemes. The relatively long lifetime of the excited state (136 ns) means we can really increase the maximum applied force, and the cycling transition requires a laser at 1060 nm. For this wavelength there are extremely high power lasers available, up to several kW, thanks to advanced fiber-optic based amplifiers. The only limit is cost, and your willingness to deal with extremely high powered lasers. Theoretical work we recently published [73], but I will not discuss in this thesis, shows we can obtain forces up to 100 times the limit imposed by spontaneous emission. We have also shown how this coherent force scheme can be extended to provide velocity dependent forces and allow for cooling. This is an exciting theoretical proposal for an entirely new type of optical cooling force, with a much higher peak force and capture velocity than traditional techniques. Looking to the future, as laser power increases, I think this type of cooling will become increasingly important. High forces at the cost of increased laser power becomes a better trade-off as lasers become cheaper, and that historically has been the case. In addition to the benefit of higher peak forces, because these schemes do not rely on spontaneous emission, there are fewer opportunities for the molecules to decay to dark states. This means more complex molecules with a higher number of vibrational decay modes could potentially be cooled more efficiently. This has been experimentally demonstrated for a polyatomic molecules [74], and I think it has huge potential for the future.

1.5 Thesis Outline

Structurally, this thesis will walk through the experiments required to first understand and then control BaH in the order they occurred. Chapter 2 is an overview for how energy levels in a diatomic molecule are labeled, and how these energy levels scale. I will also discuss how cycling is possible for diatomic molecules by introducing selection rules and Frank-Condon Factors (FCF). In Chapter 3 I will introduce the experimental techniques that make this work possible, and briefly discuss how they all work together. This is the “Hardware" section of the thesis. For chapter 4 I will discuss the cryogenic buffer gas source, and experiments that were performed while the BaH molecule was immersed in this buffer gas. Chapter 5 will discuss the properties of the molecular beam, and spectroscopy that was performed using it as the molecular source. Chapter 6 I will discuss the theoretical and experimental complications that arose while trying to optimizing the scattering rate for BaH, and the repumping scheme we use to close the leakage to the first vibrational state. Chapter 7 I will discuss the results of deflection and cooling experiments, and demonstrate the understanding of the molecule obtained in previous chapters allows the optical manipulation of BaH. This chapter also discusses some of the challenged associated with slowing and trapping BaH in a magneto optical trap, based on Monte-Carlo simulations. For the final chapter (chapter 8) I will change gears completely, and introduce a new technique for the direct detection of dark matter based on acceleration measurements. This final chapter can be read separately, and does not depend on other results in the thesis.

Chapter 2: The Diatomic Molecule

The diatomic molecules, as its name implies, features two atoms and is generally agreed to contain ”One atom too many" [75]. This additional degree of freedom leads to new quantizied energy levels, and new symmetries that are not present in atomic systems. These new degrees of freedom (rotation and vibration) can be accurately described separately, using a formalism known as the Born-Oppenheimer approximation. This allows a lot of the intuition that has been developed working with atomic systems, to be directly carried over, with some additional terms. For the purpose of this thesis there are two ingredients I would like to discuss. Firstly, I will introduce the concept of a term symbol, which is used to label specific states, and show how that label defines the energy of the state. Secondly I will show how the concept of selection rules can be applied to molecules, and how they define what transition are allowed between different states. These selections rules are critical because the symmetries in diatomic molecules allow us to restrict the range of transitions down to a manageable number. In fact one of the ideas that originally enabled this field, was the recognition of how selection rules could be exploited to allow optical cycling. This chapter is by no means exhaustive but I hope it will serve as a good introduction and aid understanding. I primarily learned this topic from the excellent textbook *Molecular Spectra and Molecular Structure* by Gerhard Herzberg [76], and this chapter is based on his work. For more details I would refer the interested reader there, or to these review articles/theses [77, 78, 79, 80].

2.1 Molecular Level Structure

The Born-Oppenhiemer approximation states, that to a decent approximation, the energy levels in a molecule can be treated as the sum of separate contributions, and the wavefunction can be treated as a product of separate wavefunctions. For a diatomic molecule in a specific state, we can express its energy as directly as this sum

$$E_{total} = E_{electronic} + E_{vibrational} + E_{rotational} + E_{Nuclear/Spin} \tag{2.1}$$

Where electronic refers to the energy of the electrons in a the state, vibrational refers to the energy in the relative motion of the two atoms, rotational refers to the energy bound in rotation about the center of mass, and nuclear spin is the energy of any interactions between the spin of the nucleus and either the spin of the electrons, or the rotation of the molecule. I will work through each of these terms individually using analogies to simpler systems, then introduce how they come together to completely define the energy levels and states in the BaH molecule. This will include the relevant quantum number for each contribution, and how the its energy scales.

2.1.1 Electronic Levels

The electronic levels can be best understood as direct analogs to the electronic levels in an atom. However, the additional degrees of freedom lead to additional quantum numbers. The direct calculation of the energy associated with an electronic excitation molecule is not a simple task, and is beyond the scope of this thesis. However many simple diatomic systems have been studied extensively, so ab-initio work on the electronic structure is not typically needed. For the electronic energy levels in diatomic molecules we use a single letter label, where the ground state electronic level is X, and the excited states are labeled A B C etc. where A is the first electronic excited state, B is the second etc. etc. However the states may not have been discovered in order of increasing energy, which leads to breaks from this pattern. For example, in BaH the energy ordering goes X, A, H, B, E, C, D. This means you have to be careful assuming the order of any excited states. The other three quantum numbers needed to label a diatomic electronic energy level are

$$^{2S+1}\Delta_{\Omega}^{(+/-)}, \tag{2.2}$$

Where S is the total spin quantum number, Δ is the projection of the orbital angular momentum along the internuclear axis, Ω is the projection of the total angular momentum along the internuclear axis, and the (+/-) labels the reflection symmetry of the electronic wave-function along an arbitrary plane containing the internuclear axis. The projection of the orbital momentum Δ will determine the shape of the electronic wavefunction, and is given a symbolic label using capital Greek letters ($0 \rightarrow \Sigma\ \ 1 \rightarrow \Pi\ \ 2 \rightarrow \Delta$). This should be compared to the S, P, D,... orbitals familiar from atomic hydrogen. For BaH, there are 3 types of electronic transitions. The ground state is a $X^2\Sigma^+$, which means we do not need to specify the projection of total angular momentum, because it only has one. There are also $^2\Sigma^+$ and $^2\Pi$ excited states that will be used throughout this thesis, and a $^2\Delta$ state which we did not directly study. The $^2\Pi$ states split into two bands because the different projections of the total angular momentum (Ω) have very different energies. Formally, this large splitting compared to the rotational splitting means these states are known as Hunds case a, but I will not discuss this in detail. The lower branch is the $^2\Pi_{1/2}$ and the upper branch the $^2\Pi_{3/2}$. These are both shown in Fig. 2.2.2. Due to selection rules that will discussed later in this chapter, we primarily use the $^2\Pi_{1/2}$ state, but have used a few transitions in the $^2\Pi_{3/2}$ states for optical pumping. For BaH electronic transitions have an energy scale in the NIR (the A state is at 1060 nm) up into the UV for higher lying states.

2.1.2 Vibrational Levels: The an-harmonic Oscillator

Atoms form molecules because it is energetically favorable for certain atoms to sit with a finite separation, as compared to having each atom be free. However, the nucleus of each atom is positively charged so we know they will not want to sit exactly on top of each other. These two simple facts lead us to have some immediate understanding for what the bond potential for a diatomic molecule should be. Let us to define zero energy, to be the energy when the two molecules are infinitely separated. As they get closer this energy will start to become negative and at somepoint reach a minimum and start to increase again, diverging as the distance becomes very small. The exact shape of this curve is different for every combination of atoms, for each electronic state of a molecule itself, and calculating these curves is a part of theoretical physical chemistry.

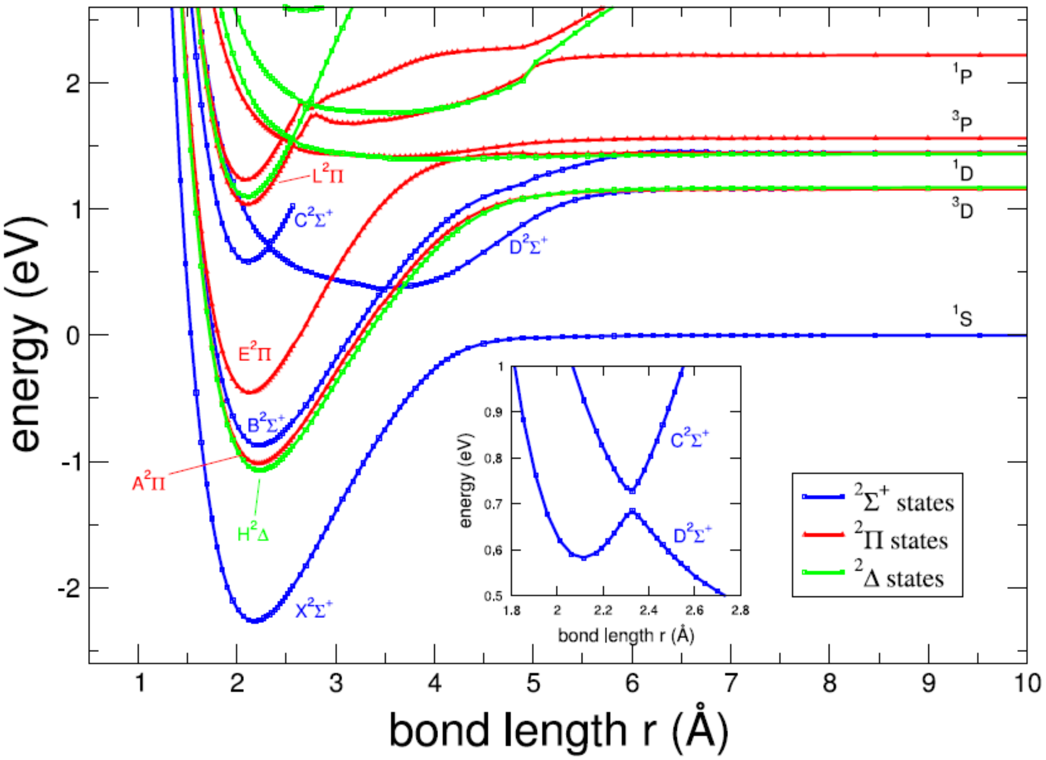

Figure 2.1: Molecular potentials for various electronic states of BaH from Ian Lane [81].

Looking closely we see that to a decent approximation the shape of each potential near the bottom of the curve looks quadratic. That implies that a good model the energy levels in this system, for low vibrational levels, is a quantum harmonic oscillator. We go one step further and account for deviations for quadratic using the energy levels of the an-harmonic oscillator in the vth excited state.

$$E_{vibrational}(v) = \omega_e(v + 1/2) - \omega_e x_e(v + 1/2)^2 + \omega_e y_e(v + 1/2)^3 + \ldots \tag{2.3}$$

The determination of ω_e, x_e, and y_e can either be performed by ab-initio theory, or fit experimentally by measuring where the energy levels of the molecule. Spectroscopy for BaH has already been done several time over the last 100 years, at varying accuracy, so these coefficients have been previously measured. This means we do not need to rely on theory to estimate where the energy levels in BaH are, and that theorists have experimental data they can use to tune their models. This additional contribution also breaks the equal spacing in energy levels typical of a harmonic oscillator, and we expect the spacing to decrease as vibrational quantum number increases. More details of the vibrational degrees of freedom will be included later in this chapter. For BaH, the vibrational energy spacing is on the order of 30 THz.

2.1.3 Rotational Levels: The Rigid and Floppy Rotor

The next additional energy scale, and degree of freedom, for a diatomic molecule is rotation. For this new variable, we can start by looking at it's symmetry. Because diatomic molecules have cylindrical symmetry, we expect them to have only one rotational degree of freedom, and therefore one additional quantum number to define this rotation. This is reminiscent of a classic model in quantum mechanics, the quantum rigid rotor. We know if we have two particles a distance r, each with a mass m_i we can define the moment of inertia for this system as,

$$I = \frac{m_1 m_2}{m_1 + m_2} r^2 = \mu r^2, \tag{2.4}$$

where μ is known as the reduced mass. We can solve for the energy levels of this system, and find

$$E_{rotational}(N) = \frac{h^2 N(N+1)}{8\pi^2 I}. \tag{2.5}$$

From this we can draw two important insights. The first, is how the spacing of rotational levels scales as we increasing rotational quantum number N. Additionally, because there is such a large mass imbalance in BaH the reduced $\mu \approx m_H$ which means I is smaller than for other more mass balanced diatomic molecules. This means there should be a larger rotational splitting than for other species, and that's exactly what we see. For BaH typical rotational splitting in the ground state, occurs on the order of 200 GHz, for CaF it is only 20 GHz.

Going beyond this approximation of completely rigid rotor one would expect that for higher rotational levels, the molecule will stretch and the moment of inertia will no longer be a constant. Additionally, for higher lying vibrational levels the average separation between the molecules will increase and that will also change the moment of inertia. In a similar spirit to the an-harmonic oscillator, we can solve these issues by taking higher order terms, and recognizing that the Born-Oppenheimer approximation will start to break down in this case, because vibration and rotation are not completely separate. There are several ways to parameterize this, but a general one that I personally find instructive is with an explicit dependence of the coefficients in the expansion on the vibrational state

$$E_{rotational}(N, v) = B(v)N(N+1) - D(v)N^2(N+1)^2 + ... \tag{2.6}$$

Typically the expansion coefficients (B and D) will be specified for each vibrational level separately, and the parameters are extracted by fit to spectroscopy data. This is a very convenient formulation for fitting to experimental data.

2.1.4 Spin-Rotation and Hyperfine Structure

The last contribution to the energy of a specific state is the interaction between rotational angular momentum, electronic spin, and nuclear spin. For BaH we have two contributions from these interactions. The first is the spin rotation splitting, from coupling between the spin S and the rotational angular momentum. For the $^2\Sigma$ and $^2\Pi$ states in BaH we have S=1/2 so their are two possible projections for each rotational state, $J = N - 1/2$ and $J = N + 1/2$. This rule is broken for the ground rotational state where there the rotational angular momentum is zero and only the positive projection exists. More explicitly, we can write this Hamiltonian for this spin rotation interaction between the electronic spin angular momenta S, and the rotational angular momentum N, as

$$H_{SR} = \gamma \mathbf{S} \cdot \mathbf{N}. \tag{2.7}$$

In general the spin rotation constant γ will be different for each vibrational level, and we observe this dependence in BaH. For these experiments we use Ba^{138} (which is spin-less) so the only nuclear spin comes from the hydrogen, which has a nuclear spin of 1/2. This gives two projections for each spin rotation level $F = J + 1/2$ and $F = J - 1/2$, and which introduces hyperfine splitting. This can be written as,

$$H_{HF} = b_f \mathbf{S} \cdot \mathbf{I} + c I_z S_z, \tag{2.8}$$

where I is nuclear spin angular momenta. The two constants b_f (the Fermi contact constant) and c (the dipolar coupling constant) are of similar magnitude in BaH. Measurements of these constants for each relevant state will be provided in Chapter 4. This final quantum number F also determines the multiplicity of the states, with each manifold comprising of $2F + 1$ sublevels ranging from $m_f = -F, m_f - F + 1, \dots, m_f = F$. For BaH the spin rotation splitting is on the order of 10 GHz, and the hyperfine is on the order of 10 MHz. hyperfine splitting will be relevant in later chapters, but is not included in either Fig. 2.2.2 or Fig. 2.2.1.

2.2 Electronic transitions

How the energy levels in a molecule are studied, and how we plan on controlling them, relies on transitions between distinct levels. Dipole allowed transitions are only possible from a given state, to a small sub-set of other states, and this coupling is defined by a series of selection rules. Focusing on electric dipole transitions, we know that the photon is a spin one particle, and that spin is a conserved quantity. Similarly, we know that angular momentum is conserved. Therefore when a transition is either driven (decays) from absorption (emission) of a photon, there are a finite number of choices that are allowed. Detailed selection rules can be derived for the coupling between each type of state, but we will focus on the two types of electronic transitions relevant to this work. For $^2\Sigma$ to $^2\Sigma$ we have no ambiguity, because $^2\Sigma$ states are always Hund's case b. For the $^2\Sigma$ to $^2\Pi$ transitions will will only consider Hund's case a, because that is the only case relevant for BaH. In addition to other quantum numbers, each state also has a parity denoted by (±).

This term specifies whether the wavefunction for this state changes sign or remains constant under reflection. Because we are interested in electric dipole transitions (simple absorption and emission of a photon) transitions must always change sign, so (+) couples to (−) but coupling between (+) and (+) or (−) and (−) do not occur.

With quantum numbers defined above it is useful to introduce some of the conventions used when labeling states, and provide some examples. For historical reasons the quantum numbers used to define the ground state in a system are labeled with a single dash, while excited electronic states are labeled with two dashes. For example, if I want to refer to the first rotational state in the ground electronic level, I would label that as $N' = 1$. If I wanted to refer to the same rotational level in the excited electronic state, it would be $N'' = 1$.

2.2.1 $^2\Sigma$ to $^2\Sigma$ Transitions

The simplest transitions in BaH occur between two $^2\Sigma$ states. In this case each transition must change the rotational states by an integer margin ($\Delta N = \pm 1$) and $\Delta N = 0$ transitions are forbidden. Transitions where the excited state has higher (lower) rotational quantum number, are known as R type (P type). Each of these classes of transitions are further split by selection rules in J, $\Delta J = 0, \pm 1$. X_1 transitions have $\Delta J = +1$, X_2 transitions have $\Delta J = -1$ and X_{Q12} transitions have $\Delta J = 0$, where X can be either R or P. It can confusing to keep these types of transitions straight, but I find a diagram (Fig. 2.2.1) helps makes the patterns clear.

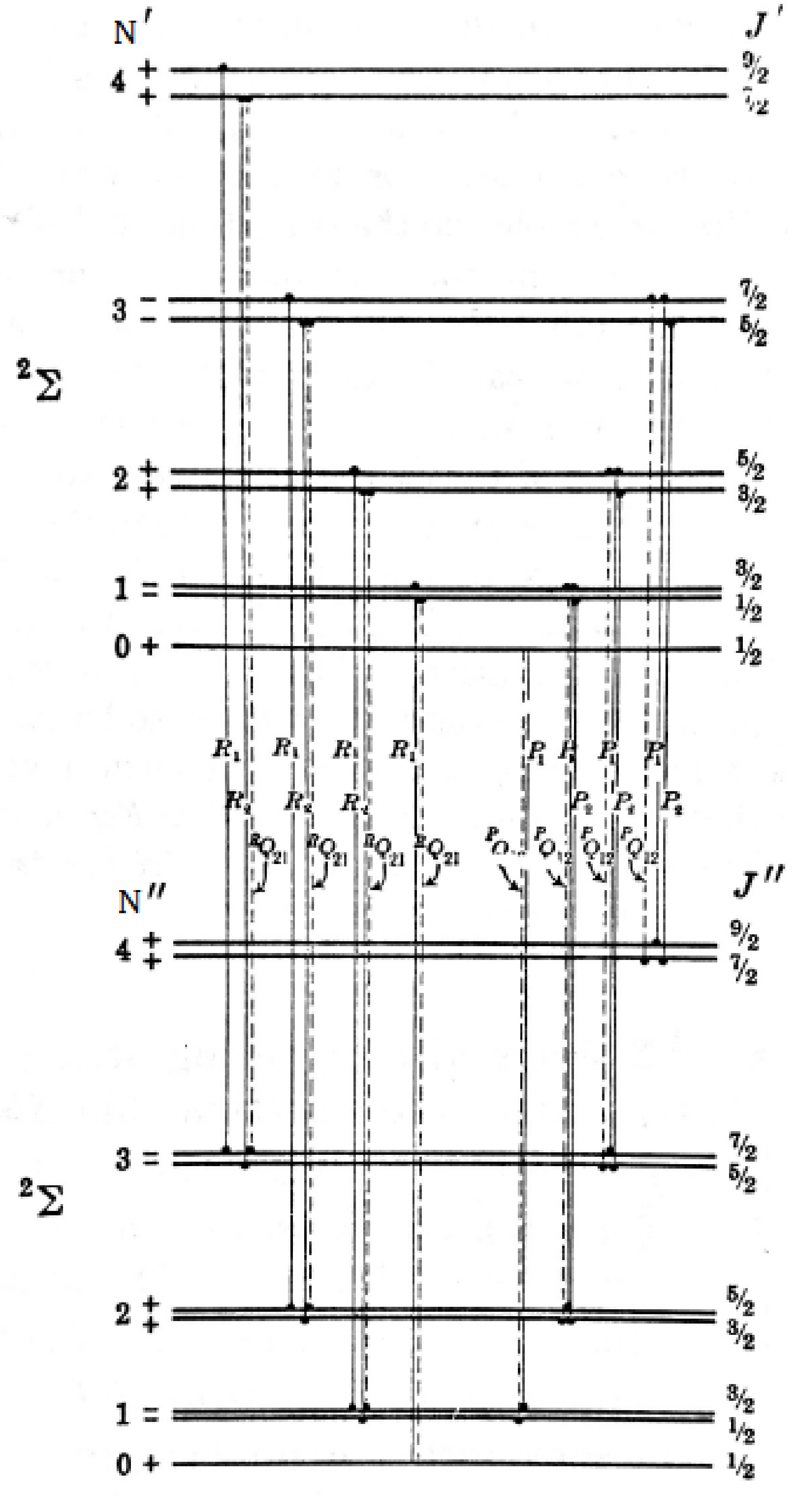

Figure 2.2: Allowed transitions for a $^2\Sigma \rightarrow ^2 \Sigma$ system. Each allowed transition is shown and labeled based on the selection rules described in the text. Note the special case when $N' = 0$ has greatly reduced decay pathways, allowing for optical closure. Taken from Herzberg [76]

Looking closely at the $N' = 0$ state, we can see that being the lowest rotational state means no R type transitions exist, and only P_1 and P_{Q12} transitions remain. These states both decay back to the $N'' = 1$ state, and that is exactly why we have rotational closure for this transition. This closure can be broken if there are nearby levels that perturb this $N' = 0$ state and cause mixing with different states, but for BaH we have no evidence that this occurs.

2.2.2 $^2\Sigma$ to $^2\Pi$ Transitions

For transitions between $^2\Sigma$ and $^2\Pi$ states, we have some additional complication. First of all, for $^2\Pi$ state $\Delta = 1$ and this leads to two different projections of the total angular momentum Ω. In Bah the Π states are Hunds case a, which means these different Ω values form two well separated bands. In this case we no longer have selection rules for ΔN, and only $\Delta J = 0, \pm 1$ selection rules remain, in addition to the usual parity requirements. This leads to more 12 possible transition types instead of the previous 6. I will not list them out, because we only care about a subset of them for the purpose of the work, for completeness they are all shown in Fig. 2.2.2.

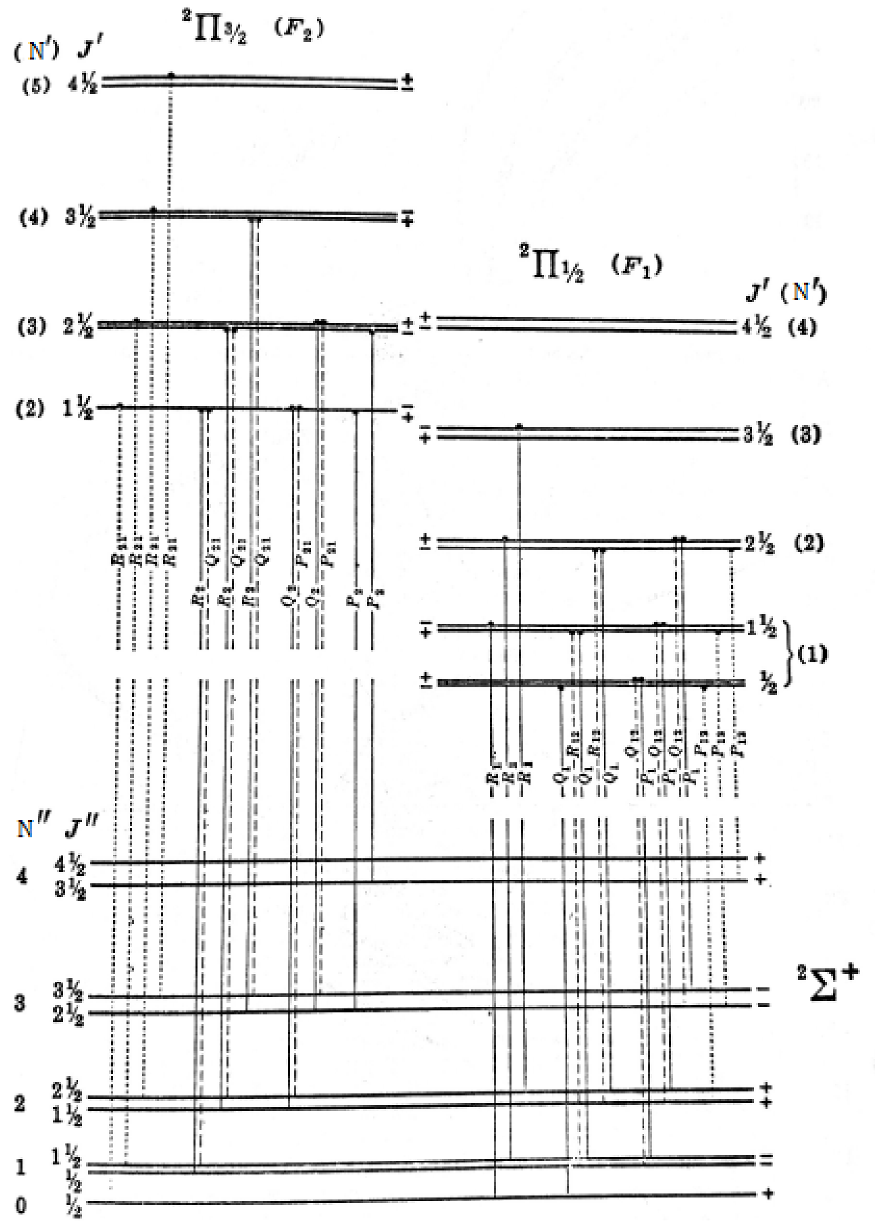

Figure 2.3: Allowed transitions for a $^2\Sigma \rightarrow ^2\Pi$ system. Each allowed transition is labeled, and for this case there are no longer selection rules limiting ΔN. Taken from Herzberg [76]

Again, because we are interested in rotational closure, we need to find excited state which only couple to a single ground state. Thankfully this situation also occurs here for positive parity portion of lowest levels of the $^2\Pi_{1/2}$ state. Just like for the $^2\Sigma$ case, if we drive Q_{12} and P_1 transitions from the $N' = 1$ state, they have will decay back to the same state and we can continue to cycle.

2.2.3 Rotational Closure

Optical cycling, and the majority of laser cooling techniques, all rely on the ability to continuously scatter light from the object your interested in. For simple atoms the relatively sparse energy structure makes this straightforward. However, as I have introduced here, the case of even simple diatomic molecules does not seem vary promising. The large number of states lead to new types of decay channels with no analog in atomic systems, and finding closed cycles seems daunting. Thankfully, it was noticed, that there are indeed some closed cycles with respect to rotational levels. The idea here, is that because each of the transitions shown in Fig. 2.2.1 and Fig.2.2.2 (for the $^2\Pi_{1/2}$ manifold) decay from the lowest lying excited rotational level can only decay the $N = 1$ rotational state of the ground potential. This means if I drive transitions from $N = 1$ ground state to the $N = 0$ excited state, they will decay back, and are ready to be excited again.

This leads to complications, because for BaH the spin rotation splitting (responsible for the splitting of the $J = 1/2$ and $J = 3/2$ states in the $N = 1$ ground state has a splitting on the order of 10 GHz, and both spin rotation states must be addressed. Additionally, we are now discussing optical cycling in a system where there are a larger number of ground states than excited state. There are $1 + 3$ from the $J = 1/2$ spin rotation state, and $3 + 5$ for the $J = 3/2$ state while both the $^2\Sigma$ and $^2\Pi_{1/2}$ ground rotational states have $1 + 3$ states. Such a system is not typically used in atomic experiments, and leads in general to the creation of dark states, which are super-positions of ground states that do not couple to the excited state. This will be discussed in further detail in Chapter 6 when we discuss optical cycling in this system.

2.3 Vibrational Closure and Franck-Condon Factors

We can exploit selection rules to ensure rotational closure, because angular momentum is a conserved quantity. However there is no conservation of vibration, so it is not obvious why molecules will not simply decay from an excited electronic state into a range of excited vibrational states in the ground potential. The likelihood that any given decay will occur is determined by the Franck-

Condon factor for that transition specific transition, which is proportional to overlap between the vibrational wavefunction of the initial and final state. To visualize this, it is helpful to consider a simplified model of a molecular potential, known as the Morse potential.

$$V(r) = D_e(e^{-2a(r-r_e)} - 2e^{-a(r-r_e)}) \tag{2.9}$$

Where D_e is the depth of the potential, r_e determines the location of the minimum energy, and a control the width of this potential. Here the potential is written such that the energy goes to zero as r runs to infinity. This potential is simple enough that you can analytically solve both for the eigenvalues (energies of the bound vibrational states) as well as analytic expression for their wavefunctions. This is shown for a specific potential, in Fig. 2.3.

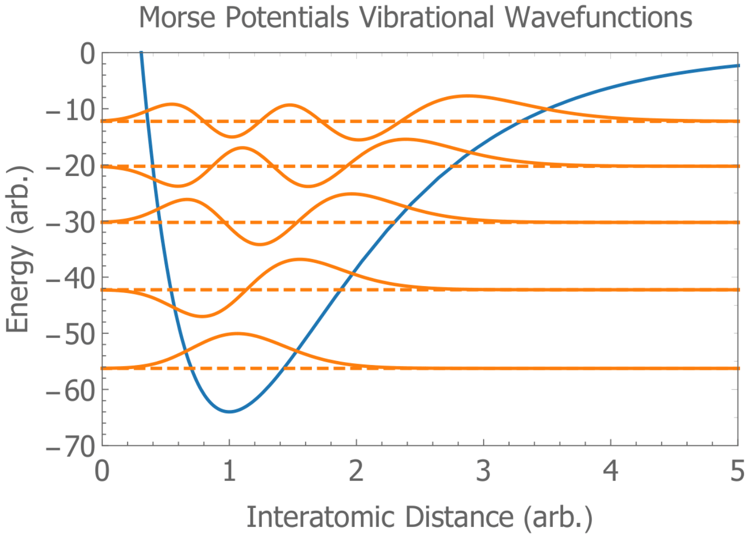

Figure 2.4: Morse Potential and the first 5 vibrational wavefunctions ($D_e = 64$, $r_e = 1$, $a = 1$). Dashed lines show bound state energies, and wavefunctions are vertically centered about their eigenenergy for clarity.

Now to visualize how wavefunctions overlaps will affect decay, lets add an additional molecular potential for some excited state, and look at the overlap between the wavefunctions in two different regimes. The first, is for two different shaped potentials, visualize the states (Fig. 2.3 (a)) and see what the numerical value of each FCF ($q_{v',v''}$) is (Fig. 2.3 (b)) where we define $q_{v',v''}$ as

$$q_{v',v''} = \int_0^\infty \psi^*_{v'}\psi_{v''}dr. \tag{2.10}$$

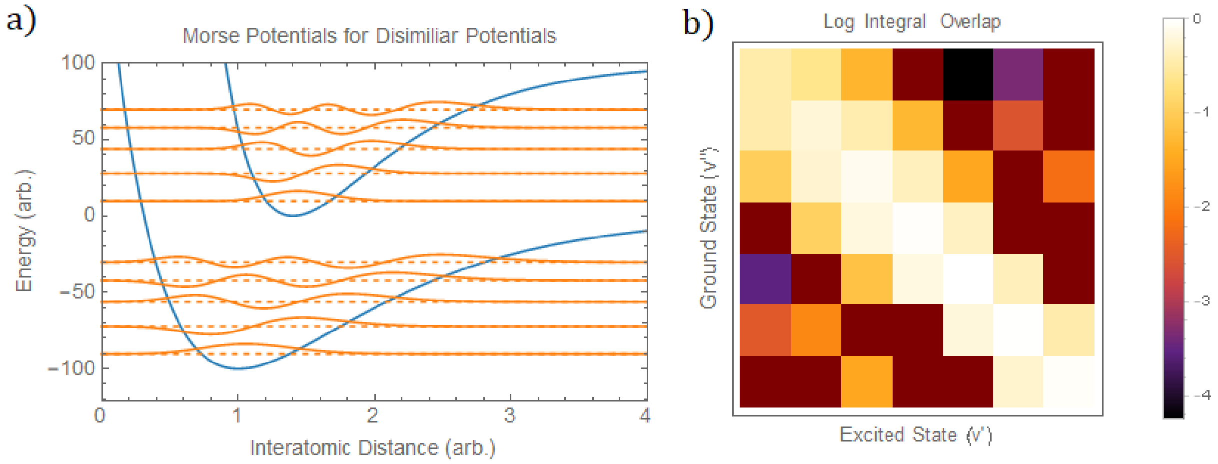

Figure 2.5: a) Potential curves for the ground and excited state for a model system b) Log of the integral overlap between combination of states. The 0-0 overlap in the top left corner.

Here, we can see that the ground vibrational level in the excited state, (left most column) has substantial overlap with the first three vibrational levels in the ground state. This would not be a molecule we can laser cool, because the potentials are shaped too differently, and there is not good matching between the wavefunctions. To contrast this, a system we could potentially laser cool is shown in Fig.2.3.

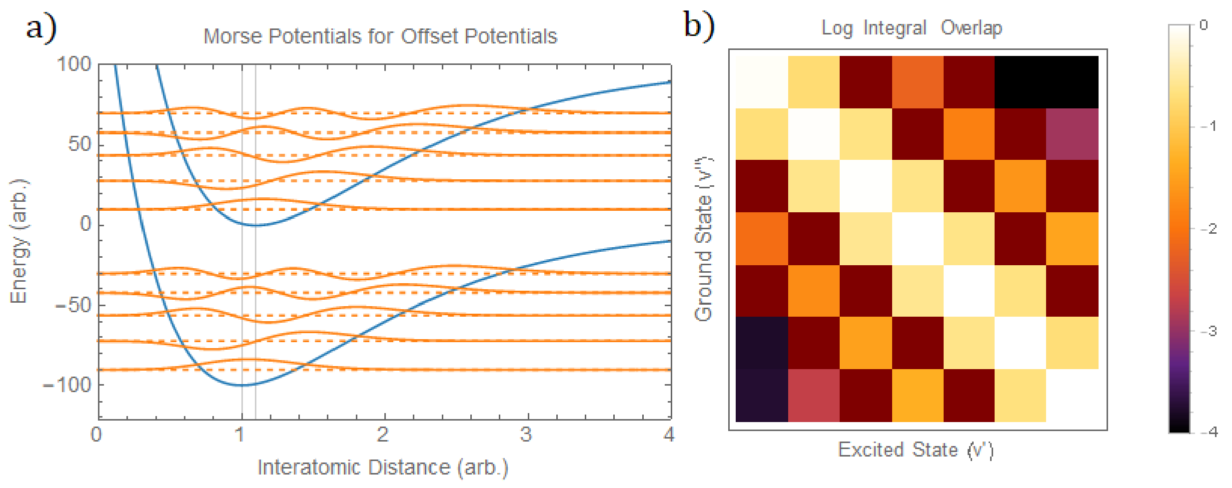

Figure 2.6: a) Potential curves for the ground and excited state for a model system, where the potentials only differ by a small displacement b) Log of the integral overlap between combination of states, the 0-0 overlap in the top left corner. Here we see strong overlap for diagonal transitions (0-0,1-1, 2-2, etc.)

For this case the two potential curves vary by only a small offset, and we see much stronger overlap between each excited state, and one specific ground state. This is a system we could laser cool, because we have a substantial portion of the molecules going back to the ground state. This problem will be treated again more quantitatively in chapter 4, when we represent measurements of the FCF for BaH.

2.4 Thermal Population Distributions

For molecular laser cooling experiments we need to be careful about how we define temperature. While the kinematic motion of molecules can be controlled, and lowered to tiny factions of a degree kelvin, the internal degrees of freedom will be far from equilibrium. This is because, as discussed previously, we can only laser cool molecules that start from the $N = 1$ rotational level. To be in true thermal equilibrium, the equipartition theorem tells us this we will have a distribution of internal states with equal energy to the kinematic motion. This means for a fixed temperature, T we would expect many rotational and vibrational levels to be occupied.

Beginning with the vibrational levels, we know that the ratio of probabilities that two states are populated is given by the Boltzman factor, so looking at the population of the first vibrational state relative to the ground state, we have

$$\frac{P_{v1}}{P_{v0}} = e^{\frac{-\Delta E}{kT}} \tag{2.11}$$

Where ΔE is the separation of the two states, k is the Boltzmann constant, and T is the temperature. To determine if there is any population in the first vibrational state at our temperatures we can solve for the temperature where the populations are comparable. This occurs at the extremely high temperature around 2000 K. When our sample is first created we have temperatures on this order (as will be discussed in chapter 4), but they rapidly cool to order of a 10 kelvin where this vibrational degree of freedom is effectively frozen out. However for experiments with more complicated polyatomic molecules this vibrational splitting for some normal modes is substantially lower, and will eventually be one of the limitations to these techniques.

For rotational levels, we have an additional complication that each rotational level has a different number of states, which scales as $2N + 1$ for the N'th rotational state. This means we need to include this changing multiplicity as a statistical weight. Ignoring normalization we can write the relative population of the N'th state as

$$P_N \propto (2N+1)e^{\frac{-\Delta E}{kT}} = (2N+1)e^{\frac{BN(N+1)}{kT}}, \tag{2.12}$$

Where we are using the rigid rotor approximation. For the ground state of BaH, $B = 3.38cm^-1$, and we can directly solve for this distribution as a function of temperature. As an important design consideration, we find the relative population of the N=1 state, is maximized at around 10 K.

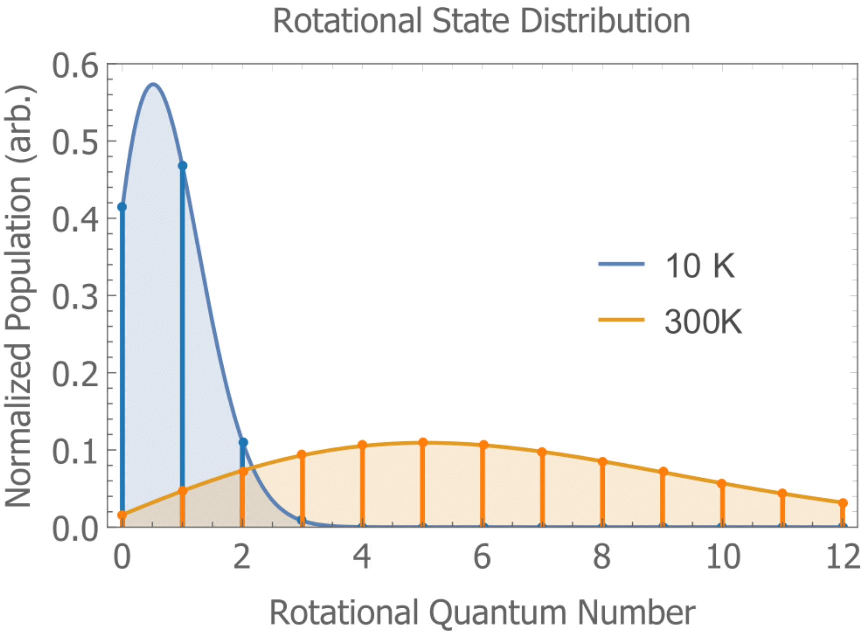

Figure 2.7: Relative population of each rotational level as a function of temperature. We expect to maximize the population of the N=1 state, which can use for laser cooling, around 10K. This is hotter then many species being used due to the large rotational splitting, as discussed previously.

Chapter 3: Experimental Apparatus

The direct laser cooling of molecules relies on a wide range of experimental techniques. These include tools familiar to cold atom experiments such as frequency tunable lasers, and acousto/electro-optical modulators, as well as less commonly used tools such as cryogenic systems and pulsed ablation lasers. The combination of these techniques makes molecular laser cooling experiments uniquely challenging, but especially fun to develop. In this chapter I will describe the major subsystem of the experiment, with an emphasis on practical implementation.

3.1 The CBGB Source

The additional vibrational and rotational degrees of freedom present in diatomic molecules mean it is challenging to generated a high flux of molecules in a specific state using an oven source. This is because high oven temperatures result in a many rotational, and in some situations vibrational, states being occupied as discussed in Chapter 2. To concentrate the distribution down to the first rotational state where we can attempt laser cooling, we need to start at cryogenic temperatures. We achieved this by thermalization of the molecules with a cryogenically cooled buffer gas of helium, as shown in fig. 3.1. This allows us to leverage the commercially available, high power, pulse tube refrigerator (PTR) technology to cool the molecules down to a few kelvin using purely classical techniques. Here I will detail the construction of the Cryogenic Buffer Gas Beam (CBGB) source. Data collected while characterizing the CBGB will be discussed in Chapter 4.

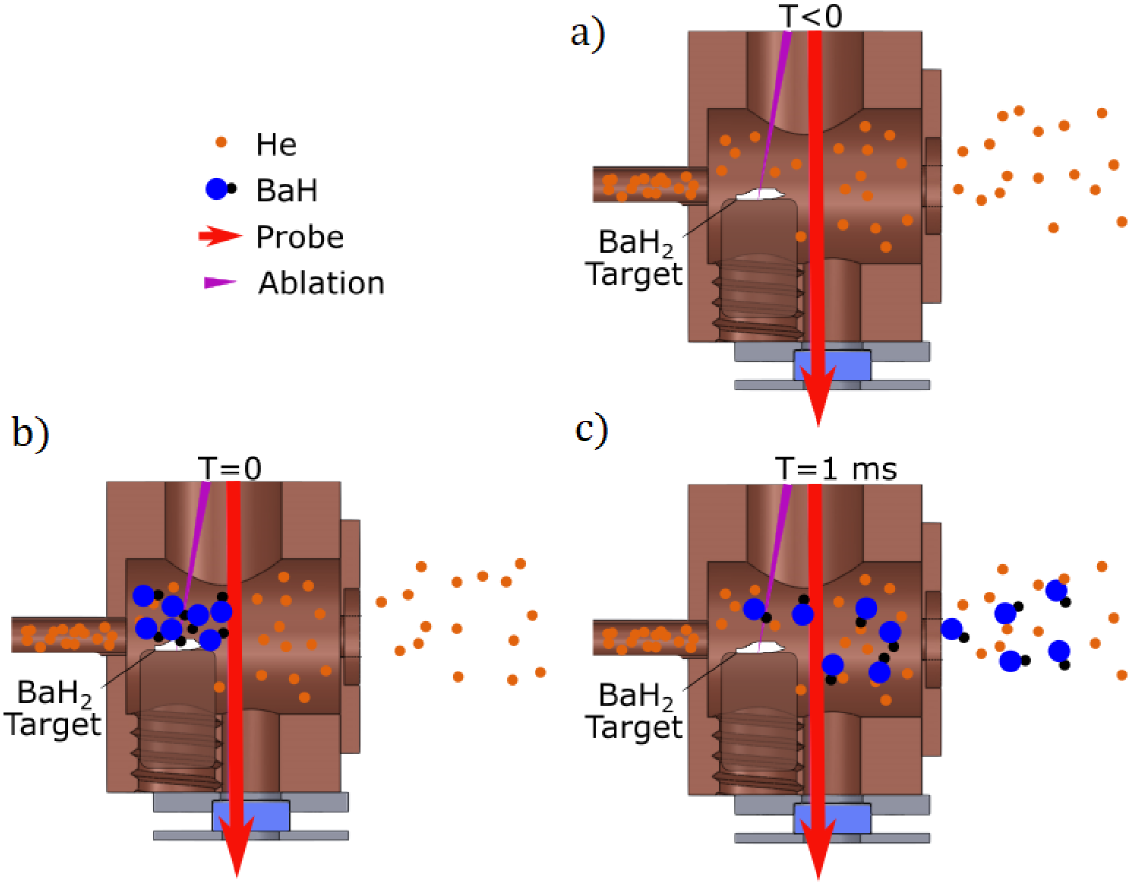

Figure 3.1: a) Cyrogenically cooled He buffer gas inside the cell. b) Laser ablation introducing a hot plume of the target of interest (BaH in this case) c) Thermalization with the He gas, and extraction from the cryogenic cell.

The CBGB serves as the initial state preparation for the experiment, and is a quite general technique [82, 83]. By relying on helium collisions to cool the molecular sample, we are able to cool the internal and external degrees of freedom for a wide class of molecules. This technique has found extensive application for cooling simple diatomic molecules, as well as increasingly complicated polyatomic samples. It is also a convenient way to study chemistry in cold environments [84, 85], without the additional complications of laser cooling. The CBGB can be broken down into three main elements, the cryostat, the cell, and the buffer gas delivery.

3.1.1 The Cryostat

The core of our cryostat is a two stage PTR-415 pulse tube refrigerator from Cryomech. This system has a base temperature of 4K, with a cooling power of 1.5 Watts. Based around this device, we designed a cryostat consisting of an external vacuum chamber, and two layers of thermal shielding anchored to the 40K and 4K cold heads of the PTR. The outer 40K shield is made from aluminum, the inner 4K shield is made from OFHC copper. Each shield is supported from the top via structural connection to the outer vacuum chamber, and thermally connected to the PTR's cold heads via a braided copper connection to minimize vibrations. The vacuum system used for the cryostat is described in further detail later in this chapter.

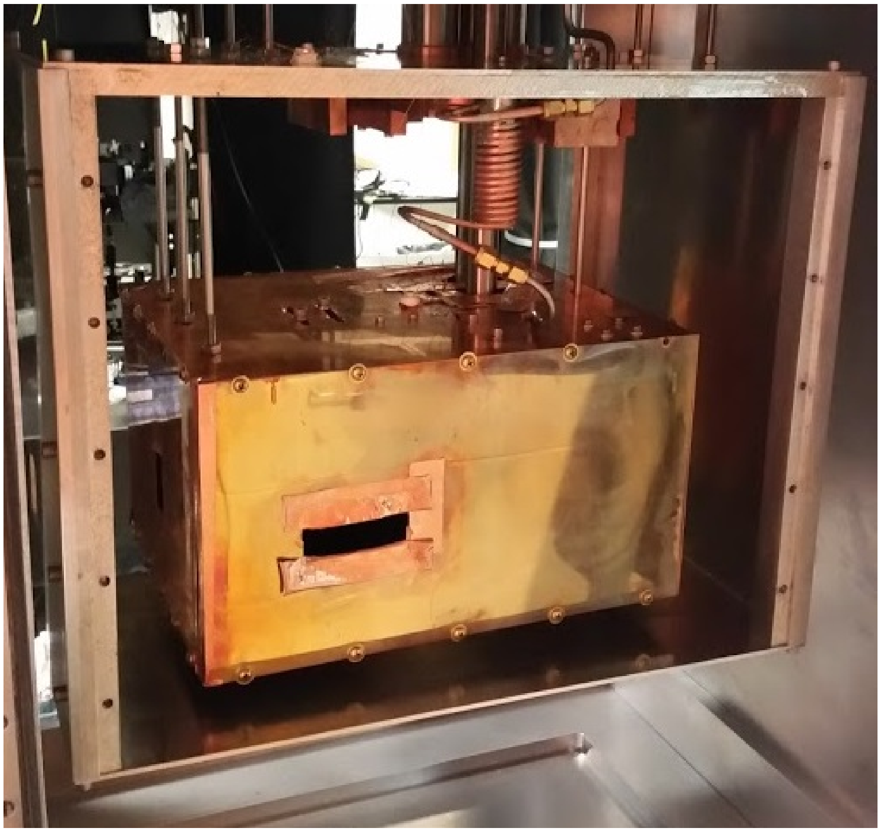

Figure 3.2: Photo showing 40k (aluminum) and 4K (copper) thermal shielding. The gap in the 4K shield allows from the absorption probe to pass into the cell, and two panels of the 40K shield have been removed.

The large internal volume of this design allows us a lot of flexibility when adding additional features to the cryostat. This includes several iterations of cryogenic beam apertures, and a large volume of “fins" to increase the amount of charcoal inside the 4K region. In addition to this, it allows a wider variety of cell geometries, that we explored in order to maximize the brightness of the molecular beam. We find typical cooling times on the order of 12 hours, and stable beam performance over the course of $\approx$ 8 hours, but the system must be allowed to warm each night (see section 4.1 of this chapter for details).

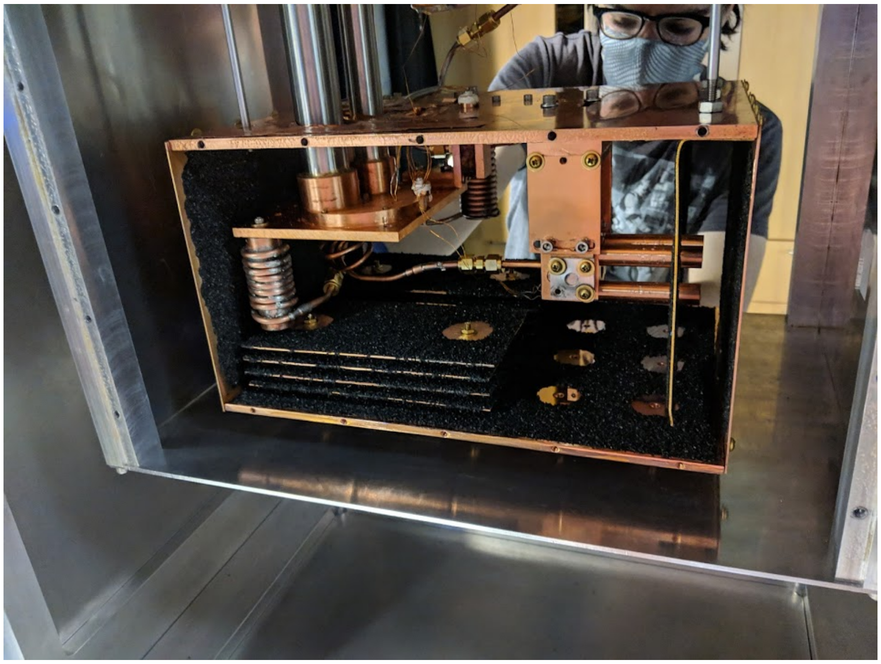

Figure 3.3: Interior of the 4K shield. The additional charcoal coated fins are designed to increase the cryogenic pumping capacity. The window on the side of the cell allows us to probe the interior of the cell, and the beam exits to the right.

3.1.2 The Cell

Cell geometry is very important to the design of CBGB sources, because you must carefully balance several time constants in order maximize performance. This is best described in the excellent review paper on CBGB sources [82], but is worth discussion in the context of this design. We have direct experimental access to the first time scale, and that is the thermalization time of the molecule of interest. This happens rapidly and depends only on the collisional cross section σ_0 and the density of the buffer gas which is determined by the rate that we flow He into the system

f_{He}. The other two time constants we need to balance are the diffusion (τ_{diff}) of the molecules to the wall of the cell (where they stick and are lost) and the time it takes to extract the molecules from the cell $\tau_{extract}$. In order to generate a large flux, of cold molecules, we need thermalization to happen more quickly than extraction, and extraction to happen more quickly than diffusion to the walls. I found a ratio of the diffusion and extraction times useful for cell design, scales as

$$\gamma_{cell} = \frac{\tau_{diff}}{\tau_{extract}} \propto \frac{\sigma_0 f_{He}}{L_{cell}\bar{v}_{He}}, \tag{3.1}$$

where f_{He} is the flow rate of the helium buffer gas into the cell, L_{cell} is the length of the cell (distance from the target to the exit aperture) and $\bar{v}_{He}$ is the mean thermal velocity of the buffer gas. While the scaling on this equation is useful as a design tool, the exact environment inside the buffer gas cell is quite complicated, and we have not been able to quantify the diffusion time accurately. However we can estimate the thermalization time, and the extraction time, based on in cell measurements discussed in Chapter 4.

In order to generate a bright beam, we would like $\gamma_{cell} > 1$ so molecules are extracted from the cell (into the beam) faster than they diffuse to the walls of the cell. The cross section (σ_0) is a constant, and not something we can control experimentally. The thermal velocity $\bar{v}_{He}$ is fixed because in order to maximize the population of the $N = 1$ state we want a cell temperature of $6K$. This leaves the flow rate and the length of the cell as free parameters. Experimentally, we observe an increase in the molecular beam's forward velocity for flow rates above 10 sccm, which limits the range we can tune this parameter and maintain a slow beam. In order to optimize the cell we played with a variety of lengths to get decent cell performance for low flows, and various aperture sizes, because different aperture sizes gave different forward velocity distributions of the beam. This is discussed in the detail in Chapter 4. A drawing of the cell we found the optimal performance from is shown in Fig. 3.1.2.

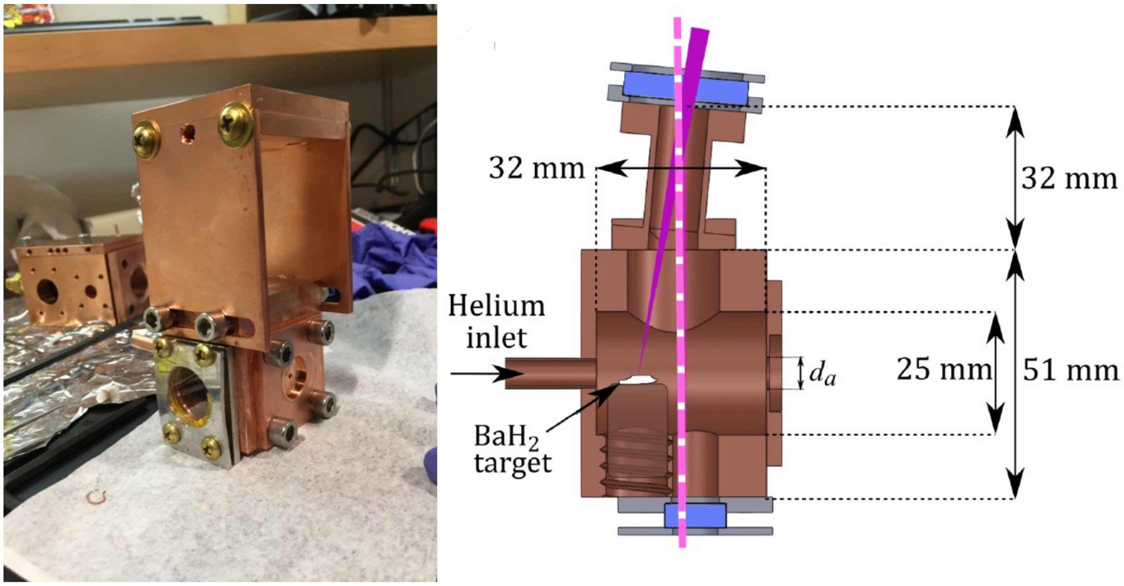

Figure 3.4: Details of the cell geometry used for the majority of these experiments. In addition to the provided details, a fine copper mesh is also placed in front of the helium inlet, to help diffuse helium homogeneously throughout the cell. We found this mesh decreased our sensitivity to the exact ablation spot we chose on the BaH Target.

There are a design requirements that are not captured in the simple scaling I have already introduced. The first is that repeated ablation of the sample leads to a coating building up on the inner surface of any window attached to the cell. For the window that the ablation laser enters through (top of the drawing in Fig. 3.1.2) this is a problem, because a tightly focused ablation beam will crack the coated windows. To get around this an extension was installed on the cell so the laser spot size on the window is increased. This coating leads to decreased transmission of the probe laser used to monitor molecular production, but for most experiments incell signals are used as a diagnostic tool and the decreased signal is not important. For careful incell spectroscopy frequent window replacements (≈ 1 a month) are required. When the ablation sample is changed, we always remove the cell and carefully clean out the residual dust generated by ablation. We find this leads to a slower molecular beam, but I am not entirely sure why.

3.1.3 Buffer Gas Delivery

The final ingredient for the CBGB is well controlled flow of the cryogenic buffer gas. For our system we utilized two different mass flow controllers (AERA FC780C, and MKS 1259C) each capable of regulating the flow rate in different regimes. The controllers feed into a partially closed needle valve in order to step down the pressure, and then through several bobbins thermally anchored to the 4K head in order to ensure the helium is well cooled prior to it's introduction into the cell.

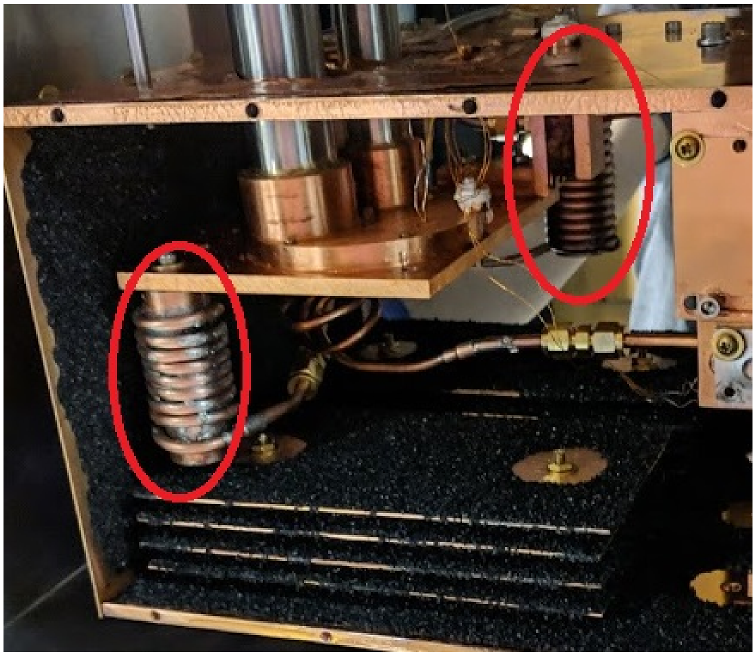

Figure 3.5: Thermally anchored bobbins are used to ensure the Helium buffer gas is well thermalized prior to reaching the cell.

Each flow controller was calibrated by monitoring the pressure in the cryostat when the system was at room temperature, and the vacuum pumps were valved off. The increase in pressure from out-gassing was quantified, then various flow rates of Helium were introduced and the rate of increase in the pressure was recorded. In the end, the factory calibration of both devices agreed to within 5% of the measured value. This was worth checking because the flow controllers are not designed to work with large pressure differentials across them, so we were unsure of their performance. We occasionally had leaks in the Helium delivery system from bad connectors or when swapping to a new Helium bottle that lead to freezes in the line. These freezes were due to non Helium contaminants getting into the system and icing somewhere along the feed-line. These blocks require the system to be warmed for them to be cleared, and would cost a day of data collection. Care should be taken when swapping out helium bottles, to avoid this.

3.1.4 Sample Preparation Techniques

There have been several different techniques used to inject the molecular sample of interest into CBGB sources but the most versatile, and the most common, is laser ablation. This technique requires a sample which either contains or is chemically similar to the molecule of interest. This sample is prepared into an ablation target and then hit with a focused pulsed laser. For our system we used a BigSky Ultra CFR 50 mJ pulsed ND:YAG.

In order to optimize the molecular yield we explored a wide variety of ablation targets. These included pressed and sintered ablation targets made from BaH_2 powder, BaH_2 pellet targets directly ablated, and the ablation on Ba in combined He + H_2 buffer gas (with Hydrogen concentration between .01 and 1 %). After trying each of these techniques, we found that BaH_2 “rocks" purchased from Sigma Aldritch were the best ablation target. Each technique generated similar average yields, which was a bit surprising, but the rocks targets had the most consistent yield and the targets lasted the longest time. Our sample preparation took place entirely in a home built glovebox because BaH_2 reacts aggressively with water, and we found that to contaminate the samples. In order to ensure a clean sample each “rock" was initially broken in half and the interior surface that had never been exposed to air was placed facing the ablation laser. We then arranged ≈ 5 samples onto the sample holder and glued them in place with locktite. We see increased sample lifetime (maintained signal strength after thousands of ablations events in the same spot) when we used more glue than necessary, and the glue “wicked" up the sides of the sample. I believe this helped hold the sample together, and decreased the rate at which the ablation laser physically removed material from the sample. This makes a substantial difference in sample lifetime.

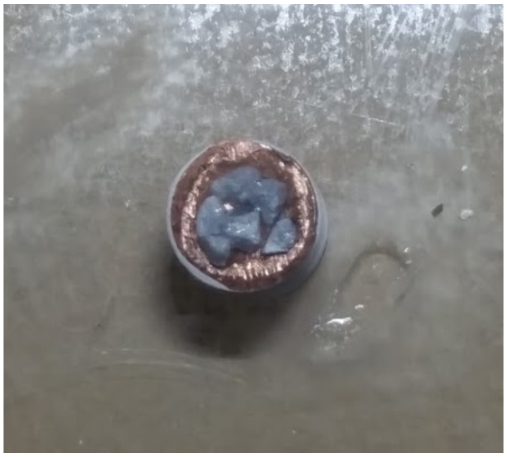

Figure 3.6: Example image of the BaH targets ready to be loaded into the cell. Note that slight "shine" caused by glue wicking up the sides of the targets. We found this greatly improved the lifetime of the sample during sustained ablation.

3.2 Laser Systems

In order to properly control cycling and applied optical forces we need to build laser systems that enable this control. Diode lasers make this relatively straight forward, and allow us to build the systems we need, on a smaller budget. I will not go into the basic's of laser operation, but instead focus on the practical implementation of external cavity diode lasers (ECDL), amplifiers, laser frequency stabilization based on a WS-7 wavemeter, and the various modulation techniques we use to control the frequency distribution of the lasers.

3.2.1 ECDL

In its most general form a laser is simply of a gain medium placed inside a leaky optical cavity. The cavity selects a specific mode that the gain medium amplifies, and the leak from the cavity is used to couple useful light out of the system, to be used for whatever application is desired. For the ECDL, the gain medium in a semiconductor chip, driven electronically, that is capable of emission at the wavelength of interests. The cavity is generated by a mirror placed behind the gain median, and an external element that used to selectively reflect light back into the chip, forming the cavity. This element usually consists of a diffraction grating, allowing the user to tune the wavelength of the reflected light, and therefore the frequency of the laser. In recent years these diodes have rapidly improved, leading to higher power outputs, and a broader spectral coverage. The two most common types of ECDL's, and the types used in this thesis, consist of the Littrow (Fig 3.2.1a) and Littman-Metcalf (Fig. 3.2.1b).

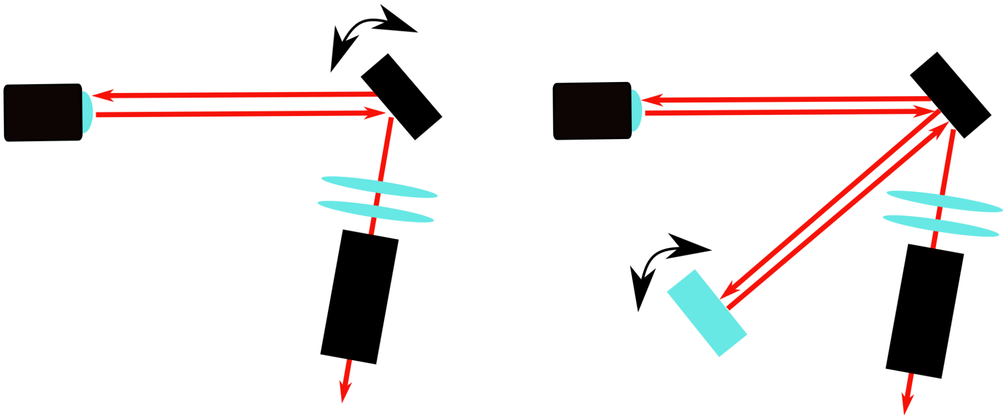

Figure 3.7: Schematic for the Littrow (left) and Littman Metcalf (right) ECDL configurations.

In the Littrow configuration, the first order diffraction mode of the grating is sent directly back to the chip, and the wavelength of the laser is tuned via the angle of this grating. The output of the laser is the reflection from the grating which is then sent to shaping optics (to get a circular Gaussian beam) and an optical isolator to avoid optical feedback destabilizing the laser mode. The Littrow configuration offers very strong feedback and higher power. The downside, is they generally have wider linewidth ($\approx 1MHz$) and the complication that changing the wavelength of the laser changes the angle of the output. Additionally, for applications where the desired wavelength is on the extreme reaches of the diode's specified output, the strong feedback allows for wider range of stable operation.

In the Littman-Matcalf configuration, the grating is stationary, and the first order diffraction peak is sent to a secondary mirror. The angle of this secondary mirror is tunable, and this allows the wavelength of the laser to be controlled. The output of the laser is again the reflection from the grating, and must undergoes the same shaping and isolation. The power of the Littman-Metcalf laser is typically $\approx 20\%$ lower than a Littrow laser, but the feedback requiring two diffraction's from the grating, and the increased length of the cavity, generally give a lower linewdith while lasing ($\approx$ 100 kHz). In addition, the output does not change when the laser is tuned, so realignment is not required when the laser is set to different wavelengths.

The performance of these two ECDL designs, is very dependent on the laser diodes they are implemented with. For the NIR around 1060 nm there are numerous very high power, and extremely stable diodes that make the cycling lasers used in this experiment extremely robust. However, for other wavelengths the performance is not always as good. I have found that Anti-Reflection coated diodes are required to make stable Littman-Metcalf lasers, but the strong feedback of the Littrow configuration mean non AR coated diodes can be used. The wider availability and reduced price of non AR coated diodes makes this a notable advantage.

3.2.2 Wavemeter Locking

Laser frequency stabilization in experiments with cold atoms is normally achieved by locking the lasers directly to the desired atomic transition using some form of saturation spectroscopy. However, for molecular experiments we cannot generate vapor cells with high enough molecular density in the state of interest to make this technique feasible. Instead, we have developed a digital locking scheme based on frequency measurements made with a WS-7 Wavemeter to accurately lock each laser for extended periods of time.

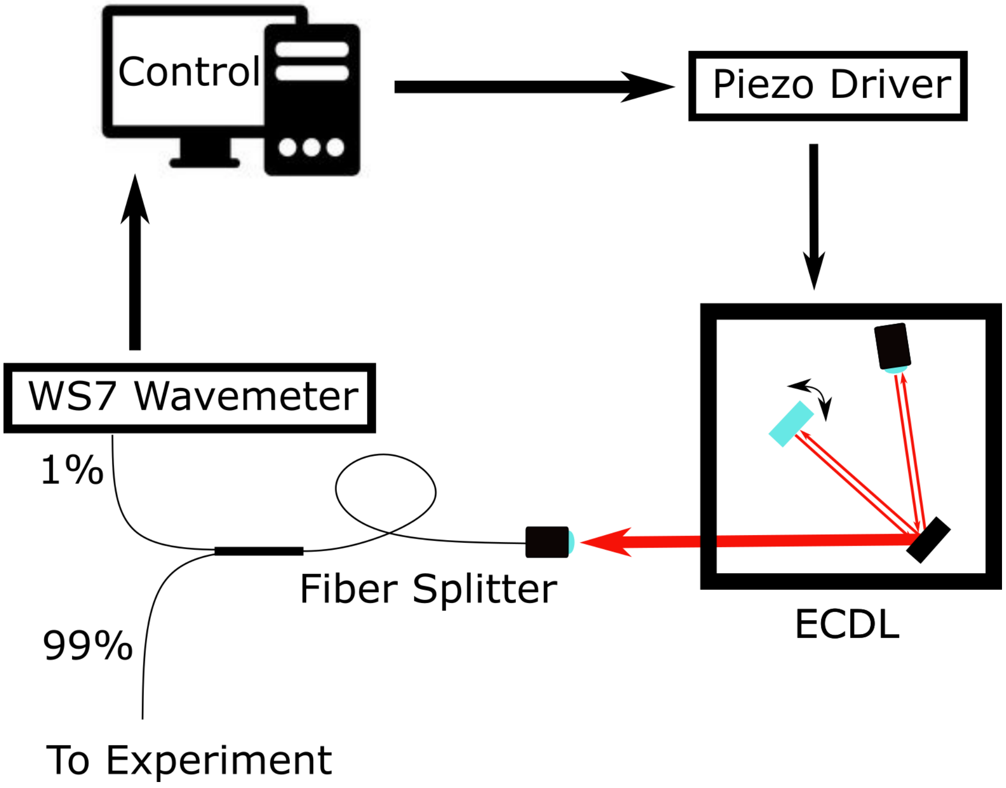

Figure 3.8: Block diagram for the digital laser locking servo. Control is implemented using a digital PID loop, based on measured error signals from the WS-7.

The system works by continuously monitoring the wavelength of each laser of interest using the WS7, then feeding that measurement into a digital PID loop on the central control computer. The control output for this loop is then passed digitally to an Attocube piezo driver, and the piezo used to control the feedback for each ECDL is adjusted. This loop operates at about 50 Hz for each laser and allows us to stably lock the lasers all day, limited only by occasional mode-hop. This technique is very convenient but does not narrow the laser below its free running linewidth. This is because the latency of the loop (limited by the time the WS7 wavemeter takes to acquire the signal) means feedback is relatively slow. It may be more accurate to think of this as a steering vs more traditional locking.

In order to verify the accuracy/stability of this scheme we performed a frequency comparison between the WS-7, a stabilized HeNe (Thorlabs HRS015B), and the Sr clock laser used by our sister experiment in the ZLab. The experiment operated by locking the clock laser to a frequency comb and establishing it as a stable absolute frequency reference. We then locked each laser used in the molecular cooling experiment to a constant wavelength, and left the system to collect data over the period of several hours. We found that when binned, the frequency spread of the clock laser had a FWHM of 1.6 MHz, indicating an instantaneous accuracy for the wavemeter lock, of $\approx 1.6MHz$. This was actually more accurate than the stabilized HeNe (2.7 MHz) indicating the wavemeter is a more precise reference than the HeNe. For long term stability tests, we have shown a day to day drift on the order of 5 MHz, by measuring the molecular transitions at the beginning of each day, and recording how they vary. No substantial drift on longer time constants then a day has been observed.

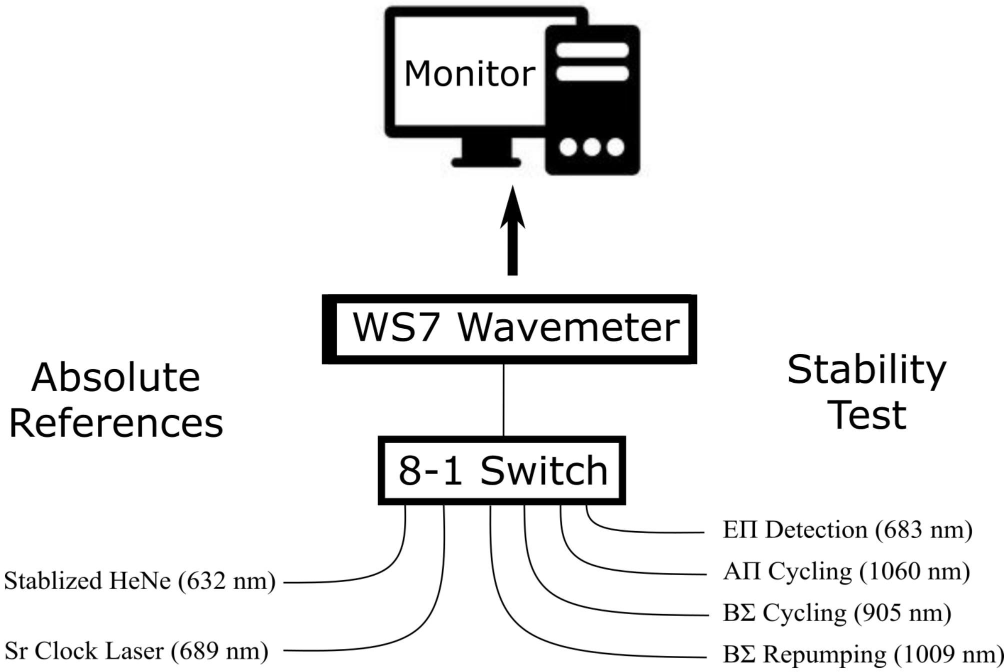

Figure 3.9: Setup used to test the stability of the wavemeter, and the wavemeter locking system

With an understanding of how accurate the WS7 can measure the wavelength of each laser we can also study how well the digital locking scheme can operate. We found that in general the infrared ECDL's used for cycling and repumping (1060 nm and 1009 nm) showed a FWHM frequency spread of $2.5MHz$ operating under normal conditions. This is consistent with the accuracy of the wavemeter limiting the lock, as the in loop error should be about the same as the open loop error of the sensor used for feedback. However, we did find that the “quality" of the mode and the thermal stability of the laser to be extremely important to achieving this performance. When the thermal control loops were improperly tuned, or the laser was slightly multi-mode (an un-observable difference on the wavemeter itself, but visible on a scanning Fabry Perot Interferometer) an order of magnitude worse performance was observed. This must be carefully monitored because unlike locking to a saturation spectroscopy setup, the lasers will not always tell you when they are misbehaving.

This system is a scalable way to lock many lasers, and the only cost to increasing the number of lasers your control is a reduction in the speed of the feedback. We currently use a 8-1 multiplexing input to the wavemeter, so 8 lasers can be stabilized, but laser switches are available. Because molecule cooling experiments require many lasers, and the large splitting in the ground state make hydrides particularly challenging, an easily scalable solution like this digital lock has proven to be very important.

3.2.3 Laser Amplification

In order to achieve efficient cycling and laser cooling high optical powers are required, typically above what is possible with ECDL’s alone. To increase the available laser power we used two technologies, fiber amplification, and tapered amplifier amplification. The fiber amplifier was bought commercially from NKT, and operated as a turn key solution to amplify 10 mW of seed light, up to 2 Watts of output light. For the tapered amplifier we built our own system in house, to use the high power NIR chips sold by DILAS systems. Drawings for this design are provided in the appendix. Tapered amplifiers are essentially the gain chip from a diode laser, without the mirror required to form a cavity. Light is focused into the input facet (as shown in Fig. 3.2.3) and as the input is amplified, the transverse width of the gain medium increases, to keep the intensity inside the gain medium low. The output is then re-collimated, goes through beam shaping and isolation, and is then fiber coupled.

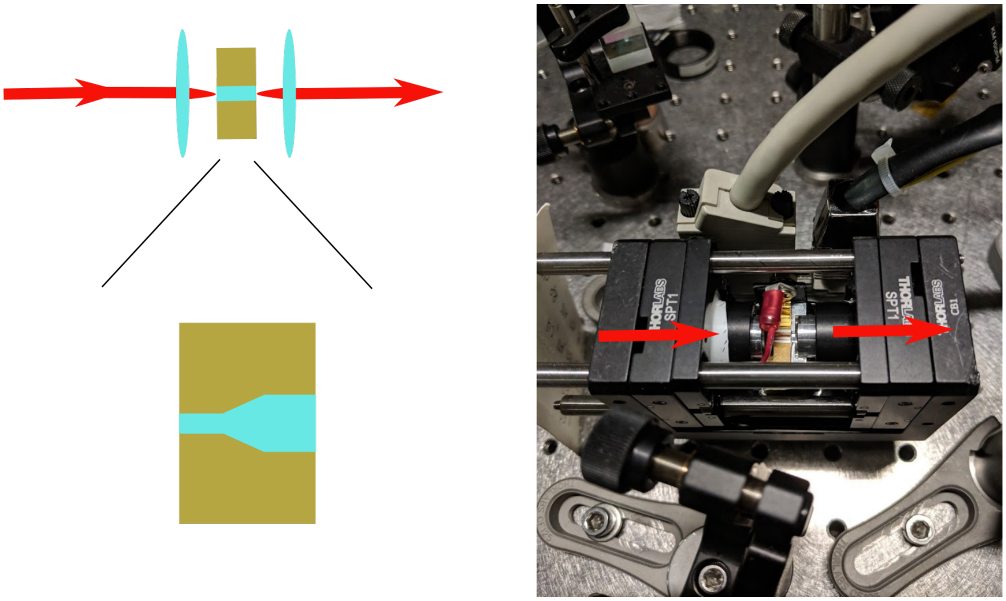

Figure 3.10: Simplified schematic, for laser amplification using a tapered amplifier chip, and photo of the implemented system

For this experiment, we actually used two seed lasers separated by $\approx$ 10 GHz as the input to the amplifier. We find this works well, as long as the spacing between the two inputs is greater than about 1 GHz. For smaller separations, we observe non-linear mixing in the gain medium, resulting in the generation of a comb type spectrum. This has been previously measured, but was surprising when we first observed it. Tapered amplification provides a cost efficient way to amplify laser light but the imperfect shape of the amplified beam limits fiber coupling efficiency to $\approx$ 50%. Fiber amplification however is capable of much higher powers, has excellent beam quality, but does not cover as broad a range of wavelengths.

3.3 Laser Modulation Schemes

ECDL's and amplifiers are responsible for the rough shaping of the spectra we use for addressing the molecules but finer control is also needed. The splitting of energy levels due to various couplings introduced in Chapter 2 must each be addressed, with a typical energy splittings from 1 MHz and 10 GHz. For splitting above 1 GHz we address each transition with a separate laser. For smaller splittings we use two modulation techniques. Phase modulation using the Electro-Optical Modulator (EOM), and direct sideband addition using an Acoustic Optical Modulator (AOM).

3.3.1 The EOM

EOM's are based on the Pockel's effect inside a crystal. By applying an electric field, we can control the index of refraction of the crystal, which effects the phase of the laser as it passes through the crystal. By applying a time varying voltage across the crystal (leading to a time varying internal electric field) we can modulate the phase of the laser. To demonstrate how this can be used for sideband generation, first let us consider the electric field generated by a monochromatic laser beam.

$$E(t) = Ae^{i\omega t}. \tag{3.2}$$

Where, the amplitude of the electric field A depends on the intensity of the laser, and the field oscillates at the angular frequency ω. Now, if a periodic phase modulation is applied, we can write this without simplification, as

$$E(t) = Ae^{i(\omega t + Dsin(\Omega t)))}, \tag{3.3}$$

Where Ω is the angular frequency of the modulation, and D is known as the modulation depth. This expression, can be rewritten using the Jacobi–Anger expansion as a sum of terms, each with a fixed frequency.

$$E(t) = Ae^{i\omega t}\left(J_0(D) + \sum_{k=1}^{\infty} J_k(D)e^{ik\Omega t} + \sum_{k=1}^{\infty}(-1)^k J_k(D)e^{-ik\Omega t}\right), \tag{3.4}$$

where J_n is the nth order Bessel function of the first kind. We see that based on the modulation depth (D) we add symmetric side-bands each spaced Ω away from the carrier frequency ω. An example for how these Bessel function behave vs. the modulation depth, and an example of how the side-bands appear is shown in 3.3.1.

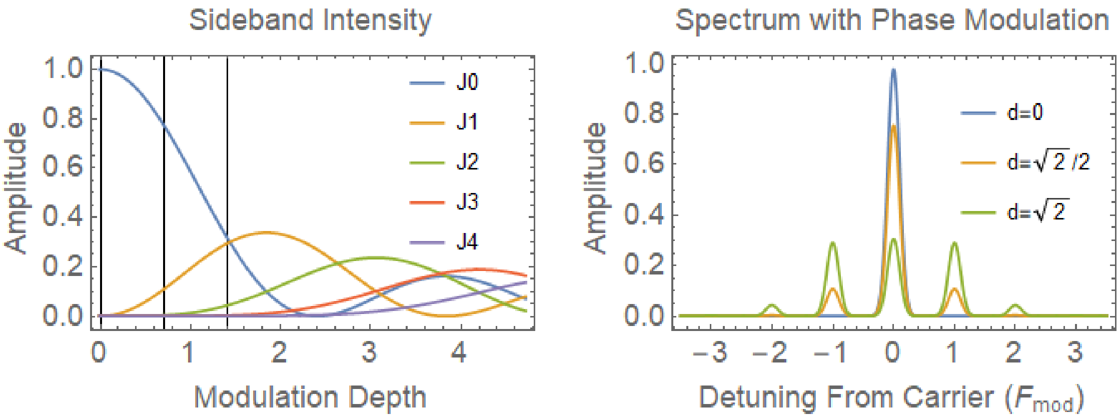

Figure 3.11: Bessel Functions, and the resulting spectrum for three different modulation depths. Note that the spectra is symmetric, and only the modulation depth and frequency are free parameters.

The crystals that make up the core of the EOM, are Lithium tantalate with gold electrodes placed on two sides (provided by Almaz Optics). The two electrodes act like a parallel plate capacitor, and that allows use to add a tuned inductor to build LC tank circuits at the desired modulation frequency. This is helpful because by building a resonantor, we can apply a larger voltage across of the inductor for the same drive power, increasing the modulation depth. For convenience, we want the system to have 50 Ohms input impedance so it can be easily driven using commercial RF amplifiers, so we use a transform at the input of the circuit for impedance matching. The electrical schematic, and the implemented system are shown in 3.3.1

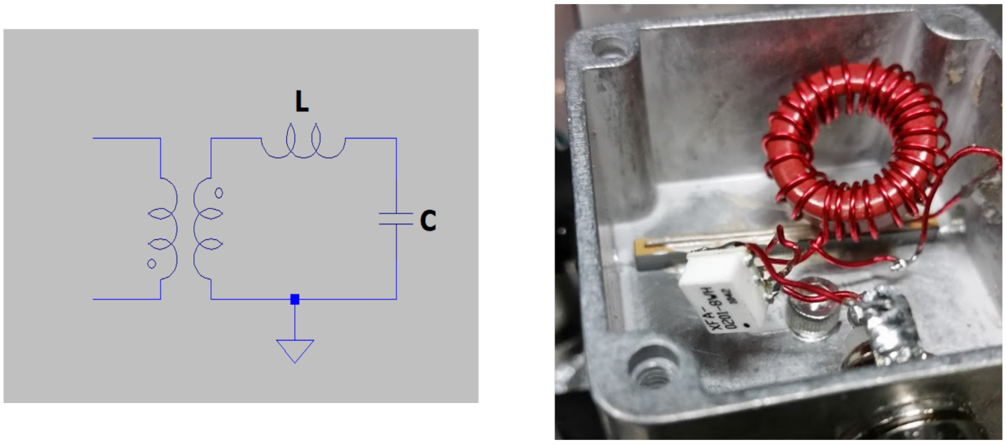

Figure 3.12: Electrical schematic, and physical implementation of a resonant tank circuit to drive an EOM

The addition of multiple EOM's in the row, can be used to broaden the spectra of a laser in a controllable way. This is used in the technique known as "White Light" slowing, by broadening the laser so it stays resonant with a wider range of velocity classes. By varying the modulation depth, and having multiple modulation frequencies, you gain a lot of control over the spectrum. To demonstrated this, a simulated spectra for the white light slowing of BaH is shown in fig.3.3.1. The relatively flat top, ensures an even force, and the range of velocities you address is easily tuned.

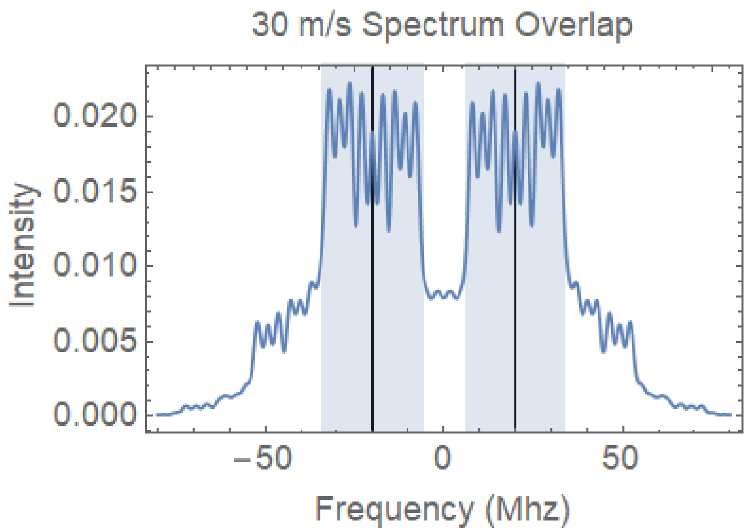

Figure 3.13: Simulated spectra for the white light slowing of BaH. The two bands indicate the absorption range for the J=3/2 ground state (hyperfine splitting of 40 MHz) with a 30 m/s spread in forward velocity. 60% of the light, ends up being resonant with this desired class of molecules.

3.3.2 The AOM

For this experiment AOM's are used when we wish to add side-bands that are not symmetric. AOM's work by generating an acoustic wave using a piezo element attached to a crystal, resonantly driven at some desired frequency. When the angle between this acoustic wave, and the laser passing through the crystal satisfy the Bragg condition, diffraction occurs. This diffracted beam has an angular displacement, and the frequency is shifted by an integer of the driving frequency. Typically these devices are designed to operate at the +/- first order, but higher order diffraction is possible. The optical layout used for the generation of balanced sidebands, is provided in fig.3.3.2.

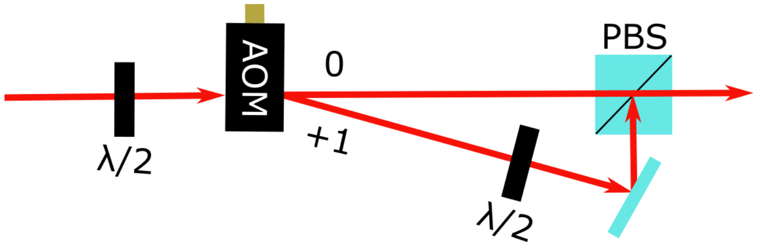

Figure 3.14: Optical layout to add a sideband to a laser using an AOM. The first order diffraction is realigned with the 0th order using a mirror, and combined using polarization on a polarizing beam splitter. Results in crossed polarization for the two sidebands, and the height of the relative sidebands can be controlled using the drive power of the AOM.

Note, that because polarization is used to recombine the laser light after the AOM this scheme has very low loss for adding a single sideband but has ≈ 50 % loss when trying to add 2 side bands. This makes EOM sidebands potentially more efficient, but it depends on the details of the spectrum you are trying to obtain. For this experiment we used commercially purchased AOM's from ISOMET, and used an amplified DDS for all the driving frequencies.

3.4 Vacuum System and Beam Chamber

Like other cold atom experiments we require the samples to be well isolated from the environment, and in particular from collisions with background gases. To avoid these collisions typical experiments need to operate in ultra high vacuum (UHV) with pressures as low as 10^{-10} Torr. In this UHV region, background gas collisions become negligible, but it quite hard to achieve experimentally. For our system we do not require as low a vacuum because the lifetime of our experiments is on the order of 10-100 ms (versus 10-100 seconds) so we can tolerate a higher background collision rate. A schematic for the vacuum system we designed is given in fig.3.4. Both turbos are backed with XDS-10 scroll pumps. We find that the cryostat, when it is being pumped down the first time after opening, requires the ballast of the scroll pump to be open for $\approx$ 3 hours to remove moisture from the system. If this is not done moisture builds in the scroll pump and it's base pressure is never reached. I believe this is due to the charcoals affinity for collecting moisture from the room when exposed directly to air.

For the cryostat we have a Pfieffer TPU-170 turbo pump to provide rough vacuum prior to the cryostat cooling down. We find that while the cryostat is at room temperature we hit a base pressure of mid 10^{-6} Torr, limited by out-gassing in the system and not by the O-ring seals used on the cryostat. When the cryostat is fully cold we reach a base pressure low 10^{-8} Torr, consistent with the base pressure you can achieve with O-ring seals. This is partly due to the reduced out-gassing of the cold components, but is primarily due to cryogenic pumping provided by the charcoal in the 4K region. We have not performed a carefully measurement of the charcoals pumping speed, but when the turbo is valved off from the cryostat we see no reduction in the pressure of the cryostat. This implies the pumping speed on cryogenic charcoal is much higher than that of the pump itself. It also worth noting that after several years of operation a micro crack in one of the welds of the cryostat was discovered. Fixing this with UHV epoxy lead to an order of magnitude improvement in the vacuum level while warm, but no improvement while cold, implying the pumping rate is so high even a micro-crack worth of gas load can be efficiently pumped. More details of the charcoal sorbs are discussed in section 3.4.1.

When the buffer gas beam is operating, and 1-5 SCCM of He is being sent into the system, we see the pressure rise to the high 10^{-7} or low 10^{-6} Torr level. The exact vacuum level depends on the flow rate, and how long the system has been operating since we last warmed up. This is currently being improved, with the addition of more charcoal sorbs, to increase the pumping speed (lowering the vacuum level under operation) and extending the lifetime of the system.

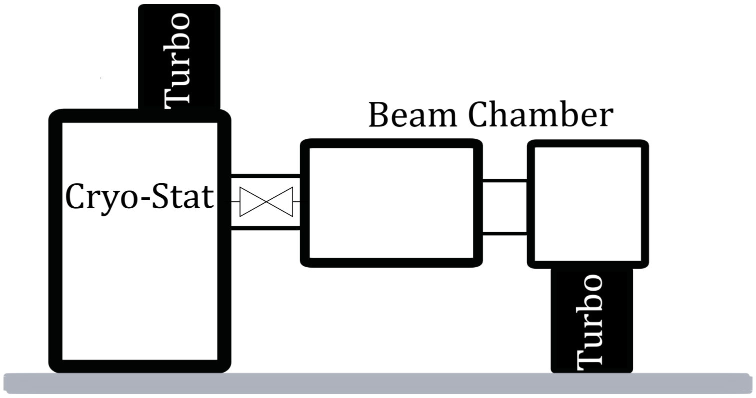

Figure 3.15: Representative schematic for the vacuum system used in these experiments. Separate turbo pumps and a gate valve allow us to break vacuum on either region independently, allowing for faster upgrades and tolerance in the case of pump failure.

The cryostat is separated from the rest of the beam region, using a KF 50 gate valve, allowing the two regions to be fully isolated. The pumping in the beam region is provided by a HiPace 700 l/s turbo pump mounted at the end of the beam region, ensuring there is no helium build up under operation. This system has a base pressure of 10^{-8} Torr limited by the KF connection to the cryostat, and the O-Ring seal for the extended interaction region (shown in fig.3.4). While He is flowing we see an increase of the pressure in the beam region to the low 10^{-7} Torr. Various iteration of the vacuum system were used, but always featured an Pfieffer PKR 360 ion gauge to monitor the pressure in the region, and ExTorr RGA to help find any leaks. The final system capable of 3D trapping will require improved vacuum performance, and a differential pumping stage in order to not be limited by the vacuum of the cryostat itself.

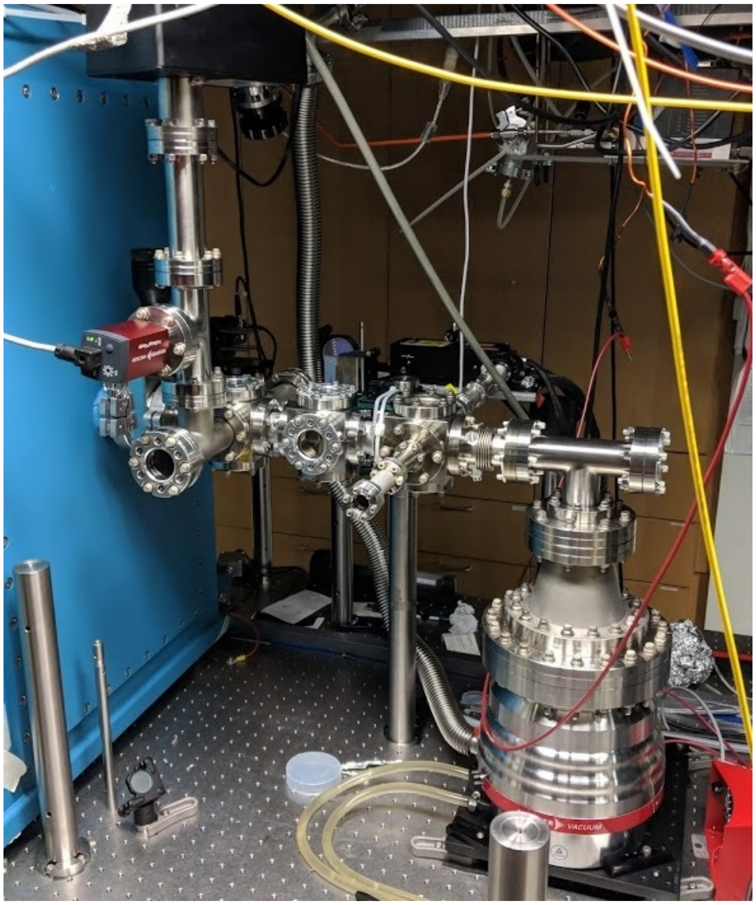

Figure 3.16: Photo of an early version the beam region, prior to the installation of optics.

By using commercially available vacuum components, early versions of the beam region were quite cheap, and could be assembled very rapidly. However, the limited optical access from commercial 2.75 inch CF windows lead to relatively small interaction times and made the detection of transverse cooling/deflection of the molecular beam challenging. To extend the interaction time a custom 2D cooling region was designed using long rectangular windows to increase the optical access. This, along with custom rectangular mirrors, allowed is to have sustained interaction over an $\approx$ 13cm region, by sending the laser light back and fourth through the molecular beam. An image of the this long interaction region is shown in fig.3.4. This extended interaction region has been used for 1D cooling of the molecular beam (Chapter 7) and can also be used for 2D cooling in the future.

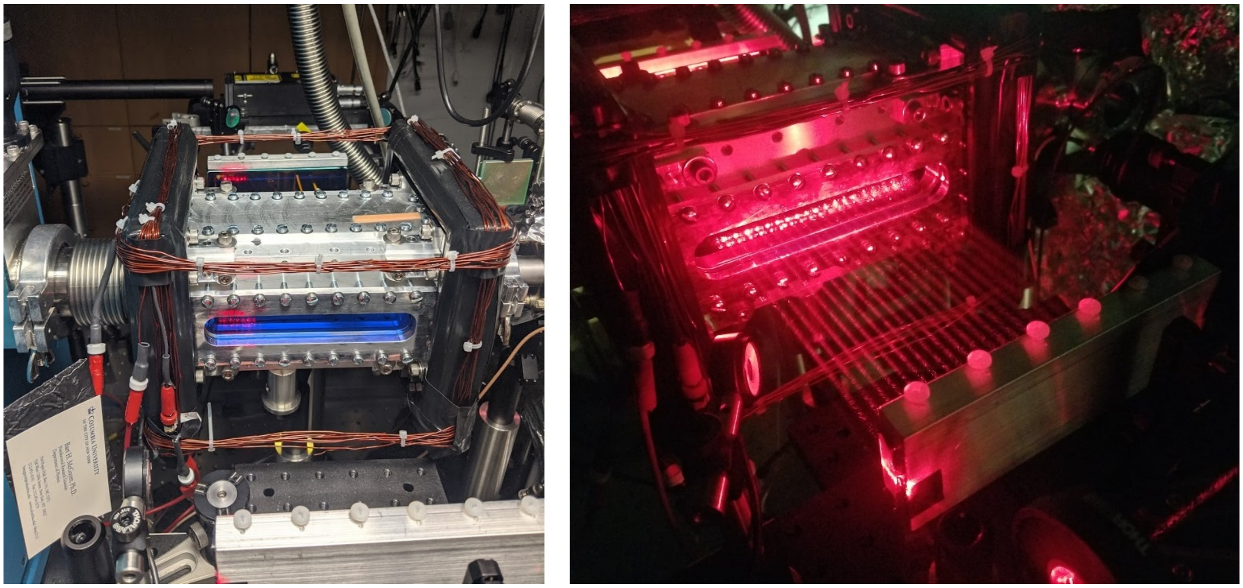

Figure 3.17: Side image of the custom interaction region, and laser light for ≈ 40 passes through the molecular beam.

3.4.1 Cryo-Sorb Performance

It is bit surprising that CBGB sources can be integrated with laser cooling experiments because high vacuum and the active introduction of a buffer gas seem to be conflicting requirements. The incredible pumping speed of cryogenically cooled coconut charcoal makes this possible, A happy coincidence that enables each of these experiments. When cooled below ≈ 14K, the surface of the charcoal begins to act as an extremely good physio-sorb pump. That is to say, when helium collides with the surface, it physically (versus chemically) bonds and sticks to the surface. This combined with the massive surface area of charcoal, a highly amorphous solid, allow coconut charcoal to act as a rapid pump with a high pumping volume able to efficiently pump enough He to maintain high vacuum in the cryostat for an entire day of data collection. Each internal surface of the 4K region is covered in charcoal, which is glued to the copper shields using a thermal epoxy (see appendix for details). In addition, we saw greatly improved beam performance with the addition of several fins, and with a coated skimmer the molecular beam must pass through prior to leaving the cryostat.

The sorb pumps are reactivated nightly, by allowing the cryostat to warm up. When the temperate reaches around 14K the helium no longer sticks to the charcoal and a large spike in pressure occurs, often driving the pressure above 1 Torr. This pressure spike is pumped out using a turbo attached to the top of the cryostat (see fig.3.4) and the system is left to pump down overnight. The PTR is then restarted automatically around 6 hours before we plan on taking data, allowing time for the system to cool back down. We see that even if the in cell absorption signal is strong (indicating we are still making molecules), data collected at the end of the day typically has a diminished signal size down stream. We believe this is due to decreased pumping speed of the sorbs as they saturate, leading to higher pressure in the cryostat which attenuates the beam. Increasing the total surface area of charcoal in the system improved the performance, but it still limits us to $\approx$ 8 hours of continuous data.

Chapter 4: Cryogenic Buffer Gas Source and Absorption Studies

A CBGB is the first step towards the direct laser cooling of molecules, but it also provides an excellent environment to study the molecule of interest. The high density generated post ablation leads to high SNR for absorption spectroscopy, and the cryogenic environment limits Doppler broadening, and concentrates the population into low lying rotational levels. In this chapter I will discuss experiments performed both to characterize the CBGB source as well as experiment done with the molecules immersed in the buffer gas. This work was essential to understand the system we built (the CBGB) and the system we want to use (BaH itself).

4.1 CBGB Source Characteristics

In order to be useful as a source for cold molecules for laser cooling applications, the CGBG needs to act a stable and high output source of molecules in the N=1 rotational level. This requires stable molecular production, as well as thermalization of the external and internal degrees of freedom. For BaH we quantified the thermalization rates of the rotational state and the motional degree of freedom. This served to validate the source is able to generate the cold molecules we need for the rest of the experiments in beam. This is essentially a study of the elastic collisions that thermalize the velocity distribution, and the inelastic collisions that thermalize the molecules internal rotational distribution. In this experiment we were unable to observe higher lying vibrational states as a product of ablation, so we did not study vibrational relaxation. To begin, it is useful to consider the on resonance absorption of a laser passing through the cell after the ablation laser has fired.

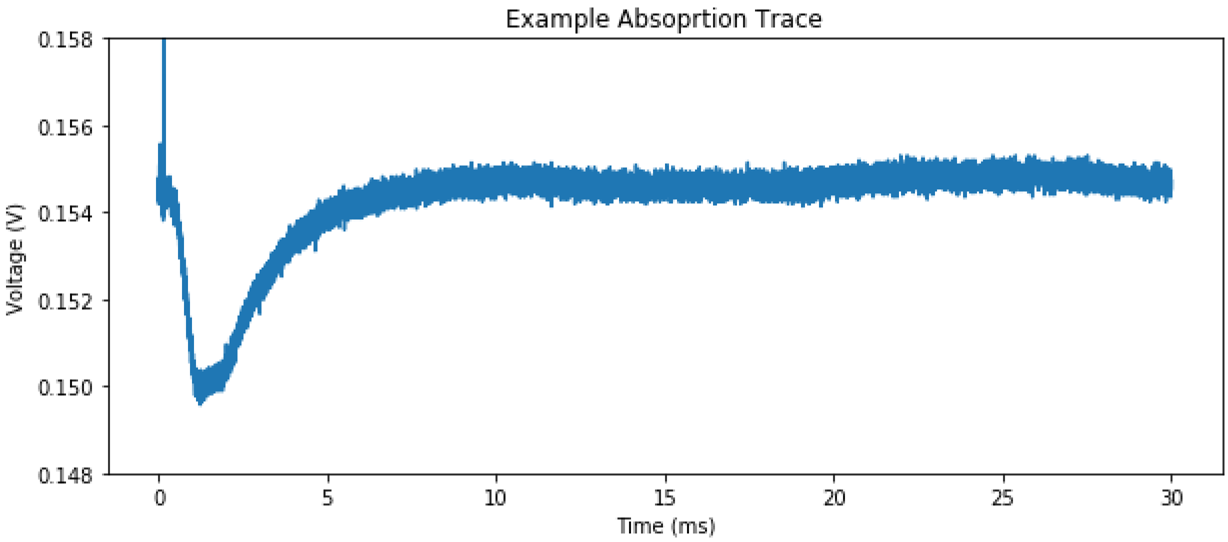

Figure 4.1: Typical absorption trace, for an on resonance probe. The initial spike is caused by electrical noise from the firing of the ablation laser. Exact shape of these traces is highly dependent on the details of where on the sample ablation occurs, as well as the detuning of the probe laser

We see the molecules pass through the probe laser $\approx$ 1 ms after the ablation laser has fired, with a fairly broad arrival time. Depending on the flow rate and the quality of the sample we see between 3% and 20% peak absorption of the probe light, however higher in cell absorption does not always correlate with a brighter molecular beam outside the cell. As a crude measurement of the signal strength we can integrate this absorption signal and use that as a metric to perform spectroscopy.

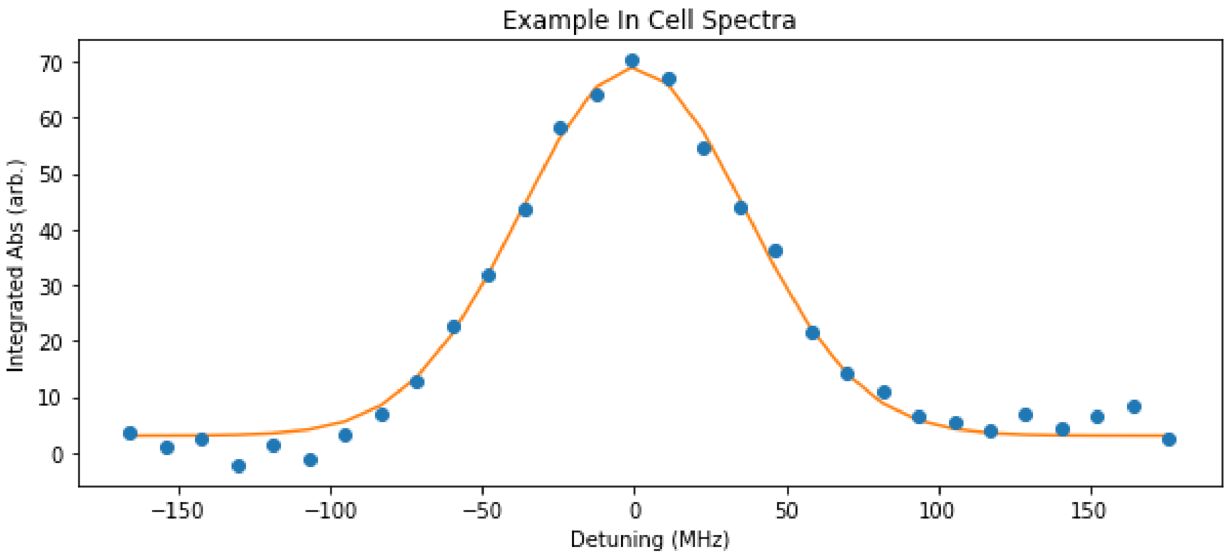

Figure 4.2: By integrating the absorption trace and varying the probe detuning we can perform in cell spectroscopy for any transition of interest. This is the highest sensitivity way to find transitions in our experiment

4.1.1 Motional Temperature

Based on previous studies, we know that immediately after ablation the ejected molecular cloud is extremely hot, on the order of 1000 K. Thanks to collisions with the He buffer gas we can reduce this temperature, but the rate of this thermalization is very important. We need thermalization to be faster than the cell extraction time (so the molecules are fully cooled) and faster then the diffusion time of the molecules to the walls of the cell (where the molecules are lost).

To quantify this we performed in cell spectroscopy then looked at the time dependence of the center location and width of the absorption resonance. This allows for a real time measurement of the molecules velocity distribution, and therefore the rate of thermalization. there is also collisional broadening in cell, and unresolved hyperfine structure, so the final linewidth is an upper bound. This data is analyzed by taking time slice of absorption traces for various laser detunings, and fitting them each to a Gaussian distribution.

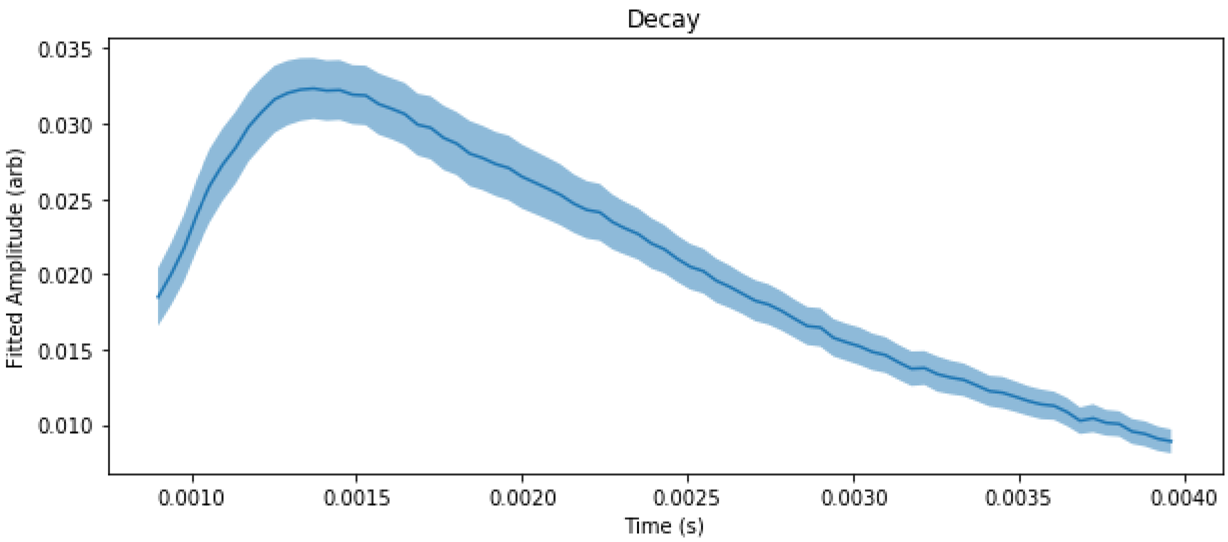

Figure 4.3: Fitted amplitude of the spectra taken at each time slice. Shows the same approximate shape as Fig. 4.1.

As expected, we see a pulse like structure when we just consider the amplitude of the fitted spectra. This is a direct measurement the molecular density passing through the probe laser after ablation occurs.

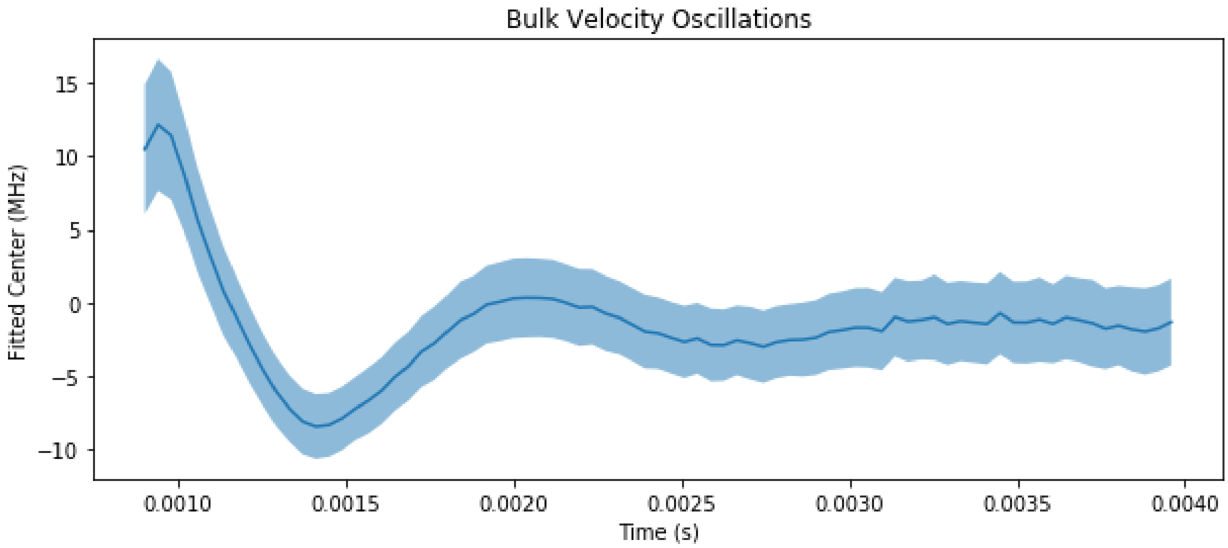

Figure 4.4: Here we see a clear time dependence for the fitted line center after ablation. This is consistent with the molecules having a net velocity after ablation, that takes some time to settle down as they thermalize with the buffer gas

Somewhat surprising we see that there is a meaningful oscillation in the fitted line center after ablation. This is consistent with “sloshing" of the molecules post ablation. Because the molecules have preferred direction after ablation (ejection from the surface of the sample) it takes a while for that net velocity to be damped.

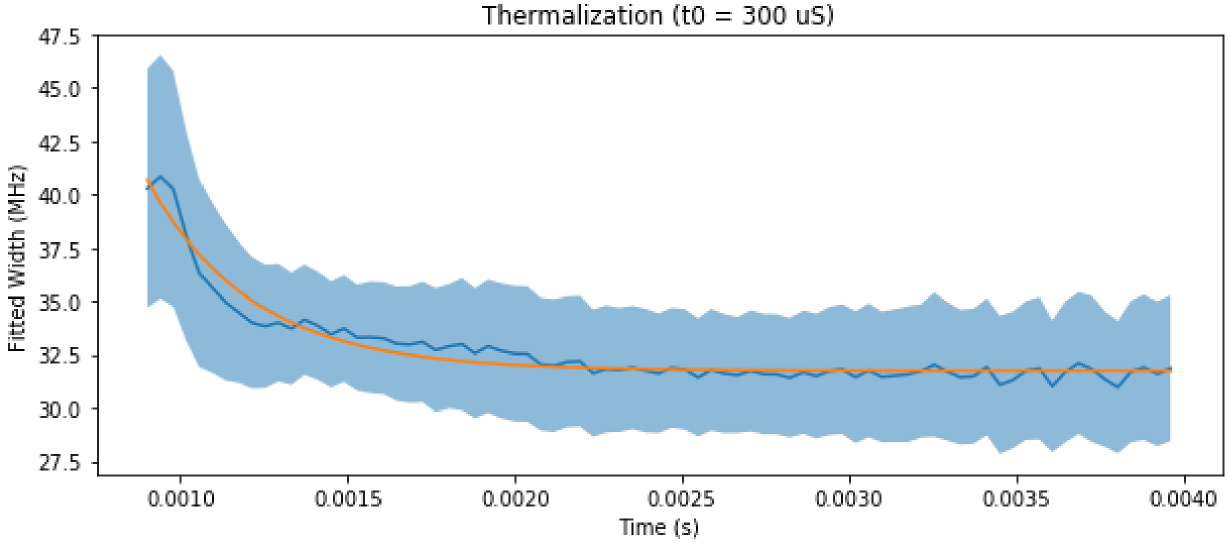

Figure 4.5: We see the measured linewdith decrease as the molecules thermalize with the He buffer gas. This allows us to estimate the thermalization time, to be on the order of 300 μs by fitting this measured linewidth to an exponential. Note, that due to unresolved hyperfine structure, this final linewidth is artificially large, but we only care about its time dependence to estimate the thermalization time.

Finally, we can see that the width of spectra meaningfully decreases over the course of its transit through the laser beam, with a decay constant of $\approx$ 300 μS. This is encouraging, because we see that thermalization has occurred. Final linewdith here is not important, as there are unresolved hyperfine transitions in this spectra, and there will be some amount of collisional broadening in cell. However, the rate of change of this width is a useful confirmation that thermalization occurs faster than extraction time. This time constant is quite fast, and happens before the molecules are extracted from the cell. In fact, we see that thermalization occurs before the majority of the molecules even reach the probe laser location.

4.1.2 Rotational Temperature

To study the thermalization of the rotational degree of freedom, we took repeated measurements of the absorption vs. time for various different rotational states in the molecule. We did this ensuring that the analogous transition was driven each time, so the relative absorption of each state was a faithful representation of that's states population. We can then take the population of each rotational state at a given time, and fit it to a the known relationship between temperature and rotational distribution. This allows us to extract the rotational temperature, and study how it evolves post ablation. For this data, we were unable to simultaneously collect absorption measurements on each transition at the same time, so we quickly changed which transition we addressed, maintained the same ablation properties, and collected the data in a random order. A snapshot of the thermal distribution at 1 mS post ablation is shown below.

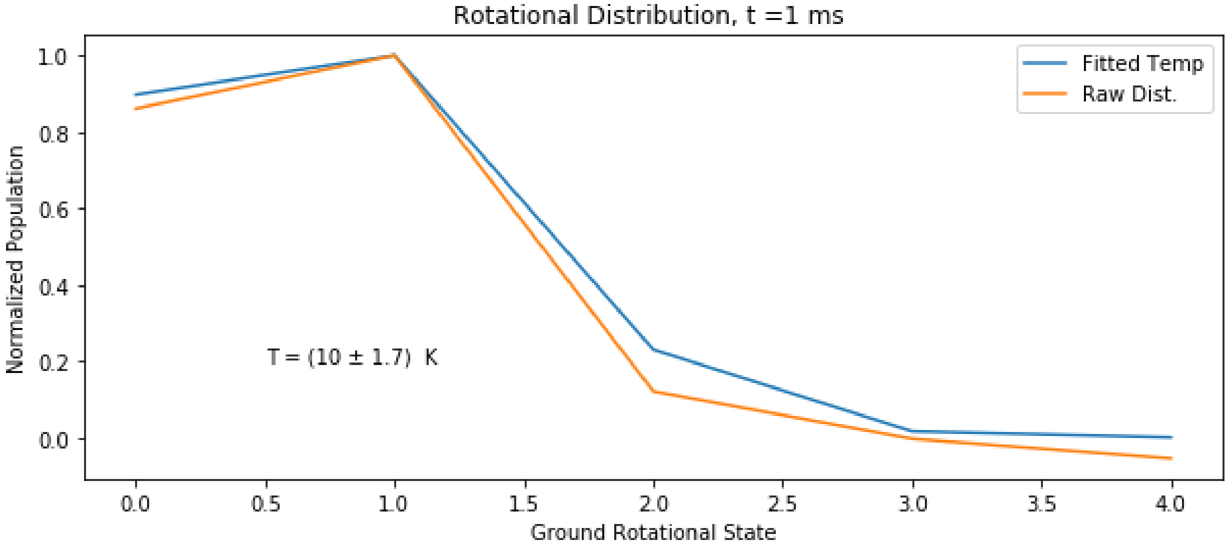

Figure 4.6: By measuring the relative population of each rotational state, we can estimate the internal temperature of the molecule by fitting it to the weighted Boltzmann distribution discussed in Chapter 2

We are then able to take this distribution, and the fitted temperature with uncertainties, to estimate the rotational temperature post ablation, and extract the thermalization rate.

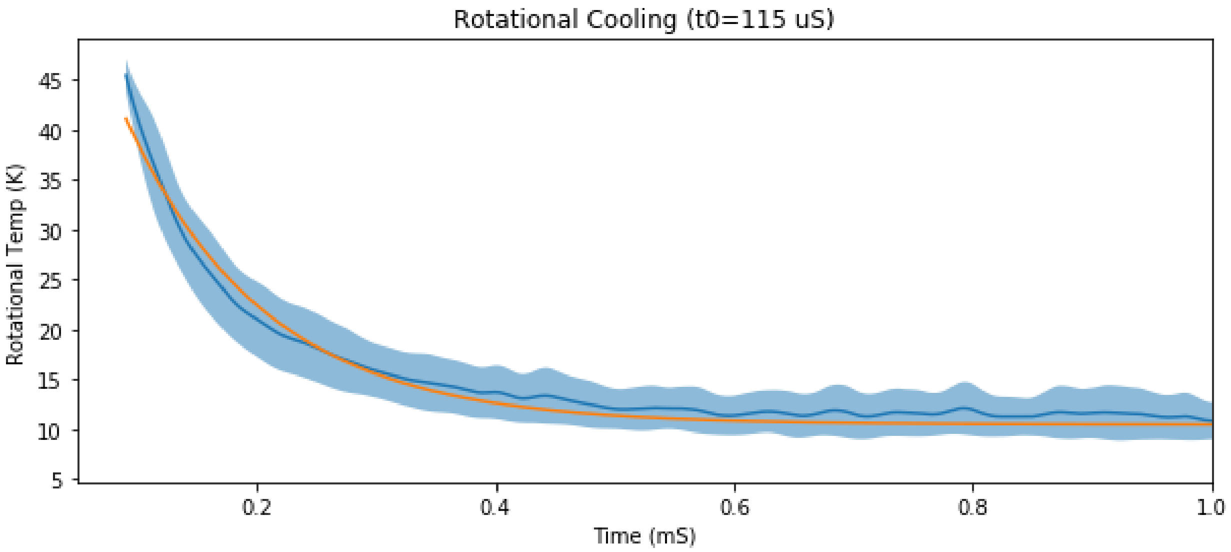

Figure 4.7: By estimating this population distribution as a function of time, we can estimate the rotational thermalization rate, finding it occurs at $\approx 100\ \mu$s, faster than the motional thermalization rate.

We find that the the rotational distribution thermalizes on the order of 100 μs, which is sufficiently fast to ensure a large population in the N=1 state, as the target state for laser cooling. We find the final rotational temperature to be above the measured temperature of the cell (10 K vs 6K) but are primarily concerned with maximizing the N=1 state, so the discrepancy is not a concern.

4.2 In Cell State Searches

Thanks to the high sample density in cell, it is the ideal place to search for new transitions and states in the molecule. This allows us to focus more precise in beam searches on a narrower range. In particular, we used in cell absorption measurements to find the vibrational repumping states in BaH, which proved to be the best way to perform this search.

4.2.1 v=0 → v=1 Pumping Search

In order to close the vibrational loss the the v=1 state, and maintain closure of the cycling transition, we need to efficiently pump molecules out of the v=1 state. This requires precise knowledge of the transition energy, which was beyond the measured accuracy of measurements available for

BaH before we began this project. This means we must go and find these transitions ourselves. However, the v=1 state is not naturally populated in cell post ablation. Therefore, we first need to pump molecules into the v=1 state. We achieved this by optically pumping the molecules using an off diagonal v=0 → v=1 transition.

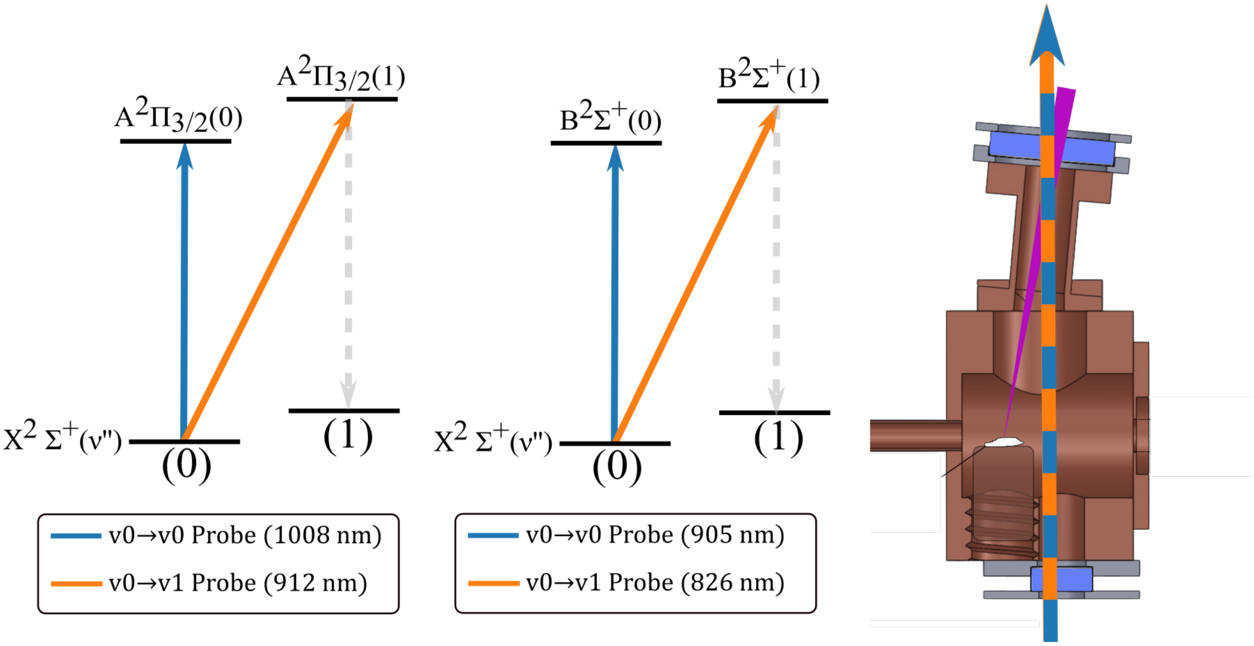

Figure 4.8: Experimental diagram showing the energy levels, and experimental setup, that were used to search for off diagonal transition in the $B^2\Sigma^+$ and $A^2\Pi$ states.

For this search we used previous measurements to estimate the location and performed simultaneous absorption measurements of the pumping state and a known cycling transition. This allows us to monitor the molecular yield even when the pumping laser is off resonance.

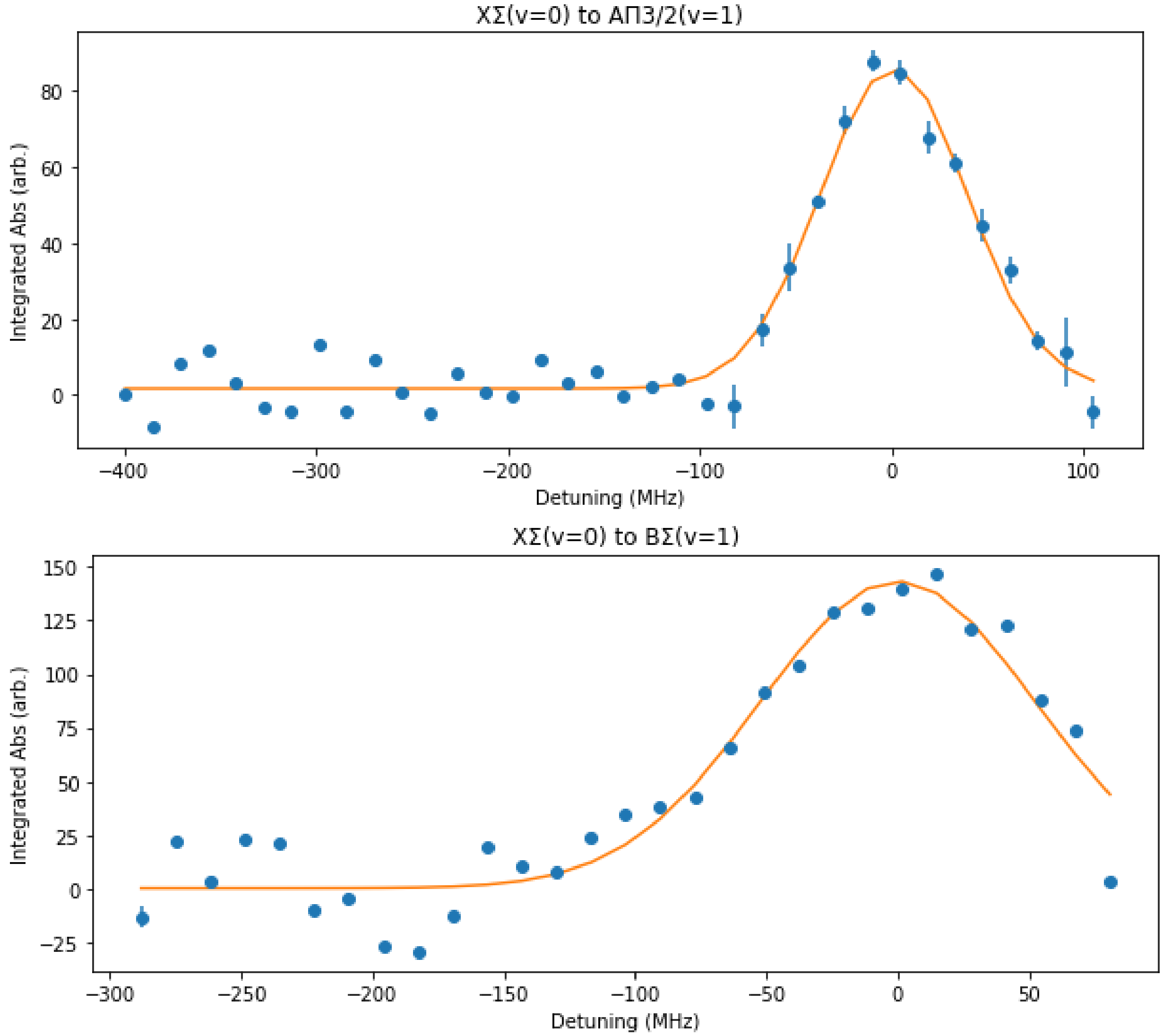

Figure 4.9: Absorption spectra for two $X^2\Sigma^+$(v=0) to higher lying vibrational states. These were used for Frank-Condon factor measurements (see Section 3 of this chapter) and for direct population of the $X^2\Sigma^+$(v=1) state.

By finding each of these transitions we can efficiently populate the v=1 state in order to search for the vibrational repumping transition. Note, that we can also use the this data for direct measurements of the FCF, as discussed in section YYY

4.2.2 v=1 → v=0 Repumping Search

With confirmation that we can pump into the v=1 state, we can now search for the repumping transition. In order to perform accurate spectroscopy we also need to pump the the molecules into the v=1 through an alternative state so as not to perturb the resonance. This is performed using a displaced pump laser. A diagram for this experiment is shown in fig.4.2.2.

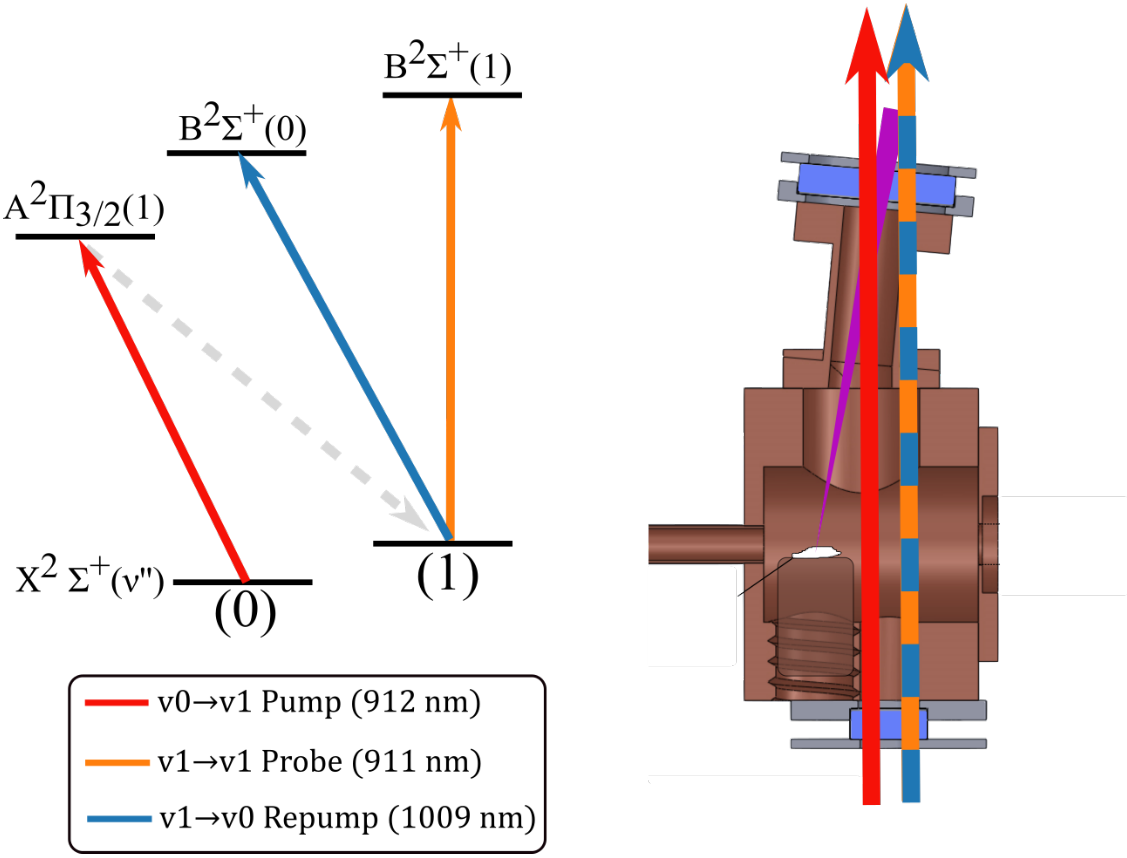

Figure 4.10: Level structure diagram, and experimental setup used for the $X^2\Sigma^+$(v=1) repump search. The 912 nm pump light was used to populate the $X^2\Sigma^+$(v=1) state, and two different transitions were used to probe the population, and perform spectroscopy.

With this scheme, we were able to directly find the repumping transitions, and accurately measure the spin rotation splitting of the $X^2\Sigma(B = 1, v = 1)$ state. This was a crucial step, as direct searches for the repumping transition in the molecular beam (vs. incell) were not successful. The increased SNR of incell absorption was critical.

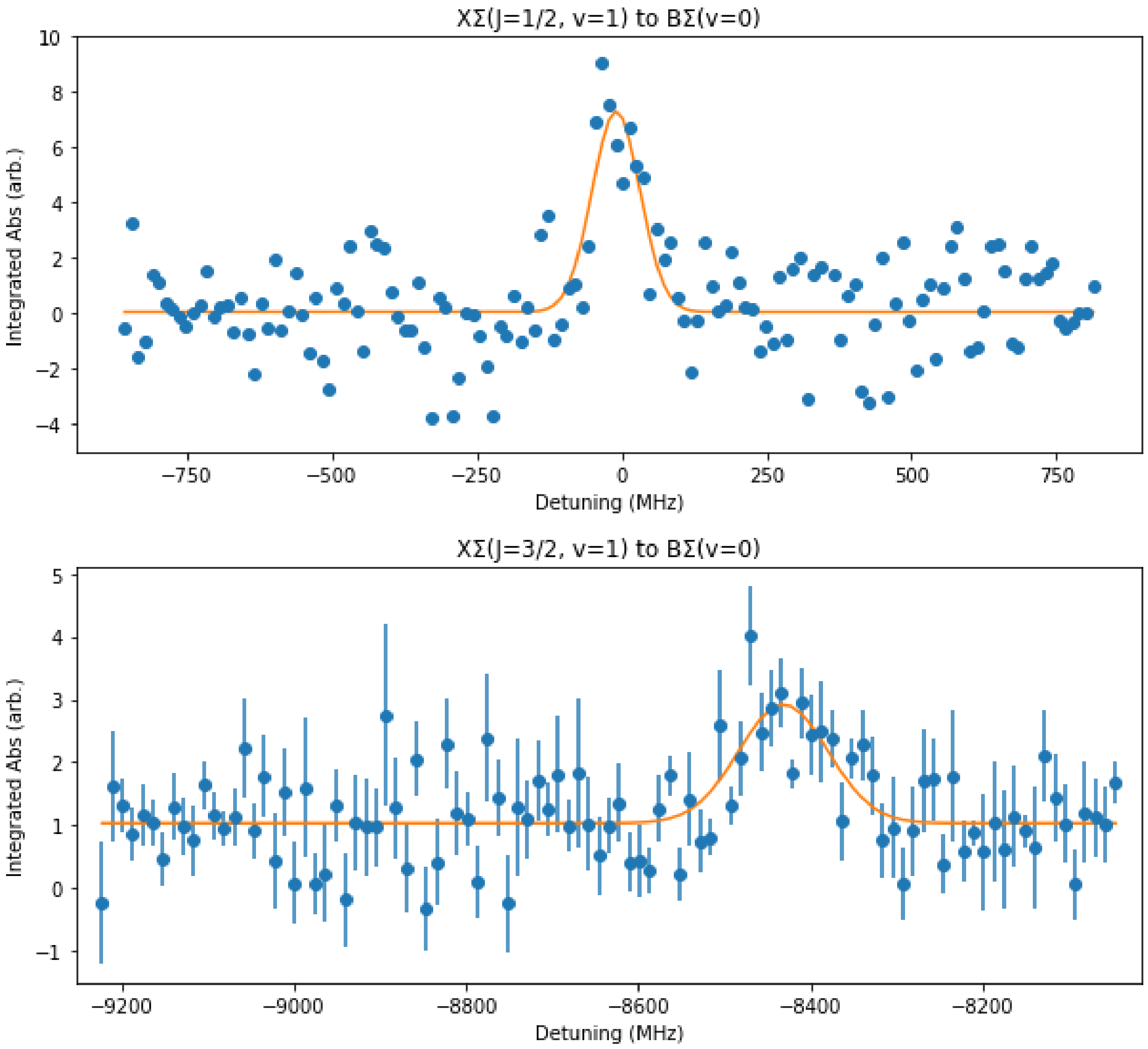

Figure 4.11: Direct measurement of the transition frequencies, for both repump transitions.

As further confirmation of the state identification, we parked the repump laser on resonance, and studied how the absorption signal depended on the pumping light. We see a clear dependence (Fig. 4.2.2) and were able to verify that the transitions saturates at a relatively low power Fig 4.2.2.

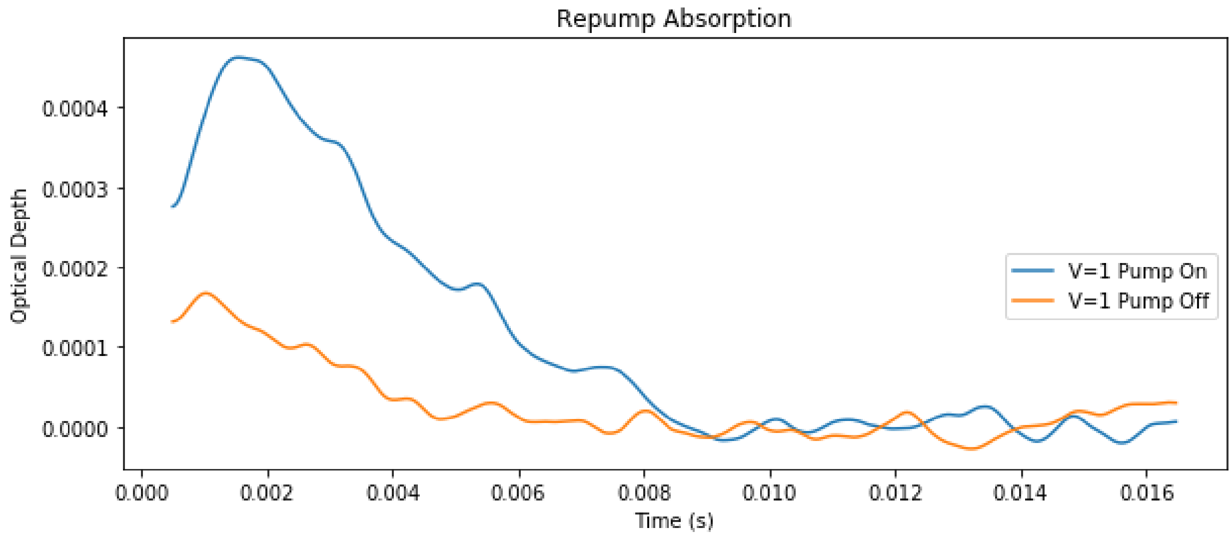

Figure 4.12: Experimental evidence supporting the classification of these states as originating from the $X^2\Sigma^+$(v=1) state. We see a greatly enhanced population when the pump light is applied.

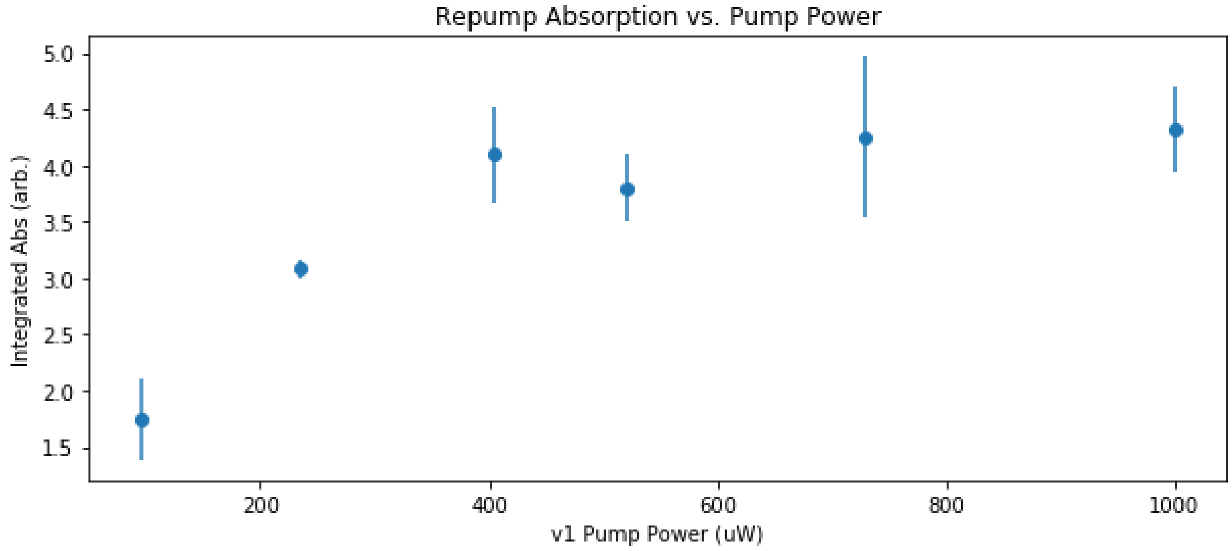

Figure 4.13: Saturation measurement of the $X^2\Sigma^+$(v=0) to $A^2\Pi_{3/2}$(v=1). We see the pump transition saturates at relatively low power, and more than doubles signal.

With the states located and identified we can now use incell absorption to study properties of the cycling transition. Of particular interest, is a measurement of the how closed the cycling transition is, via a measurement of the states Franck-Condon Factor (FCF) as first introduced in chapter 2.

4.3 Franck-Condon Factor ratio measurements

To perform measurements of the branching ratios for the relevant electronic transitions in BaH, we utilize two complimentary techniques, absorption ratios and fluorescence ratios. The absorption technique is based on a differential measurement of the absorption cross-section from one ground vibrational state v'', to two different excited vibrational levels v'. This concept of a FCF was introduced in Chapter 2, but now lets revisit it more carefully. We begin by writing the integrated absorption cross-section for a rovibronic transition as

$$\sigma_{v'J'v''J''} = \frac{(2J'+1)}{4(2J''+1)} \frac{A_{v'J',v''J''}}{(\tilde{\nu}_{v'J'v''J''})^2} = \frac{4\pi^3 \tilde{\nu}_{v'J'v''J''}}{3\varepsilon_0 h(2J''+1)} S_{v'J',v''J''},$$

where $\tilde{\nu}_{v'J'v''J''}$ is the line-centre wavenumber, $A_{v'J',v''J''}$ is the Einstein A-coefficient describing the absorption to the $v'J'$ excited ro-vibrational state from the $v''J''$ ground level and $S_{v'J',v''J''}$ is the transition line strength,

$$S_{v'J',v''J''} = |\langle \Lambda' v' J' \epsilon' | \mu | \Lambda'' v'' J'' \epsilon'' \rangle|^2 = |M|^2 S_{J',J''}, \tag{4.1}$$

where ϵ is the parity label, $|M|^2$ is the square of the vibronic transition moment and $S_{J',J''}$ is the Honl - London factor for the transition (explicit expressions for these rotational factors can be found in Watson). As all the transitions studied originate on a level where $J = 1/2$, and the principle result is measuring ratios between transitions with identical $\Delta J = J' - J''$ values, we will drop the explicit references to J. $|M|^2$ is approximately the product of the transition's Franck-Condon (FC) Factor $q_{v'v''}$ and $|R_e|^2$, the square of the electronic transition dipole moment (all the transitions studied here preserve the electronic spin)

$$|M|^2 = |\langle \Lambda' v' | \mu | \Lambda'' v'' \rangle|^2 \approx q_{v'v''} |R_e|^2.$$

In the results we quote these FC factors $q_{v'v''}$, even though it is more accurate to say we actually measure the vibronic moments. We relate the cross-section $\sigma_{v'v''}(\omega)$ to an experimentally measurable optical absorption to give the absorbance $\mathbb{A}(v', v'')$

$$\frac{\Delta I}{I} = 1 - e^{-N\sigma_{v'v''}(\omega)l} = \mathbb{A}(v', v''),$$

where N is the molecular density, ω is the angular frequency and l is the path length. By taking the ratio of absorption between two transitions that differ only in the excited state vibrational number ($v' = 0$ or 1), we can cancel the dependence on every term (including the molecular density) except $q_{v'v''}$ and $\tilde{\nu}$, the latter we have previously measured to high accuracy. We can then relate the experimentally measured ratio of absorption to the ratio of the FC Factors for the two transitions in question or the absorption vibronic transition ratio (VTR):

$$VTR = \frac{\mathbb{A}(v_1, v'')\tilde{\nu}_{v_2 v''}}{\mathbb{A}(v_2 = v'', v'')\tilde{\nu}_{v_1 v''}} \approx \frac{q_{v_1 v''}}{q_{v_2 v''}}. \tag{4.2}$$

This definition ensures the quoted VTR is always < 1 for a diagonal system such as the electronic transitions in BaH. Measurements of the VTR using this technique are consequently invariant to potential changes in the beam density (molecule number) and relies only on quantities we can accurately measure in the lab. The measurement of the emission VTR relies on direct observation of the decay probability between two states. The ratio $\mathcal{R}_{v'v''}$ of the measured emission to the total overall decay rate (branching ratio) can be expressed in terms of the transition's FC factor:

$$\mathcal{R}_{v'v''} = \frac{q_{v'v''}\tilde{\nu}^3_{v'v''}}{\sum\limits_{k=0}^{\infty} q_{v',k}\tilde{\nu}^3_{v',k}}. \tag{4.3}$$

where the summation is over all available radiative decay channels. By observing simultaneous fluorescence from a single excited ro-vibrational state, $v' = 0$ and $J' = 1/2$, to two different vibrational ground states $v'' = 0$ and 1, we directly compare the relative decays $\mathcal{R}_{0v''}$ and we can determine the $q_{v'v''}$ ratio for the two transitions (the emission VTR) using:

$$VTR = \frac{I_{0v_1}\tilde{\nu}^3_{0v_2}}{I_{0v_2}\tilde{\nu}^3_{0v_1}} \approx \frac{q_{0v_1}}{q_{0v_2}}, \tag{4.4}$$

where I_{0v_i} in the intensity of the observed decay to the ith ground vibrational state. These two complimentary techniques allow us to measure a variety of $q_{v'v''}$ ratios, using a series of differential measurements. Experimental results, and the comparison to theoretical work presented later, are provided in Table 4.3.2. All the ground state rovibrational levels involved are of (−)-parity ($N'' = 1$).

4.3.1 Relative Absorption Measurements

For absorption measurements we utilize the high molecular density inside the cryogenic cell, as shown in Fig. 4.2.2, to increase the size of the absorption signal. We take data by alternating the probe beam between two co-aligned lasers, each tuned to the resonant frequency of the energy levels of interest, with intensities well below saturation. This allows for real-time cancellation of any variability on the molecular yield, as the lasers intersect the same region of the cell. Based on laser availability, we were able to perform three measurements, obtaining $\frac{q_{10}}{q_{00}}$ for the $B^2\Sigma^+ \leftarrow X^2\Sigma^+$ and $A^2\Pi_{3/2} \leftarrow X^2\Sigma^+$ electronic transitions, and $\frac{q_{01}}{q_{11}}$ for $B^2\Sigma^+ \leftarrow X^2\Sigma^+$ only. To measure $\frac{q_{01}}{q_{11}}$, an additional laser was co-aligned with the absorption lasers, and tuned to the $A^2\Pi_{3/2}(v = 1) \leftarrow X^2\Sigma^+$ $(v = 0)$ transition. This is required to increase the population in the $X^2\Sigma^+(v'' = 1)$ ground state, as the $v'' = 1$ population is negligibly small for BaH thermalized to 6 K [86]. Only the Q_{12} rotational lines were measured for each transition. A representative measurement, showing the absorption signal for each transition and the ratio of the two signals is shown in Fig. 4.3.1.

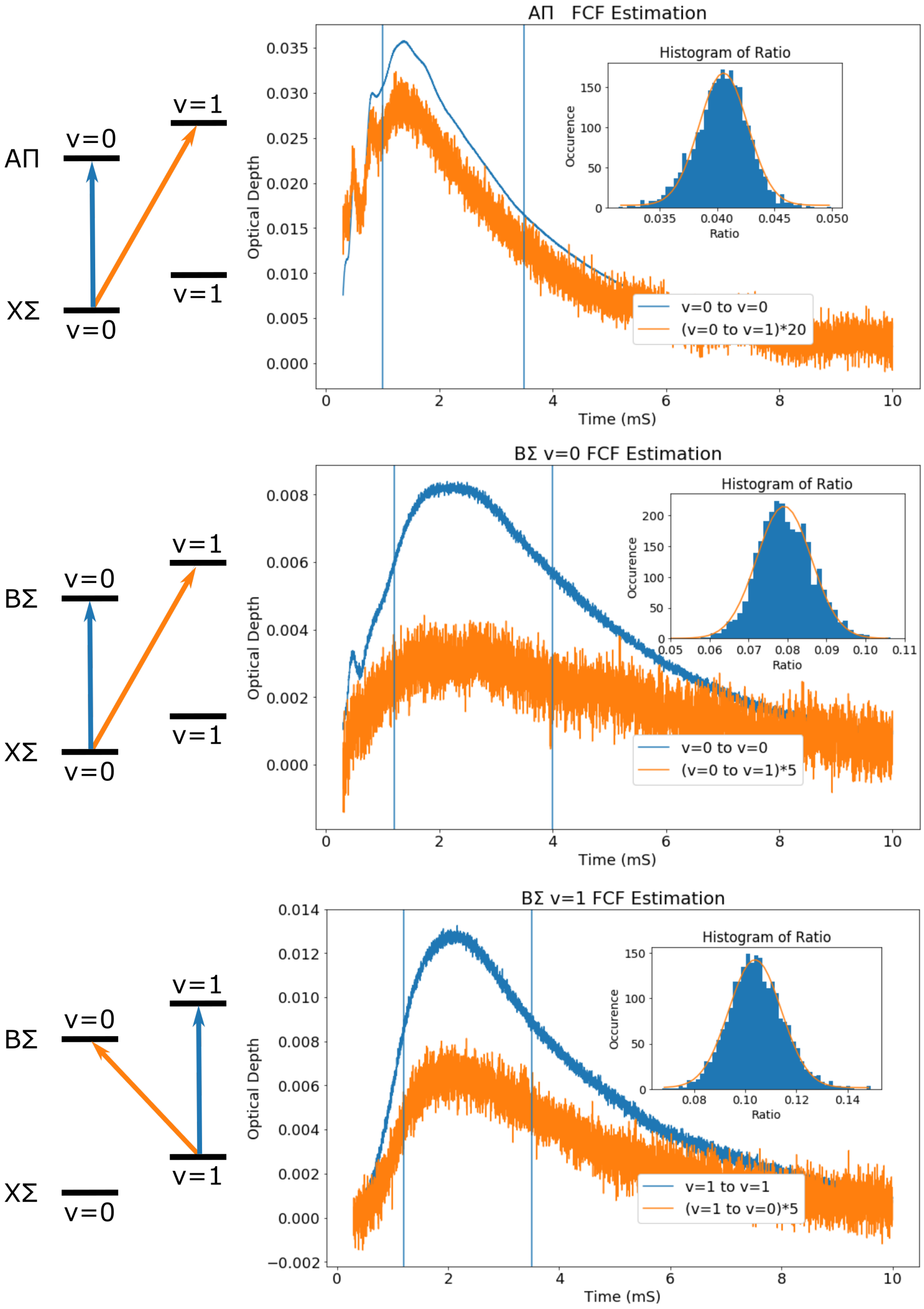

Figure 4.14: Absorption ratio measurements for each combination of states we explored. Histograms are generated by looking at the ratio of the two signals while the SNR was high, with regions denoted by the vertical bars.

4.3.2 FCF based bond length estimates

Based on these accurate measurements of the VTR, and a collaboration with theorist Professor Ian Lane, we are able to make improved estimates for the length of the $B^2\Sigma^+$ state potential. Spectroscopy is able very accurately determine the energy difference between bound states, and this constrains the shape of the potential curve, but the overall displacement is not experimentally accessible. This is discussed in Chapter 2 when I introduced the FCF. Based on these measurements, Ian Lane was able to fit the bond equilibrium distance r_e, that best fit our observations. We found excellent agreement for the ground and A state, but a meaningful adjustment was required for the B state compared to previous theoretical and experimental work.

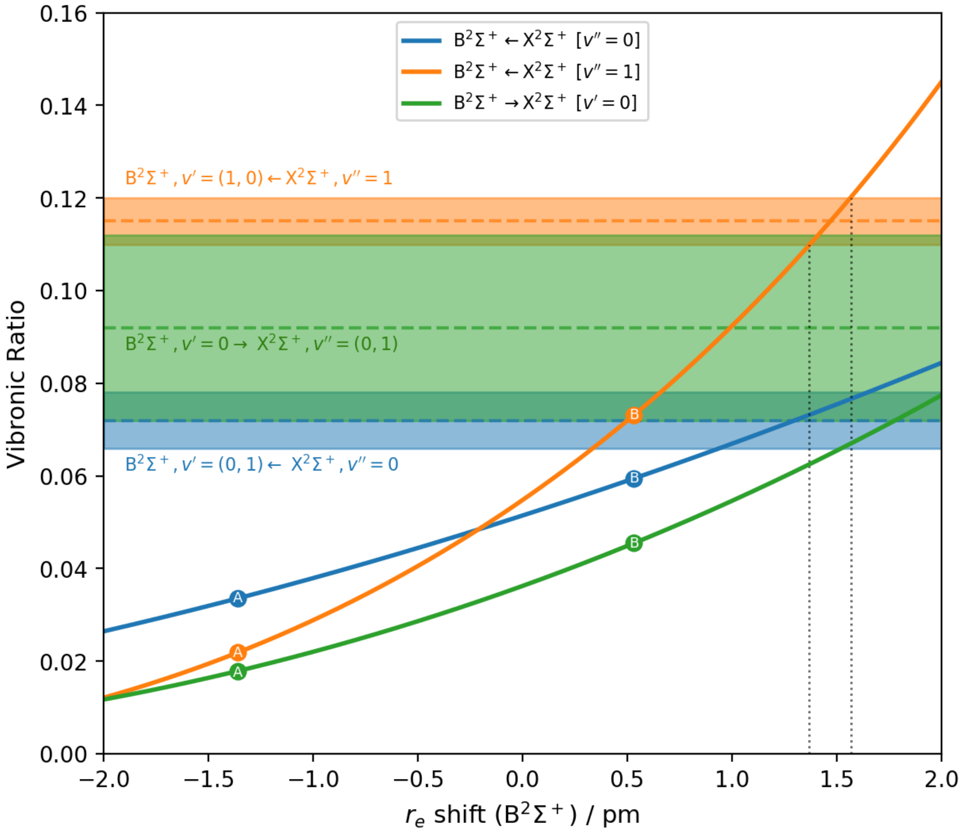

Figure 4.15: VTR for various transitions as a function of an applied shift to the $B^2\Sigma^+$ bond length. We see improved agreement with all three sets of measurements, for a shift of 1.5 pm. Here zero shift is the ab-intio results of Ian lane, and A and B denote the experimental results of Appledblad and Bernard.

The data, previous theory, and theory with the modified bond length are summarized in Table 1. We find both absorption measurements agree quite well with the new value, but the direct decay measurement (with substantially larger error bars) disagrees slightly.

Electronic transitions	VTR^a	Experimental value	Theoretical^b	Proposed
$A^2\Pi_{3/2} \leftarrow X^2\Sigma^+$	q_{10}/q_{00}	0.037 ± 0.002	0.037	0.037
$B^2\Sigma^+ \leftarrow X^2\Sigma^+$	q_{10}/q_{00}	0.072 ± 0.006	0.059	0.076
$B^2\Sigma^+ \leftarrow X^2\Sigma^+$	q_{01}/q_{11}	0.115 ± 0.005	0.072	0.118
$B^2\Sigma^+ \rightarrow X^2\Sigma^+$	q_{01}/q_{00}	0.092 ± 0.020	0.045	0.065

[a] J = 1/2 ← J =1/2 only for the absorption lines.

[b] Bernard *et al* [87] r_e value used

[c] With proposed +1.5 pm shift in $B^2\Sigma^+$ bond length

Table 4.1: Comparison between the present experimental measurements of the vibronic transition ratios (VTRs) and the corrected theoretical results. $q_{v'v''}$ is the ratio of vibronic transition moments between the v'th level in the excited state and the v''th level in ground state. The difference in equilibrium bond lengths between the ground and excited states, $\Delta(r_e)$, is set at the value proposed by Bernard *et al* for the theoretical values, and last column correspond to the longer excited bond length proposed here.

This is a demonstration that tools beyond spectroscopy are very helpful to improve our understanding of molecular potentials, and this is not always utilized in the field. Branching ratios can be very sensitive to on the difference in the equilibrium bond length between the excited and ground state. For BaH's $B^2\Sigma^+$ state a Δr_e of 1-pm (0.5%) can have a 25% effect on the branching ratios but only a 1% effect on the lifetime. Ian Lane was able to take these shifted potentials, and produce an updated estimate for each decay pathway that is relevant to the experiment, as shown in Table 4.2. As more molecule cooling experiments obtain these FCF measurements, there is an opening for theorist to take this data and improve their models.

	Decay pathways			
	Final state	v''	$\mathcal{A}$ / s^{-1}	$\mathcal{R}$atio / %
$A^2\Pi_{1/2}$	$X^2\Sigma^+_{1/2}$ ($N = 1$)	0	7.23×10^6	98.772
$v' = 0$	$X^2\Sigma^+_{1/2}$	1	8.94×10^4	1.221
	$X^2\Sigma^+_{1/2}$	2	1.50×10^2	0.002
	$H^2\Delta_{3/2}$ ($J = \frac{3}{2}$)	0	3.24×10^2	0.004
	Lifetime (ns)			**136.5**
$B^2\Sigma^+_{1/2}$	$X^2\Sigma^+_{1/2}$ ($N = 1$)	0	7.61×10^6	95.312
$v' = 0$	Q_{12}		4.13×10^6	*51.704*
	P_1		3.48×10^6	*43.609*
	$X^2\Sigma^+_{1/2}$	1	3.64×10^5	4.564
	Q_{12}		2.88×10^5	*3.611*
	P_1		7.62×10^4	*0.953*
	$X^2\Sigma^+_{1/2}$	2	3.44×10^3	0.043
	$A^2\Pi_{1/2}$ ($J = \frac{1}{2}$)	0	1.48×10^3	0.019
	$A^2\Pi_{1/2}$ ($J = \frac{3}{2}$)	0	1.37×10^3	0.017
	$A^2\Pi_{3/2}$	0	1.14×10^3	0.014
	$H^2\Delta_{3/2}$	0	2.39×10^3	0.030
	Lifetime (ns)			**125.1**
$A^2\Pi_{1/2}$	$X^2\Sigma^+_{1/2}$ ($N = 1$)	0	6.91×10^5	9.400
$v' = 1$	$X^2\Sigma^+_{1/2}$	1	6.47×10^6	87.952
	$X^2\Sigma^+_{1/2}$	2	1.93×10^5	2.633
	$X^2\Sigma^+_{1/2}$	3	5.60×10^2	0.008
	$A^2\Pi_{1/2}$ (both J)	0	1.45×10^2	0.002
	$H^2\Delta_{3/2}$ ($J = \frac{3}{2}$)	1	3.62×10^2	0.005
	Lifetime (ns)			**135.9**
$B^2\Sigma^+_{1/2}$	$X^2\Sigma^+_{1/2}$ ($N = 1$)	0	8.81×10^5	11.595
$v' = 1$	$X^2\Sigma^+_{1/2}$	1	6.16×10^6	81.081
	$X^2\Sigma^+_{1/2}$	2	5.39×10^5	7.100
	$X^2\Sigma^+_{1/2}$	3	1.00×10^4	0.132
	$B^2\Sigma^+_{1/2}$	0	9.41×10^1	0.001
	$A^2\Pi_{1/2}$ (both J)	0	5.88×10^2	0.008
	$A^2\Pi_{1/2}$	1	2.63×10^3	0.035
	$A^2\Pi_{3/2}$ ($J = \frac{3}{2}$)	0	4.07×10^2	0.005
	$A^2\Pi_{3/2}$	1	1.01×10^3	0.013
	$H^2\Delta_{3/2}$	1	2.24×10^3	0.029
	Lifetime (ns)			**131.7**

Table 4.2: Radiative decay pathways from the lowest rovibronic states of $B^2\Sigma^+$ and $A^2\Pi_{1/2}$. $\mathcal{A}$ is the Einstein A coefficient for each transition and $\mathcal{R}$atio is the value of $\mathcal{R}_{v'v''}$. This data was presented originally in [88]

4.4 Detected BaH Transitions

Over the course of these studies, we were able to perform accurate measurements for a number of transitions in BaH, beyond the accuracy of previous studies. Below is a summary of each of these transitions, the previous measurements, and the difference we observed. This can help serve more accurate determination of the BaH level structure, and to improve future estimates of transition energies.

	$\mathbf{B}\Sigma(v=1)$	$\mathbf{B}\Sigma(v=1)$	$\mathbf{A}\Pi_{3/2}(v=0)$	$\mathbf{A}\Pi_{3/2}(v=1)$	$\mathbf{A}\Pi_{1/2}(v=0)$	$\mathbf{E}\Pi_{1/2}(v=0)$	$\mathbf{E}\Pi_{1/2}(v=1)$
$\mathbf{X}\Sigma(v=0, J=1/2)$	905.296646	826.163909	1008.42539	909.215720	1060.78398	683.727374	632.427361
$\mathbf{X}\Sigma(v=0, J=3/2)$	905.320245	826.183562	1008.45183	909.237214	1060.81324	683.740838	632.438881
$\mathbf{X}\Sigma(v=1, J=1/2)$	1009.39451	911.995871	1139.29992	1014.26462	1206.58409	741.479507	681.527162
$\mathbf{X}\Sigma(v=1, J=3/2)$	1009.42309	912.019205	1139.33367	1014.29137	1206.62194	741.494929	681.540191

Table 4.3: Values from previous spectroscopy and theory [89, 90]

	$\mathbf{B}\Sigma(v=0)$	$\mathbf{B}\Sigma(v=1)$	$\mathbf{A}\Pi_{3/2}(v=0)$	$\mathbf{A}\Pi_{3/2}(v=1)$	$\mathbf{A}\Pi_{1/2}(v=0)$	$\mathbf{E}\Pi_{1/2}(v=0)$	$\mathbf{E}\Pi_{1/2}(v=1)$
$\mathbf{X}\Sigma(v=0, J=1/2)$	905.29615	826.1642	1008.42120	909.2093	1060.7868	683.72754	
$\mathbf{X}\Sigma(v=0, J=3/2)$	905.31980	826.18390			1060.8191	683.74103	
$\mathbf{X}\Sigma(v=1, J=1/2)$	1009.3931	911.9957					681.52728
$\mathbf{X}\Sigma(v=1, J=3/2)$	1009.42181						

Table 4.4: Experimentally determined values, based on in-cell absorption spectra.

	B$\Sigma(v=0)$	**B**$\Sigma(v=1)$	**A**$\Pi_{3/2}(v=0)$	**A**$\Pi_{3/2}(v=1)$	**A**$\Pi_{1/2}(v=0)$	**E**$\Pi_{1/2}(v=0)$	**E**$\Pi_{1/2}(v=1)$
X$\Sigma(v=0, J=1/2)$	182	-132	1236	2329	-751	-107	
X$\Sigma(v=0, J=3/2)$	163	-149			-1562	-123	
X$\Sigma(v=1, J=1/2)$	515	62					-76
X$\Sigma(v=1, J=3/2)$	380						

Table 4.5: Theory experiment comparison, in MHz. Accuracy of experimental values is limited by linewdith of the states, and modestly assumed to be on the order of $\approx 20MHz$

We see decent agreement for the $B^2\Sigma^+$, but the $A^2\Pi$ is quite a bit worse. Also note, there are definite correlations between similar measurements, which would imply that we can make improvements to some of the low j and low v theory for this molecule.

Chapter 5: Molecular Beam Characterization and Spectroscopy Studies

While in-cell studies have a large SNR thanks to the high molecular density, helium collisions limit the sort of physics we can study. In order to make high precision measurements, and optically manipulate the sample, we need to avoid helium collisions. We achieve this by using the cryogenic source, to generate a cryogenic beam. As the molecules travel away from the cell the pressure rapidly drops, and we can enter a regime where background gas collisions are negligible. This chapter I will discuss our beam system, and present a range of precision studies enabled by it. These studies allow the accurate determination of molecular constants to improve our understanding of the level structure.

5.1 Experimental Setup

5.1.1 Molecular Beam Baffles

For studies that require precise spectroscopy we found the addition of molecular baffles to be vital. After several iterations we found that a baffle which protrudes into the interaction region made alignment of the lasers to the molecular beam much easier. The edge of the baffle itself was sharpened to a point, and the encasing structure had a series of fins cut out, to ensure there is as little helium build up as possible. A CAD drawing, and installation image is show in Fig. 5.1.1.

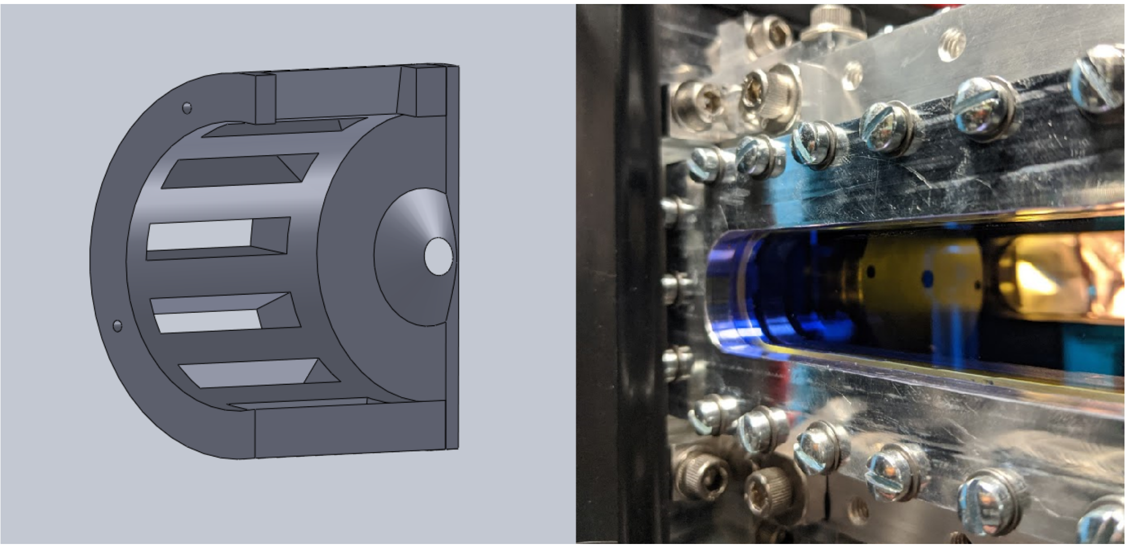

Figure 5.1: CAD drawing and photo of the molecular beam baffle system.

We saw a reduction in the total flux of about 6 when the baffle was installed, which is consistent with the reduction expected from the geometric constraints. This indicates that additional Helium collisions introduced by the baffle are not likely to limit the performance. The addition of the molecular baffle was critical when optimizing the scattering rate, and observing optical manipulation. Without the baffle installed we were unable to optimize the system, due to a large fraction of the molecules that the cycling/cooling light never interacted with.

5.1.2 Fluorescence Collection

For studies in the molecular beam, we have two primary detection methods, PMT's for time sensitive analysis, and an EMCCD for spatially sensitive detection. The collection efficiency of the PMT system is ≈ 2 times that of the EMCCD, due to the use of a spherical reflector, effectively doubling the collection. Both systems required the chamber to be blackened, and extensive baffles for the probe laser to be installed, as discussed in further detail in the Appendix. For a further discussion of the imaging system used with the camera, see Chapter 6.

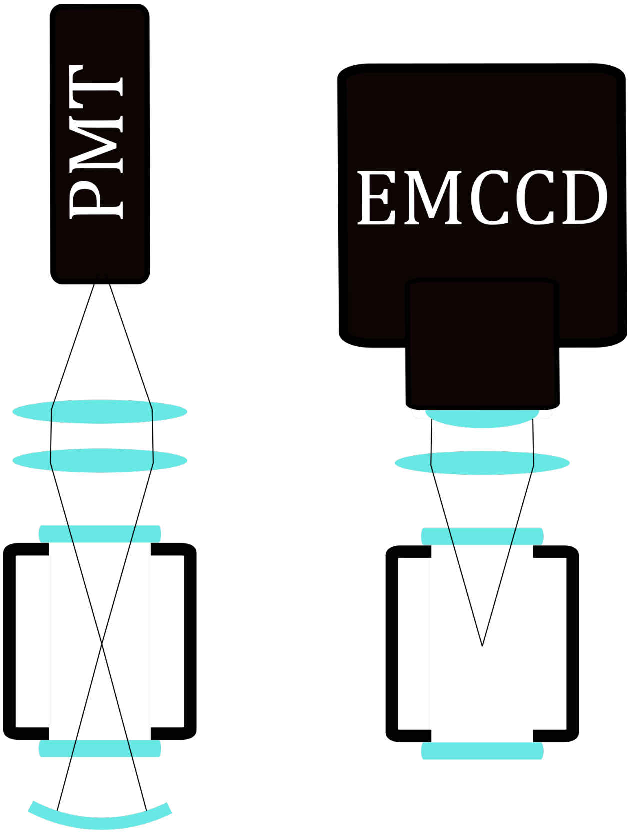

Figure 5.2: Detection optics for the each system. Collimating lens are 2 inch diameter 60 mm focal length biconvex lenses from Thorlabs, and the camera objective is a MVL35M1 fixed focal lengths lens.

Several collection systems with a higher collection efficiency were also attempted, and designs for one of the systems in provided in the Appendix. However, we found that these improved collection systems also increased the background light scattering, and therefore the SNR was not actually improved. Ways around this using a two photon detection scheme is discussed at the end of this chapter.

5.2 Beam Characterization

In the context of creating samples of trapped ultracold molecules the most important molecular beam properties are the flux, forward velocity distribution, and transverse temperature. We are limited by the radial size of the slowing light so only the central portion of the beam can be slowed. We are limited by interaction time, and the total distance of the slowing region, to only slow molecules below a fixed forward velocity. Finally, we always want to have as many molecules as possible. These constraints drive the optimization we must perform for the molecular beam.

The molecular flux downstream from the source is detected via fluorescence with a PMT as shown in Fig. 5.1.2. For characterizing the molecular beam in these studies we use a single-frequency laser resonantly driving the $N'' = 1, J'' = 1/2$ spin-rotation level of the electronic ground state to the $N' = 0, J' = 1/2$ level of the $\mathrm{E}^2\Pi_{1/2}$ excited state. This means, for these experiments, there is no optical cycling. Assuming that the molecules are equally distributed in each hyperfine magnetic sublevel, we detect one third of the total molecules present in the $N'' = 1$ rotational state. In addition, the probe laser intersects slightly less than a tenth of the molecular beam cross-sectional area. The detection efficiency of the system is the product of the 2% PMT quantum efficiency at 684 nm and the 2.5% geometric collection efficiency of the detection optics. Each of these factors combined with the signal size of $\sim$ 500 PMT counts in the detection region per ablation pulse yields approximately 4×10^7 molecules in the $\mathrm{X}^2\Sigma^+$ $(v'' = 0, N'' = 1)$ state per pulse. Some of our ablation targets yield up to three times as many molecules.

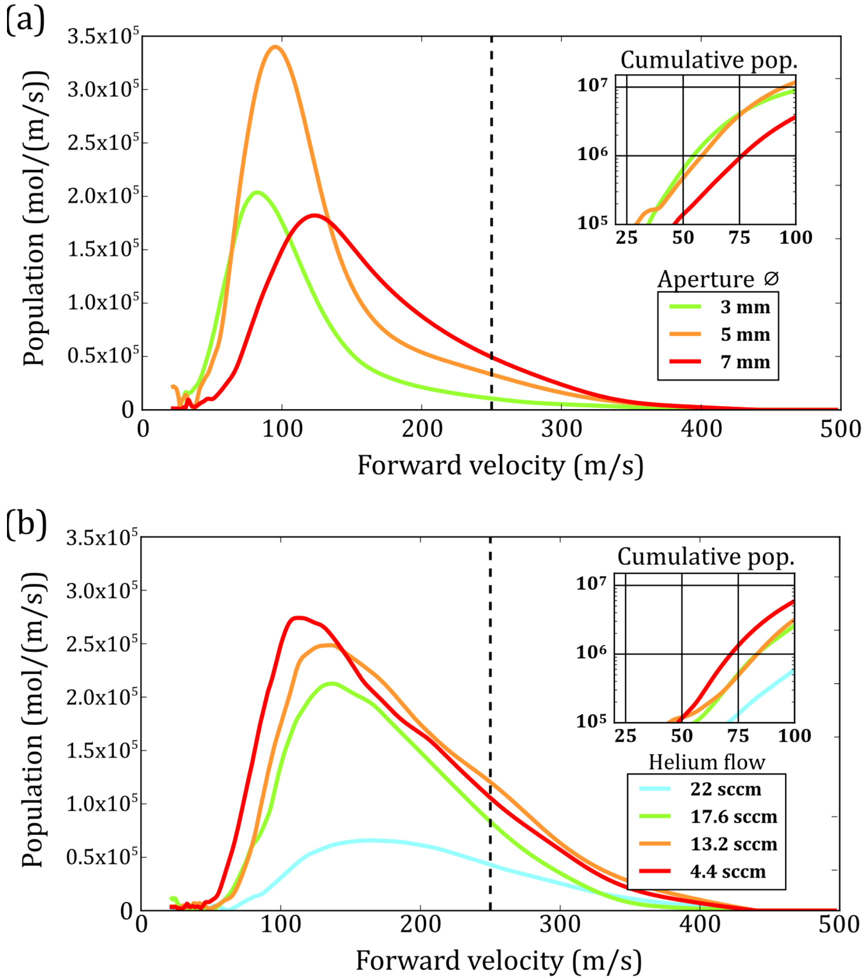

Figure 5.3: a) Measured forward velocity distributions of BaH molecules for various aperture diameters. b) Measured forward velocity distributions of BaH molecules for a range of buffer gas flow rates. Velocity distributions above ∼ 250 m/s (dashed line) are slightly less reliable due to a moderate sensitivity on specific data cuts made to reject fluorescence noise from ablation light. The inset shows the population below 100 m/s.

To determine the forward velocity distribution of the molecules, we make time-resolved molecular density measurements 2 cm away from the cell exit via absorption spectroscopy and, simultaneously, downstream in the fluorescence detection region, using the $X^2\Sigma^+$ $(v'' = 0, N'' = 1)$ ground state. These two measurements of beam density as a function of time are deconvolved to yield the forward velocity distribution in a process analogous to spatial time-of-flight analysis in quantum gas experiments. The results of this analysis are given in Fig. 5.2 for various He flow rates from 4.4 to 22 sccm. While the overall number of detected molecules per ablations pulse does not significantly vary in this range of flow rates, Fig. 5.2 and its inset show that the number of slow molecules with forward velocities below 100 m/s doubles as the He flow is reduced from 22 to 4.4 sccm, reaching a fraction of $\sim 11\%$. At even lower flow rates the molecular flux begins to degrade. It is evident from the data in Fig. 5.2 that while the low-velocity behavior is stable and systematic in its dependence on the flow rate, the overall shape of the velocity distribution can be affected by the particular choice of target or ablation spot, as is the case for the 17 sccm trace. The velocity distributions above ~ 250 m/s are slightly less reliable than those for lower velocities since this signal comes from faster molecules arriving in the detection region very shortly after ablation, while there is a minimum waiting time after ablation to begin detecting in order to avoid the stray ablation light. The present configuration of the beam source was chosen to produce a maximized number of molecules with velocities below 100 m/s, but could be further optimized by making additional changes to the buffer-gas cell geometry. It is worth noting, that we see a substantially faster beam for certain ablation spots, but this is typical performance for a “slow" spot.

In the fluorescence detection region we can limit the transverse temperature of the molecules to 0.1 K by comparing the expected natural linewidth of the $B^2\Sigma^+$ state [91] to the measured spectra Fig 5.3.1. This cold transverse temperature is consistent with geometric constraints on the beam and allows us to characterize the relevant properties of BaH at a higher optical resolution than was previously possible, enabling direct measurements of hyperfine structure and molecular g-factors, as will be discussed later on.

Alternatively, we can also estimate the divergence angle of the molecular beam, by measuring how the density of the beam decreases as it propagates, and the molecules spread out. To achieve this, we performed a series of measurements using the same detection laser, and identical detection systems at two points along the molecular beam 70 cm and 135 cm away from the source. By taking simultaneous measurements then swapping the detection systems to control for differences in collection and detection efficiency of two systems, we can estimate the reduction in the molecular density between these two regions. We start, by taking a simultaneous measurement in the first configuration, and obtain two signals.

$$\begin{aligned} s1 &\propto \rho_{close}\Omega_a N_{mol1} \\ s2 &\propto \rho_{far}\Omega_b N_{mol1} \end{aligned} \tag{5.1}$$

Where ρ is the density in the two regions, Ω_X is the total detection efficiency in region X and N_{mol1} is the number of molecules generated in this first set of data. Because both regions use the same detection laser this term is common to both measurements, so when we take a ratio of them (as we will at the end) this dependence, as well as dependence of the flux of the molecular beam (N_{mol1}), cancels. Now, we repeat the same measurement, by swap the A and B detection systems.

$$\begin{aligned} s3 &\propto \rho_{close}\Omega_b N_{mol2} \\ s4 &\propto \rho_{far}\Omega_a N_{mol2} \end{aligned} \tag{5.2}$$

Here, the molecular flux may have changed, but again if we only consider the ratio of these two signals, this dependence cancels. Finally, by multiplying the ratio of these two signals, we can extract the relative molecular density in the two regions.

$$\frac{\rho_{close}}{\rho_{far}} = \sqrt{\frac{s1}{s2}\frac{s3}{s4}} \tag{5.3}$$

For this analysis, we simply integrate the signal over all time to get the total signal size for s for each configuration.

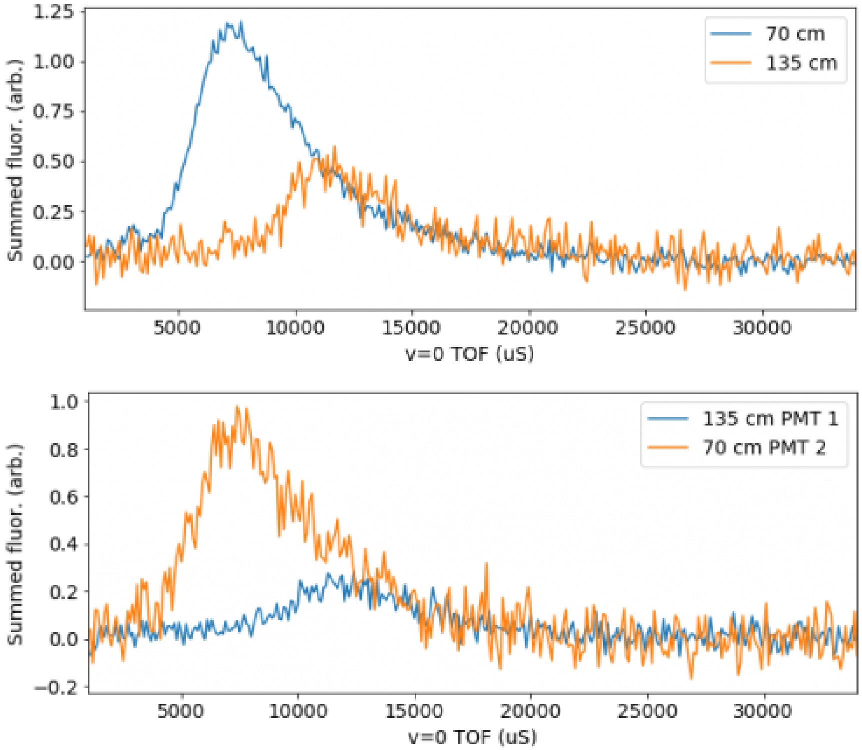

Figure 5.4: Fluorescence signals in the two detection regions, for both combinations of PMT's

We find that the molecular density, is 38% lower at the far (135 cm) region, as compared to the close (70 cm) region. This is quite encouraging, because it shows the molecules are quite well collimated, and longer slowing regions are possible. This is consistent with blooming we would expect, based solely on geometric constraints of the molecular beam.

5.3 In Beam Spectroscopy

In beam the low vacuum pressure and small transverse velocity enable high precision spectroscopy of the molecular transitions. This is critical because we need to understand the structure of the molecule of interest, before attempting to cool and trap it.

5.3.1 Hyperfine Characterization

While BaH has been studied for over 100 years (we even used some papers in microfilm for the Columbia Library), it is less well explored than other molecular candidates for laser cooling. The cold molecular beam we have built is well suited for optical spectroscopy to measure the hyperfine structure of the ground and excited states.

The transverse Doppler width of the molecular beam in the fluorescence detection region, in combination with our signal-to-noise ratio, allows us to resolve hyperfine energy splittings at the ~ 4 MHz level. As mentioned, it is challenging to directly detect fluorescence from the $A^2\Pi_{1/2}$ or $B^2\Sigma^+$ excited states due to their NIR emission. However, these states can be probed by optically pumping molecules between the two ground-state spin-rotation levels ($J'' = 3/2$ and $J'' = 1/2$) while detecting population in one of them via the $X^2\Sigma^+ \leftarrow E^2\Pi_{1/2}$ transition. This is possible due to the highly favorable vibrational branching ratios of the $A^2\Pi_{1/2}$ and $B^2\Sigma^+$ excited states into the ground state [92, 81].

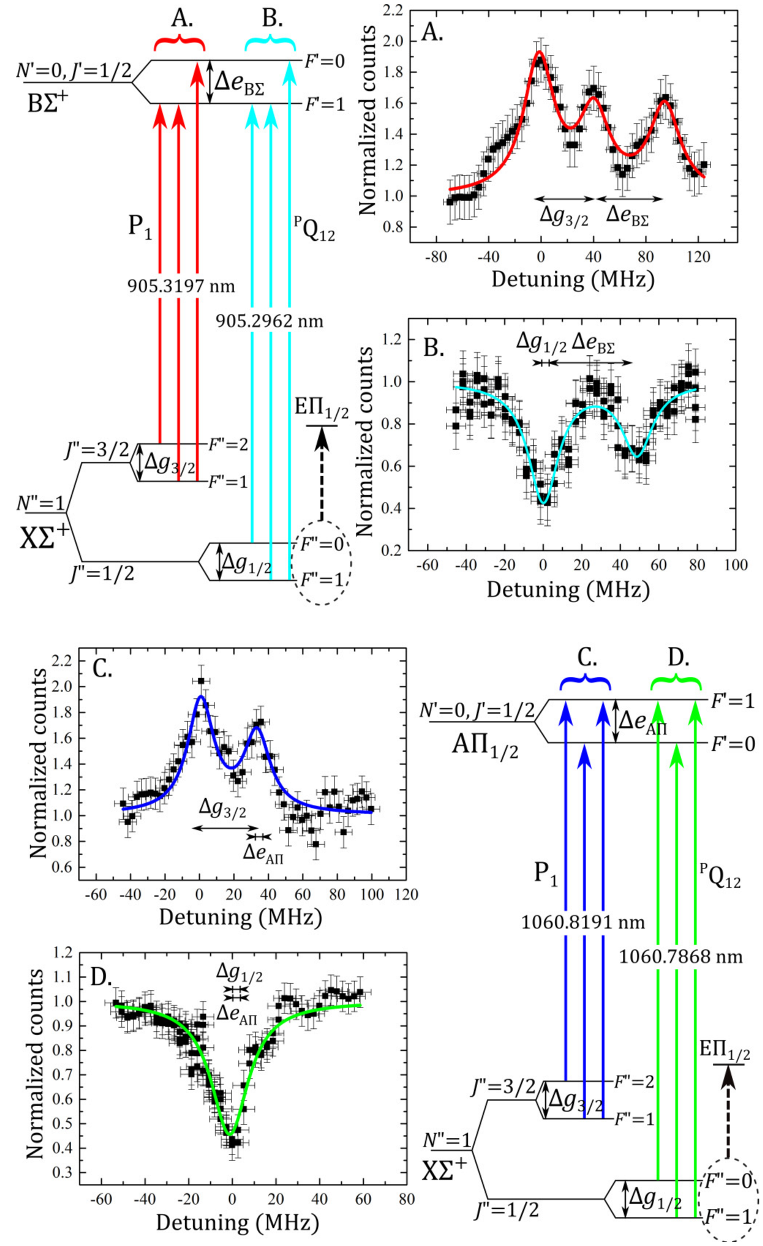

Figure 5.5: Hyperfine-structure-resolved energy levels and measurements for BaH electronic states relevant to laser cooling. Four types of spectra are collected (labeled A, B, C, and D). In all cases, detection is made by monitoring the fluorescence of molecules excited from the $X^2\Sigma^+(N'' = 1, J'' = 1/2)$ ground state to the $E^2\Pi_{1/2}$ excited state, indicated by the dashed arrows. Transitions labeled A and C show population enhancement due to pumping from the $X^2\Sigma^+(N'' = 1, J'' = 3/2)$ state via $B^2\Sigma^+$ or $A^2\Pi_{1/2}$. Transitions labeled B and D show population depletion due to pumping out of the $X^2\Sigma^+(N'' = 1, J'' = 1/2)$ state. The studied ground-state and excited-state hyperfine intervals are marked as Δg or Δe in the diagrams and in the spectra.

Hyperfine structure measurements are outlined in Fig. 5.3.1 and the results are reported in

Table 5.1. Four types of optical spectra were collected to fix the values of the four unknown hyperfine intervals. These are labeled A, B, C, and D in Fig. 5.3.1. In each of these experiments, the $X^2\Sigma^+(J'' = 1/2)$ population is monitored by sending a 683.7268 nm laser beam through the detection region and recording fluorescence from the spontaneous decay of the $E^2\Pi_{1/2}$ state. Several beam waists upstream, a probe laser drives transitions from one of the ground electronic spin-rotation levels through the $B^2\Sigma^+$ or $A^2\Pi_{1/2}$ excited state. The A and C transitions (905.3197 nm and 1060.8191 nm) enhance the detected fluorescence as the molecules get pumped from the $J'' = 3/2$ ground-state level to $J'' = 1/2$, while the B and D transitions (905.2962 nm and 1060.7868 nm) decrease the fluorescence as the molecules are pumped out of the $J'' = 1/2$ level. Each data point in the spectra of Fig. 5.3.1 is an average of 5 ablation shots.

State	Measured hyperfine spacing (MHz)
$X^2\Sigma^+(J'' = 1/2)$	−0(4)
$X^2\Sigma^+(J'' = 3/2)$	39(4)
$B^2\Sigma^+(J' = 1/2)$	−52(5)
$A^2\Pi_{1/2}(J' = 1/2)$	0(4)

Table 5.1: Measured hyperfine intervals for the electronic states of BaH that are relevant to laser cooling. Negative values denote ‘flipped’ hyperfine structure.

The peaks and their spacing’s in the spectra can be identified by assuming an ordering for the excited-state hyperfine structure and fitting the peak positions. The relative peak amplitudes are given by the hyperfine level multiplicities, and are not independently fit. A correctly chosen ordering yields peak spacing and heights that are consistent for all four data sets in Fig. 5.3.1. The shown fits to the fluorescence spectra are constrained only by the expected peak height ratios. The hyperfine structure data can be analyzed to extract molecular hyperfine constants which have been previously measured for ground-state BaH in cryogenic solid argon [93]. Excluding negligible terms, the hyperfine structure of $X^2\Sigma^+$ is described by the Hamiltonian

$$H_{\mathrm{hf}} = b_F \mathbf{S} \cdot \mathbf{I} + c I_z S_z \tag{5.4}$$

where b_F is the Fermi contact interaction constant, c is the dipolar coupling constant, and $\mathbf{S}$ and $\mathbf{I}$ are the electronic and nuclear spin angular momenta. Each term in Eq. (5.4) can be evaluated as in Sec. 9.5 of Ref. [94]. The resulting hyperfine interaction matrix elements for $^2\Sigma^+$ states are

$$H_{\mathrm{hf}} = \begin{pmatrix} \frac{b_F}{4} + \frac{c}{20} & 0 & 0 & 0 \\ 0 & -\frac{b_F 5}{12} - \frac{c}{12} & \frac{b_F\sqrt{2}}{3} + \frac{c\sqrt{2}}{6} & 0 \\ 0 & \frac{b_F\sqrt{2}}{3} + \frac{c\sqrt{2}}{6} & -\frac{b_F}{12} + \frac{c}{12} & 0 \\ 0 & 0 & 0 & \frac{b_F}{4} - \frac{c}{4} \end{pmatrix}.$$

Our hyperfine structure measurements yield $b_F = 50(7)$ MHz and $c = 39(8)$ MHz. The value for b_F is consistent with previous measurements of 47(2) MHz [93]. The value for c, while lacking previous reliable measurements, is consistent with those for other alkaline-earth-metal monohydrides [93].

The hyperfine structure results in Table 5.1 can guide experiments on radiation-pressure slowing and cooling of BaH. For the lower spin-rotation level of the ground state ($J'' = 1/2$) hyperfine structure is unresolved, while for the higher level ($J'' = 3/2$) the splitting is 39(4) MHz and can be easily covered by sidebands imprinted on the laser light with standard techniques introduced in Chapter 3. Hyperfine structure is also small, or on the order of the natural linewidth, in the $A^2\Pi_{1/2}$ excited state as is the case for other diatomic molecules that have been investigated as laser cooling candidates. This feature allows all excited-state sublevels to participate in optical cycling, thus maximizing radiation pressure forces. The 52(5) MHz hyperfine interval in the $B^2\Sigma^+$ excited state is $\sim$ 30 times larger than the natural linewidth and is of a similar magnitude to that of the ground-state $J'' = 3/2$ level, such that the combination of the two can be easily managed.

5.3.2 G Factor studies

Magnetic g-factors are crucial for understanding magneto-optical trapping forces on molecules. In particular, the trapping forces depend strongly on the ratios of the g-factors in the ground and excited states [95]. Here we report predictions and measurements of the relevant magnetic g-factors in BaH.The Zeeman shifts for $^2\Pi$ states are strongly influenced by the parity dependent contributions $g_l' \approx \frac{p}{2B}$ and $g_r^{e'} \approx \frac{q}{B}$, where p and q are the Λ-doubling constants and B is the rotational constant. These constants have been measured in BaH for the $\mathrm{A}^2\Pi_{1/2}$ excited state [89] and for the detection state $\mathrm{E}^2\Pi_{1/2}$ [96]. The matrix elements of the applicable Zeeman Hamiltonian are expressed in Eq. (9.71) of Ref. [94], and the dominant parity dependent term can be described with a single effective g-factor as $g_{\mathrm{eff}} = (g_l' - g_r^{e'})/3$. This contribution alone would result in a g-factor value of -0.27 for $\mathrm{A}^2\Pi_{1/2}$, while a purely semiclassical prediction would yield a value of 0. The predicted g-factor, however, is -0.44 in this case, because additional contributions to g_{eff} result from interactions between electronic states. In BaH, the lowest $5d$ excited states form an interacting complex [90] where the strongest mixing is between $\mathrm{B}^2\Sigma^+$ and $\mathrm{A}^2\Pi_{1/2}$. This results in an enhancement of the $\mathrm{A}^2\Pi_{1/2}$ state g-factor and a slight reduction of the $\mathrm{B}^2\Sigma^+$ state g-factor.

State	Measured g_{eff}	Prediction
$X^2\Sigma^+(N'' = 1, J'' = 1/2)$	$-1.39(3)$	-1.4
$X^2\Sigma^+(N'' = 1, J'' = 3/2)$	$+0.56(10)$	$+0.50$
$B^2\Sigma^+(N' = 0, J' = 1/2)$	$+2.54(11)$	$+2.86$
$A^2\Pi_{1/2}(N' = 0, J' = 1/2)$	$-0.56(4)$	-0.44
$E^2\Pi_{1/2}(N' = 0, J' = 1/2)$	$-0.16(10)$	-0.04

Table 5.2: Measured and predicted effective g-factors in the m_J basis which is most pertinent to the field regimes used in magneto-optical trapping.

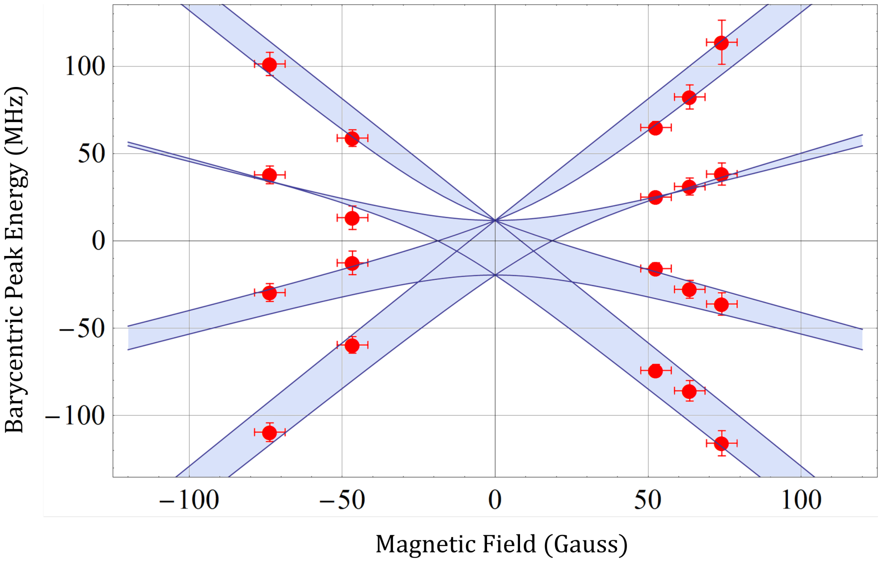

Figure 5.6: Measured Zeeman shifts of the $X^2\Sigma^+(J'' = 3/2)$ magnetic sublevels, overlayed with a prediction from the Zeeman Hamiltonian. Solid lines represent energies of the m_F sublevels. Shaded areas between pairs of sublevels emphasize structure that is spectroscopically unresolved even if selection rules allow both sublevels to couple to the excited state.

While at very low magnetic fields it is natural to use the m_F basis for the Zeeman interaction Hamiltonian, at fields exceeding ∼ 10 G the Zeeman shifts are best described in the m_J basis. As a result, the reported factors g_{eff} describe the measured energy shifts for magnetic field strengths of tens of gauss. These shifts are $\Delta E = g_{\text{eff}}\mu_B m_J B$, where B is the applied field and μ_B is the Bohr magneton. High-resolution Zeeman spectra were collected for both excited states, for both spin-rotation levels of the ground state, and for the $E^2\Pi_{1/2}(N' = 0, J' = 1/2)$ state used in the detection scheme. Figure 5.3.2 shows data for Zeeman shifts of the $X^2\Sigma^+(J'' = 3/2)$ ground state sublevels, along with the prediction from the Zeeman Hamiltonian.

The experimental results together with the predictions are listed in Table 5.2. For all experiments, magnetic field was applied perpendicularly to the probe laser propagation direction and calibrated in situ with a commercial gaussmeter. Measurements of the ground-state Zeeman shifts were done via the $X^2\Sigma^+ \leftarrow E^2\Pi_{1/2}$ transition, where we could separately identify the ground and excited state splittings, as well as the relative signs of their g-factors, by switching the probe laser polarization between π and $\sigma^\pm$ transitions. The Zeeman shifts in the $B^2\Sigma^+$ and $A^2\Pi_{1/2}$ excited states were measured via the fluorescence depletion method as in the hyperfine structure studies, and polarization was again switched to drive π and $\sigma^\pm$ transitions in order to determine the relative signs of all the g-factors. To fix the absolute signs, a calibration measurement was made by applying a magnetic field along the laser propagation axis and using circularly polarized light.

The results in Table 5.2 highlight an interesting difference in laser cooling prospects between BaH and other diatomic molecules currently in use such as SrF [97] and CaF [98]. Unlike the fluorides, BaH has a large magnetic moment in both excited states that could be used for optical cycling, $B^2\Sigma^+$ and $A^2\Pi_{1/2}$. This could allow several approaches to magneto-optical trapping using simpler MOT schemes than what is needed for the fluorides [95].

5.4 Cycling Detection Scheme

A complication of BaH, compared to other diatomic molecules currently being studied, is both cycling transitions are in the NIR. For in-cell detection this is not a limiting feature, because photo diodes sensitive to the NIR are readily available. However, for beam studies we need single photon sensitive detection and in the NIR this requires extremely expensive cameras. To get around this we use a higher lying state, the $E\Pi$ state, which decays in the visible (680 nm) as was mentioned in the previous discussions. However by only using one laser beam, we are limited in the fluorescence signal we see, to less than one photon per molecule. The $\mathrm{E}\Pi$ state does not have excellent FCF's so we are limited in the number of photons we can scatter to image the molecular beam, but we can still see some cycling. By applying two lasers, and one EOM, we can improve the SNR and scatter a handful of photons before the molecules decay to dark states. A schematic of this scheme, and the laser spectra used, is shown in fig.5.4

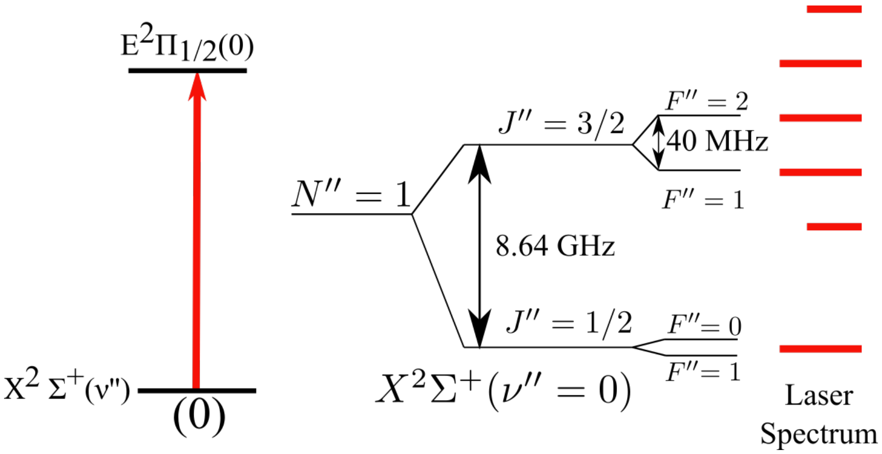

Figure 5.7: Level structure relevant for the fluorescence detection of the molecular beam. Sidebands are generated using an EOM to address the J=3/2 hyperfine splitting.

With both lasers on resonance, we see a clear increase in the PMT counts as the molecular beam passes through the detection region, compared to the background light that is introduced by the detection lasers themselves. For PMT detection the SNR is primarily limited by this background light, so further improvements to the light baffle system, or more complicated detection schemes using two lasers have potential to improve the SNR. Schemes to achieve this are discussed later in this chapter. An example TOF curve is shown in fig.5.4.

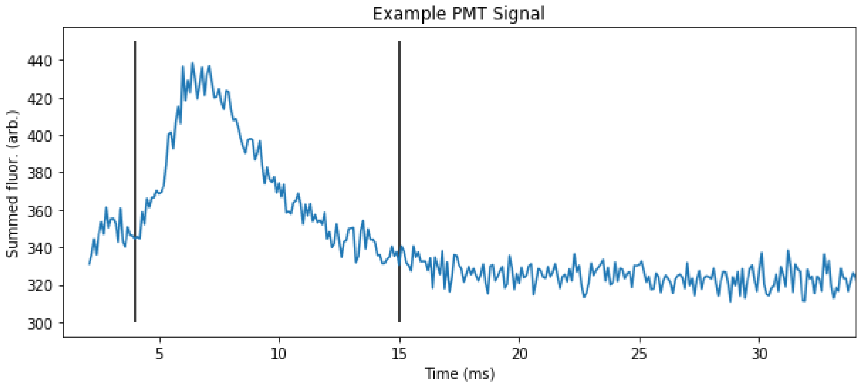

Figure 5.8: TOF signal using the EΠ state for detection. Typical region of interested used to analyze these traces, is shown using the black bars. Early time data is sometime corrupted by increased backgrounds introduced by the ablation laser, but this can be removed.

To confirm we are on resonance independent spectra of the two excitation lasers were performed and the results for the J=3/2 lase are shown if 5.4. For this spectra, the J=1/2 laser remains on resonance, and we see that the symmetric sidebands on the J=3/2 laser optimize the signal when the detuning between the two lasers matches the spin rotation splitting of 8.65 GHz.

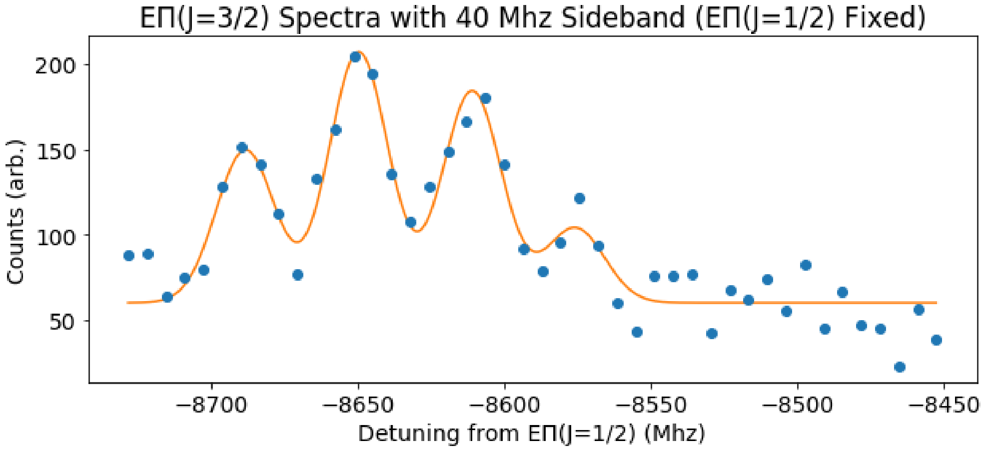

Figure 5.9: Spectra taken with the EΠ(J=3/2) laser only. Multiple resonances are observed due to the EOM sidebands overlapping with the molecular levels.

When the detuning between the two lasers in locked to this optimal value, we can sweep them together to characterize how sensitive the detection is to the exact lock point of the lasers fig. 5.4.

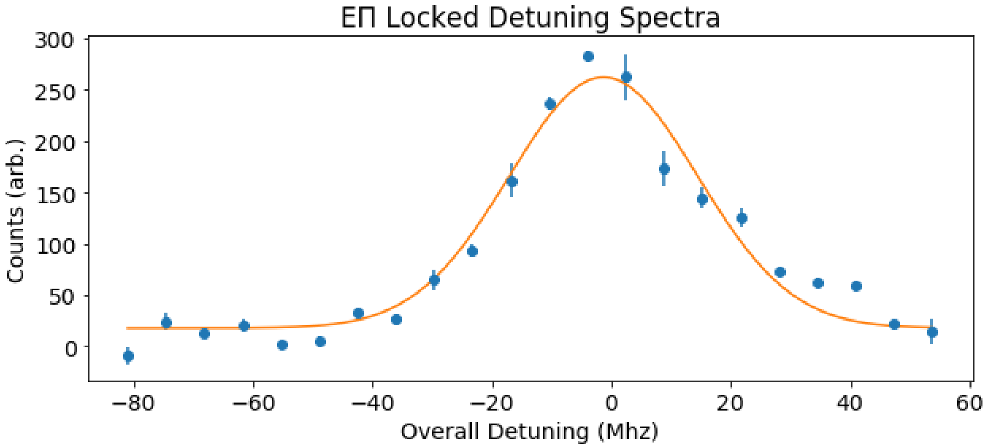

Figure 5.10: Spectra obtained by sweeping the detuning of the both laser used for detection.

Finally, we can characterize the amount of photon cycling that occurs in the detection system, by comparing the fluorescence when just one leg of the excitation laser is present, compared to the case when both are present. When only one laser is present, we expect to quickly pump into the spin rotation state (either J=1/2 or J=3/2) that is not being addressed. By comparing the signal we see in these two cases, to the signal when cycling is occurring, we can estimate that we scatter ≈ 3 photons per molecule. This is not a huge number, but greatly enhances the SNR.

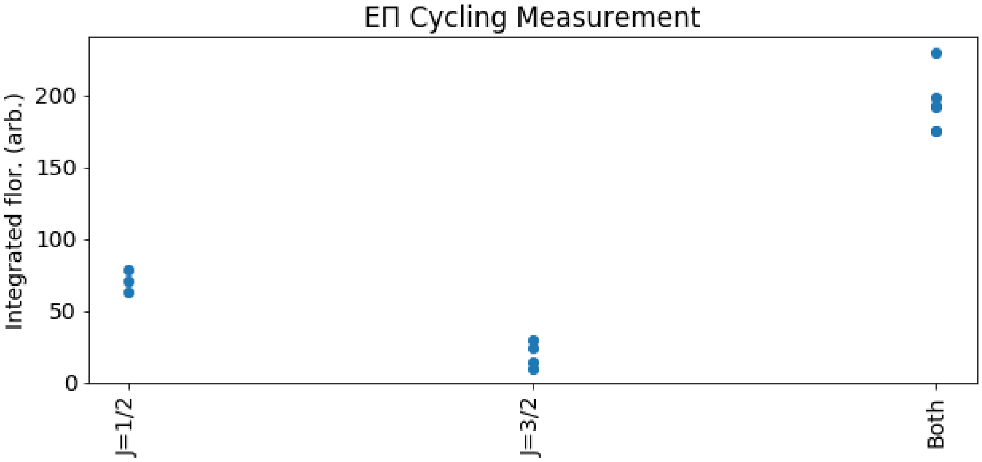

Figure 5.11: Confirmation and quantification of cycling with the EΠ detection system. We find an average scattering of ≈ 3 photons per molecule.

5.4.1 Biased Detection Issues

Beyond the SNR enhancement cycling is important for the $E\Pi$ detection scheme because we want our measurement to be a faithful measurement of the total population of the v=0 state. This is critical for later measurements of photon cycling rates, and repumping efficiencies, and was an early source of confusion in this work. When the sideband structure is not well optimized, you do not detect each hyperfine manifold equally, and this can lead to apparent depletion/enhancement of the v=0 state, that is actually attributable to a change in the population distribution in each hyperfine state.

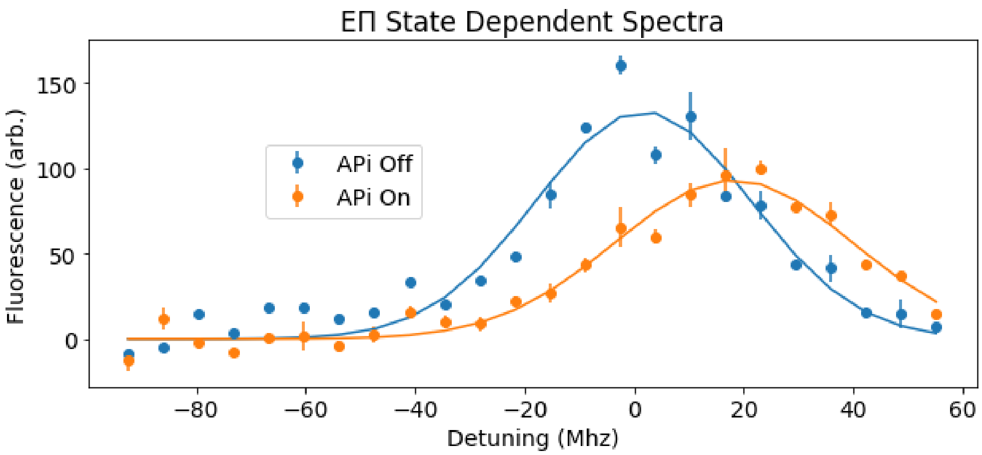

Figure 5.12: EPi Spectra for different ground state distributions with un-optimized detection. When Detection lasers are optimized, we see no change in the line center, and the collected counts are a good measurement of the ground state population.

To illustrates this Fig.5.4.1 shows early data, before the $E\Pi$ detection was optimized. By pumping turning on one leg of the $A\Pi$ laser light, the initial distribution of hyperfine states is perturbed, and we measured a different apparent line center when sweeping the $E\Pi$ laser across the transition. This is a major problem because if we do not change the $E\Pi$ detuning our data becomes hard to interpret. After optimization, and the addition of a 3 MHz EOM broadening the $E\Pi$ detection lasers, we were able to solve this issue, and ensure a consistent interpretation of the detected fluorescence as proportional to the total population in the ground state.

5.5 In Beam Re-pumping Detection

With precise measurements of the level structure and g-factor for the ground and relevant excited states, and a stable means of quantifying the v=0 population, we now move on to characterization of the repumping transition. In order to maximize the scattering rate we chose to repump through the $B\Sigma$ excited state while cycling on the $A\Pi$ state. This means there is no direct coupling between the ground and first vibrational levels, and the we do not double the number of effective ground states. Previous spectroscopy of BaH provided estimated locations of the repumping transition, but with an uncertainty on the order of several GHz. We initially found the location of these states in Chapter 4, but precise measurements in beam are needed. For this search we monitored the v=0 population using the $E\Pi$ detection lasers, then directly pumped into the v=1 ground state using an off diagonal transition (Fig 5.5). We then pump the molecules back to v=0.

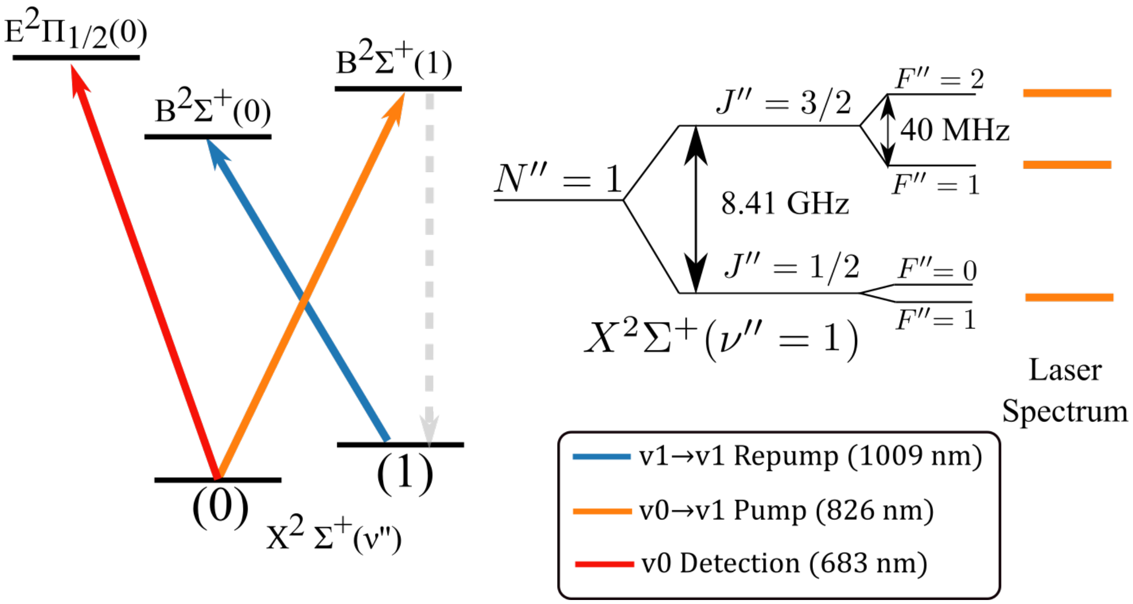

Figure 5.13: Level of states and lasers used for the vibrational repumping search.

For the v=1 pump, we only had one laser, so we are unable to pump the ground state completely to v=0 directly. Instead, we combined the v=1 pump light, resonant with the J=1/2 spin rotation leg, with J=3/2 leg of the $A\Pi$ cycling transition. This allows us to pump molecules into the J=1/2 state, and then into the v=1 state, increasing the population we are able to transfer. A spectra showing the depletion of the ground state with and without the additional $A\Pi$ light is shown in Fig. 5.5. Note that this data was taken on two different days so the total molecules number is different, and the for the first spectra wee swept over a more narrow region, and did not resolve the hyperfine splitting in the $B\Sigma$ excited state.

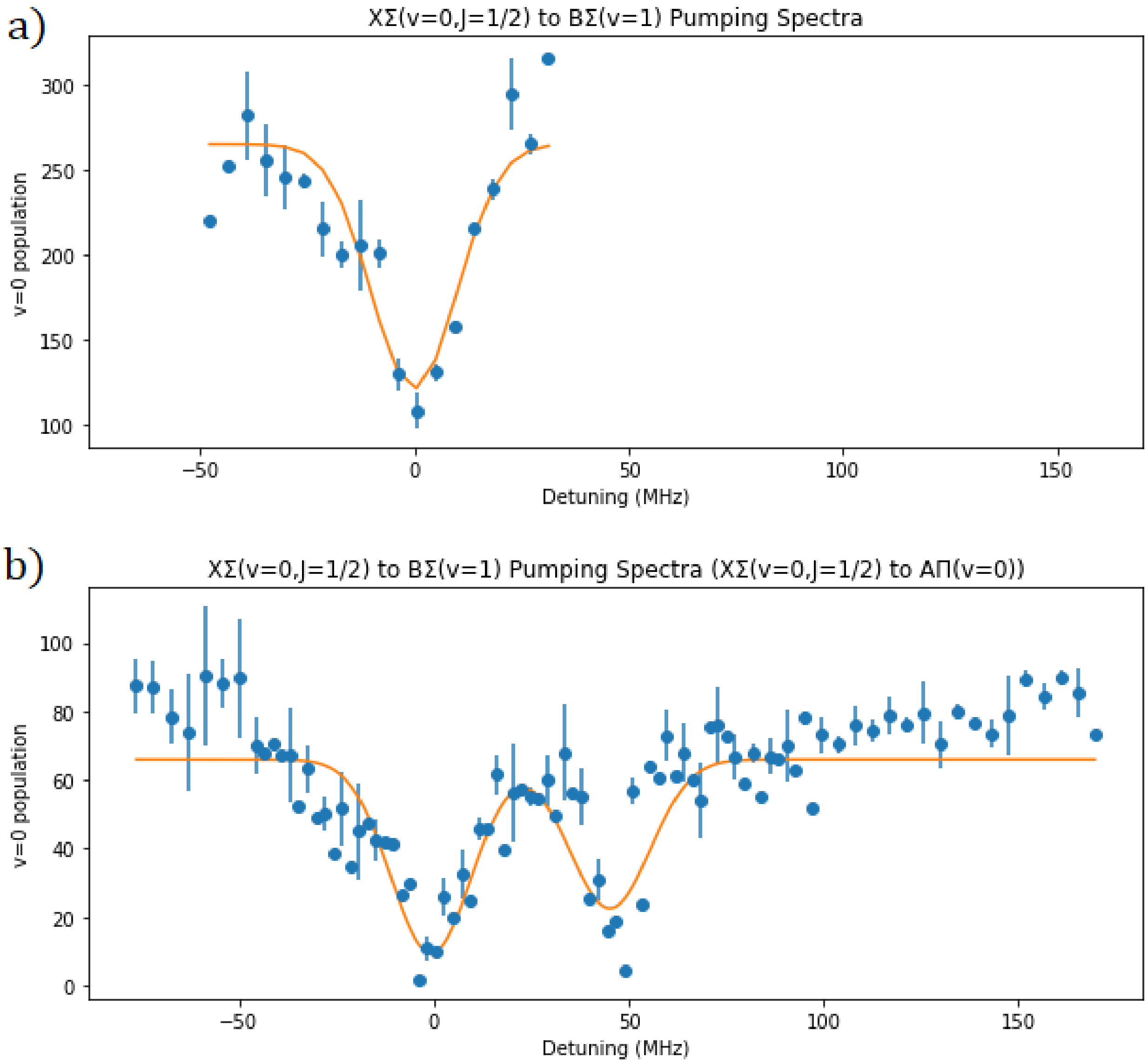

Figure 5.14: A) Depletion of the ground state, using only the $X^2\Sigma^+(v = 0, j = 1/2)$ to $B^2\Sigma^+$(v=1) pump laser. Note that we only deplete around half of the ground state, consistent with the state multiplicity. b) Depletion of the ground state with the additional $X^2\Sigma^+(v = 0, j = 3/2)$ to $A^2\Pi$(v=0) laser. The additional laser allows us to reach almost complete depletion. The two transitions come from hyperfine splitting the in $B\Sigma$ state, as measured previously.

With confirmation that we can directly transfer ≈ 80% of the molecules into the v=1 state (based on the depletion we see from the ground state) we can now try and put them back. By sweeping each laser repumping independently, we can confirm the incell measurements, by looking for an enhancement of the v=0 population when the repumping light is on resonance with either of the spin rotation components (Fig.5.5). We find the same results as incell, as expected.

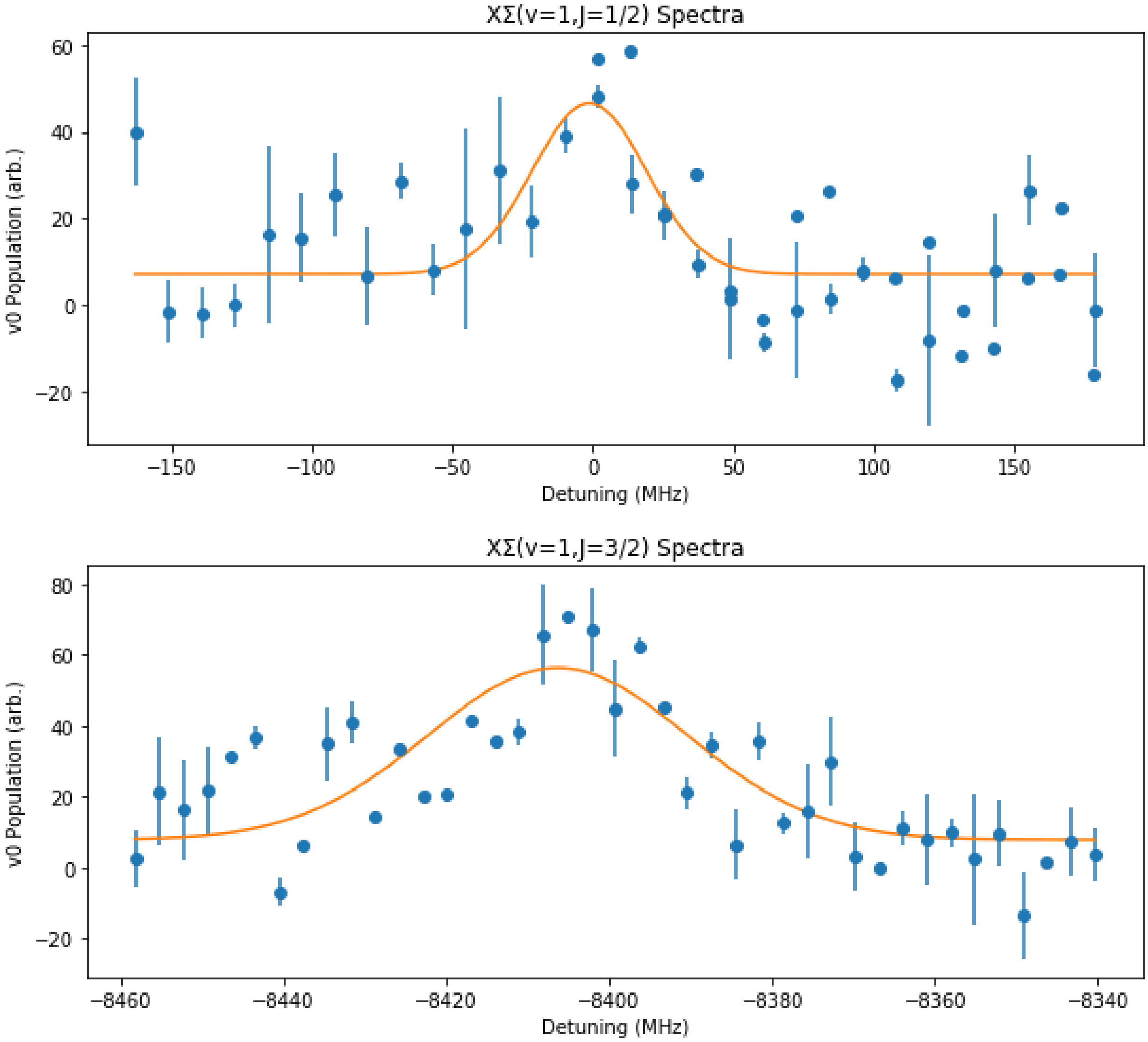

Figure 5.15: Enhancement of the v=0 population, by repumping both spin rotation components of the $X^2\Sigma^+(v = 1)$ state. Spin rotation splitting matches what was previously measured in cell.

This is confirmation that we understand the vibrational splitting, and can achieve vibrational repumping in beam, as well as incell. For this measurement we did not perform a careful measurement of the repumping percentage, and the details of that will be discussed in the next chapter.

5.6 Higher Lying States

In the interest of the eventual photo-dissociation of BaH, we must explore dissociation pathway's. The $C^2\Sigma^+$ state is a potentially good candidate because it is above the continuum ($\approx$ 7400 cm^{-1} or 1350 nm), and it's strong mixing with the $D^2\Sigma^+$ state means different vibrational levels can have very different overlaps with the ground state and the continuum (Fig. 5.6.1). For this purpose I will present all the data we have collected about the $C^2\Sigma^+$ state. This has the additional benefit, of being a potential candidate for two photon detection, and therefor a background free measurement.

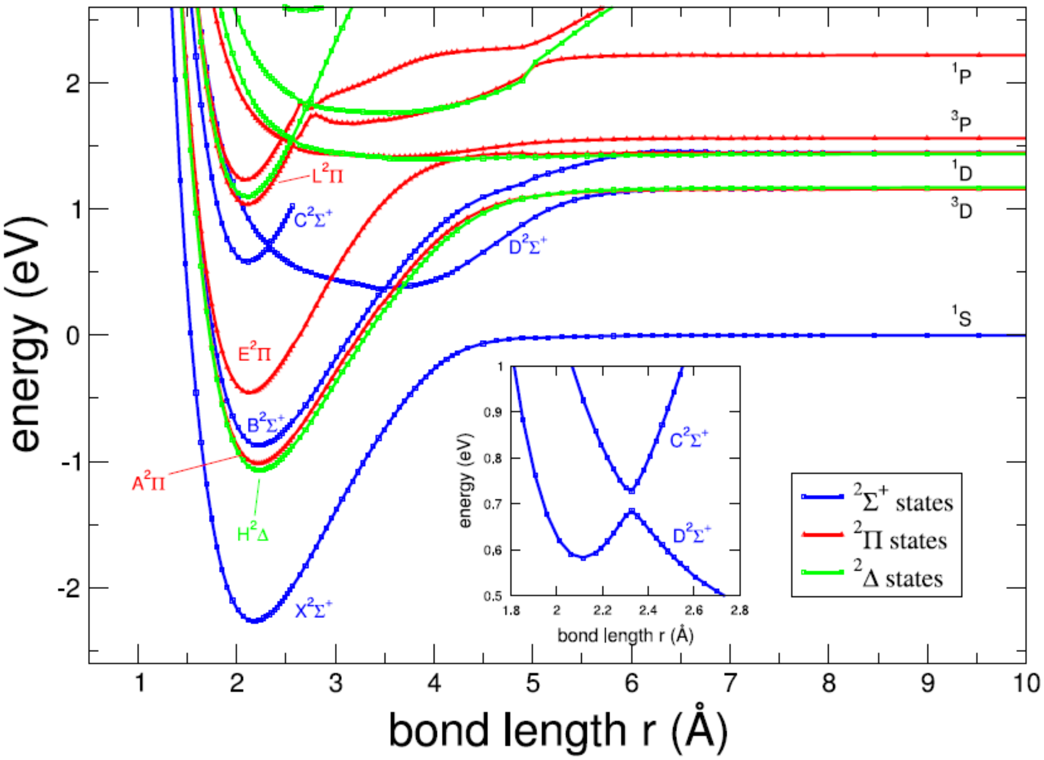

Figure 5.16: Potentials from Ian Lane. Note the highly perturbed $C^2\Sigma^+$ state, which depending on what vibrational level we consider, could have decent overlap with both the ground, and the continuum.

We were able to collect three pieces of data about the C state of BaH. The first is an accurate measurement (within 10 MHz) of the $A^2\Pi_{1/2}(N'' = 0, J = 1/2) \rightarrow C^2\Sigma^+(N' = 1, J = 3/2)$ transition energy, and therefore the most accurate measurement of the energy of this electronic state. The second is an accurate measurement of the linewidth of the $A^2\Pi_{1/2}(N'' = 0, J = 1/2) \rightarrow C^2\Sigma^+(N' = 1, J = 3/2)$ transition. The third is a measurement of the saturation intensity of this transition. As I will argue, the first two pieces of data are useful, and will help pin down the nature of the $C^2\Sigma^+$ state. However, I do not believe we have enough data to get useful information from the saturation intensity measurement. This because the $C^2\Sigma^+$ state is not well closed, and we cannot isolate the effect of saturating the transition (in the sense that the Rabi rate is higher then the decay rate) and saturation in the sense that the molecules are pumped into dark states during the interaction time. If we repeated this experiment, and varied the interaction time to separate the two effect, this may be possible.

5.6.1 State Assignment

The assignment of the observed resonance to the $C^2\Sigma^+(N' = 1, J = 3/2)$ is based on earlier spectroscopy results from Kopp "Rotational analysis of the perturbed C and D states of BaH and BaD" [89]. This paper is very useful, as it describes the energy levels of the highly perturbed C and D states in BaH. To predict where the transition will occur, we took the provided term value for the $X^2\Sigma^+(N = 1, J = 1/2)$ state (587.57 cm^{-1}), and the term value for the $C^2\Sigma^+(N' = 1, J = 3/2)$ (24298.77 cm^{-1}). This is a transition into the vibrational manifold the paper labels as the C0a level, as their is a splitting in the ground vibrational level of the C state (labeled a and b). See the paper for additional details. This term value and the precisely measures transition energy for the $X^2\Sigma^+(N' = 1, J = 1/2) \rightarrow A^2\Pi_{1/2}(N'' = 0, J = 1/2)$ transition (9426.97 cm^{-1}) allows us to predict the energy for the $A^2\Pi_{1/2}(N'' = 0, J = 1/2) \rightarrow C^2\Sigma^+(N' = 1, J = 3/2)$ transition of 14284.2 cm^{-1} or 700.07259 nm.

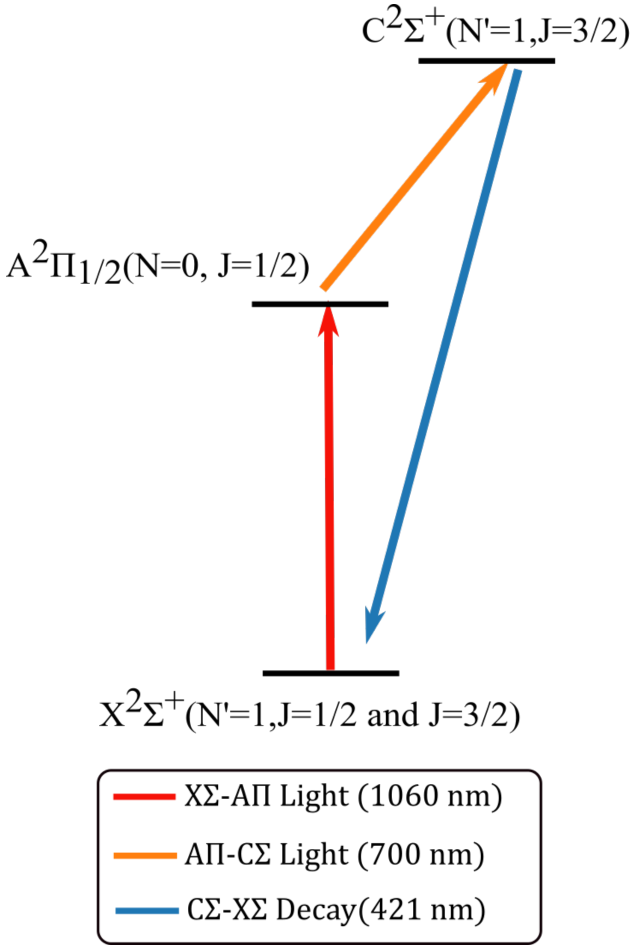

Figure 5.17: Level Structure for the experiments performed in this paper. Here all detection happens on decay from the $C^2\Sigma^+ \rightarrow X^2\Sigma^+$ state, with dichroic filters blocking light from all other decay paths.

5.6.2 Spectroscopy Results

Because we are monitoring decay from the $C^2\Sigma^+$ state directly, each spectra requires a two photon transition. For each experiment, there are 3 frequencies present in the $A^2\Pi_{1/2}$ laser, in order to efficiently excite every ground hyperfine state to the $A^2\Pi_{1/2}$ where it can in turn be excited to the $C^2\Sigma^+$ state. We took spectra of the $A^2\Pi_{1/2} \rightarrow C^2\Sigma^+$ transition, for various $A^2\Pi_{1/2} \rightarrow C^2\Sigma^+$ powers, and $X^2\Sigma^+ \rightarrow A^2\Pi_{1/2}$ powers to try and study any power dependence. We did not see any but we can use the data to get a good estimate of the line center and the uncertainty in the line center, by combining all the spectra. Here is one example spectra. For all of this data, the

$X^2\Sigma^+(N' = 1, J = 1/2) \rightarrow A^2\Pi_{1/2}(N'' = 0, J = 1/2)$ Laser was fixed at 1060.78657 nm.

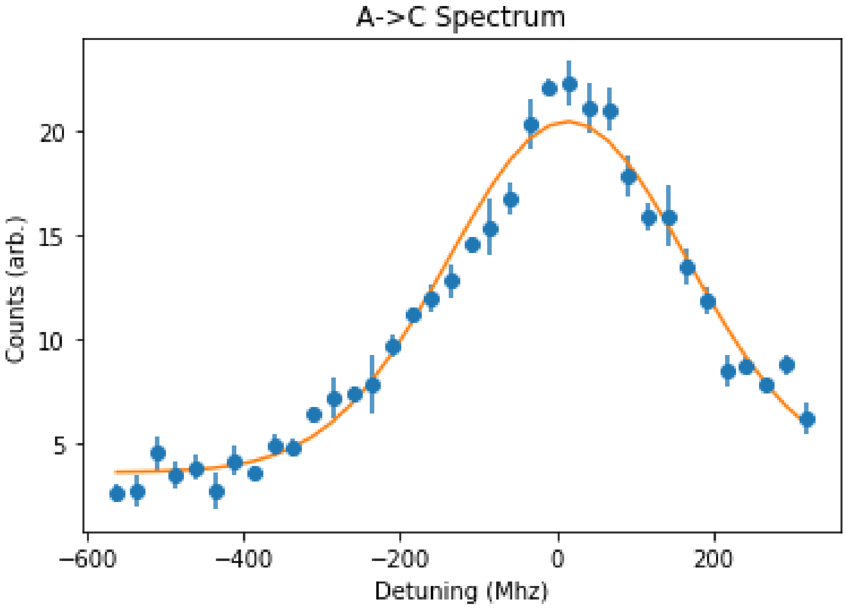

Figure 5.18: Binned data, and the best fit curve

We took a total of 6 good spectra for various values of $X^2\Sigma^+ \rightarrow A^2\Pi_{1/2}$ and $A^2\Pi_{1/2} \rightarrow C^2\Sigma^+$ Power, and fit each to a Gaussian. Here is the spread in this fit location, about the average. Note that each of these was taken for different powers, but no systematic dependence was found.

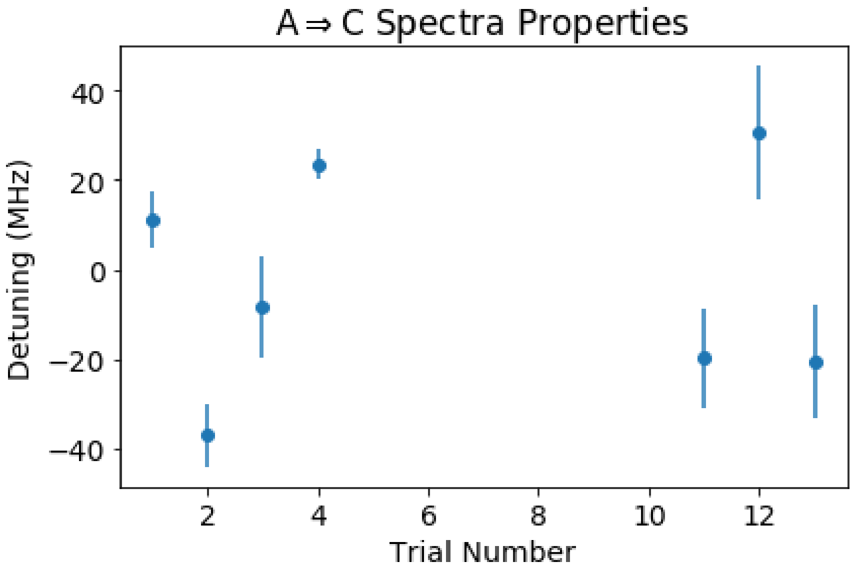

Figure 5.19: 1 to 4 are various $X^2\Sigma^+ \longrightarrow A^2\Pi_{1/2}$ powers, 11-13 are for different $A^2\Pi_{1/2} \longrightarrow C^2\Sigma^+$ powers.

If we average these best fit parameters for these spectra, we get an estimate of central wavelength of $700.07155 \pm 2 * 10^{-5}$ nm. Which is a uncertainty of 10 MHz on this transition. This means we know the $X^2\Sigma^+(N' = 1, J = 1/2) \longrightarrow$-$C^2\Sigma^+(N'' = 1, J = 1/2)$ transition occurs at $421.741247 \pm 3 * 10^{-5}$ nm. Based on your exact assignment of the $X^2\Sigma^+(N' = 1, J = 1/2)$ term value, this allows us to pin down the location of the $C^2\Sigma^+$ electronic levels. This is about 600 MHz away from the predicted transition energy, which is reasonably close given the accuracy of the prediction.

5.6.3 Line Width and Saturation Intensity Theory

Before I present the data we collected on the linewdith and saturation intensity, I want to introduce some theory results to give the data context. This is taken from a very relevant paper by Michael Tarbutt "Lifetime of the A state and Franck-Condon factor of the $A - X$ transition of CaF measured by the saturation of laser-induced fluorescence". Interpreting the linewdith measurements is straight forward, and gives us a direct estimate of the total decay constant for a state Γ

and the states lifetime τ

$$\Gamma = \frac{1}{\tau}. \tag{5.5}$$

Analyzing the saturation intensity measurements is a bit more complicated. We can obtain an an expression for the saturation intensity of a transition between a ground state with label i, and an excited state labeled j based on the standard definition of saturation intensity.

$$\frac{I}{I_s} = \frac{2\Omega^2}{\Gamma^2} \tag{5.6}$$

Here $I = \frac{1}{2}\epsilon_0 c E_0^2$ is the intensity of the drive, $\Omega = E_0 z_{ij}/\hbar$ is the rabi rate (with $z_{jk} = \left\langle j|\hat{d}.\hat{z}|k\middle|j|\hat{d}.\hat{z}|k\right\rangle$ being the transition dipole element) and we can redefine Γ based on a sum of all the decay pathways from the j'th state.

$$\Gamma = \frac{1}{\pi\hbar\epsilon_0 c^3}\sum_k \omega_{jk}^3 z_{jk}^2 = \frac{1}{\tau} \tag{5.7}$$

Now, we can directly measure Γ based on the measurement of the linewidth, and that gives us experimental access to the value of this potentially very hard to calculate sum. By contrast, if we instead consider the saturation intensity of a transition we can obtain a different expression.

$$I_s = \frac{1}{4c^5\pi^2 z_{ij}^2\epsilon_0}\left(\sum_k \omega_{jk}^3 z_{jk}^2\right)^2 \tag{5.8}$$

To summarize the measurement of the linewidth gives us access to the value of the sum term and to the lifetime of the state. The measurement of the saturation intensity gives us access to one specific dipole transition element, assuming we can recover the value of the sum from the linewidth measurement.

5.6.4 Line Width Results

Using the same data, we can also analyze the width of the $A^2\Pi_{1/2} \rightarrow C^2\Sigma^+$ transition, relative to the $X^2\Sigma^+ \rightarrow A^2\Pi_{1/2}$ transition. Again, we took this data for several different powers of both lasers, and so no observable dependence.

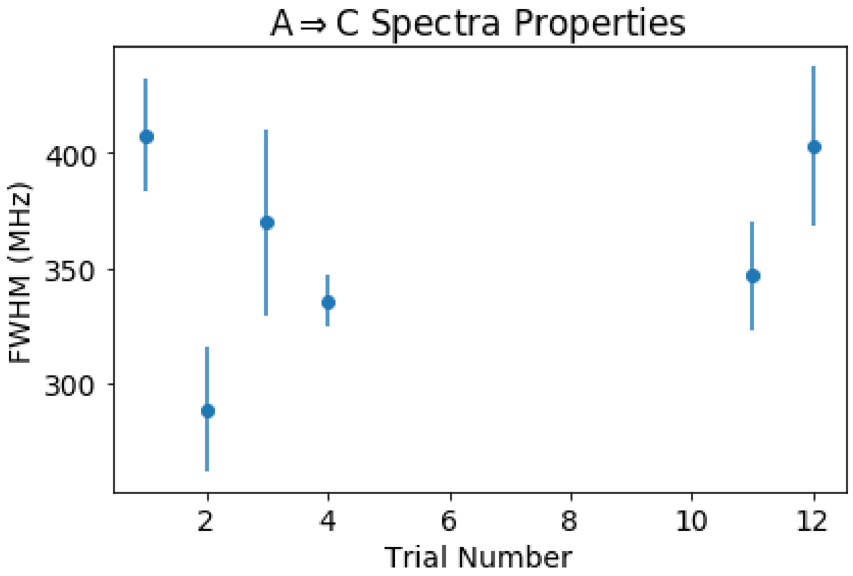

Figure 5.20: 1 to 4 are various $X^2\Sigma^+ \rightarrow A^2\Pi_{1/2}$ powers, 11-13 are for different $A^2\Pi_{1/2} \rightarrow C^2\Sigma^+$ powers. Here we report the fitted FWHM of the distribution, and obtain similar values when a functional form of a Gaussian, or Lorentizian in used.

Now, we can compare this width to $X^2\Sigma^+ \rightarrow A^2\Pi_{1/2}$ width taken at lower power, which has a width of 41 MHz (using data collected on the same day). This shows that the $X^2\Sigma^+ \rightarrow A^2\Pi_{1/2}$ is broadened past the natural linewidth due to a combination of needing many side-bands, and Doppler broadening (there was no aperture installed for this data collection period). Because the $A^2\Pi_{1/2} \rightarrow C^2\Sigma^+$ is substantially broader than the $X^2\Sigma^+ \rightarrow A^2\Pi_{1/2}$ this indicate that the $C^2\Sigma^+$ state must have a shorter lifetime then the $A^2\Pi_{1/2}$ state. Averaging the widths we get 358 ± 15 MHz. Similar (within error bars) fit parameters are obtained when the data is fit to either a Lorentzian or a Gaussian, but we do not have the SNR to identify which functional form fits the data best. This would indicate the lifetime of the C state is $4 \pm .2 * 10^{-10}$ seconds which is very short. One caveat of this measurement, is there may be some hyperfine structure in the $C^2\Sigma^+$ excited state (the hyperfine $A^2\Pi_{1/2}$ state is less than 4 MHz) which leads to a broadened transition. I would expect the hyperfine splitting to be similar to the $X^2\Sigma^+(N = 1, J = 3/2)$ and $B^2\Sigma^+(N = 0, J = 1/2)$ states, which is $\approx 40MHz$, but I am not 100% sure.

5.6.5 Saturation Results

The last data point, we locked the lasers at the observed optimal values, then varied the power for both the $X^2\Sigma^+ \rightarrow A^2\Pi_{1/2}$ laser, and the $A^2\Pi_{1/2} \rightarrow C^2\Sigma^+$ laser. We then looked at the counts observed on the PMT. We also used a camera to make sure the two beams were well coaligned, and the same size (≈ 1 cm radius). This is a useful measurement for the $X^2\Sigma^+ \rightarrow A^2\Pi_{1/2}$ transition, because the closure of the state allows us to use the theory developed above. However, for the $C^2\Sigma^+$ state (which is not closed) we cannot be sure we are measuring saturation in the sense of sufficiently high rabi rate, or saturation in the sense of optical pumping into dark states, so the data is very hard to interpret. However I have included the data, as it may be useful anyway.

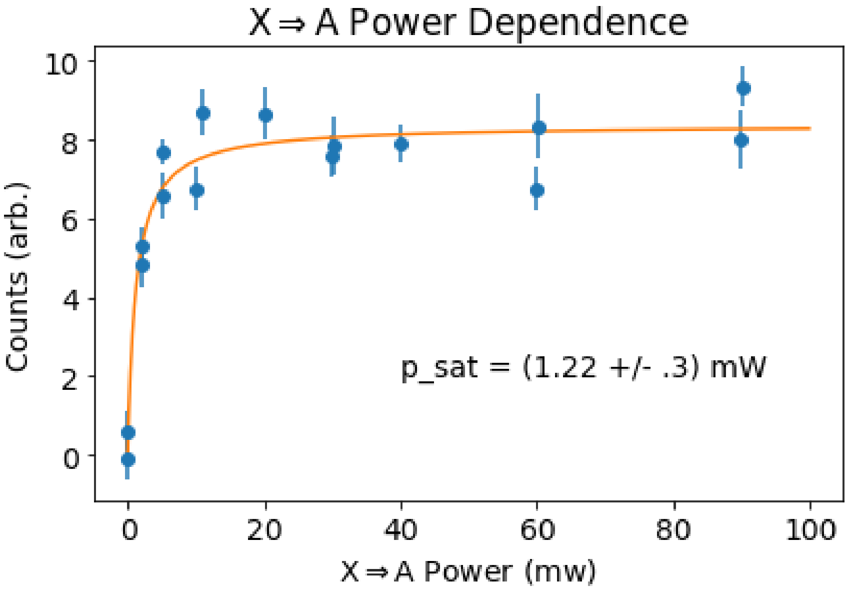

Figure 5.21: It takes a very small amount of power, to saturate the AΠ transition. Here the $A^2\Pi_{1/2} \rightarrow C^2\Sigma^+$ laser had 10 mW. With a measured beam radius of 1 cm, this corresponds to a saturation intensity of 3.8 W/m^2

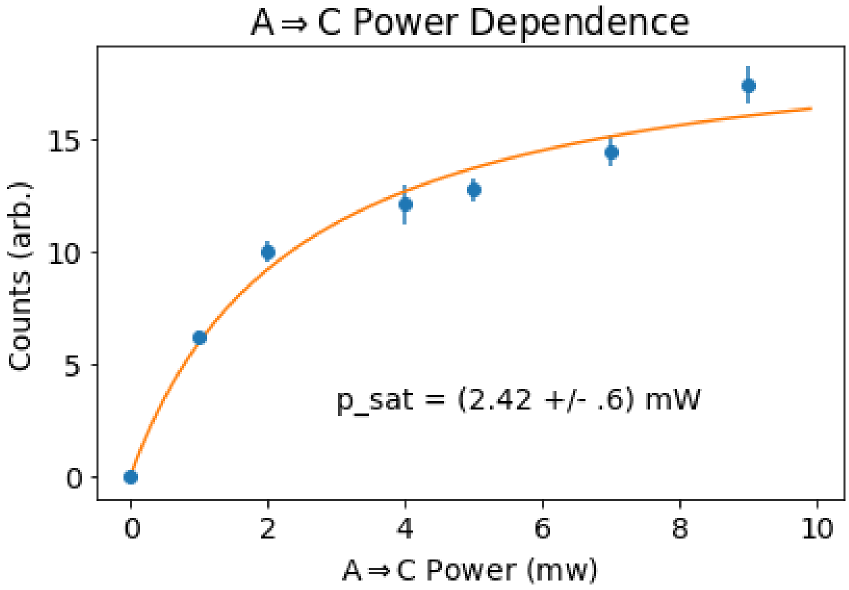

Figure 5.22: Here we see it takes about twice the power to saturate the $A^2\Pi_{1/2} \longrightarrow C^2\Sigma^+$ transition. Here $X^2\Sigma^+ \longrightarrow A^2\Pi_{1/2}$ was set to 100 mW. With a beam radius of 1 cm, this corresponds to a saturation intensity of 7.7 W/m^2

5.6.6 AΠ Benchmark

We independently know that AΠ state has a lifetime of 138 ns. This allows us to directly estimate the value for the sum term presented before (and repeated below).

$$\Gamma = \frac{1}{\pi\hbar\epsilon_0 c^3}\sum_k \omega_{jk}^3 z_{jk}^2 = \frac{1}{\tau} \tag{5.9}$$

We obtain $\sum_k \omega_{jk}^3 z_{jk}^2 = 5.8 * 10^{-13}$ for this term. We can use this, to estimate the value of the specific coupling between the $X^2\Sigma^+ \longrightarrow A^2\Pi_{1/2}$ state $z_{ij} = 1 * 10^{-29}$. We also know one additional thing about the AΠ state, which is that it is very diagonal, so we can reduce this sum down to a single term reducing

$$I_s \approx \frac{1}{4c^5\pi^2 z_{ij}^2 \epsilon_0}\left(\sum_k \omega_{jk}^3 z_{jk}^2\right)^2, \tag{5.10}$$

to

$$I_s = \frac{1}{4c^5\pi^2\epsilon_0}\left(\omega_{ij}^6 z_{ij}^2\right). \tag{5.11}$$

This allows us to do a sanity check, and estimate the saturation intensity a second way. Alternatively you can think of this as way to calibrate the beam size based on a known transition. For a beam radius of 1 cm, they agree very well (within 5%).

Another way to look at this result is as measurement of the closure of this state. We find the contribution to the sum from this single term is 98% of the value of the total sum. This means the FCF is something like 98%. This is a nice result, but the result depends on the measurement of the beam width, which is very hard to do accurately, so I don't trust it as much as other techniques.

5.6.7 $A^2\Pi_{1/2} \rightarrow C^2\Sigma^+$ Analysis

We can repeat the same analysis covered above, for the $A^2\Pi_{1/2} \rightarrow C^2\Sigma^+$ transition which we know much less about. We obtain $\sum_k \omega_{jk}^3 z_{jk}^2 = 1.7 * 10^{-10} s^{-1}$ and $z_{ij} = 1 * 10^{-27}$. However, there is a problem with this analysis. Because we know the wavelength of the $A^2\Pi_{1/2} \rightarrow C^2\Sigma^+$ transition, and have an estimate for the dipole element for this transition, we can calculate the contribution of this one decay channel to the sum. We find, that this single term, is larger then our estimate for the entire sum. Clearly this is nonsensical so something in the analysis must wrong. I believe it comes down to the fact, that this analysis holds, when the interaction time is less than the time it takes to deplete a state. Because the AΠ is pretty closed, this analysis works for that transition. However, the C state is NOT closed, and has an extremely short lifetime, so we do not appear to be in that limit.That means interpreting this measurement alone, cannot be used to get the dipole element. We are only able to recover the energy of the state, and it's lifetime, but this is still useful result for theorist to help guide work on dissociation. A collaboration with Professor Ian Lane using this measurement is ongoing.

Chapter 6: Optical Cycling, and Vibrational Repumping

6.1 Optical Cycling

In order to optically manipulate an atomic or molecular species you need to scatter as many photons as possible, in order to maximize the applied force. In this chapter I will introduce a theoretically the requirements we must satisfy to maintain a high scattering rate, and then show how optical cycling was experimentally obtained and optimized in our system. This represents a shift in the work, from trying to understand the properties of BaH, to exploiting those properties. Optical cycling is a prerequisite to laser cooling, laser slowing, and the eventually trapping in a magneto-optical trap.

6.1.1 Rate Equation Formulation

Theoretically the goal of maintaining high scattering rate comes down to the ability to maintain a large state population in the excited state. This provides a simple optimization that we can consider when approaching a new system. In general, there are two approaches to study a system like this theoretically. The first is the so called rate equation model where we model the evolution of the system while neglecting any coherence in the system. This results in a system of coupled ODE's where each variable is the population of a specific state, and the couplings between states are either spontaneous decay coupling excited states to ground states, or laser fields coupling two states together. As a simple example we can express a driven two level system using the following set of ODE's.

$$\begin{aligned}\frac{d\rho_g(t)}{dt} &= -\Omega\rho_g(t) + (\Gamma+\Omega)\rho_e(t) \\ \frac{d\rho_e(t)}{dt} &= \Omega\rho_g(t) - (\Gamma+\Omega)\rho_e(t)\end{aligned} \tag{6.1}$$

Here the population of the excited (ground) state is denoted as ρ_e (ρ_g). The spontaneous decay rate of the excited state back to the ground state is Γ and the excitation rate (which drives both stimulated absorption and stimulated emission) is Ω. Solving for the steady state population, with the requirement that the total state population is one, we find.

$$\rho_e = \frac{\Omega}{\Gamma + 2\Omega} \tag{6.2}$$

We see that as we increase the laser power (Ω) we not only increase the excitation, but we also increase the stimulated decay. This results in a balance where in steady state we cannot fully transfer the population to the excited state. This results in a maximum excited state population of 1/2. In fact, it can be shown that the best you can do under strong coupling, is get an equal population in each state. This means the maximum excited state fraction in general, is limited by the number of excited states (N_e) divided by the total number of state ($N_e + N_g$). As discussed in chapter two, the requirement of rotational closure limits optical cycling in diatomic molecules to $\Delta N = -1$ rotational transitions. This means there will always be more ground states than excited states, and that reduces the scattering rate. This is also why we repump through a different excited state than we cycle on, because if the repump lasers coupled to the same excited state that effectively doubles the number of ground states and reduces the maximum scattering rate by 50%.

6.1.2 Linblad Master Equation

The rate equation is a very useful and very intuitive way to understand population dynamics in driven systems, but it does have limitations, because it does not have any coherence. This is to say, we are talking about quantum states (ρ_e and ρ_g) but this approach only relies on their population, not their phase. The more complete approach is known as the Linblad master equation, based on the density matrix formulation of quantum mechanics. To obtain accurate theoretical estimates for the photon scattering rate we numerically solved the master equation for time evolution of the density matrix ρ in the Lindblad form,

$$\frac{d\rho(t)}{dt} = \mathcal{L}\rho(t), \tag{6.3}$$

with $\mathcal{L}$ being the Lindblad superoperator of the form

$$\mathcal{L}\rho(t) = -i\hbar[H,\rho] + \sum_{i=1}^{N^2-1} \gamma_i \left(C_i \rho C_i^\dagger - \frac{1}{2}\left\{ C_i^\dagger C_i, \rho \right\} \right), \tag{6.4}$$

where C_i belong to a set of orthonormal operators with eigenvalues γ_i and N is number of states included [99, 100]. We used jump operators as our orthonormal set [101], and in our case the dissipative part of the superoperator included only effects of spontaneous emission: for a decay from state $|i\rangle$ to $|f\rangle$ with rate $\Gamma_{i\to f}$, we used $G_{i\to f} = \sqrt{\Gamma_{i\to f}} C_{i\to f} = \sqrt{\Gamma_{i\to f}}\,|f\rangle\langle i|$.

Practically, solving this equation for large systems is challenging and requires a modest amount of computer time. In our group Konrad Wenz took point on these simulations and for details I would refer you to his upcoming thesis. However, we can still tackle small systems analytically and there are useful insights to be gained. For these calculations I used the excellent AtomicDensityMatrix Mathematica package to build these states, and solve for the resulting dynamics. The poor performance of Mathematica on large numerical simulations limits the usefulness of this technique to systems of ≈ 10 states, it is a great help to visualize and understand toy systems.

There are some interesting consequences one only appreciates when the full master equation is considered, and I want to take a little time to discuss some toy systems that capture this. We have not seen experimental signatures for some of these, but they have been observed in atomic systems. Nevertheless, it is important to keep them in mind as they may observed in the future. The core of these effects can be captured in two systems, a 3-1 (3 ground, 1 excited) state, and a λ

system usually discussed in the context of EIT.

6.1.3 3-1 System

The first toy model to consider is 3 ground states each coupled to a single excited state, that decays equally to all three. This system is driven by a single laser field with a Rabi rate Ω_0, there is a symmetric splitting between the ground states of Δg, and the excited state has a total decay rate of Γ. This ground state splitting, can be thought of as Zeeman splitting. For clarity, this system is shown in Fig. 6.1.3.

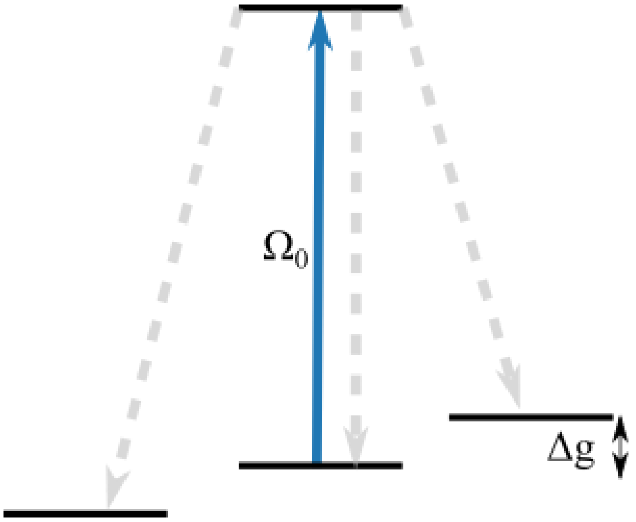

Figure 6.1: The 3-1 toy model for optical cycling in $\Delta J = -1$ systems

Using the linblad master equation, we can solve for the steady state population distribution of this system analytically. Because we are interested in the scattering rate, we can solve for the excited state population (ρ_e), and we find a simple expression, thanks to the relative simplicity of this system.

$$\rho_e = \frac{6\Delta g^2\Omega_0^2}{6(\Gamma^2 + 4\delta^2)\Delta g^2 + 16\Delta g^4 + 9\Omega_0^4} \tag{6.5}$$

Immediately, we can draw some interesting insights. In steady state, if the ground states are degenerate ($\Delta g = 0$) there is no excited state population, and no scattering will occur. This is referred to as dark state remixing, and there are several techniques available to break this degeneracy including microwaves and magnetic fields. In addition to this, we see an unexpected behavior as the Rabi rate increases. In the limit of very strong drive ($\Omega_0 >> \Gamma$ and Δg) the scattering rate goes to zero. So as compared to the two level system discussed previously, when there are more ground states than excited states, increasing the drive power does not necessarily increase the scattering rate. Exploring this we see there exist some optimal drive rate (at zero detuning) depending on the exact splitting in ground state Fig 6.1.3. We see as expected, that the maximum population is .25 ($1/(1+3)$) but this is only true for a range of splittings and drive rates.

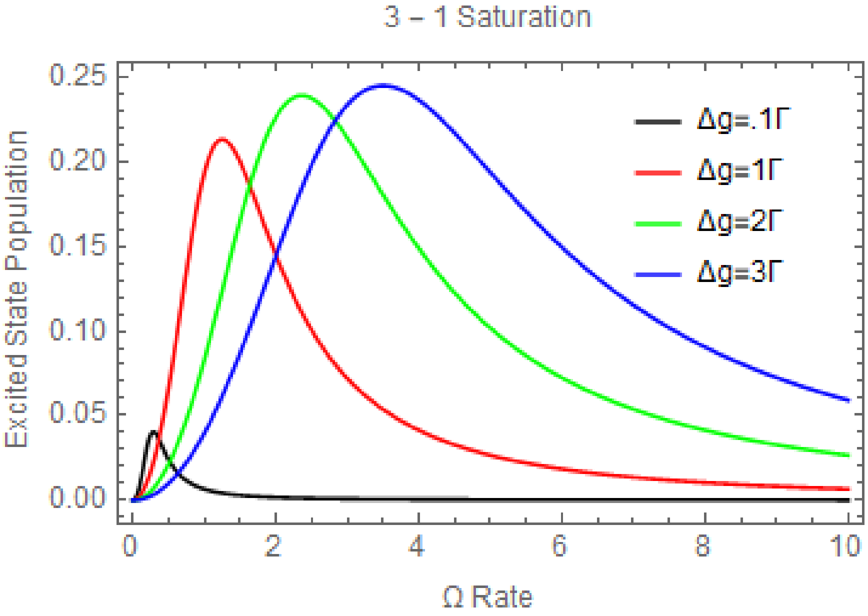

Figure 6.2: Steady state excited fraction for various splittings and Rabi rates. The Rabi rate is expressed in units of Γ. We see for small splittings reduced optimal scattering, and a non-montonic dependence on the Rabi rate, which is not captured in more simple systems.

In general, it seems that a Rabi rate comparable to the ground state splitting leads to the highest scattering. More explicitly, when $\delta = 0$, we can solve for the optimal Rabi rate as a function of the ground state splitting.

$$\Omega_0^{max} = \frac{2^{1/4}(3\Gamma^2\Delta g^2 + 8\Delta g^4)^{1/4}}{\sqrt{3}} \tag{6.6}$$

This result is for a toy model with equal couplings but the result holds for more realistic systems (BaH included) that are less analytically friendly. The lesson here is that higher power doesn't equate to increased scattering.There has to be a balance of the splittings, and the drive intensity, that is not present in more traditional cycling systems with more excited states than ground states. The analogy between this system in our molecule, is for the hyperfine levels on the ground state.

6.1.4 Λ System

We now move to classic system in atomic research, commonly referred to as the Λ system. Here, we have two well separated ground states, each driven with a independent optical field with a Rabi rate of Ω_X and detuning from resonance of δ_X. Schematically this is shown in Fig. 6.1.4. For this discussion, the two optical fields are coherent with each other.

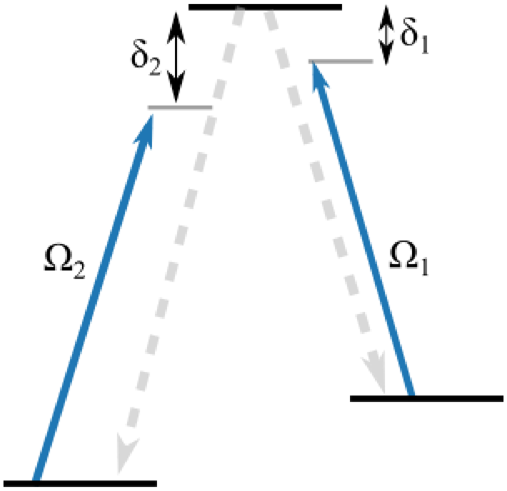

Figure 6.3: The lambda system with unequal detunings and drive intensity.

We can solve this system analytically, using the simplification that the Rabi rates for each laser are equal (Ω_0) to keep things simple, and find the steady state excited population.

$$\rho_e = \frac{(\delta_1 - \delta_2)^2 \Omega_0^2}{(\delta_1 - \delta_2)^2(\Gamma^2 + 2(\delta_1^2 + \delta_2^2)) + (\delta_1 - \delta_2)^2 \Omega_0^2 + \Omega_0^4} \tag{6.7}$$

Again, we can immediately see some interesting behavior. In the limit where the two detunings are equal ($\delta_1 = \delta_2$), the steady state population of the excited state is zero, regardless of any other parameters. This implies that if we set the sidebands from our lasers exactly equal to the hyperfine splitting we will see reduced scattering. We also see that as the drive power goes to infinity, the scattering rate go to zero. Exploring the detuning dependence (Fig. 6.1.4) we can see asymmetric detuning leads to the optimal scattering rate, but again this is all power dependent.

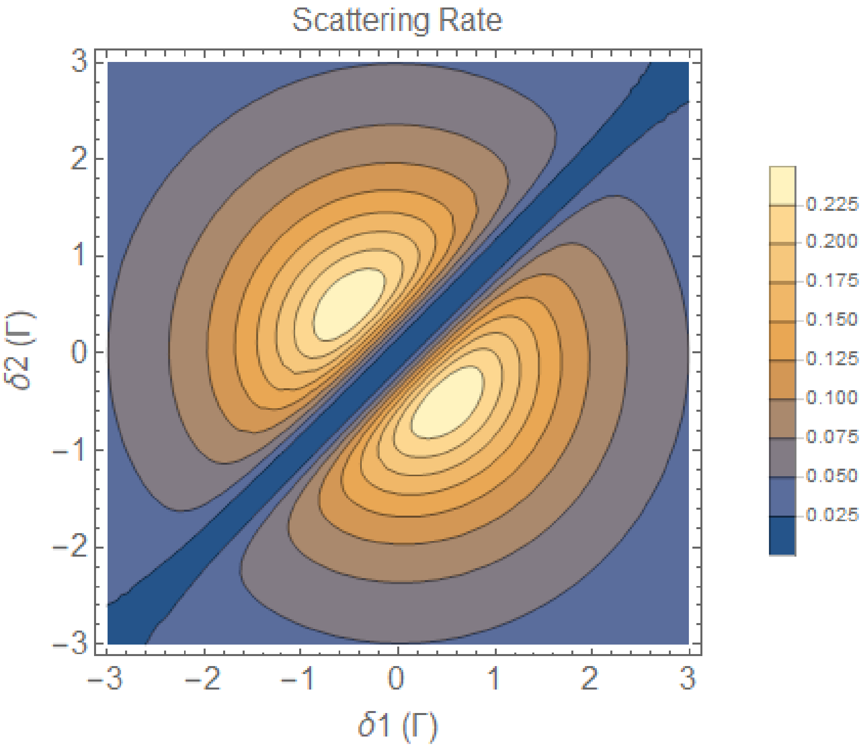

Figure 6.4: Maximum excited state population when $\Omega_1 = \Omega_2 = 1\Gamma$. Notice that asymmetric detuning leads to the optimal scattering rate.

The lesson here is that just putting everything on resonance, is not always what will lead to the optimized scattering rate. Everything must be in balance, and all rates must be comparable. We have seen limited evidence that these effects have limited our experimental efforts, but they have been observed in some systems, and I want to emphasize their presence, which is not widely appreciated.

6.1.5 Full System

With help from Konrad Wenz, we are also able to simulate the response of the full system. Here, we neglect decay to first vibrational level, and have lasers resonant with the $A\Pi$ state as shown in Fig.6.1.5. Side-bands are generated with an AOM with 38 MHz detuning. This generates an additional off resonant sideband, that we include in the simulation as well.

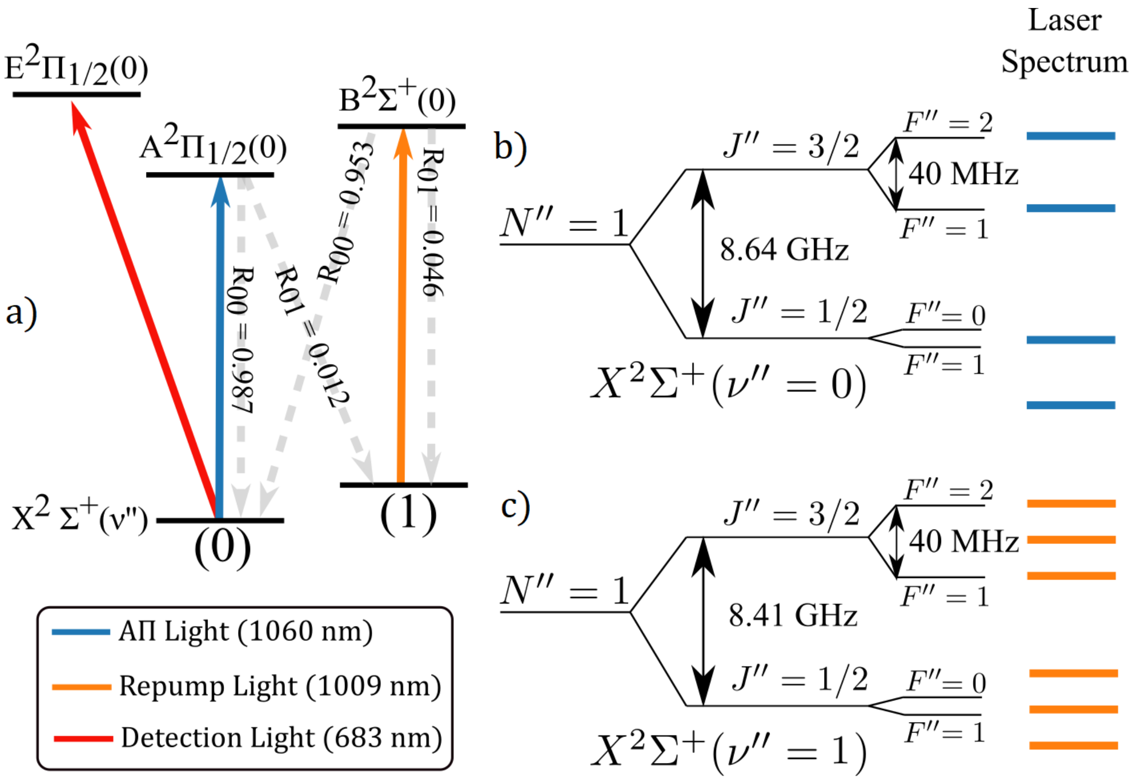

Figure 6.5: Level Structure and laser spectra used for optical cycling studies.

The simulation results in Fig. 6.1.5 were performed with the $J = 1/2$ light on resonance with Rabi rate $\Omega = 13\,\Gamma$ and a background magnetic field $B = 9\,\mathrm{G}$. Both lasers have linear polarization perpendicular to each other, and the $J = 1/2$ laser polarization was at an angle of 1 rad with respect to the quantization axis defined by the magnetic field. Magnetic field and laser polarization were assumed to lie in the same plane.

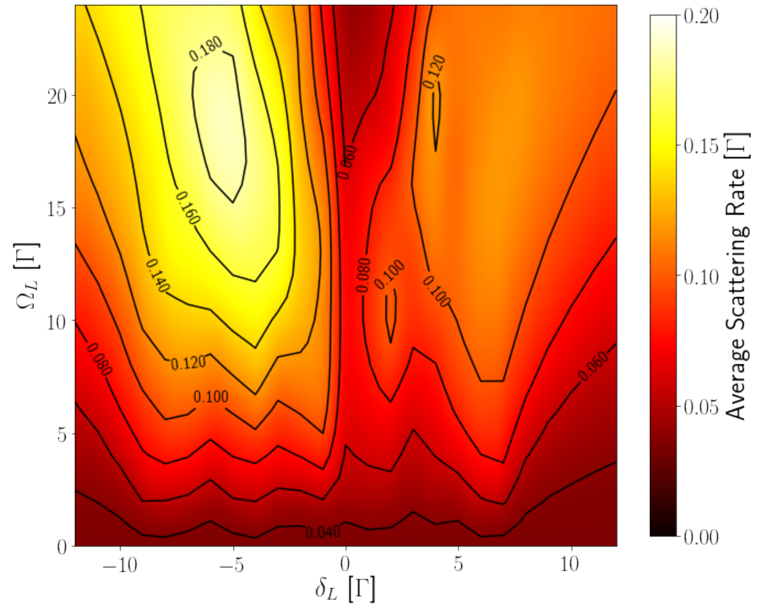

Figure 6.6: Average scattering rate in the BaH model as a function of the Rabi rate and detuning of the $J = 3/2$ light. Notice, that we see an optimal scattering rate when the J3/2 laser is off resonance by $\approx -5\Gamma$. We also see the non-monotonic dependence of drive intensity present in simpler systems.

In our calculations we included both spin-rotational manifolds $J = 1/2$ and $J = 3/2$ in the $v'' = 0$ vibrational state of the $X^2\Sigma^+$ ground electronic state with all the hyperfine levels and the $J' = 1/2$ rotational manifold of the $A^2\Pi_{1/2}$ excited electronic state. We have also assumed no decay into higher vibrational states ($\mathcal{F}_{00} = 1$). Having set up the equations, we also performed an optimization of the average scattering rate over the experimental interaction time T,

$$\overline{\Gamma} = \sum_i \frac{1}{T} \int_0^T \rho_{e_i e_i}(t) \Gamma dt, \tag{6.8}$$

where the sum is over all excited states decaying with the same rate Γ. To find the maximum scattering possible, an optimization was performed with respect to the Rabi rate for the $\left|X^2\Sigma^+; J = 1/2\right\rangle$ to $\left|A^2\Pi_{1/2}; J = 1/2\right\rangle$ transition, Rabi rate for the $\left|X^2\Sigma^+; J = 3/2\right\rangle$ to $\left|A^2\Pi_{1/2}; J = 1/2\right\rangle$ transition, detunings of both transitions, polarization of the light fields, and the background magnetic field responsible for dark state remixing. Given the experimental constraints, we found the maximum achievable average scattering rate of $\overline{\Gamma} \approx \Gamma/5.21$, which agrees well with the highest scattering rate we achieved in the experiment (see Sec. 2).

In Fig. 6.1.5 we observe that the scattering rate is highest for relatively large Rabi rates, which can be expected since the excitation rates have to match remixing rates in order to reach optimal values [102]. We also see that, because of the nature of our coupling scheme where we effectively create a Λ-type system with many more ground states than excited states, having both lasers on resonance is detrimental to achieving high scattering rates.

We find that a lot of the dynamics I present in the toy models, are also present in the full system. The optimal detuning actually occurs when the lasers are off resonance, and increasing the laser power past a given point, leads to reduced scattering. After an optimization over the full parameter space, we found that the highest steady state population we could achieve, was actually .2, reduced from what you would expect based on the rate equation model. I think comes from the fact, that some of the splittings (the hyperfine splitting in particular) is out of our control, and leads so “imperfect" values that are inherent to BaH. We are unable to confirm some predictions from this model, due to limited SNR, and imperfect control over experimental parameters (B-Field in particular) and limited laser power. A major takeaway from this numerical work, is the importance of optimizing each parameter in the full system. It is not enough to scan the transition then lock the laser, you should vary and optimize each set point, and the sidebands in order to maximize the scattering rate, and that is exactly what we did.

6.2 Experimental Optimization

The first step in achieving laser control and cooling of molecular motion is to establish repeated scattering of photons (optical cycling) and characterize dominant loss channels. As discussed previously our detection scheme relies on a non-cycling transition at 683 nm, necessitating a different approach to characterizing the photon scattering dynamics for the main laser cooling transition at 1060 nm. The experimental setup used for characterizing the $(0,0)\ X^2\Sigma^+ \leftrightarrow A^2\Pi_{1/2}$ scattering rate is shown in Fig. 6.2(a): the $(0,1)\ X^2\Sigma^+ \rightarrow B^2\Sigma^+$ repumping light (orange) was blocked, and the number of passes of the $(0,0)\ X^2\Sigma^+ \rightarrow A^2\Pi_{1/2}$ laser (blue) was varied from zero to ~ 20

passes. The 1060 nm laser beam was alternated between “on" and “off" to account for any drift in the molecular beam yield, and each data point is the average of 200 molecular beam pulses. These depletion measurements were performed with a total power of 100 mW (30 mW for repumping) divided evenly between each hyperfine component. Accounting for the beam forward velocity (160 ± 40 m/s [103]) and the measured diameter of the laser beam (1.5 ± 0.1 mm), we can convert the number of passes to the molecule-light interaction time. As seen from the error bars in Fig. 6.2(c,d), this conversion is the dominant source of uncertainty, primarily because of the substantial spread in the beam forward velocity. We can estimate the number of photons scattered (N_{scat}) based on the fraction of molecules that remain in ground vibrational state ($P_{v=0}$), and the known diagonal FCF $\mathcal{F}_{00}$ from previous measurements [104, 88]. Figure 6.2(b) provides a representative ToF data for an unperturbed BaH beam (blue) and with the $(0,0)$ $X^2\Sigma^+ \longrightarrow A^2\Pi_{1/2}$ cycling laser on (orange) resulting in 15% of the molecules remaining in $v'' = 0$ at the detection region. We found no significant dependence of the scattering rate on an applied magnetic field used to destabilize the dark states, most likely because residual field in the interaction region of a few Gauss was sufficient to cause a dark state precession rate comparable to the excitation rate ($\sim 10^6$ s^{-1}).

Following Di Rosa [105], we model the repeated spontaneous emission events by a molecule as a Bernoulli sequence with probability $p = 1 - \mathcal{F}_{00}$ that decay will result in populating an excited vibrational level $v'' > 0$. The probability that a molecule initially in the vibrational ground state will still be in $v'' = 0$ after scattering N_{scat} photons is given by:

$$P_{v''=0} = (\mathcal{F}_{00})^{N_{\mathrm{scat}}} . \tag{6.9}$$

Therefore, we can convert the fraction $P_{v''=0}$ into the number of scattered photons for the remaining molecules:

$$N_{\mathrm{scat}} = \frac{\log P_{v''=0}}{\log \mathcal{F}_{00}} . \tag{6.10}$$

The expectation value of N_{scat} for a molecular ensemble can be estimated by modeling the photon scattering process before the molecule is optically pumped into $v'' = 1$ as a geometric distribution with the expected value of

$$\langle N_{\text{scat}} \rangle = \frac{1}{1 - \mathcal{F}_{00}} \approx 80, \tag{6.11}$$

and the standard deviation in N_{scat} of

$$\sigma_{N_{\text{scat}}} = \frac{\sqrt{\mathcal{F}_{00}}}{1 - \mathcal{F}_{00}} \approx 80. \tag{6.12}$$

Equation 6.10 allows us to estimate the photon scattering rate for the molecules remaining in $v'' = 0$ as a function of the laser interaction time, $N_{\text{scat}} = R_{\text{scat}} t_{\text{int}}$. However, as shown in equations 6.11 and 6.12, for any specific molecule there is a wide range of actual number of scattering events, meaning this setup would not be efficient for optical manipulation, as a wide range in transverse momentum would be imparted. As shown in Fig. 6.2(c), a constant scattering rate of $1.4(1)\times10^6$/s can be maintained, which is ~ 80% of the expected maximum scattering rate $R_{\text{scat,max}}$ based on the ground and excited state multiplicities,

$$R_{\text{scat,max}} = \frac{1}{\tau_{\text{sp}}} \frac{n_e}{n_e + n_g} = 1.8 \times 10^6/\text{s}, \tag{6.13}$$

where $\tau_{\text{sp}} = 136.5$ ns [88] is the spontaneous excited state lifetime and n_g (n_e) is the number of ground (excited) m_F magnetic sublevels. While Eq. (6.13) provides a useful way to approximate the maximum possible scattering rate for molecules, our estimates for the achievable scattering rate in the experiment using both a multilevel rate equation model as well as an optimized numerical simulation of the full system using the Lindblad master equation predict $R_{\text{OBE}} \approx 1.4 \times 10^6$ s^{-1}. The data presented in Fig. 6.2(c) shows that we achieve $R_{\text{scat}} \approx 0.96 R_{\text{OBE}}$ in this experimental configuration with maximum interaction time $t_{\text{int}} \approx 900\tau_{\text{sp}}$. However, we were not able to obtain this high scattering rate for deflection and slowing experiments, instead only obtaining ≈ 60% of the maximum value. We attribute this to reduction in scattering rate due to slower then optimal repumping, or presence of dark states we were unable to remix efficiently. We find good agreement with the full simulation, which is about 25% lower than the rate equation solution.

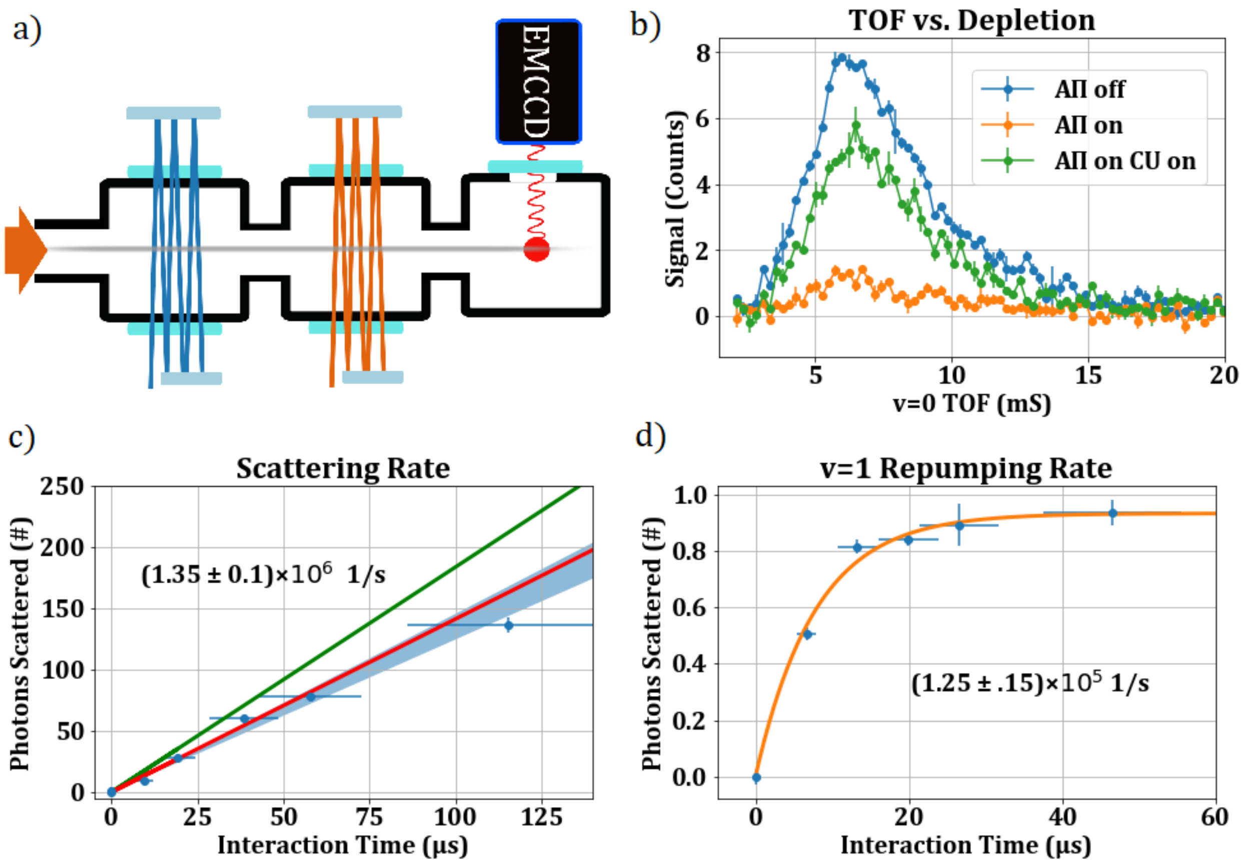

Figure 6.7: (a) Diagram of the experimental setup showing the spatially separated depletion and clean-up (CU) regions, followed by $(0,0)$ $X^2\Sigma^+ \longrightarrow E^2\Pi_{1/2}$ fluorescence detection. b) Example time-of-flight signals for the unperturbed (AΠ off), depleted (AΠ on), and vibrationally repumped (AΠ on and CU on) molecular beam signals. c) Scattering rate for the $(0,0)$ $X^2\Sigma^+ \longrightarrow A^2\Pi_{1/2}$ transition, based on depletion of $v'' = 0$ population as a function of interaction time. Blue points and band represent the data and the 1σ uncertainty from a linear fit. Green (slope 1.84×10^6 s^{-1}) and red (slope 1.41×10^6 s^{-1}) lines show the theoretical estimates obtained from Eq. 6.13 d) Estimation of scattering rate for the repumping transition based on repopulation of the $v'' = 0$ state. We find a rate of 1.25×10^5 photons/s.

Our measurement of the scattering rate relies on $(1,0)$ $X^2\Sigma^+ \longleftarrow A^2\Pi_{1/2}$ being the dominant loss mechanism out of the quasi-cycling transition. As shown in Fig. 6.2(b), with an addition of the $(0,1)$ $X^2\Sigma^+ \longrightarrow B^2\Sigma^+$ repumping laser in the "clean-up" region, we return most of the molecules (green curve) back into the ground vibrational level. The $B^2\Sigma^+$ $(v' = 0)$ state has a good Franck-Condon overlap with $X^2\Sigma^+$ $(v'' = 0)$ ($\mathcal{F}_{00} = 0.953$ [88]) so molecules excited to this state decay to the desired ground state $|v'' = 0, N'' = 1\rangle$ with a 95% probability. In order to determine the photon scattering rate for the $(0,1)$ $X^2\Sigma^+ \longrightarrow B^2\Sigma^+$ repumping transition, we begin by depleting $v'' = 0$

on the main cycling transition (0, 0) $X^2\Sigma^+ \longrightarrow A^2\Pi_{1/2}$ at the maximum interaction time. Then in a separate region (Fig. 6.2(a)) we apply the repumping light, while varying the number of passes through the molecular beam. Because $\mathcal{F}_{00} \approx 1$ for the (0, 0) $X^2\Sigma^+ \longleftarrow B^2\Sigma^+$ transition, it will only take $1/\mathcal{F}_{00} \approx 1$ photon scattered from the repumping laser to optically pump a molecule back to $v'' = 0$. As shown in Fig. 6.2(d), we model the interaction time required for scattering one photon in the CU region as an exponential distribution with a cumulative distribution function given as $N_{\text{scat}} = N_{\text{offset}}\,(1 - \exp\{-R_{\text{scat}}t_{\text{int}}\})$, which becomes $N_{\text{scat}} \approx N_{\text{offset}}R_{\text{scat}}t_{\text{int}}$ for $t_{\text{int}} \ll 1/R_{\text{scat}}$ and allows us to extract a scattering rate of $1.3(2) \times 10^5$ s^{-1}. Note that an offset (N_{offset}) is included in the fit to account for imperfect alignment of the CU laser and the depletion laser in Fig. 6.2(d), resulting in incomplete vibrational repumping. For perfect alignment, we would expect $N_{\text{offset}} = 1$, and for the fit shown, we obtain $N_{\text{offset}} = 0.9 \pm 0.1$, indicating that we repump almost all molecules.

Since $R_{\text{scat}} \propto \sigma_{\text{abs}} I_0$ and the resonant absorption cross section depends on the corresponding FCF $\sigma_{\text{abs}} \propto \mathcal{F}_{v''v'}$, the scattering rate will be lower for the off-diagonal transition for a given laser intensity I_0. However, using the experimentally measured R_{scat} for the main cycling (0, 0) $X^2\Sigma^+ \longrightarrow A^2\Pi_{1/2}$ excitation, together with the estimate of the off-diagonal FCF $\mathcal{F}_{01} \approx 0.012$, we determine that the rate of optical pumping into the excited vibrational level $v'' = 1$ in the optical cycling region ($\sim 1.7 \times 10^4$ s^{-1}) is a factor of 7 less than our measured repumping rate, indicating that there is sufficient repumping laser intensity to rapidly return the molecules into the optical cycle. We attribute the incomplete repumping for long interaction times to imperfect alignment of the repumping laser relative to the molecular beam, and not to loss to $v = 2$. This is because when repumping light is co-aligned with the $\mathrm{A}^2\Pi_{1/2}$ light, no increase in this offset is observed, even though more photons are scattered per molecules, and therefore more opportunities to scatter to $v = 2$ occur. This rate is sufficiently high to maintain fast scattering given the small probability of decay to $v = 1$, and is limited by laser power (total power of ≈ 100 mW at the chamber).

6.3 Sustained Cycling in a Longitudinal Configuration

We have confirmed optical cycling for ~ 80 photons via depletion as well as transverse deflection of the molecular beam (see chapter 7). However, for slowing the beam to a magneto-optical trap (MOT) capture velocity over 30,000 photons need to be scattered in a longitudinal configuration. To demonstrate that we can maintain optical cycling for BaH in a slowing setup, we performed experiments with the cooling and repumping light counter-propagating against the molecular beam. The $(0,0)\, X^2\Sigma^+ \rightarrow A^2\Pi_{1/2}$ main cycling and $(0,1)\, X^2\Sigma^+ \rightarrow B^2\Sigma^+$ repuming light were both detuned to address a central velocity class of $140\,\mathrm{m/s}$ and broadened with a series of three EOMs (2, 5, and 15 MHz) until the observed laser spectrum was approximately flat on a scanning Fabry-Perot cavity, with a FWHM of ~ 70 MHz. This so-called "white light" slowing [106, 107] allows the laser light to be resonant with a majority of the forward velocity distribution of the cryogenic molecular beam.

To study the scattering rate, we monitored the instantaneous $X^2\Sigma^+(v'' = 0)$ population at two points along the molecular beam propagation direction as a function of the $\mathrm{A}^2\Pi_{1/2}$ light power, alternating the $\mathrm{A}^2\Pi_{1/2}$ light on and off every shot. By taking the ratio of consecutive shots we reduce our sensitivity to molecular beam fluctuations and can isolate the effect of the $\mathrm{A}^2\Pi_{1/2}$ light (Fig. 6.3(a)). Because we detect molecules with the excitation to the $\mathrm{E}^2\Pi_{1/2}$ state, while simultaneously cycling on the $(0,0)\, X^2\Sigma^+ \leftrightarrow A^2\Pi_{1/2}$ transition, we can observe the instantaneous vibrational ground state fraction 75 cm and 150 cm from the beam source; the presence of optical cycling will manifest as a reduction in the fraction of molecules residing in $v'' = 0$. While for laser powers below 90 mW the measured $v'' = 0$ population fraction is the same for both regions, for high $\mathrm{A}^2\Pi_{1/2}$ light powers (>90 mW) we observe a $v'' = 0$ population of $49 \pm 3\%$ in the near region and $37 \pm 4\%$ in the far region (Fig. 6.3(b)). Using ab initio calculations that utilized spectroscopically accurate molecular potentials for BaH [88], we attribute this population decrease to a combined loss into the $X^2\Sigma^+(v'' = 2)$ excited vibrational state and $H^2\Delta_{3/2}$ metastable electronic state. We experimentally confirmed there is no dependence of the signal in the far region, on the presence of the

$E^2\Pi_{1/2}$ laser in the close detection region. Based on the previous measurements and calculations of the BaH vibrational branching ratios [88], this $v'' = 0$ population reduction allows us to estimate $\sim 4,500$ scattering events between the near and far regions or $\sim 8,500$ total photon cycles. Given the time it takes the average molecule to reach the far detection region (11 ms), this gives a rate of $R_{\text{scat}} \sim 8 \times 10^5$ photons/s, consistent with what we measured using transverse beam deflection (Chapter 7). We see equal depletion for the full ToF beam profile, which indicates that we are able to maintain this high scattering rate for all forward velocities despite the additional complexity of achieving rapid photon cycling in the slowing configuration.

The data in Fig. 6.3(b) suggests that the scattering rate bottleneck in this measurement is the repumping rate out of the $v'' = 1$ state. If the repumping light power was not limiting the overall scattering rate, there would be very little population in the $X^2\Sigma^+(v = 1)$ state as we are decoupling the cycling and repumping lasers using two different electronic states. The main cycling $X - A$ laser light couples 12 ground state to 4 excited state sublevels, making 75% an expected population fraction residing in $X^2\Sigma^+(v'' = 0)$ in a steady-state cycling configuration. Combining the $X^2\Sigma^+(v'' = 0)$ population measurement with the measured scattering rate from Sec. 6.1, we can estimate state population of 50%, 37.5% and 12.5% for the $X^2\Sigma^+(v = 0)$, $X^2\Sigma^+(v = 1)$ and $A^2\Pi_{1/2}(v = 0)$ states, respectively. This reduction of the excited state population from the maximum attainable value of 25% to 12.5% leads to a reduction in the scattering rate to a value of $R_{\text{scat}} \sim 9\times10^5$ photons/s, consistent with the estimate based on the molecule loss to $X^2\Sigma^+(v'' = 2)$ and $H^2\Delta_{3/2}$. This reduced repumping rate is not entirely understood, and is not a product of insufficient RP power, because saturation is clearly observed Fig.6.3.

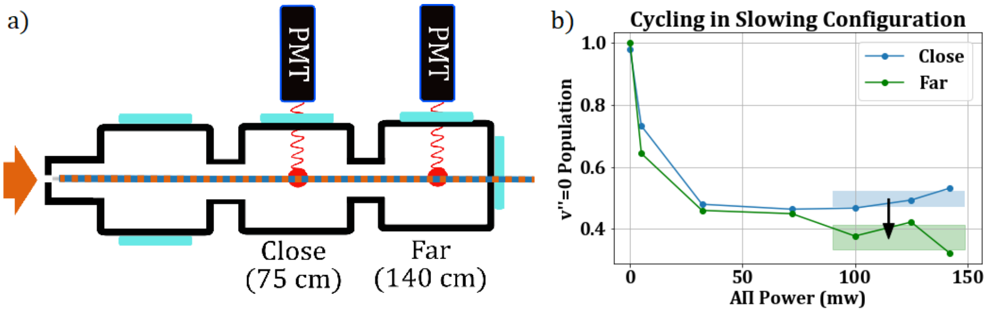

Figure 6.8: a) Schematic of the experimental setup for the slowing experiment. The instantaneous $v'' = 0$ population is measured in two locations, 75 cm and 140 cm downstream from the molecular source. b) Fractional population of $v'' = 0$ for a range of $(0,0)$ $X^2\Sigma^+ \rightarrow A^2\Pi_{1/2}$ light powers, with the $(0,1)$ $X^2\Sigma^+ \rightarrow B^2\Sigma^+$ power fixed at 100 mW. This measurement, shown for both the close and far locations, yields the average scattering rate in two ways, as described in the text.

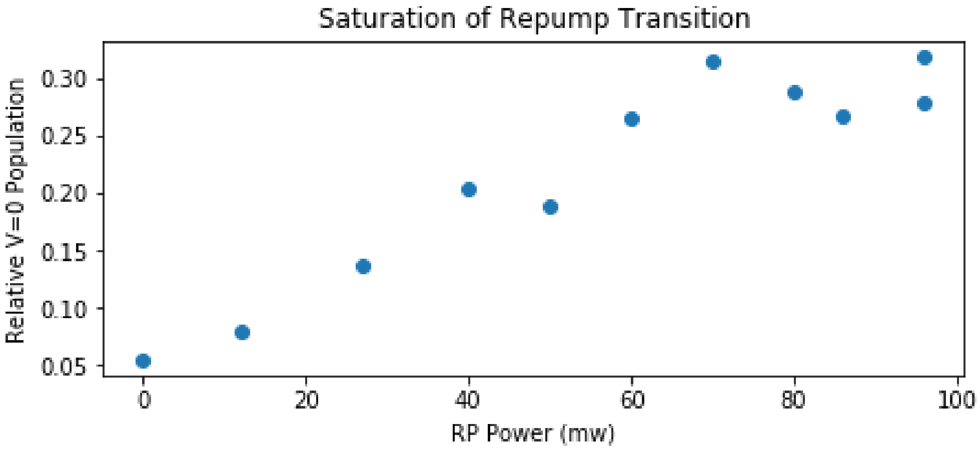

Figure 6.9: Measured saturation of the repumpng transition in a slowing configuration. Power is split evenly between each hyperfine state, and the total power is reported.

This high number of observed photon scattering events implies a reduction in the average beam velocity of ~ 25 m/s, or ~ 15%. Unfortunately, the current apparatus is not capable of Doppler-sensitive forward velocity measurements since the narrow linewidth of the cooling transition and the large spread in forward velocities would reduce the signal-to-noise ratio by a factor of ~ 20. A planned upgrade using two-photon detection via a higher-lying electronic state, combined with a high-solid-angle detection system, should make this possible. See appendix for details.

Chapter 7: Optical Manipulation and Cooling

7.1 Camera and Beam Imaging

Cooling and deflection of the molecular beam require spatially sensitive measurements to quantify the shape and position of the molecular beam. Thankfully, the cycling transition we used for PMT detection (683 nm) allows a range of single photon sensitive cameras to be used. Due to the extremely low light levels, and the desire to bin multiple pixels together, we went with an Andor Ixon EMCCD camera. The EM gain and controllable hardware binning allow us to suppress read noise and maintain as high an SNR as possible. For the imaging we used a two component system with 60 mm biconvex lens collecting and collimating the light from the detection region and a MVL35M1 fixed focal lengths lens to image the collimated light onto the focal array. To calibrate and focus the lens we broke vacuum and inserted an 8-32 screw into the center of the detection region. This allows us to focus the system onto the expected image plane, and the known periodicity of the screw allowed us to calibrate the mm/px amplification.

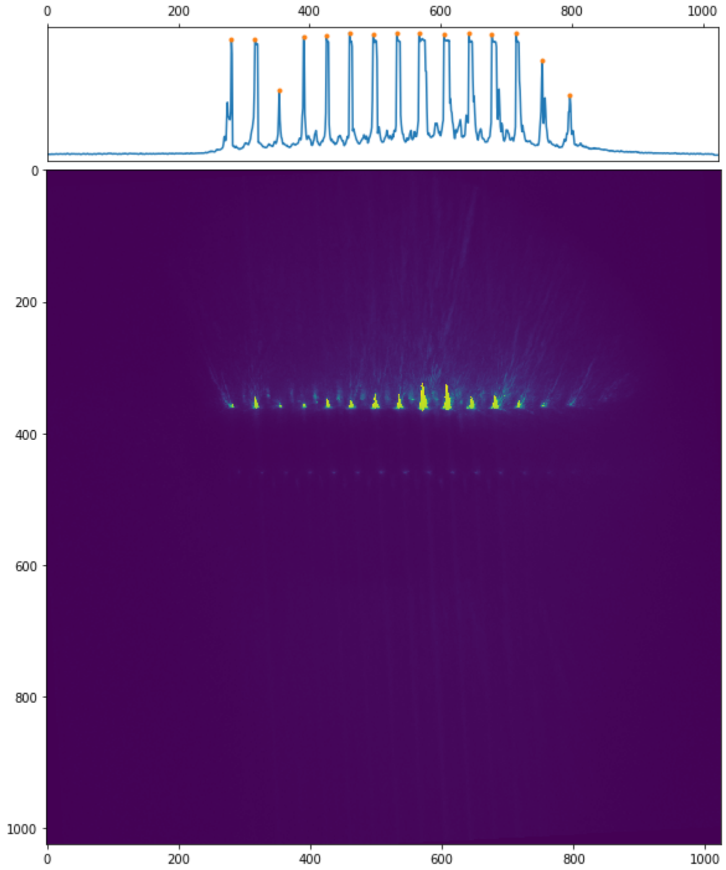

Figure 7.1: Image of the screw, and the resulting 2D cut. We find the conversion to be .020 pixels per mm, with an uncertainty of around 2%.

In front of the final lens, we placed a Semrock band-pass filter to limit background light from the room. One advantage of a camera, compared to a PMT, is the spatial information allows an additional way to suppress background light introduced by the probe laser. In Fig. 7.1 You can see 3 images, background only, background and signal, and the background subtracted result. In these images, the molecular beam is heading upwards from the bottom to the top of the page. Because we are imaging the fluorescence, the resulting image is the overlap between the Gaussian laser beam, and the collimated molecular beam.

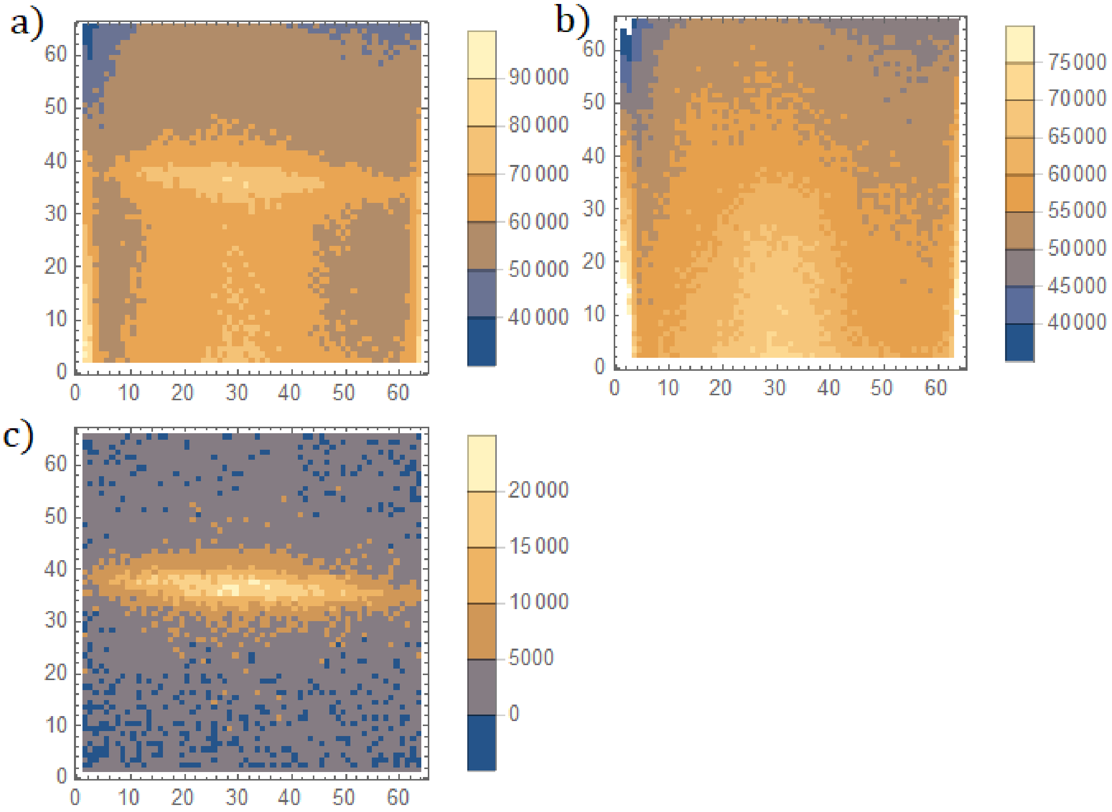

Figure 7.2: Images taken with an EMCCD gain of 800, and 16x16 hardware binning to improve the SNR a) Raw image of the molecular beam b) Raw image taken 30 mS after the ablation pulse, collecting only stray light. c) Background subtracted image, showing only the fluorescence from the molecules.

Once the background subtracted image was obtained we used a variety of analysis techniques to extract the spatial properties of the beam. The first technique, was to fit the image directly to a 2D Gaussian, and use the central location and width. This worked best for seeing relatively small changes in the width. We also analyzed some of the data by binning the 2D image, down into a 1D cut across the molecular beam. We found that this binning worked well when there was relatively low SNR.

7.2 Radiative Deflection

The depletion-based scattering measurements described in chapter 6 provide strong evidence that we maintain a sufficiently high scattering rate in the optical cycling region to pump most of the molecules from the $v'' = 0$ vibrational manifold into $v'' = 1$. Moreover, we achieve a repumping rate that is significantly higher than the rate of optical pumping into $v'' = 1$. Therefore, by merging both $(0,0)$ $X^2\Sigma^+ \rightarrow A^2\Pi_{1/2}$ main and $(0,1)$ $X^2\Sigma^+ \rightarrow B^2\Sigma^+$ repumping lasers (Fig. 7.2(a)) we expect to deflect the BaH molecular beam using the radiation pressure force. In this experiment, the deflection laser passes through the vacuum chamber perpendicular to the molecular beam and strikes a 90° mirror prism (a hollow rooftop mirror, HRM) which reflects the light back through the vacuum chamber but displaced downward by ~ 2 cm, thus traversing below the molecular beam. The light then strikes another 90° mirror prism that translates the beam upward and redirects it back through the molecules, deflecting the molecular beam in the same direction as the first pass (Fig. 7.2(b)). The process is repeated $\gtrsim 10$ times to increase the interaction time while maximizing the laser intensity. Since the number of mirror bounces is doubled in order to propagate the light from a single direction and because the reflectivity $r_{\text{HRM}} < r_{\text{mirror}}$, the effective molecule-light interaction time is shorter than in the depletion studies. This experiment was performed with the same beam size and power as the scattering rate measurements in chapter 6.

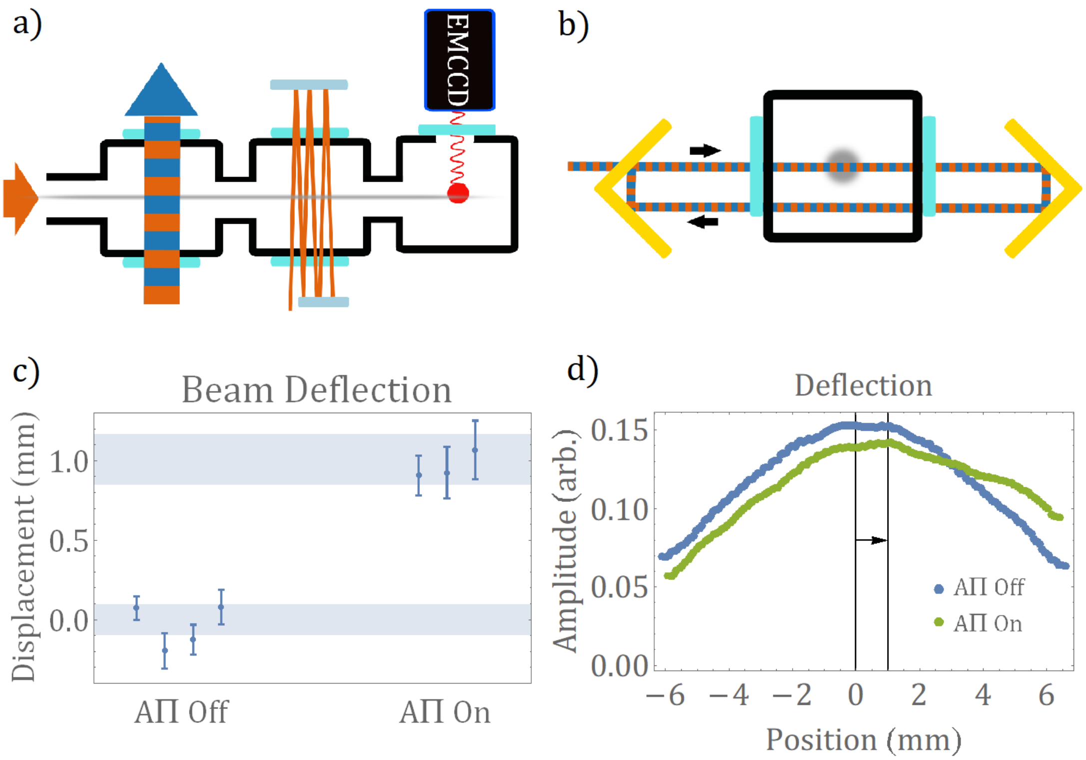

Figure 7.3: a) Schematic of the beam deflection experiment. In the first interaction region, the molecular beam interacts with both the cooling and the repumping light, with each pass coming from the same direction, with each pass spatially separated from the preceding pass in a “zig zag" pattern. The molecules then enter a clean-up region where they are pumped back to $v'' = 0$, and subsequently a detection region 75 cm away where their spatial location is imaged on an EMCCD camera. b) Diagram of the mirror prisms that allow the laser light to interact with the molecular beam while always traveling in the same direction. c) Measured deflection of the molecular beam, where the deflection light is either blocked or applied, showing the statistical uncertainty. Each point is the average of ~ 200 images. d) Taking 1D cuts of each beam image, combining them, and applying a smoothing average filter allows us to visualize the 1 mm beam deflection.

Figures 7.2(c,d) summarize the radiative deflection experiments for BaH. The magnitude of the displacement is determined by fitting the molecular beam images to a 2D Gaussian distribution and monitoring the fitted center of the molecular beam with and without the deflection light. Quoted error bars are determined based on the statistical fit uncertainty. By using the change in the fitted center of the whole molecular beam we provide a conservative lower bound on the number of scattered photons per molecule. The measured center-of-mass molecular beam deflection is ~ 1 mm, which is consistent with each molecule scattering ~ 80 photons at the average rate of 8×10^5

photons/s. A number of experimental differences could explain why this scattering rate is 40% slower than that measured via depletion experiments: i) slower than anticipated repumping in the main region, ii) the presence of transverse Doppler shifts,and iii) the presence of imperfectly remixed “dark” states which do not play a dominant role in depletion experiments. Importantly, we do not see a statistically significant increase in the width of the molecular beam (Fig. 7.2(d)), indicating consistent scattering for each detected molecule. The scattering rate of 8×10^5 s^{-1} extracted from the deflection of the molecular beam accurately represents the scattering rate that we can achieve and maintain for the entire ensemble of molecules.

7.3 Transverse Laser Cooling

While laser deflection results presented in Sec.7.2 provide a valuable benchmark for the development of radiative slowing of BaH molecules, the data does not demonstrate a decrease in the entropy of the molecular ensemble (as can be seen from the beam widths in Fig. 7.2(d)). To achieve a reduction in transverse velocity spread for the molecular beam, we establish a 1D standing light wave intersecting the molecular beam (Fig. 7.3(a)). Figure 7.3(b) demonstrates effective transverse temperature of the molecular beam as a function of the common detuning for the $(0,0)\ X^2\Sigma^+ \rightarrow A^2\Pi_{1/2}$ cooling laser with the repumping $(0,1)\ X^2\Sigma^+ \rightarrow B^2\Sigma^+$ laser fixed on resonance. We observe broadening of the molecular beam for red-detuned laser frequencies and narrowing for blue-detuned frequencies, consistent with Sisyphus laser heating and cooling of the ensemble, respectively [108, 109, 110, 111].

To estimate the temperature of the beam we performed Monte Carlo simulations of the molecular beams spatial propagation. We begin with molecules uniformly sampled across a 5 mm radius circle (the size of the collimation aperture in the experiment). We then give each molecule a transverse velocity (sampling from a Maxwell-Boltzman distribution at a fixed temperature), and propagate them from the collimation aperture, through the interaction region where they feel the optical force, and into the detection region at a typical forward velocity. Based on the width of the distribution at the detection region, relative to the 5 mm width defined at the aperture, we can extract the effective transverse temperature. For example, if the transverse temperature is effectively zero, the beam will not expand at all, and will remain 5 mm wide. This allows us to map a relationship between a measured width, and an effective transverse temperature. Sisyphus cooling applied over a 3 cm long interaction region reduced the effective transverse temperature by ~ 25%, from 20 mK to 15 mK, as shown in Fig. 7.3(b). This experiment and simulations were performed with the same beam size and power as the depletion experiments in Sec. 6.1. We benchmark the strength of the Sisyphus cooling force by comparing a Monte Carlo simulation with only Doppler cooling to one with both Doppler and Sisyphus cooling. We find that the at the experimentally determined optimal detuning of 5 MHz the magnitude of the damping coefficient for the Sisyphus force is ~ 5.6 ± 1.7 times greater than Doppler, with error dominated by fit uncertainty. This explains why we were unable to observe Doppler cooling, because the signature is below the signal-to-noise ratio. The experimental power and optimal detuning corresponds to a damping coefficient with a magnitude of 330 ± 100 s^{-1} for Sisyphus cooling.

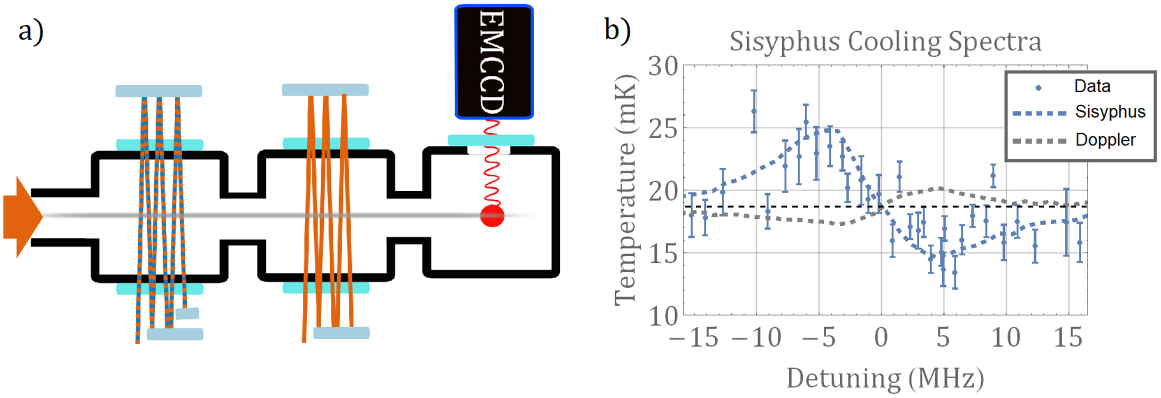

Figure 7.4: a) Experimental diagram showing the standing wave generated by the cooling light that includes both the cycling and repumping lasers. Before molecules enter the detection region, they are optically pumped back to $v'' = 0$ using the off-diagonal $(0,1)$ $X^2\Sigma^+ \rightarrow B^2\Sigma^+$ excitation. b) Effective transverse temperature as a function of the common detuning of both spin-rotation components of the $(0,0)$ $X^2\Sigma^+ \rightarrow A^2\Pi_{1/2}$ cooling lasers. The blue (gray) dashed lines are the result of a Monte Carlo simulation of Sisyphus (Doppler) cooling of the molecular beam, [112]. The only free parameter in the fit is the amplitude of the Sisyphus force relative to Doppler.

7.4 Imaging Anomalies

In the course of optimizing and and investigating optical manipulation, several interesting and unexpected signatures were discovered. While these may not be of immediate scientific importance, I think an explanation of them is useful to help other groups who may see similar signatures.

7.4.1 Anomalous Transverse Displacement

While attempting to observe Doppler cooling of the BaH beam, we have observed a systematic shift in the molecular beam position as shown in Fig. 7.4.1. The small natural linewidth of the cooling transition ($\Gamma_{\text{nat}}/2\pi \approx 1.2$ MHz) leads to an acute dependence of the cycling rate on the alignment and detuning of the cooling laser relative to the molecular beam (Fig. 7.4.1(a)). The asymmetric Doppler shifts lead to a unidirectional deflection of the molecular beam in the cooling configuration (Fig. 7.4.1(b)), where the direction of the deflection depends on the alignment angle as shown in the data in Fig. 7.4.1(c). While such shifts were not important for transverse beam cooling of molecules with larger natural linewidth like SrF [110] and SrOH [108], a pronounced effect for misalignment of $< 1^\circ$ observed in our work indicates that a careful geometry optimization will be required for performing precision spectroscopy for molecular beams of laser-coolable molecules with $\Gamma_{\text{nat}}/2\pi \approx 1$ MHz (e.g. TlF [113] or TlCN [114]). For a two level system, we can provide a simplified model of this effect as shown in Fig. 7.4.1(d). This model uses a realistic Rabi rate for our experiment, and realistic distribution of forward velocity. Force imbalance (ΔF) is based on the detuning dependent force from the left $F_l(\delta)$ (right $F_r(\delta)$) propagating laser beam:

$$\Delta F = \frac{max(F_l(\delta)) - max(F_r(\delta))}{max(F_l(\delta), F_r(\delta))}. \tag{7.1}$$

We see that even small angular misalignment can lead to large imbalance in the maximum force pushing the beam to either direction. As shown in Fig. 7.4.1(d) an imbalance as large as 60% is possible for even a small misalignment of 1 degree. This is consistent with the data showing a 0.6 mm deflection in Fig. 7.4.1(c), and the maximum deflection of 1 mm we observed in Fig. 7.2.

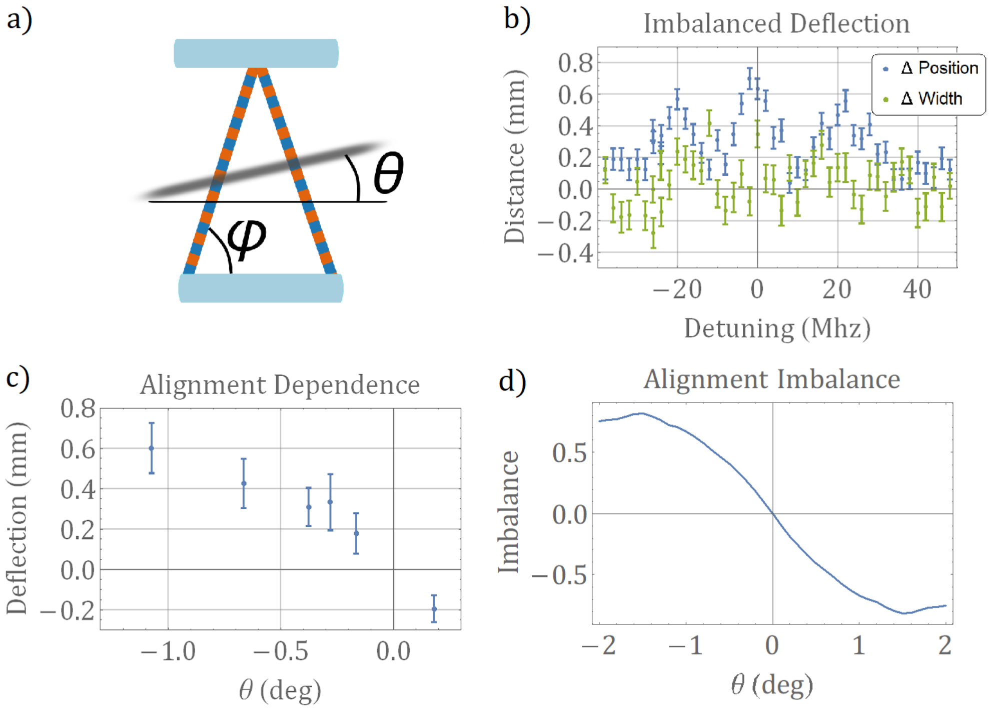

Figure 7.5: a) A misalignment of the molecular beam relative to the multi-passed cooling laser. ϕ is the unavoidable angle present in the system to allow multiple passes, and θ is the misalignment between the parallel retroreflecting mirrors and the molecular beam. This misalignment results in different projections of the light propagation vectors onto the molecular beam forward velocity. b) Measured position and width of the molecular beam in a Doppler cooling configuration. The data shows a displacement due to a finite angular misalignment θ. The three peaks are due to hyperfine structure of the cycling transition and the laser sidebands used to address them. c) As θ is varied in a controlled way, it can be experimentally minimized by zeroing the molecular beam deflection. d) A model accounting for the spread in the molecular beam's forward velocity can explain the observed beam deflection. Here, the imbalance is defined as the difference between the optimal force for each laser beam's direction divided by the maximum force.

7.4.2 Anomalous Longitudinal Displacement

When imaging, the region we expect light to originate from is the overlap of the probe laser with the molecular beam. Because the probe laser is stationary,] you would naively expect the position and width along that dimension to be fixed, and depend only on of the alignment of the camera relative to the probe beam and the width of the probe beam. However, as was discussed previously in chapter 6, cycling on the detection transition is not a pure representation of the ground state population, and depends on the exact distribution of ground states the molecule has when it is detected. If a given state scatters photons more quickly before it is pumped into dark states, that will result in a shift of the observed center of the image towards the molecular source, and reduce the width. This is because the molecules will only scatter when they first enter the probe region. A similar argument can shift the observed center of the beam away from the source and broaden it, if the molecules scatter more slowly. This was observed experimentally as we varied the cycling laser detuning and changed the distribution of states the molecules had when they entered the detection region (Fig. 7.4.2).

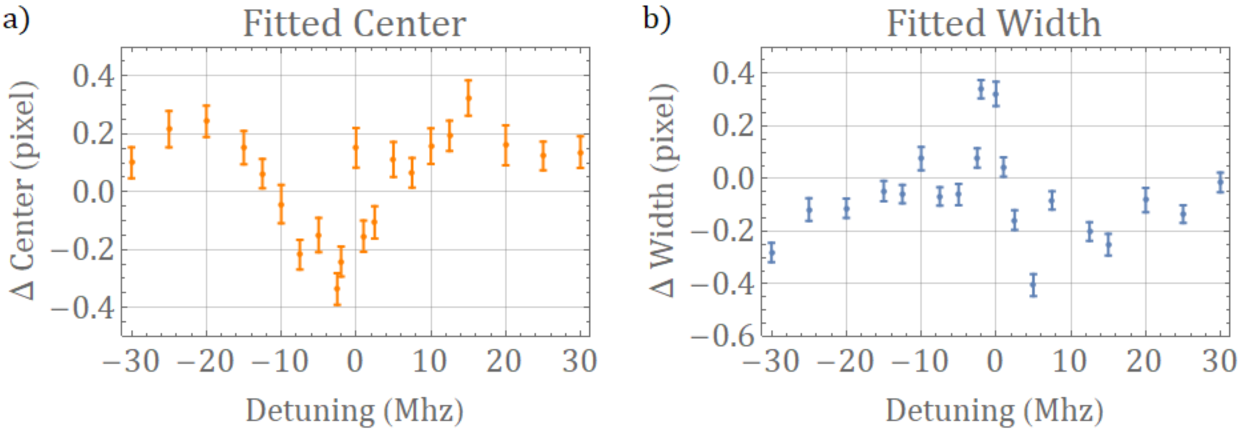

Figure 7.6: The exact spin rotation distribution effects of location and width of the imaged beam. This is along the propagation direction of the molecular beam. Different detunings, lead to one or the other spin roation state being preferentially populated, and that changes how the beam is imaged. This is not important for our experiment, but highlights that care must be taken in detecting the molecular beam, and could introduce systematic effects in other experiments.

This can important to consider when analyzing data generated in these experiments as this change must be accounted for. We found that two dimensional fits lead to better results, and I think this is one of the reasons why. Simply compressing the data into one dimension doesn't capture the full behavior. This also shows that for detection, we are not in a steady state, and steady states in general can take long time to reach for these complex systems. Exploring this in more detail, we can pump the molecules entirely into either the J=1/2 or J=3/2 spin rotation state, and compare an image of the molecules starting in that state, compared to an even distribution Fig.7.4.2.

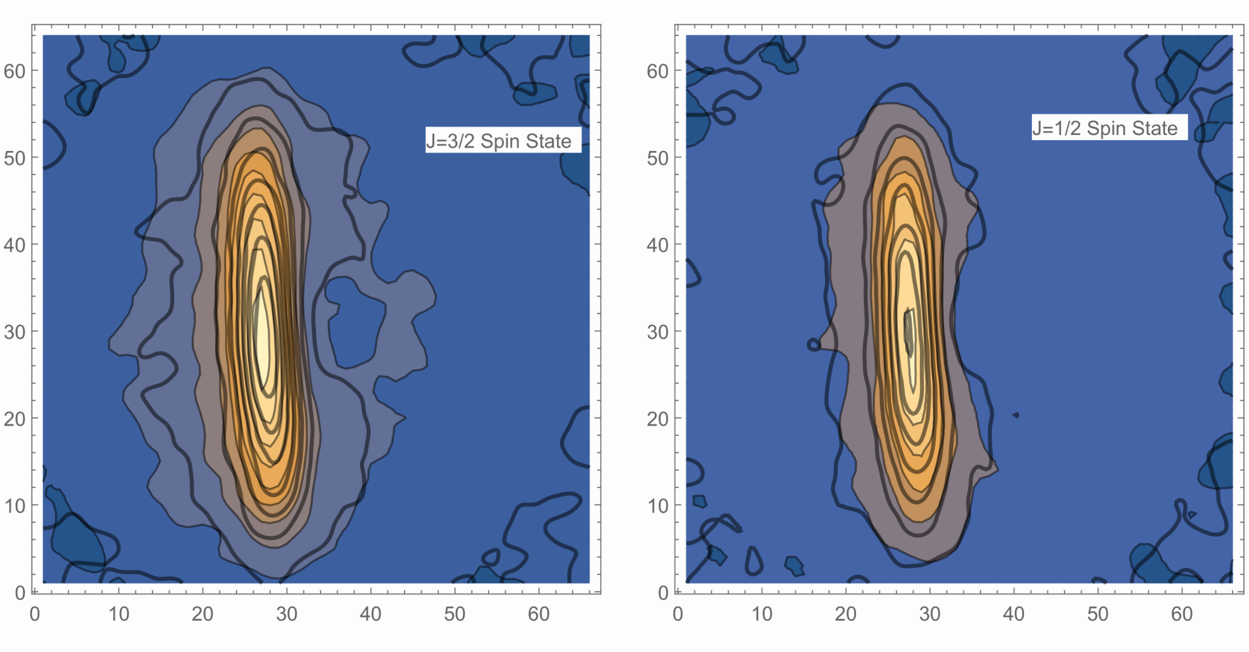

Figure 7.7: Gray contours show the unperturbed beam images, and the colored contours show the beam images when the molecules are pumped into either the J=1/2 or J=3/2 spin rotation state. Notice a horizontal displacement in either direction, based on which states are populated

We see a small, but noticeable shift in the center as predicted. This indicates that the J=3/2 state has faster scattering in this measurement, as the center is shifted closer to the molecular source. This result is not general and depends on the details of the detection laser, which were fixed for this measurement. However, short of actively balancing the power of the two detection lasers, this sort of effect will remain present.

7.5 Simulated Magneto Optical Trapping

In order to characterize the feasibility for magneto-optical trapping for BaH molecules, we perform studies of confining forces using numerical solutions of the multilevel rate equation model following the framework presented in Ref. [95] and later used to model the MgF MOT properties [115]. These simulations will not capture coherent effects, but have been proven to accurately model MOT behavior in existing experiments. The simulation included $n_g = 12$ magnetic sublevels of the $N'' = 1$ rotational manifold in the vibronic ground state (Fig. 5.6.1(b)), $n_e = 4$

magnetic sublevels of the $J' = 1/2$ manifold ($F' = 0, 1$) of the $v' = 0$ vibrational level of the excited $A^2\Pi_{1/2}$ electronic state, and between three and six light frequency components from each direction. Because of the complex interplay between the ground and excited state g-factors as well as the specific nature of spacings between the hyperfine components in the ground vibronic state, a detailed numerical study is necessary in order to identify the optimal laser polarization structure and detunings [95]. Depending on whether the current in magnetic field coils used for MOT operation is static (DC) or alternating (AC), there are two types of molecular MOT operating regimes, correspondingly [116, 117]. Moreover, in order to enhance the confining force in the DC MOT configuration, both "blue" and "red" detuned laser beam components can be applied resulting in a dual-frequency DC MOT [118].

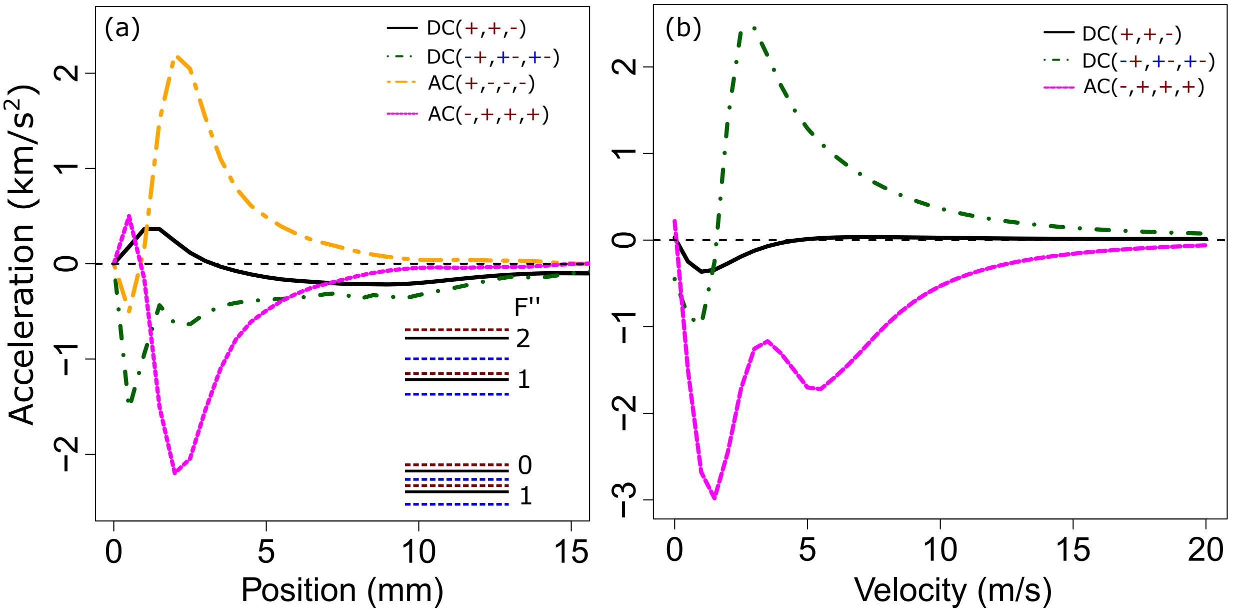

Figure 7.8: Calculated BaH MOT confining (a) and cooling (b) characteristics for different polarization configurations for DC or AC MOT operation. The order of circular polarization labels in the legend starts with the lowest hyperfine substate, i.e. $(-, +, +, +) = (-$ for $J'' = 1/2$, $F'' = 1$; $+$ for $J'' = 1/2$, $F'' = 0$; $+$ for $J'' = 3/2$, $F'' = 1$; $+$ for $J'' = 3/2$, $F'' = 2)$ and $(+, +, -) = (+$ for $J'' = 1/2$, $F'' = 1$; $+$ for $J'' = 3/2$, $F'' = 1$; $-$ for $J'' = 3/2$, $F'' = 2)$. For the dual-frequency DC operation, two frequency components separated by approximately $3\,\Gamma_{\mathrm{sp}}$ were applied.

Following earlier work [118, 95, 115], we present the strength of the achievable BaH magneto-optical trapping configurations by plotting molecular acceleration as a function of (a) the distance to the trap center for the $v = 0$ velocity class, and (b) as a function of the velocity for a fixed position slightly displaced from the trap center ($d = 0.1$ mm), in order to have a well defined quantization axis set by the direction of the magnetic field.

Figure 7.5 provides a summary of the predicted acceleration profiles as a function of distance to the MOT center (for $v = 0$ m/s) and molecular velocity (for $d = 0.1$ mm) under experimental conditions approximating those in the experiments above ($P_{\mathrm{tot}} = 200$ mW and 1-inch 1/e^2-diameter laser beams) and previously achieved in molecular MOT experiments (15 G/cm magnetic field gradient [119]). By comparing different MOT operation parameters (varying the number of laser frequencies and polarization settings) and configurations (AC vs DC vs DC dual-frequency), we conclude that the AC MOT has the highest potential for future trapping of BaH molecules providing both the highest peak deceleration ($\sim$ 2 km/s^2) and the largest velocity range affected by the MOT potential (up to $\sim$ 15 m/s). We determine that the optimal polarization setting for the AC MOT is the same as that used for capturing CaF molecules [119].

A unique property of BaH that distinguishes it from other molecules to which magneto-optical forces have been applied (SrF [120], CaF [119], YO [34, 121] and CaOH [122]) is that a large excited state g-factor ($g_{\mathrm{eff}} \approx -0.51$ for the $A^2\Pi_{1/2}$ state [103]), arising from a strong mixing with the adjacent $B^2\Sigma^+$ electronic state, is approximately the same as that of the ground state ($g_{\mathrm{eff}} \approx +0.56$ for $J'' = 3/2$ [103]). Based on the model proposed in Ref. [95], it was anticipated that the DC configuration will lead to strong MOT confining forces for BaH molecules [103]. However, as can be seen from Fig. 7.5(a), a complex interplay between the Zeeman shifts for the ground and excited magnetic sublevels contributes to a relatively weak confining force with an undesirable spatial structure with a repulsive trap center and a small effective velocity range (Fig. 7.5(b)). It was previously shown that for molecules with small Zeeman shifts in the excited state (like CaF [95] and MgF [115]), the “dual-frequency" contribution to the MOT forces far outweighs the confining effects arising from non-zero g-factors in the excited state. As can be seen from Fig. 7.5, using the dual-frequency method outlined in Ref. [118] we can significantly improve the BaH MOT properties. However, in order to obtain a large velocity capture range, the use of the AC

MOT configuration is necessary.

Estimation of escape and capture velocities (v_{esc}, v_{cap}) are experimentally relevant ways to characterize the magneto-optical trapping potential. 3D MOT capture velocities have been measured for CaF ($v_{\mathrm{cap}} \approx 11$ m/s) [123] and SrF ($v_{\mathrm{cap}} \approx 5$ m/s) molecules [124] and provide useful benchmarks for our calculations. Previously it has been experimentally observed that an approximately linear relationship can be established between the MOT capture and escape velocities, $v_{\mathrm{cap}} = b v_{\mathrm{esc}}$, with a proportionality coefficient $b \gtrsim 1$ [125, 126]. Figure 7.5 presents the simulated trajectories of BaH molecules that start at the geometric center of the MOT, for different initial velocities. As shown in the plotted curves, we estimate v_{esc} for the BaH AC MOT to be ~ 3 m/s, leading to the MOT capture velocity ~ 3.5 m/s.[1]

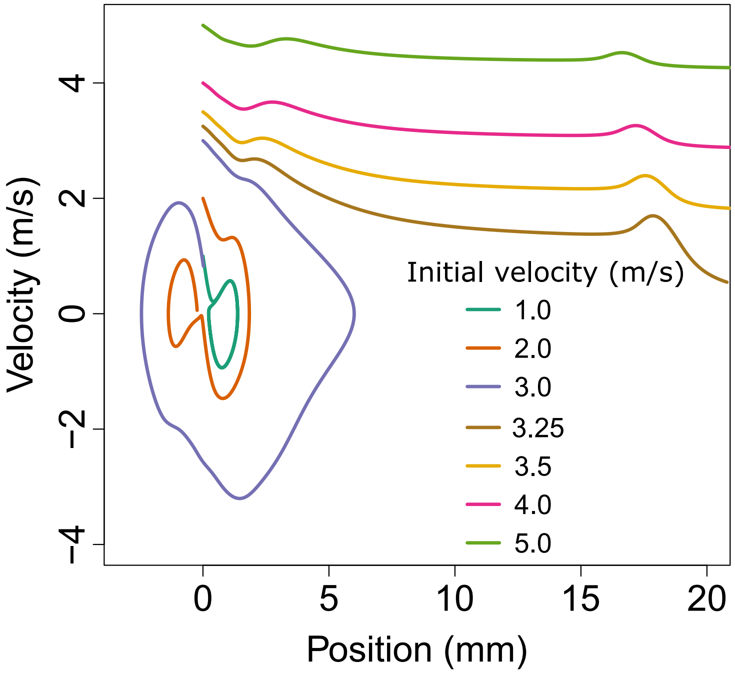

Figure 7.9: Trajectories of BaH molecules inside a magneto-optical trapping potential, starting from the trap center with different initial velocities. From these trajectories, we estimate the MOT escape velocity to be $v_{\mathrm{esc}} \approx 3$ m/s. The simulations are performed for the AC MOT configuration in Fig. 7.5(b).

Large vibrational spacing for diatomic monohydrides (MH) compared to monofluorides (MF)

---

[1] Previously, the proportionality coefficient b has been measured to be 1.2 – 1.4 [125, 126, 127].

and monohydroxides (MOH) will lead to enhanced vibrational decay from the $v'' = 1$ levels populated during the MOT loading process. Previous accurate ab initio calculations for BaH predict spontaneous vibrational lifetime for $v'' = 1$, $N'' = 1$ state of $\tau_{\text{vib}} = 12.6$ ms [88]. In order to understand the time evolution of BaH trajectories inside a magneto-optical potential for different initial velocities, we plotted both trapped and untrapped BaH trajectories in Fig. 7.5 with the time information provided as a color gradient. In order to minimize the loss of molecules to dark rotational sublevels due to spontaneous vibrational decay, one would ideally transfer BaH molecules from a MOT into a conservative magnetic [33, 128] or optical [129] trap within the first ~ 10 ms of capturing them in a MOT. However, if one can minimize the population in the $v'' = 1$ state by using a large amount of re-pump light this requirement could be avoided. This means that for BaH you must re-pump with a different excited state than you cycle on, otherwise all ground states will be evenly occupied, and this mechanism will be a dominant source of loss.

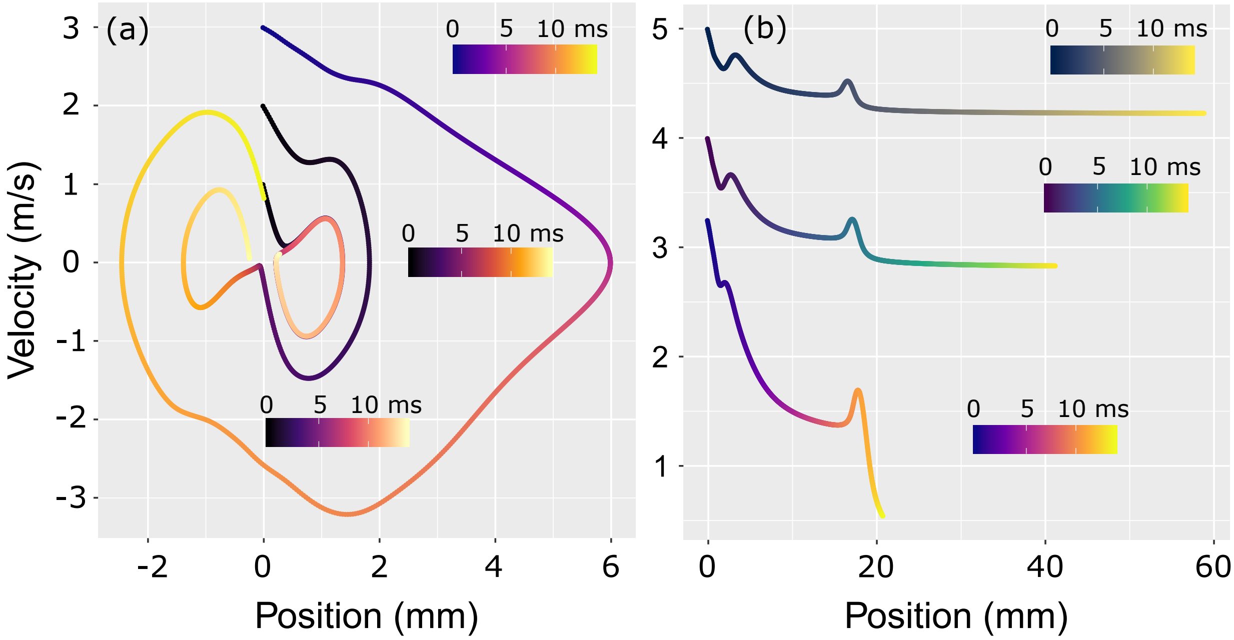

Figure 7.10: Simulated time evolution of BaH molecules inside a magneto-optical trapping potential for different initial velocities starting at the trap center for (a) trapped and (b) untrapped trajectories. Color gradient scale provides time information not available in Fig. 7.5.

7.6 Simulated Slowing

One of the primary barriers for the magneto-optical trapping of molecules is the efficient slowing of the molecular beam. This has proven to be a bottleneck in other experiments, and a potential limit as the field becomes interested in larger, and more exotic molecular candidates. While we were unable to observe slowing in BaH, I think a brief discussion and comparison of the various slowing techniques is worth the time to benchmark their performance, and to help guide the design of future experiments.

To model slowing we use a Monte-Carlo simulation similar to the one used in modeling Sisyphus cooling. We use forward velocity distribution that matches previous measurements (discussed in chapter 5) and limit the total laser power available for cooling to 1 Watt. This is the amount of power readily available from an NKT fiber amplifier we have in the lab. For simulations I discuss here the molecules are assumed to be very well collimated and transverse blooming of the beam during the slowing process is ignored. Therefore the slowing efficiency is an upper bound. We do not solve the full rate equation or Linblad equation for this simulations, and instead use a scaled two level system, greatly reducing the computational complexity. The maximum attainable force is limited by the maximum attainable scattering rate, which is 8×10^5 photons/s in the pushing/slowing configuration. The change in a velocity from a single scattering event is given by the recoil velocity $v_r = \frac{h}{\lambda M_{BaH}} = .27 cm/s$. Combining these two terms we find the maximum experimentally obtained acceleration in our system is 2200 m/s^2. This is below the theoretical maximum, but multiple groups have been unable to achieve the theoretical maximum scattering rate in these experiments, and being conservative is important for experimental design. This provides a benchmark for what we can achieve, based on what we have already demonstrated.

7.6.1 White Light Slowing

This first slowing scheme we investigate, is known as white light slowing. For this technique, the cooling laser is detuned relative to the transition, and then spectrally broadened by a series of over-driven EOM (see chapter 3). If properly setup, this can take a single laser, and allow it to address a large range of velocity classes. This is needed, because we want to be able to slow the beam to rest, and a single laser by itself is in capable of this. The force profile used in these simulations, is shown in Fig 7.11.

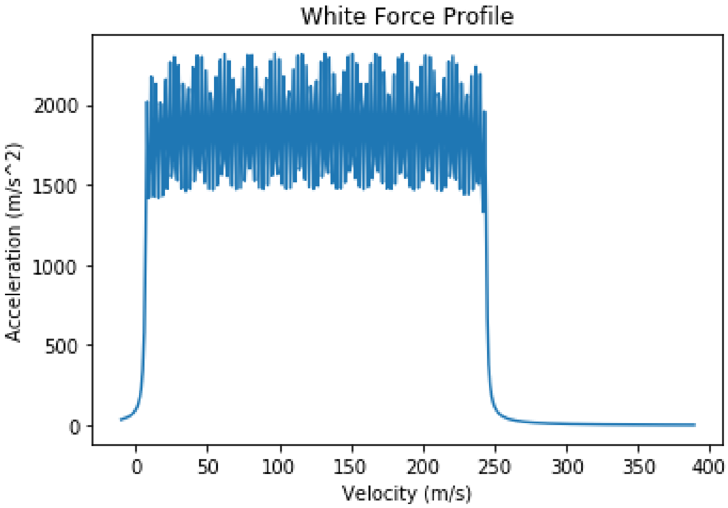

Figure 7.11: Acceleration generated for a white light slowing configuration. The fall off around v=0 is essential, as it allows molecules to bunch at low velocity, and compresses the velocity distribution.

This profile is generated using 75 sidebands, each separated by 3 MHz, and a detuning from resonance of 120 MHz. The exact shape may be different based on the exact EOM setup used, but the results are not sensitive to these details. The total laser power is limited to 1 Watt, and the slowing beam has a radius is 13 mm. A relative large beam is required, to match the slowing volume with the size of the MOT. Note, that the force profile falls off around zero velocity, allowing molecules to accumulate. This is important because if the force profile is flat across the entire range there is no phase space compression, and MOT loading is very inefficient. We need as many molecules as possible to enter the MOT region, with a velocity below the capture velocity. If we do not have any phase space compression only a tiny subset of the molecules will meet these requirements, due to the low capture velocity.

After ablation, we can model the evolution of the molecular velocity distribution, by enacting this force profile on an ensemble of particles selected from the forward velocity distribution Fig 7.12a). The simulation uses newton's method to directly propagate the molecules, under the force profile defined in Fig 7.11. We see an initial evolution of constant slowing across the ensemble as expected, but for later times an accumulation around v=0. This shows efficient compression of the beam in velocity space, based on where the edge of the force profile is placed, which is easily controlled in the lab.

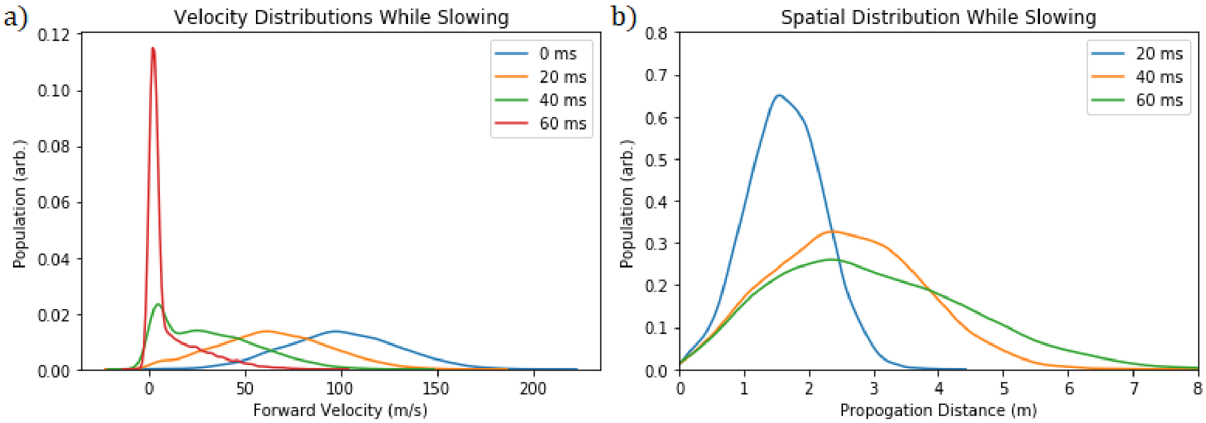

Figure 7.12: a) Evolution of the forward velocity distribution under whitelight slowing. after 60 ms we see substantial compression of the initial distribution. b) Evolution of the position of the molecules in the beam. We see a wide spread, and no compression.

However, when we observe the spatial distribution of the molecules (Fig. 7.12b) we see a different story. Unlike the velocity distribution there is nothing encouraging compression in position space and this leads to a large spread. To determine the optimal MOT location, we vary the location of the MOT along the molecular beam axis. We then calculate the percentage of the molecules that enter the variable trap position, with a velocity below the capture velocity. Based on simulation discussed above, the trap is assumed to have a radius of 13 mm, and a capture velocity of 3.5 m/s. We use hard cutoffs to determine whether a particular molecules is captured, which is not entirely accurate, but is a useful approximation.

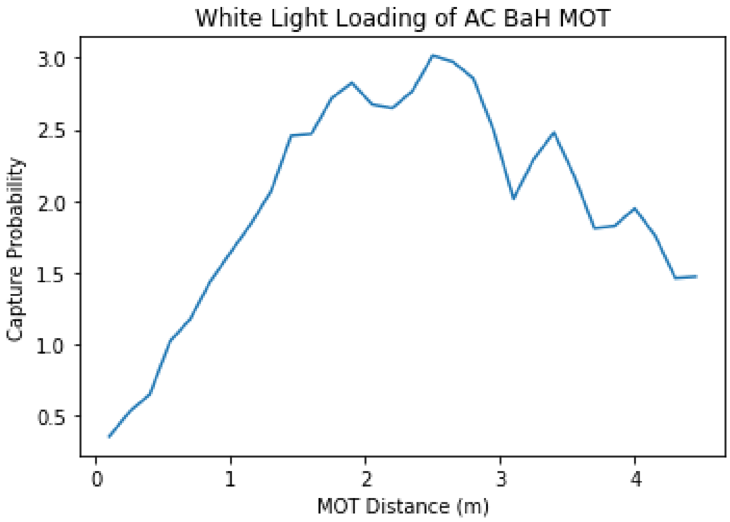

Figure 7.13: Capture probability for an AC MOT (as simulated previously) for white light slowing of BaH. We see a low capture percentage, due to the small capture velocity of the MOT, and because the relatively long time it takes to slow leads to the molecules spreading out in space.

We find relatively consistent MOT loading, for a range of MOT positions between 1.5 and 3 meters. Because this simulation does not account for the finite transverse spread in the beam it is likely that 1.5 is better because shorter slowing distances lead to less blooming. 3% is a relatively low capture probability, and will be a substantial bottleneck in the system. To benchmark this code I also ran simulations for CaH (an alternative candidate we are exploring) and CaF a molecule that has been successfully slowed and trapped by a number of groups. For these molecules capture efficiencies as high as 30% are possible and require a substantially shorter slowing distance. This is due to higher scattering rate, lower mass and shorter wavelength cycling transition. These simulation helped motivate a switch to CaH, that is currently in process.

7.6.2 Chirped Slowing

Another slowing scheme that has been used in the field, is that of chirped slowing. Here, instead of broadening the laser to address multiple velocity classes at once, the laser is swept (or chirped) to maintain resonance as the molecules are slowed. The primary advantage of this technique is that because the laser does not need to be broadened out, the power requirements are much lower. This also means a wider velocity class can be slowed for a fixed laser power. For some molecules with a lack of high power laser options, this makes the technique very attractive. However for BaH we have plenty of power so it is less of an issue.

The laser for this technique has the same size and power as for white light slowing, but we will sweep it from an initial detuning of 150 MHz, to a final detuning of 0MHz at a rate of (240 MHz)/(100 mS). This is an easily achievable chirp, either through a current sweep of the laser diodes themselves, or with a double passes AOM setup. The chirp speed here is limited by the force we can apply to the molecules. Chirp too slow, and the cooling distance is elongated unnecessarily. If you chirp too fast, the force will be too small to keep the molecules on resonant, and they will leak out of the system. This chirp rate was determined by optimizing the system, and is consistent with back of the envelope estimates based on the maximum acceleration.

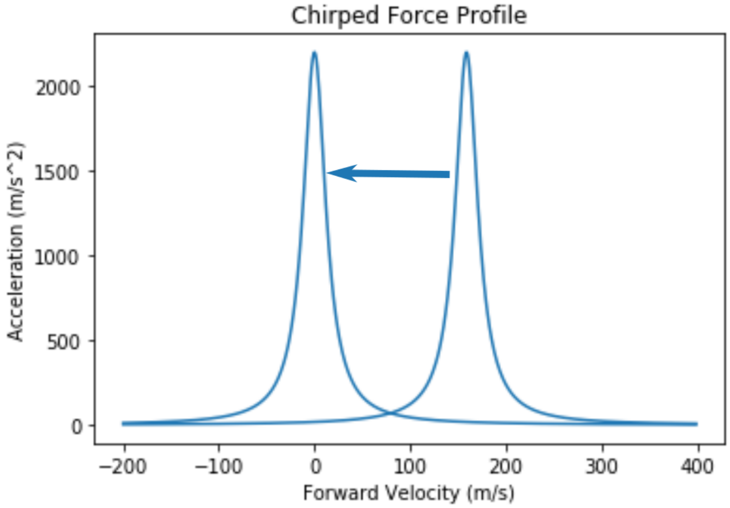

Figure 7.14: Initial and final acceleration profiles for the laser used in chirp slowing. This beam is swept 150 MHz in total, at a rate of (240 MHz)/(100 ms). Due to the high power, we expect substantial power broadening, ans that is apparent in the two level scaled model.

Now, as the laser sweeps across the velocity distribution, we see a clear compression just as we expected Fig. 7.15 a. We also see that the spatial distributions are not quite as broad (relatively speaking) as for white light slowing, but that this technique requires almost twice the slowing distance. This means that blooming will be a larger issue, and we are starting to get to slowing distances that are unfeasible experimentally. It all has to fit inside a room after all.

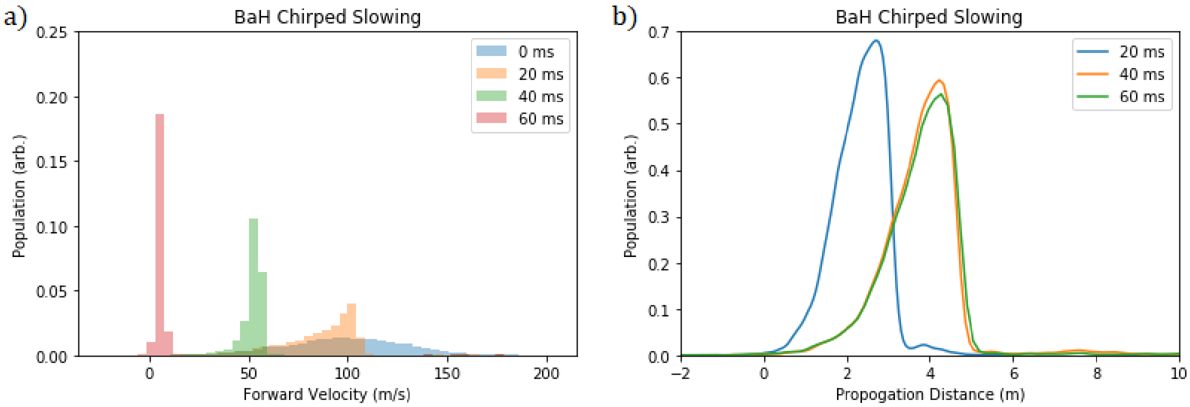

Figure 7.15: a) Evolution of the forward velocity distribution under chirped slowing. We see as the laser is swept strong compression occurs, and is eventually concentrated at low velocities b) Evolution of the position of the molecules in the beam.

It is worth emphasizing here, that this increased slowing distance is entirely expected. For white light slowing each molecule will feel the slowing force immediately, until it is slowed below the cutoff. Here, only a range of molecules will feel the force at any given time, and most of them will keep traveling unperturbed. White light slowing, for this region, is able to slow more efficiently.

Now, we can again see what MOT capture we are able to achieve, and how long a slowing region chirped slowing would require Fig. 7.16. We find that chirped slowing is able to capture about half the molecules, at a distance that is twice as far.

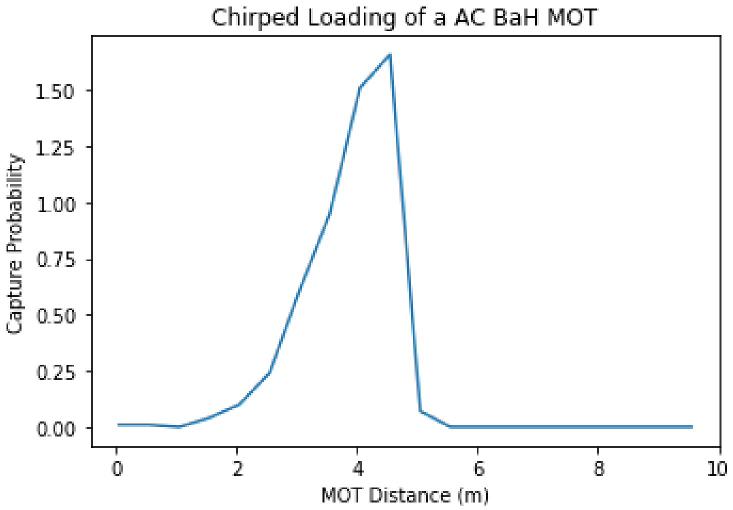

Figure 7.16: We see that chirped slowing has a worse capture percentage. This is because the spatial spread of the beam is even more pronounced, because not all of the molecules feel the force at the same time, and therefore it takes longer to slow. This long slowing distance would make chirped slowing challenging.

While chirped slowing can be tailored to focus on slower molecules, by changing the initial detuning, I focused on settings that allowed the entire beam to be cooled for comparisons sake. For white light slowing no such trade-off exists because we have sufficient laser power to address all the velocity classes at once. The slow molecules take less distance to slow so if we put the MOT chamber closer, they are the ones we capture. The inverse applies to the fast molecules, so all that matters is the capture percentage in optimizing the distance. For these reasons, I believe that white light slowing is preferred for BaH. However, simulation with experimentally achievable powers for CaH, indicate that white light slowing is not feasible. Instead, for that system, chirped slowing is clearly preferred, and capture probabilities of 70% are possible. This simulation show that BaH is a challenging candidate for slowing using traditional techniques. However, the large laser power make it an ideal test-bed for coherent slowing techniques, as discussed in our recent paper.

Chapter 8: Kinematic Detection of Scalar Dark Matter

8.1 Niche Dark Matter Searches

The direct detection of dark matter is among the best motivated search for physics beyond the standard model. There is an abundance of cosmological evidence for its existence, yet we have been unable to probe its nature in the laboratory. As the search for WIMPs approaches the background limits set by neutrino interactions [130], it has become increasingly important to consider a broader range of models and experimental platforms. However, when one starts considering the extremely broad range of candidates, it becomes clear that financial limitations will be a major constraint. It is therefore important to be as efficient as possible to try and maximize the range of these searches. This logic has lead to an explosion of smaller scale experiments, each interested in searching for one specific model, a collection of which are cited here [131, 132, 133, 134, 135, 136, 137, 138]. However, in addition to a range of new detection ideas, we can also ask how existing measurements can be re-purposed. This is very cost effective, as no hardware development is needed, and a graduate student's time is cheap. Several examples of these reanalysis style searches are cited here [139, 140, 141], but the best known is the search for ultralight dark matter using GPS satellites [142].

One category of these less common models attributes DM to the existence of an ultralight field with mass ranging from 10^{-22} to 10^{4} eV. An example of such a field is the axion [143] which has been the focus of tremendous experimental effort [144]. These searches are also performed using modern atomic clocks, but this is happy coincidence, and not the primary motivation for building better clocks so I do not consider these experiments to be “dedicated" searches.

8.2 Quadratic Scalar Dark Matter

Here, I will discuss the details of a proposed detection scheme based on a new phenomenological signature. For some models dark matter forms inhomogeneous clumps that couple to standard model particles in such a way that it changes the apparent value of fundamental constant. An analogy of this, would be the effective mass of a charge carrier changing based on the interactions inside a conductor. These changes in fundamental constant would in turn cause anomalous accelerations we can measure in the lab, using superconducting gravimeters (SCG) in the IGETS network, and with gravitational wave detectors such as LIGO and LISA. This search technique complements existing efforts to detect spatially structured ultralight DM using atomic clocks [145, 146, 142, 147] and atomic magnetometers [148, 149, 149, 150, 151, 152]. We point out (as derived in Eq. (8.11)) that a large enhancement can be achieved with these proposed acceleration measurements for a range of domain wall sizes d: in terms of the fractional change in a fundamental constant, ϵ, the acceleration scales as $\epsilon c^2/d$. While 2D (sheet-like), 1D (line-like), and 0D (point-like) spatial distributions of ultralight scalar fields are possible in stable formations, we focus on the domain wall (2D) distribution [153].

8.2.1 Quadratic scalar couplings and fundamental constants

For this work, We focus on fields with quadratic scalar couplings to the Standard Model because limits on linear scalar coupling are already stringent, and derivative couplings are better suited for spin-dependent searches [152]. Neglecting interactions at lower orders, we can denote the interaction Lagrangian between an ultralight DM field at a specific position and time, $\phi(r,t)$, and any Standard Model (SM) field as

$$-\mathcal{L}^{DM-SM} = \phi^2(r,t)\left(\Gamma_f m_f c^2 \bar{\psi_f}\psi_f - \frac{\Gamma_\alpha}{4} F_{\mu\nu}F^{\mu\nu} + ...\right), \tag{8.1}$$

where m_f and ψ_f are the mass and field for each fermion (with an implied sum over the fermions), $F_{\mu\nu}$ is the electromagnetic tensor, and Γ_X is the coupling constant between the Xth component of

SM field and the DM field. Comparing this to the SM Lagrangian

$$-\mathcal{L}^{SM} = m_f c^2 \bar{\psi}_f \psi_f + \frac{1}{4} F_{\mu\nu} F^{\mu\nu} + ..., \tag{8.2}$$

we observe that to lowest order this DM-SM interaction acts by changing the effective value of the coupling constant for each field. Stated another way, the presence of the DM field has the effect of shifting the apparent values of fundamental constants in the following way:

$$\alpha^{eff} = \alpha \left(\frac{1}{1 - \Gamma_\alpha \phi(r,t)^2} \right) \approx \alpha(1 + \Gamma_\alpha \phi(r,t)^2), \tag{8.3}$$

$$m_f^{eff} = m_f (1 + \Gamma_f \phi(r,t)^2), \tag{8.4}$$

where m_f can refer to the mass of the electron, proton, or neutron (the three terms our measurement will be sensitive to), and α is the fine-structure constant which captures the strength of the electromagnetic interaction. This type of interaction, will be the focus of the detection scheme I propose here.

It is worth taking a second here, to emphasize some subtle issues when taking about changes in fundamental constants. Conventional wisdom says that you can only talk about unitless fundamental constants changing, but in the equations above I also include Fermion masses. In this case I am not talking about the bare value of the fundamental constant, I am talking about the effective value. This means what matters is m_{eff}/m_{bare} which is itself unitless. This applies to spatial variations, as well as time averaged variations, where we can discuss the instantaneous value, over the average value. This distinction was discussed at length in a very good paper by Jun Ye and Dimitry Budker[154], and I think it clarifies the issue quite well. This logic applied to the search at hand, means we are looking for changes in the effective value of the constant inside a clump of dark matter, compared to value in vacuum.

8.2.2 Frequency Domain Searches

In the case where Dark matter is distributed evenly, or approximately evenly, throughout the galaxy these ultralight fields are spatially coherent with a wavelength given by the Compton wavelength. Because of this a detector travelling through this medium will see a coherent oscillation in the field density, and therefore a coherent oscillation in some fundamental constant, that the sensor may be able to resolve. From a detection standpoint this means a frequency domain search is every will suited because you will be looking for a very narrow band signal, and this greatly improves the detection capability. This is also powerful because, in my opinion, detection will need to be made by several independent experiments to be reliable. The fact that these experiments will have to agree of the frequency of the signal is an excellent check, especially if the detection is made in very different systems. We have not analyzed how frequency based searches could be used based on IGETS, but a recent publication explored the applicability of LIGO and other gravitational wave detectors to these frequency domain searches [155]. There are also several experiments using atomic clock based detection [16, 156]. They found very encouraging results, with performance at or beyond the state of the art. This detection scheme also has a lot of promise, because there is enormous funding available to improve gravitational wave detectors in the near term. Piggy backing on these searches is a great chance to get more data for free.

8.2.3 Time Domain Searches

In different models, the ultralight scalar field forms spatially inhomogeneous structures [157, 158, 159]. This results in apparent changes of fundamental constants as the Earth travels through areas of varying field density. This means a time domain search for these signals as transient events make the most sense. We would require multiple sensors, each spread out spatially, and require any detection to be present in a consistent way across each detector. This dispersed sensor model is also used by LIGO (which looks for small transient signals) and the GNOME collaboration which is looking for similar types of dark matter models, based on a different standard model coupling.

For clumpy DM models, $\phi(r,t)$ can generate spatially varying effective values for the fundamental constants. If we assume that this field constitutes all of DM, and that each defect has the same peak field amplitude (ϕ_{max}), then we can relate the size of the defect to ϕ_{max} using the known density of DM over galactic scales. We begin by expressing the energy density inside the DM field defect with a characteristic size d (related to the mass scale of the DM field by its Compton wavelength, $d \sim \hbar/(m_{\phi}c)$), as

$$\rho_{inside} = \frac{\phi_{max}^2}{\hbar c d^2}. \tag{8.5}$$

Since the average energy density over many defects must be equal to the overall energy density measured over the Milky Way of $\rho_{DM} \approx 0.4$ GeV/cm^3, we can connect the overall DM density to the density inside a defect of dimension n (where $n = 0$ is a point defect, $n = 1$ is a line defect, and $n = 2$ is a domain wall defect) using simple scaling arguments [142],

$$\rho_{DM} \approx \rho_{inside} d^{3-n} L^{n-3} (\hbar c)^{-1} \approx \phi_{max}^2 d^{1-n} L^{n-3} (\hbar c)^{-1}, \tag{8.6}$$

where L is is the typical separation between defects, which we can be related to the expected time between defect encounters τ based on the velocity of the Earth relative to the galactic frame, $v_r \approx 300$ km/s. So for a given defect size and geometry we know the amplitude of the field inside the defect. This can be related to the fractional change in fundamental constants inside a defect, where we focus on domain walls ($n = 2$):

$$\frac{\Delta m_f}{m_f} = \Gamma_f \phi_{max}^2 = d\tau v_r \hbar c \Gamma_f \rho_{\text{DM}}, \tag{8.7}$$

$$\frac{\Delta \alpha}{\alpha} = \Gamma_{\alpha} \phi_{max}^2 = d\tau v_r \hbar c \Gamma_{\alpha} \rho_{\text{DM}}. \tag{8.8}$$

This allows us to relate any measured change in fundamental constants to the coupling between $\phi(r, t)$ and the standard model (Γ_f), and the distribution of the DM defects in the galaxy (defined by τ and d). Every other parameter is known. Furthermore, the length scale of the defect d and the mass of the field are related by the Compton wavelength. For comparison to other work, we will express limits in the effective energy scale, which is related to the the coupling constant,

$$\Lambda_X = \frac{1}{\sqrt{|\Gamma_X|}}. \tag{8.9}$$

8.2.4 Anomalous Acceleration from Changes in Rest Mass

The changes in the effective mass of fundamental particles will also change the masses of macroscopic objects. This has a pronounced effect on their motion, because conservation of energy requires a force associated with the gradient of the object's rest mass energy,

$$\vec{a} = \frac{-\vec{\nabla} mc^2}{m}. \tag{8.10}$$

This expression has significant consequences [160, 161] as it implies an apparent violation of the universality of free fall: since ∇M is not the same for different fermions, the anomalous acceleration is composition-dependent.

The test mass composition determines how a fractional change in fundamental masses affects the total mass, and a fractional change in the fine structure constant affects the electronic binding energy of each atom in the test mass. This analysis will be presented in Table 1. For simplicity, here we focus on the overall fractional change in a test mass. For a defect of size d that provides a fractional change ϵ of the test particle mass, the maximum acceleration is

$$|a| \approx \frac{\epsilon c^2}{d}. \tag{8.11}$$

This means gravimeters have a high sensitivity to these signals for defect sizes when $c^2/d >> g$. Therefore, this technique can compete with high-precision measurements such as atomic clocks, since the fractional change we are searching for is enhanced relative to ϵ. To emphasize this point, domain wall dark matter search using GPS satellites [147] is most sensitive to a fractional change in fundamental constants on the order of 10^{-12} for a defect size of 10^4 km. These parameters would result in an acceleration of 10^{-2} m/s^2 that lasts $\sim$ 30 s. This is a large acceleration, for quite a long duration. For comparison, the SCGs that make up the IGETS network are capable of acceleration measurements of 10^{-11} m/s^2 over minute timescales [162, 163], making them very competitive for these searches using existing technology and data sets. This acceleration signature has not been widely discussed, but I think it shows some important points. When you start talking about variations in fundamental constants, there are a lot of potentially tricky consequences, and its important to consider them all. Atomic clocks are extremely sensitive, but not necessarily the based way to search for these types of dark matter.

8.3 Detection Schemes

What makes this new search strategy particularly interesting, is the potential to perform this search on existing data, and there are two exceptional sources. The IGETS network, is a global network of extremely sensitive gravitational acceleration senors, typically used for geophysics applications and the LIGO observatory. These are both freely available data sources, and as we will show, able to match or exceed current search limits.

8.3.1 IGETS Network and the Superconducting Gravimeter

The Super-Conducting Gravimeter (SCG) is currently the most precise gravimeter design demonstrated, and a common tool in the field of Geodesy. SCG's work as force balance, using the Lorentz force between a the magnetic field from a superconducting coil and a superconducting current inside a test mass, to delicately balance against the force of gravity. The technology has been fully developed in the last 30 years, and fractional precision on the order of 10^{-12} are regularly achieved in commercially available devices. A standardized library of measurements from many of these devices is organized by the International Geodynamics and Earth Tide Services (IGETS) as a tool for monitoring, and archiving gravitational acceleration measurements at various locations around the world. This database is a powerful tool for geophyscists, and has recently been used for several Lorentz invariance studies.

To estimate the detection sensitivity for these devices, we can take the noise spectra (n(f)) for a superconducting gravimeter (SCG) in the IGETS network, during a quiet 10 day period after known tidal forces and local disturbances were removed. This sensor is a typical example of the $\approx$ 20 SCG that make up the IGETS network, which have been collecting data continuously for the last 20 years.

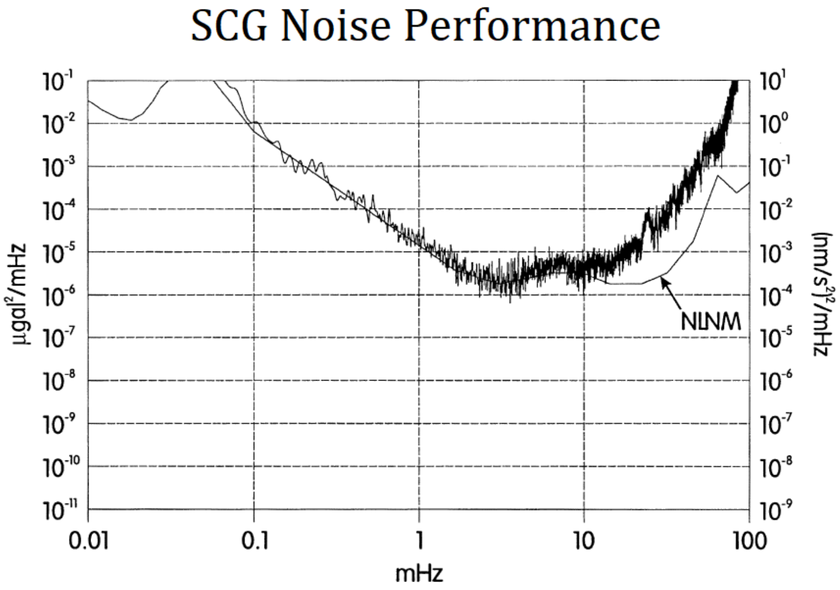

Figure 8.1: Noise power density for a superconducting gravimeter (in Germany) during seismically quiet times. For the purpose of our analysis we approximate these curves as the sum of 3 power laws that are fit to this data. Figure taken from [164].

With this noise performance we can simulate the SNR for a given signal and see what the detection threshold for a single sensor would be. There additional concerns when it comes to signal reconstruction, because we need to look for simultaneous events across many detectors, in order to be sure the signals are real and not a local disturbance. Thankfully, the dominant source of correlation between these sensors, is seismic activity, which has has a relatively slow, and well characterized speed of $\approx$ 10 km/s. Compare this to the virial velocity of the earth traveling through a clump of dark matter (300 km/s) and we can separate out seismic activity. A down side though, is the sensitivity of these devices mean seismic activity will swamp the sensors for extended periods of time, that will reduce the effective uptime of the system. To illustrate this, we can compare the sensors during seismically calm, and active times. Here, $g_0 = 9.80665$ a standard gravitational acceleration value used in geodesy.

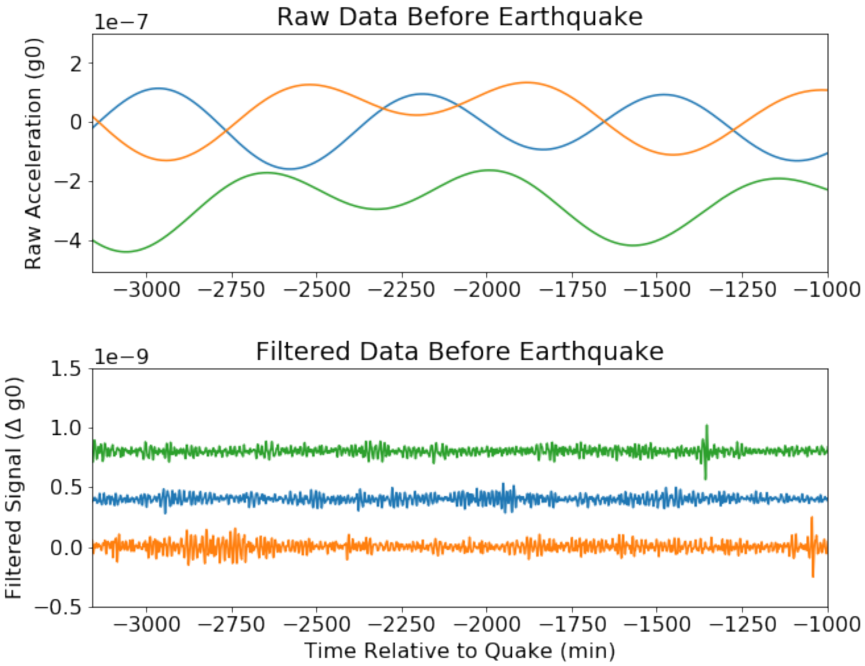

Figure 8.2: a) raw acceleration data, shown for a 30 hour period prior to the 2004 Indian ocean Earthquake for three sensors. B) The same data, with known tidal forces removed, and small residuals left. Notice, that there is no correlation between these signals, and we attribute the small fluctuations to local disturbances.

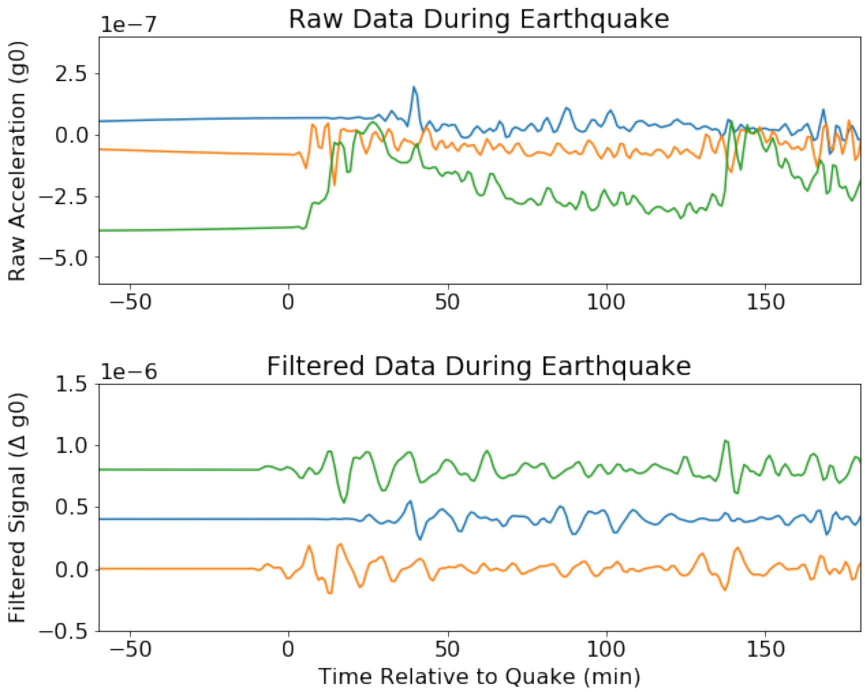

Figure 8.3: a) Raw acceleration measurements showing the onset, and ring down from the 2004 earthquake. b) The same data, with tidal forces removed. Notice the scale is some 3 orders of magnitude larger than during seismically quiet times, and despite the single event causing the signal there is a pronounced delay as measured in each sensor. This delay comes from the physical separation of the sensors, and shows that the relatively slow speed of sound can be exploited in this search. Also note the revival of the signal in the green trace, consistent with the waves from the earthquake traveling around the circumference of earth, at around 6 km/s

While these events complicate the analysis, it is possible to reject them with high certainty thanks to their characteristic speed, and other groups have shown that useful fundamental physics can still be extracted from these sensors.

8.3.2 LIGO

The sensitivity curve for LIGO has been very well characterized, and is among the most discussed plots in modern physics. This is great for this search, because we can take this as an input, and estimate the SNR for signals here we wish to measure. As a reminder, the LIGO sensitivity curve is shown below [165].

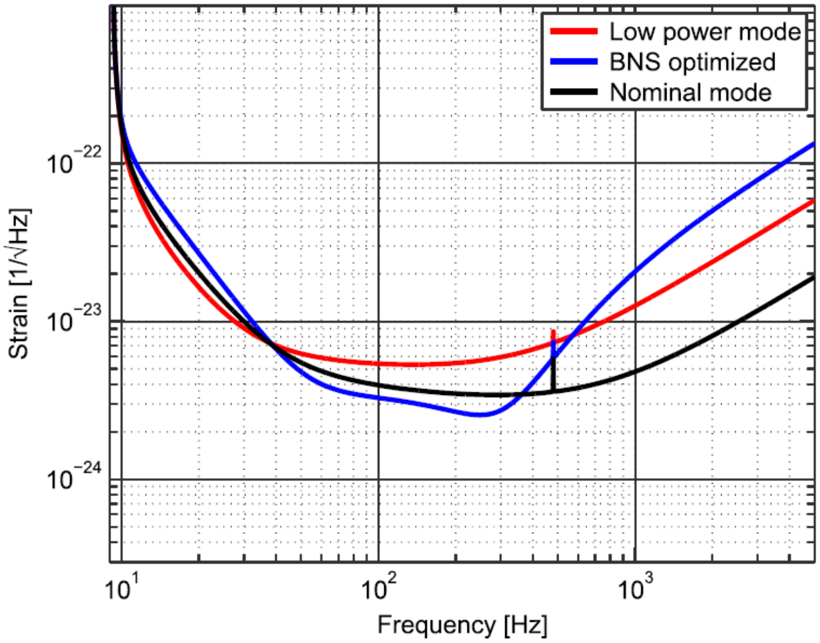

Figure 8.4: Strain sensitivity curves for the LIGO. A power law fit to the nominal mode performance was used for this analysis. This image was taken from [165]

Similar constraints from the timing of the detection also apply to LIGO. Gravitational waves move at the speed of light, and this leads to a known delay based on the direction of the waves prorogation relative to the two LIGO detectors. Here, we expect a larger delay, but still faster then any seismic activity as discussed before. There are several “unmodeled burst" search strategies used in the LIGO group that would be a good place to start for this analysis. With an idea for the detection strategy, and the sensitivity for each detector established, we can now model the expected signal to estimate the search capabilities in this application.

8.3.3 Accelerometer Based Fractional Mass Limits

For the sensitivity estimates, we assume the density of a domain wall follows a Gaussian distribution, with length scale d and a maximum fractional change in the rest mass of ϵ. This choice of distribution can be modified but, as long as the density is relatively smooth, the results will not be strongly affected. For a test particle traveling perpendicularly through such a domain wall at speed v_r, we can define the effective mass as a function of time,

$$m_{\text{eff}}(t) = m_0(1 + \epsilon e^{-t^2 v_r^2/d^2}), \tag{8.12}$$

where m_0 is the unperturbed mass. Then we calculate the effective acceleration of this test particle as a function of time using Eq. (11), keeping only the leading order in ϵ,

$$a(t) = \frac{2\epsilon t v_r c^2}{d^2} e^{-t^2 v_r^2/d^2}. \tag{8.13}$$

The fractional change in test mass (Eq. (13)) and the effective acceleration waveform (Eq. (14)), as well as a cartoon of a passing domain wall, are shown in Fig. 4.

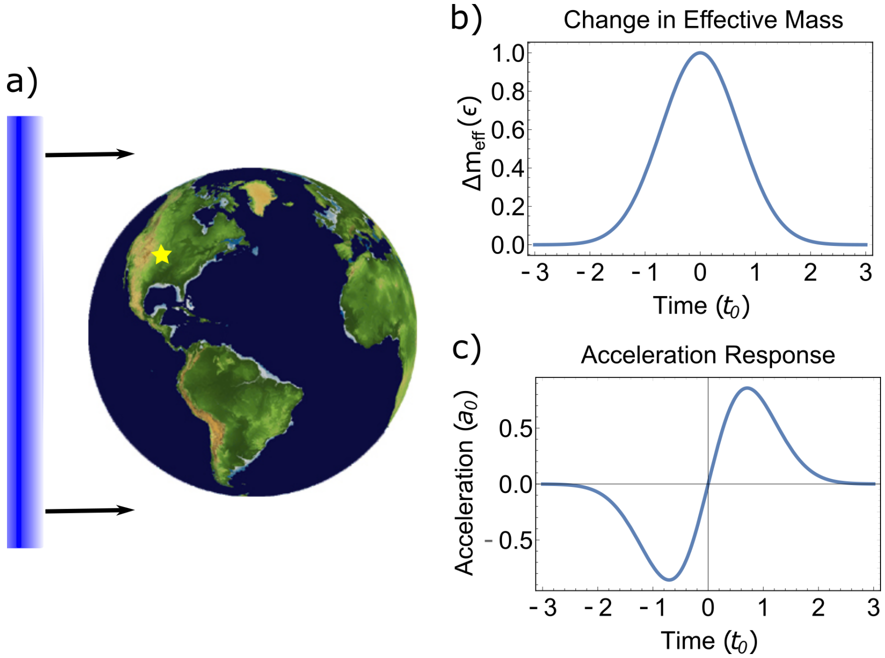

Figure 8.5: a) A domain wall approaching the Earth, with a highlighted accelerometer located in Boulder, Colorado, USA. b) Fractional change in test mass caused by the domain wall's passage ($\Delta m_{\text{eff}}/m_0 = m_{\text{eff}}/m_0 - 1$). c) Anomalous acceleration caused by the gradient in the domain wall density, resulting in a changing mass of the test particle. The transient signal has a characteristic time and acceleration of $t_0 = d/v_r$ and $a_0 = \epsilon c^2/d$, respectively, with a peak acceleration of $a_{\text{peak}} = a_0\sqrt{\frac{2}{e}}$ because of the specific density distribution chosen.

In order to be observed, the domain wall must produce a signal with high enough power in the frequency range where the accelerometer is sensitive. However, the frequency components of this waveform are quite broadband. This means that for large domain walls the signal will have more power at low frequencies, and for a specific domain size it will be well matched to the $\sim$ 0.01 Hz peak sensitivity of the SCGs. To calculate the sensitivity based on the frequency performance of these sensors, we use the waveform in Eq. (14) and take its Fourier transform. We then find the signal-to-noise ratio (SNR) at each frequency by dividing this signal amplitude by the noise amplitude, and calculate the total SNR by integrating over all frequencies. Finally, we multiply by $\sqrt{t_0}$ to account for the characteristic time over which the signal can be averaged, because the signal we are looking for is transient. We then solve for the value of ϵ that would result in a signal with an SNR of 10 for a fixed defect size. This leads to a conservative estimate for the search sensitivity, but the nature of the search would require a strong signal to be beleived.

Note that for a specifically designed acceleration based experiment, we could expect a sensitivity improvement of several orders of magnitude. This is because the SCGs do not use the free-fall-universality violating nature of the signal to cancel disturbances. In particular, a torsion balance experiment with a test mass consisting of two different materials would be a natural setup for these searches, similar to previous axion searches [166]. However, such a system would have to run continuously for several years before it is sensitive enough to limit rare domain wall events.

8.3.4 LIGO Based Fractional Mass Limits

For example, suppose a domain wall approaches the LIGO detector, perpendicular to one arm of the interferometer and parallel to the other, as shown in Fig. 5 . For the arm perpendicular to the domain wall's propagation direction, each mirror will accelerate by the same amount but the length of the arm will not change. For the arm parallel to the domain wall propagation, the mirrors will see slightly different field magnitudes (because of the 4 km separation) and therefore experience different accelerations. At $t = 0$ when the domain wall is centered between the two mirrors, the differential acceleration is

$$\Delta a(t) = a(t - L/2v_r) - a(t + L/2v_r). \tag{8.14}$$

This differential acceleration can be integrated twice to find the change in separation between the mirrors. Divided by the length of the interferometer L it is the strain $S(t)$,

$$S(t) = \frac{\epsilon d \sqrt{\pi} c^2}{2 L v_r^2} \left[\operatorname{erf}\left(\frac{L - 2 t v_r}{2d} \right) + \operatorname{erf}\left(\frac{L + 2 t v_r}{2d} \right) \right], \tag{8.15}$$

where $\operatorname{erf}(x)$ is the error function. This differential strain between the two LIGO arms is exactly what it was designed to measure extremely precisely. The strain signal in the detector has qualitatively different behaviors depending on whether the defect is larger or smaller than the 4 km length of the LIGO arms as shown in Fig. 2. We use this strain in Eq. (16) to perform a sensitivity analysis in analogy to what was done for accelerometers, using a power law approximation of LIGO's strain noise curve [167], and mandating a SNR of 10. Furthermore, this analysis was repeated for the planned LISA mission based on its projected sensitivity.

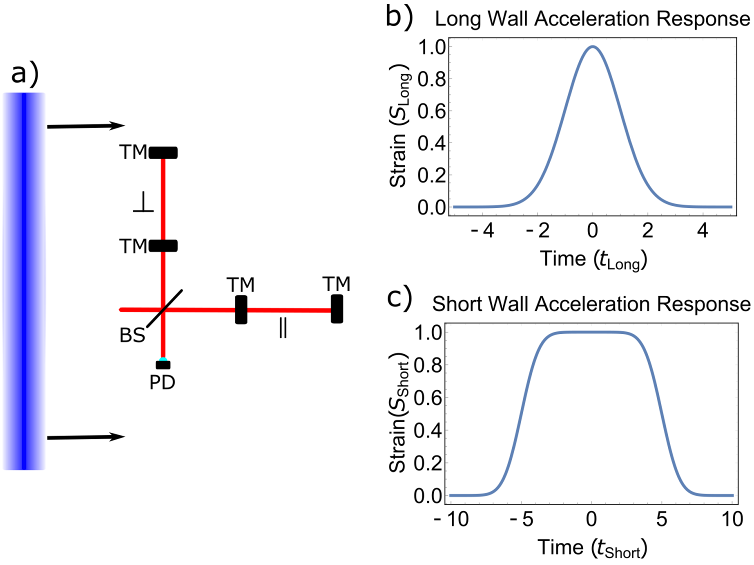

Figure 8.6: (a) Domain wall approaching a LIGO type optical interferometer, along one of the directions of maximum sensitivity. The interferometer is formed by splitting laser light with a beam splitter (BS), while the ends of each arm are free floating mirrors acting as test masses (TMs). Differential changes in the length of each arm are monitored via a photodiode (PD). In the case shown, the test masses along the arm perpendicular to the domain wall's approach direction (⊥) will feel no acceleration along the direction of the arm, while the two test masses in the parallel arm (||) will feel slightly different accelerations because of the difference in the gradient of the domain wall at each location. This results in a differential acceleration of the TMs in the parallel arm which changes the path length, while the perpendicular path length is unaffected. This change in relative path length would be observed as a transient strain in the detector as the domain wall passes. The resulting (normalized) strain wave forms show qualitatively different behavior when the domain wall is larger (b) or smaller (c) then the path length of LIGO (L = 4 km). For long domain walls the signal approaches a Gaussian with a peak strain size of $S_{\text{Long}} = \epsilon c^2/v_r^2$. For short domain walls the plateau has a fixed duration $t_p = L/v_r$, and the peak strain scales like $S_{\text{Short}} = \epsilon d c^2/(L v_r^2)$. For both signals, the characteristic time is $t_{\text{Short}} = t_{\text{Long}} = d/v_r$. For wave forms shown, $d \gg L$ for the long domain wall and $d \approx L/10$ for the short domain wall.

8.3.5 Atomic Rest Mass and Fundamental Constants

Before we derive the constraints based on the described technique, we must estimate how a fractional change in each fundamental constant affects the total test mass. This effect is composition-dependent. For LIGO the test masses are the silica mirrors [168], for LISA they are Au-Pt composites[155], and for the accelerometers they are niobium (the test mass that is being levitated)[162]. The semi-empirical Bethe-Weizacker formula [160] accounts for the nucleon mass, the electron mass, and the mass associated with the binding energy,

$$\begin{aligned} m(A,Z) \approx Zm_p + (A-Z)m_n + \\ Zm_e + (98.25\ \mathrm{MeV}/c^2)\frac{Z(Z-1)}{A^{1/3}}\alpha, \end{aligned} \tag{8.16}$$

where A is the total nucleon number and Z is the number of protons. This allows us to calculate the sensitivity coefficient for the Xth coupling to the DM field, A_X, to relate a change in a fundamental constant to the changes in test mass,

$$\epsilon = A_X \frac{\delta X}{X}. \tag{8.17}$$

The results of this calculation for each system are shown in Table 1.

Constant	LIGO	LISA	SCG
A_α	5×10^{-4}	2×10^{-4}	4×10^{-4}
A_{m_e}	2×10^{-4}	1×10^{-4}	8×10^{-5}
A_{m_p}	0.5	0.4	0.4
A_{m_n}	0.5	0.6	0.6

Table 8.1: Sensitivity coefficients quantifying how a fractional change in each fundamental constant relates to the fractional change in the test mass for each experimental platform. As expected, fractional changes in proton and neutron masses result in order unity changes in the total test mass, while changes in electron mass and α result in smaller changes.

8.3.6 Projected Limits on New Physics

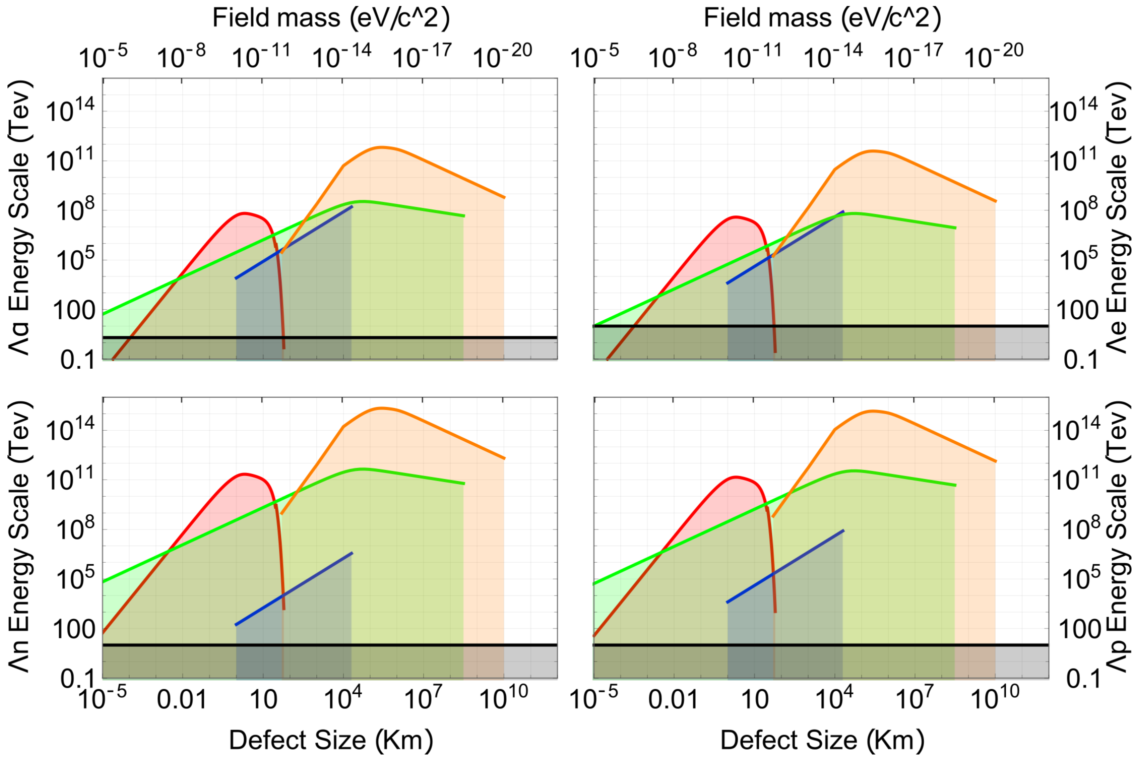

Figure 8.7: Limits on the DM-SM coupling strengths set using GPS clocks [147] (blue) and astrophysical constraints [169] (black), and the projected limits set by the IGETS network (green), LIGO (red) and LISA (orange). Here, the time τ between domain walls is 7 years to allow a comparison to GPS limits. We have access to sufficient data taken with the SC gravimeters to look for such rare events, but for LIGO, only $\tau \lesssim 1$ year is currently achievable. We see smaller sensitivities to the α and m_e couplings as they contribute less to the total system mass, making them well suited for clock based searches. Note that the constraints far from the peak of each system's sensitivity may be unreliable due to additional noise sources not present in the approximated noise power spectral density, or for small defect sizes due to finite sampling rates.

The described analysis allows us to estimate what domain wall size and effective coupling energy scale each experimental platform is sensitive to for the neutron, proton and electron masses and the fine structure constant. The results are shown in Fig (3). For these projected constraints we assume that the DM-SM coupling contribution comes entirely from one term, and that the time between domain wall crossings is $\tau = 7$ years. This timing is well matched with the 20 years of IGETS data, and the same was chosen for the previous GPS based studies [147]. Recent work with networks of atomic clocks has also set stringent limits for these coupling models [145, 146]. However, the limited duration of the data collection period with this network of $\lesssim$ 40 days (compared to 20+ years of IGETS data) limit their sensitivity to only relatively frequently occurring domain walls. As more data is collected using this clock network, this situation will improve and will likely be the most accurate way to search for coupling to α.

8.3.7 Conclusions

We have shown that in addition to atomic clocks and atomic magnetometers, accelerometers and gravitational wave detectors are natural platforms to search for domain-wall ultralight scalar dark matter. Furthermore, a detection event that is seen in multiple systems simultaneously would provide a strong evidence of interactions beyond the Standard Model. For the SCG accelerometers, 20+ years of data taken with over 20 sensors has already been recorded and archived. This will allow us to mine for these signals and investigate an unexplored parameter space for the DM-SM coupling models. For LIGO, $\gtrsim$ 1 year of data has been collected, and is also freely available for these searches. This represents a unique opportunity to explore the origins of DM with existing data sets.

References

[1] C. Wood, S. Bennett, D. Cho, B. Masterson, J. Roberts, C. Tanner, and C. E. Wieman, “Measurement of parity nonconservation and an anapole moment in cesium,” *Science*, vol. 275, no. 5307, pp. 1759–1763, 1997.

[2] T Pruttivarasin, M Ramm, S. Porsev, I. Tupitsyn, M. Safronova, M. Hohensee, and H Häffner, “Michelson–morley analogue for electrons using trapped ions to test lorentz symmetry,” *Nature*, vol. 517, no. 7536, pp. 592–595, 2015.

[3] S. Dimopoulos, P. W. Graham, J. M. Hogan, and M. A. Kasevich, “Testing general relativity with atom interferometry,” *Physical review letters*, vol. 98, no. 11, p. 111 102, 2007.

[4] M. Greiner, O. Mandel, T. Esslinger, T. W. Hänsch, and I. Bloch, “Quantum phase transition from a superfluid to a mott insulator in a gas of ultracold atoms,” *nature*, vol. 415, no. 6867, pp. 39–44, 2002.

[5] I. Bloch, J. Dalibard, and W. Zwerger, “Many-body physics with ultracold gases,” *Reviews of modern physics*, vol. 80, no. 3, p. 885, 2008.

[6] B. Bloom, T. Nicholson, J. Williams, S. Campbell, M Bishof, X Zhang, W Zhang, S. Bromley, and J Ye, “An optical lattice clock with accuracy and stability at the 10- 18 level,” *Nature*, vol. 506, no. 7486, pp. 71–75, 2014.

[7] T. Nicholson, S. Campbell, R. Hutson, G. Marti, B. Bloom, R. McNally, W. Zhang, M. Barrett, M. Safronova, G. Strouse, *et al.*, “Systematic evaluation of an atomic clock at 2× 10- 18 total uncertainty,” *Nature communications*, vol. 6, no. 1, pp. 1–8, 2015.

[8] J. M. Mcguirk, G. Foster, J. Fixler, M. Snadden, and M. Kasevich, “Sensitive absolute-gravity gradiometry using atom interferometry,” *Physical Review A*, vol. 65, no. 3, p. 033 608, 2002.

[9] D. Budker and M. Romalis, “Optical magnetometry,” *Nature physics*, vol. 3, no. 4, pp. 227–234, 2007.

[10] T. Aoyama, M. Hayakawa, T. Kinoshita, and M. Nio, “Tenth-order qed contribution to the electron g- 2 and an improved value of the fine structure constant,” *Physical Review Letters*, vol. 109, no. 11, p. 111 807, 2012.

[11] B. Odom, D. Hanneke, B d’Urso, and G. Gabrielse, “New measurement of the electron magnetic moment using a one-electron quantum cyclotron,” *Physical review letters*, vol. 97, no. 3, p. 030 801, 2006.

[12] M Tanabashi and et. all, “Review of particle physics,” *Phys. Rev. D*, vol. 98, p. 030 001, 3 2018.

[13] J. E. Kim and G. Carosi, “Axions and the strong c p problem,” *Reviews of Modern Physics*, vol. 82, no. 1, p. 557, 2010.

[14] C. A. O’Hare, “Dark matter astrophysical uncertainties and the neutrino floor,” *Physical Review D*, vol. 94, no. 6, p. 063 527, 2016.

[15] M. Safronova, D Budker, D DeMille, D. F. J. Kimball, A Derevianko, and C. W. Clark, “Search for new physics with atoms and molecules,” *Reviews of Modern Physics*, vol. 90, no. 2, p. 025 008, 2018.

[16] C. J. Kennedy, E. Oelker, J. M. Robinson, T. Bothwell, D. Kedar, W. R. Milner, G. E. Marti, A. Derevianko, and J. Ye, “Precision metrology meets cosmology: Improved constraints on ultralight dark matter from atom-cavity frequency comparisons,” *Physical Review Letters*, vol. 125, no. 20, p. 201 302, 2020.

[17] N. Ohmae, F. Bregolin, N. Nemitz, and H. Katori, “Direct measurement of the frequency ratio for hg and yb optical lattice clocks and closure of the hg/yb/sr loop,” *Optics Express*, vol. 28, no. 10, pp. 15 112–15 121, 2020.

[18] S Blatt, A. Ludlow, G. Campbell, J. W. Thomsen, T Zelevinsky, M. Boyd, J Ye, X Baillard, M Fouché, R Le Targat, *et al.*, “New limits on coupling of fundamental constants to gravity using sr 87 optical lattice clocks,” *Physical Review Letters*, vol. 100, no. 14, p. 140 801, 2008.

[19] J. Kobayashi, A. Ogino, and S. Inouye, “Measurement of the variation of electron-to-proton mass ratio using ultracold molecules produced from laser-cooled atoms,” *Nature communications*, vol. 10, no. 1, pp. 1–5, 2019.

[20] M. Romalis, W. Griffith, J. Jacobs, and E. Fortson, “New limit on the permanent electric dipole moment of 199 hg,” *Physical Review Letters*, vol. 86, no. 12, p. 2505, 2001.

[21] V. Dzuba, V. Flambaum, and J. Ginges, “Calculation of parity and time invariance violation in the radium atom,” *Physical Review A*, vol. 61, no. 6, p. 062 509, 2000.

[22] V. Andreev and N. Hutzler, “Improved limit on the electric dipole moment of the electron,” *Nature*, vol. 562, no. 7727, pp. 355–360, 2018.

[23] W. B. Cairncross, D. N. Gresh, M. Grau, K. C. Cossel, T. S. Roussy, Y. Ni, Y. Zhou, J. Ye, and E. A. Cornell, “Precision measurement of the electron’s electric dipole moment using trapped molecular ions,” *Physical review letters*, vol. 119, no. 15, p. 153 001, 2017.

[24] I. Kozyryev and N. R. Hutzler, “Precision measurement of time-reversal symmetry violation with laser-cooled polyatomic molecules,” *Physical review letters*, vol. 119, no. 13, p. 133 002, 2017.

[25] M. Denis, P. A. Haase, R. G. Timmermans, E. Eliav, N. R. Hutzler, and A. Borschevsky, “Enhancement factor for the electric dipole moment of the electron in the baoh and yboh molecules,” *Physical Review A*, vol. 99, no. 4, p. 042 512, 2019.

[26] I. B. Khriplovich and S. K. Lamoreaux, *CP violation without strangeness: electric dipole moments of particles, atoms, and molecules*. Springer Science & Business Media, 2012.

[27] C. Cesarotti, Q. Lu, Y. Nakai, A. Parikh, and M. Reece, “Interpreting the electron edm constraint,” *Journal of High Energy Physics*, vol. 2019, no. 5, p. 59, 2019.

[28] O. Grasdijk, O. Timgren, J. Kastelic, T. Wright, S. Lamoreaux, D. Demille, K. Wenz, M. Aitken, T. Zelevinsky, T. Winick, *et al.*, “Centrex: A new search for time-reversal symmetry violation in the $\Gamma\{205\}\, tlnucleus$,” *arXiv preprint arXiv:2010.01451*, 2020.

[29] B. L. Augenbraun, Z. D. Lasner, A. Frenett, H. Sawaoka, C. Miller, T. C. Steimle, and J. M. Doyle, “Laser-cooled polyatomic molecules for improved electron electric dipole moment searches,” *New J. Phys.*, vol. 22, p. 022 003, 2020.

[30] E. T. Mengesha, A. T. Le, T. C. Steimle, L. Cheng, C. Zhang, B. L. Augenbraun, Z. Lasner, and J. Doyle, “Branching ratios, radiative lifetimes, and transition dipole moments for yboh,” *The Journal of Physical Chemistry A*, vol. 124, no. 16, pp. 3135–3148, 2020.

[31] L Caldwell, J. Devlin, H. Williams, N. Fitch, E. Hinds, B. Sauer, and M. Tarbutt, “Deep laser cooling and efficient magnetic compression of molecules,” *Physical review letters*, vol. 123, no. 3, p. 033 202, 2019.

[32] L. Anderegg, B. L. Augenbraun, Y. Bao, S. Burchesky, L. W. Cheuk, W. Ketterle, and J. M. Doyle, “Laser cooling of optically trapped molecules,” *Nature Physics*, vol. 14, no. 9, pp. 890–893, 2018.

[33] D. McCarron, M. Steinecker, Y Zhu, and D DeMille, “Magnetic trapping of an ultracold gas of polar molecules,” *Phys. Rev. Lett.*, vol. 121, no. 1, p. 013 202, 2018.

[34] A. L. Collopy, S. Ding, Y. Wu, I. A. Finneran, L. Anderegg, B. L. Augenbraun, J. M. Doyle, and J. Ye, “3D magneto-optical trap of yttrium monoxide,” *Phys. Rev. Lett.*, vol. 121, no. 21, p. 213 201, 2018.

[35] W. S. Bakr, J. I. Gillen, A. Peng, S. Fölling, and M. Greiner, “A quantum gas microscope for detecting single atoms in a hubbard-regime optical lattice,” *Nature*, vol. 462, no. 7269, pp. 74–77, 2009.

[36] H. Bernien, S. Schwartz, A. Keesling, H. Levine, A. Omran, H. Pichler, S. Choi, A. S. Zibrov, M. Endres, M. Greiner, *et al.*, “Probing many-body dynamics on a 51-atom quantum simulator,” *Nature*, vol. 551, no. 7682, pp. 579–584, 2017.

[37] M. Saffman, T. G. Walker, and K. Mølmer, “Quantum information with rydberg atoms,” *Reviews of modern physics*, vol. 82, no. 3, p. 2313, 2010.

[38] D. DeMille, “Quantum computation with trapped polar molecules,” *Physical Review Letters*, vol. 88, no. 6, p. 067 901, 2002.

[39] P. Yu, L. W. Cheuk, I. Kozyryev, and J. M. Doyle, “A scalable quantum computing platform using symmetric-top molecules,” *New Journal of Physics*, vol. 21, no. 9, p. 093 049, 2019.

[40] N. Schuch and F. Verstraete, “Computational complexity of interacting electrons and fundamental limitations of density functional theory,” *Nature Physics*, vol. 5, no. 10, pp. 732–735, 2009.

[41] R. P. Feynman, “Simulating physics with computers,” *Int. J. Theor. Phys*, vol. 21, no. 6/7, 1982.

[42] T. Esslinger, “Fermi-hubbard physics with atoms in an optical lattice,” *Annual Review of Condensed Matter Physics*, vol. 1, no. 1, pp. 129–152, 2010.

[43] P. T. Brown, D. Mitra, E. Guardado-Sanchez, R. Nourafkan, A. Reymbaut, C.-D. Hébert, S. Bergeron, A.-M. Tremblay, J. Kokalj, D. A. Huse, *et al.*, “Bad metallic transport in a cold atom fermi-hubbard system,” *Science*, vol. 363, no. 6425, pp. 379–382, 2019.

[44] L. Chomaz, R. M. van Bijnen, D. Petter, G. Faraoni, S. Baier, J. H. Becher, M. J. Mark, F. Waechtler, L. Santos, and F. Ferlaino, “Observation of roton mode population in a dipolar quantum gas,” *Nature physics*, vol. 14, no. 5, pp. 442–446, 2018.

[45] T. Sowiński, O. Dutta, P. Hauke, L. Tagliacozzo, and M. Lewenstein, “Dipolar molecules in optical lattices,” *Physical review letters*, vol. 108, no. 11, p. 115 301, 2012.

[46] R. Barnett, D. Petrov, M. Lukin, and E. Demler, “Quantum magnetism with multicomponent dipolar molecules in an optical lattice,” *Physical review letters*, vol. 96, no. 19, p. 190 401, 2006.

[47] K.-K. Ni, S Ospelkaus, M. De Miranda, A Pe’Er, B Neyenhuis, J. Zirbel, S Kotochigova, P. Julienne, D. Jin, and J. Ye, “A high phase-space-density gas of polar molecules,” *Science*, vol. 322, no. 5899, pp. 231–235, 2008.

[48] L. R. Liu, J. D. Hood, Y. Yu, J. T. Zhang, K. Wang, Y.-W. Lin, T. Rosenband, and K.-K. Ni, “Molecular assembly of ground-state cooled single atoms,” *Physical Review X*, vol. 9, no. 2, p. 021 039, 2019.

[49] I. S. Madjarov, J. P. Covey, A. L. Shaw, J. Choi, A. Kale, A. Cooper, H. Pichler, V. Schkolnik, J. R. Williams, and M. Endres, “High-fidelity entanglement and detection of alkaline-earth rydberg atoms,” *Nature Physics*, pp. 1–5, 2020.

[50] V. V. Albert, J. P. Covey, and J. Preskill, “Robust encoding of a qubit in a molecule,” *Physical Review X*, vol. 10, no. 3, p. 031 050, 2020.

[51] L. W. Cheuk, L. Anderegg, Y. Bao, S. Burchesky, S. Yu, W. Ketterle, K.-K. Ni, and J. M. Doyle, “Observation of collisions between two ultracold ground-state caf molecules,” *arXiv preprint arXiv:2002.00048*, 2020.

[52] L. Anderegg, L. W. Cheuk, Y. Bao, S. Burchesky, W. Ketterle, K.-K. Ni, and J. M. Doyle, “An optical tweezer array of ultracold molecules,” *Science*, vol. 365, no. 6458, pp. 1156–1158, 2019.

[53] E. Potter, J. Herek, S Pedersen, Q Liu, and A. Zewail, “Femtosecond laser control of a chemical reaction,” *Nature*, vol. 355, no. 6355, pp. 66–68, 1992.

[54] S Ospelkaus, K.-K. Ni, D Wang, M. De Miranda, B Neyenhuis, G Quéméner, P. Julienne, J. Bohn, D. Jin, and J Ye, “Quantum-state controlled chemical reactions of ultracold potassium-rubidium molecules,” *Science*, vol. 327, no. 5967, pp. 853–857, 2010.

[55] J. W. Park, S. A. Will, and M. W. Zwierlein, “Ultracold dipolar gas of fermionic na 23 k 40 molecules in their absolute ground state,” *Physical review letters*, vol. 114, no. 20, p. 205 302, 2015.

[56] T. Takekoshi, L. Reichsöllner, A. Schindewolf, J. M. Hutson, C. R. Le Sueur, O. Dulieu, F. Ferlaino, R. Grimm, and H.-C. Nägerl, “Ultracold dense samples of dipolar rbcs molecules in the rovibrational and hyperfine ground state,” *Physical review letters*, vol. 113, no. 20, p. 205 301, 2014.

[57] X. Ye, M. Guo, M. L. González-Martínez, G. Quéméner, and D. Wang, “Collisions of ultracold 23na87rb molecules with controlled chemical reactivities,” *Science advances*, vol. 4, no. 1, eaaq0083, 2018.

[58] M.-G. Hu, Y Liu, D. Grimes, Y.-W. Lin, A. Gheorghe, R Vexiau, N Bouloufa-Maafa, O Dulieu, T Rosenband, and K.-K. Ni, “Direct observation of bimolecular reactions of ultracold krb molecules,” *Science*, vol. 366, no. 6469, pp. 1111–1115, 2019.

[59] Y. Liu, M.-G. Hu, M. A. Nichols, D. D. Grimes, T. Karman, H. Guo, and K.-K. Ni, “Steering ultracold reactions through long-lived transient intermediates,” *arXiv preprint arXiv:2002.05140*, 2020.

[60] P. D. Gregory, J. A. Blackmore, S. L. Bromley, and S. L. Cornish, “Loss of ultracold rb 87 cs 133 molecules via optical excitation of long-lived two-body collision complexes,” *Physical Review Letters*, vol. 124, no. 16, p. 163 402, 2020.

[61] I. Kozyryev, L. Baum, K. Matsuda, and J. M. Doyle, “Proposal for laser cooling of complex polyatomic molecules,” *ChemPhysChem*, vol. 17, no. 22, pp. 3641–3648, 2016.

[62] B. L. Augenbraun, J. M. Doyle, T. Zelevinsky, and I. Kozyryev, “Molecular asymmetry and optical cycling: Laser cooling asymmetric top molecules,” *arXiv preprint arXiv:2001.11020*, 2020.

[63] T. A. Isaev and R. Berger, “Polyatomic candidates for cooling of molecules with lasers from simple theoretical concepts,” *Physical review letters*, vol. 116, no. 6, p. 063 006, 2016.

[64] B. A. McGuire, “2018 census of interstellar, circumstellar, extragalactic, protoplanetary disk, and exoplanetary molecules,” *The Astrophysical Journal Supplement Series*, vol. 239, no. 2, p. 17, 2018.

[65] I. C. Lane, “Production of ultracold hydrogen and deuterium via Doppler-cooled Feshbach molecules,” *Phys. Rev. A*, vol. 92, no. 2, p. 022 511, 2015.

[66] D. G. Fried, T. C. Killian, L. Willmann, D. Landhuis, S. C. Moss, D. Kleppner, and T. J. Greytak, “Bose-einstein condensation of atomic hydrogen,” *Physical Review Letters*, vol. 81, no. 18, p. 3811, 1998.

[67] C. L. Cesar, D. G. Fried, T. C. Killian, A. D. Polcyn, J. C. Sandberg, A. Y. Ite, T. J. Greytak, D. Kleppner, and J. M. Doyle, “Two-photon spectroscopy of trapped atomic hydrogen,” *Physical review letters*, vol. 77, no. 2, p. 255, 1996.

[68] T. C. Killian, “1 s- 2 s spectrum of a hydrogen bose-einstein condensate,” *Physical Review A*, vol. 61, no. 3, p. 033 611, 2000.

[69] C. G. Parthey, A. Matveev, J. Alnis, B. Bernhardt, A. Beyer, R. Holzwarth, A. Maistrou, R. Pohl, K. Predehl, T. Udem, *et al.*, “Improved measurement of the hydrogen 1 s–2 s transition frequency,” *Physical review letters*, vol. 107, no. 20, p. 203 001, 2011.

[70] A. Beyer, L. Maisenbacher, A. Matveev, R. Pohl, K. Khabarova, A. Grinin, T. Lamour, D. C. Yost, T. W. Hänsch, N. Kolachevsky, *et al.*, “The rydberg constant and proton size from atomic hydrogen,” *Science*, vol. 358, no. 6359, pp. 79–85, 2017.

[71] S. Galica, L Aldridge, and E. Eyler, “Four-color stimulated optical forces for atomic and molecular slowing,” *Physical Review A*, vol. 88, no. 4, p. 043 418, 2013.

[72] X. Long, S. Y. Scarlett, A. M. Jayich, and W. C. Campbell, “Suppressed spontaneous emission for coherent momentum transfer,” *Physical review letters*, vol. 123, no. 3, p. 033 603, 2019.

[73] K. Wenz, I. Kozyryev, R. L. McNally, L. Aldridge, and T. Zelevinsky, “Large molasses-like cooling forces for molecules using polychromatic optical fields: A theoretical description,” *arXiv preprint arXiv:2007.01776*, 2020.

[74] I. Kozyryev, L. Baum, L. Aldridge, P. Yu, E. E. Eyler, and J. M. Doyle, “Coherent bichromatic force deflection of molecules,” *Physical review letters*, vol. 120, no. 6, p. 063 205, 2018.

[75] P. Hamilton and E. R. Hudson, “A diatomic molecule is one atom too few,” *Physics*, vol. 10, p. 43, 2017.

[76] G. Herzberg and K.-P. Huber, *Molecular spectra and molecular structure: spectra of diatomic molecules*. Toronto; New York: Van Nostrand, 1950, vol. 1.

[77] I. Kozyryev, “Laser cooling and inelastic collisions of the polyatomic radical sroh,” PhD thesis, Harvard, 2019.

[78] E. B. Norrgard, “Magneto-optical trapping of diatomic molecules,” PhD thesis, Yale University.

[79] J. F. Barry, “Laser cooling and slowing of a diatomic molecule,” PhD thesis, Yale University.

[80] G. Z. Iwata, “A cryogenic buffer-gas cooled beam of barium monohydride for laser slowing, cooling, and trapping,” PhD thesis, Columbia University.

[81] I. C. Lane, “Production of ultracold hydrogen and deuterium via doppler-cooled feshbach molecules,” *Physical Review A*, vol. 92, no. 2, p. 022 511, 2015.

[82] N. R. Hutzler, H.-I. Lu, and J. M. Doyle, “The buffer gas beam: An intense, cold, and slow source for atoms and molecules,” *Chem. Rev.*, vol. 112, no. 9, pp. 4803–4827, 2012.

[83] N. Bhatt, K. Kato, and A. C. Vutha, “Cold, dense, atomic ion clouds produced by cryogenic buffer-gas cooling,” *Physical Review A*, vol. 100, no. 1, p. 013 401, 2019.

[84] A. Jadbabaie, N. H. Pilgram, J. Kłos, S. Kotochigova, and N. R. Hutzler, “Enhanced molecular yield from a cryogenic buffer gas beam source via excited state chemistry,” *New Journal of Physics*, vol. 22, no. 2, p. 022 002, 2020.

[85] V. Singh, K. S. Hardman, N. Tariq, M.-J. Lu, A. Ellis, M. J. Morrison, and J. D. Weinstein, “Chemical reactions of atomic lithium and molecular calcium monohydride at 1 k,” *Physical review letters*, vol. 108, no. 20, p. 203 201, 2012.

[86] M. G. Tarallo, G. Z. Iwata, and T. Zelevinsky, “BaH molecular spectroscopy with relevance to laser cooling,” *Physical Review A*, vol. 93, no. 3, 2016. arXiv: `1512.06316`.

[87] A. Bernard, C. Effantin, J. D’Incan, G. Fabre, R. Stringat, and R. Barrow, “The 5d states of barium hydride; BaH and BaD,” *Molecular Physics*, vol. 67, no. 1, pp. 1–18, 1989.

[88] K Moore, I. Lane, R. McNally, and T Zelevinsky, “Assignment of excited-state bond lengths using branching-ratio measurements: The $B^2\Sigma^+$ state of BaH molecules,” *Phys. Rev. A*, vol. 100, no. 2, p. 022 506, 2019.

[89] I Kopp, M Kronekvist, and A Guntsch, “Rotational analysis of the ax band system of bah and bad,” *Arkiv foer Fysik (Sweden) Superseded by Phys. Scr.*, vol. 32, 1966.

[90] A Bernard, C Effantin, J d’Incan, G Fabre, R Stringat, and R. Barrow, “The 5 d states of barium hydride; bah and bad,” *Molecular Physics*, vol. 67, no. 1, pp. 1–18, 1989.

[91] L. Berg, K Ekvall, A Hishikawa, and S Kelly, “Radiative lifetime measurements of the b 2Σ+ state of bah by laser spectroscopy,” *Physica Scripta*, vol. 55, no. 3, p. 269, 1997.

[92] M. Tarallo, G. Iwata, and T Zelevinsky, “BaH molecular spectroscopy with relevance to laser cooling,” *Phys. Rev. A*, vol. 93, no. 3, p. 032 509, 2016.

[93] L. B. Knight Jr and W. Weltner Jr, “Hyperfine interaction and chemical bonding in mgh, cah, srh, and bah molecules,” *The Journal of Chemical Physics*, vol. 54, no. 9, pp. 3875–3884, 1971.

[94] J. Brown and A. Carrington, *Rotational Spectroscopy of Diatomic Molecules*. Cambridge: Cambridge University Press, 2003, ISBN: 0521810094.

[95] M. Tarbutt, “Magneto-optical trapping forces for atoms and molecules with complex level structures,” *New J. Phys.*, vol. 17, no. 1, p. 015 007, 2015.

[96] G Fabre, A El Hachimi, R Stringat, C Effantin, A Bernard, J d’Incan, and J Verges, “The h 2Δ state of barium hydride,” *Journal of Physics B: Atomic and Molecular Physics*, vol. 20, no. 9, p. 1933, 1987.

[97] M. H. Steinecker, D. J. McCarron, Y. Zhu, and D. DeMille, “Improved radio-frequency magneto-optical trap of srf molecules,” *ChemPhysChem*, vol. 17, no. 22, pp. 3664–3669, 2016.

[98] S Truppe, H. Williams, M Hambach, L Caldwell, N. Fitch, E. Hinds, B. Sauer, and M. Tarbutt, “Molecules cooled below the Doppler limit,” *Nat. Phys.*, vol. 13, no. 12, pp. 1173–1176, 2017.

[99] V. Gorini, A. Kossakowski, and E. C. G. Sudarshan, “Completely positive dynamical semigroups of N-level systems,” *J. Math. Phys.*, vol. 17, no. 5, pp. 821–825, 1976.

[100] G. Lindblad, “On the generators of quantum dynamical semigroups,” *Commun. Math. Phys.*, vol. 48, no. 2, pp. 119–130, 1976.

[101] J. B. Naber, A. Tauschinsky, H. B. van Linden van den Heuvell, and R. J. C. Spreeuw, “Electromagnetically induced transparency with Rydberg atoms across the Breit-Rabi regime,” *SciPost Phys.*, vol. 2, p. 015, 2 2017.

[102] D. J. Berkeland and M. G. Boshier, “Destabilization of dark states and optical spectroscopy in Zeeman-degenerate atomic systems,” *Phys. Rev. A*, vol. 65, p. 033 413, 2002.

[103] G. Iwata, R. McNally, and T Zelevinsky, “High-resolution optical spectroscopy with a buffer-gas-cooled beam of BaH molecules,” *Phys. Rev. A*, vol. 96, no. 2, p. 022 509, 2017.

[104] K. Moore and I. C. Lane, “Quantitative theoretical analysis of lifetimes and decay rates relevant in laser cooling BaH,” *J. Quant. Spectrosc. and Radiat. Transf.*, vol. 211, pp. 96–106, 2018.

[105] M. Di Rosa, “Laser-cooling molecules,” *Eur. Phys. J. D*, vol. 31, no. 2, pp. 395–402, 2004.

[106] J. Barry, E. Shuman, E. Norrgard, and D DeMille, “Laser radiation pressure slowing of a molecular beam,” *Phys. Rev. Lett.*, vol. 108, no. 10, p. 103 002, 2012.

[107] B. Hemmerling, E. Chae, A. Ravi, L. Anderegg, G. K. Drayna, N. R. Hutzler, A. L. Collopy, J. Ye, W. Ketterle, and J. M. Doyle, “Laser slowing of CaF molecules to near the capture velocity of a molecular MOT,” *J. Phys. B*, vol. 49, no. 17, p. 174 001, 2016.

[108] I. Kozyryev, L. Baum, K. Matsuda, B. L. Augenbraun, L. Anderegg, A. P. Sedlack, and J. M. Doyle, “Sisyphus laser cooling of a polyatomic molecule,” *Phys. Rev. Lett.*, vol. 118, no. 17, p. 173 201, 2017.

[109] B Sheehy, S. Shang, P Van Der Straten, S Hatamian, and H Metcalf, “Magnetic-field-induced laser cooling below the Doppler limit,” *Phys. Rev. Lett.*, vol. 64, no. 8, p. 858, 1990.

[110] E. S. Shuman, J. F. Barry, and D. DeMille, “Laser cooling of a diatomic molecule,” *Nature*, vol. 467, no. 7317, pp. 820–823, 2010.

[111] J Lim, J. Almond, M. Trigatzis, J. Devlin, N. Fitch, B. Sauer, M. Tarbutt, and E. Hinds, "Laser cooled YbF molecules for measuring the electron's electric dipole moment," *Phys. Rev. Lett.*, vol. 120, no. 12, p. 123 201, 2018.

[112] S. Li, M. Zhou, and X. Xu, "Analysis of atomic beam collimation by laser cooling," *Sci. Rep.*, vol. 8, no. 1, pp. 1–9, 2018.

[113] E. Norrgard, E. Edwards, D. McCarron, M. Steinecker, D DeMille, S. S. Alam, S. Peck, N. Wadia, and L. Hunter, "Hyperfine structure of the $B^3\Pi_1$ state and predictions of optical cycling behavior in the $X \rightarrow B$ transition of TlF," *Phys. Rev. A*, vol. 95, no. 6, p. 062 506, 2017.

[114] A. V. Kudrin, A. Zaitsevskii, T. A. Isaev, D. E. Maison, and L. V. Skripnikov, "Towards the search for thallium nuclear schiff moment in polyatomic molecules: Molecular properties of thallium monocyanide (TlCN)," *Atoms*, vol. 7, no. 3, pp. 1–8, 2019.

[115] S. Xu, M. Xia, R. Gu, Y. Yin, L. Xu, Y. Xia, and J. Yin, "Three-dimensional modeling of magneto-optical trapping of MgF molecules with multilevel rate equations," *Phys. Rev. A*, vol. 99, no. 3, p. 033 408, 2019.

[116] M. Tarbutt, "Laser cooling of molecules," *Contemp. Phys.*, vol. 59, no. 4, pp. 356–376, 2018.

[117] D. McCarron, "Laser cooling and trapping molecules," *J. Phys. B*, vol. 51, no. 21, p. 212 001, 2018.

[118] M. Tarbutt and T. Steimle, "Modeling magneto-optical trapping of CaF molecules," *Phys. Rev. A*, vol. 92, no. 5, p. 053 401, 2015.

[119] L. Anderegg, B. L. Augenbraun, E. Chae, B. Hemmerling, N. R. Hutzler, A. Ravi, A. Collopy, J. Ye, W. Ketterle, and J. M. Doyle, "Radio frequency magneto-optical trapping of CaF with high density," *Phys. Rev. Lett.*, vol. 119, no. 10, p. 103 201, 2017.

[120] E. Norrgard, D. McCarron, M. Steinecker, M. Tarbutt, and D DeMille, "Submillikelvin dipolar molecules in a radio-frequency magneto-optical trap," *Phys. Rev. Lett.*, vol. 116, no. 6, p. 063 004, 2016.

[121] M. T. Hummon, M. Yeo, B. K. Stuhl, A. L. Collopy, Y. Xia, and J. Ye, "2D magneto-optical trapping of diatomic molecules," *Phys. Rev. Lett.*, vol. 110, no. 14, p. 143 001, 2013.

[122] L. Baum, N. B. Vilas, C. Hallas, B. L. Augenbraun, S. Raval, D. Mitra, and J. M. Doyle, "1D magneto-optical trap of polyatomic molecules," *Phys. Rev. Lett.*, vol. 124, p. 133 201, 2020.

[123] H. Williams, S Truppe, M Hambach, L Caldwell, N. Fitch, E. Hinds, B. Sauer, and M. Tarbutt, "Characteristics of a magneto-optical trap of molecules," *New J. Phys.*, vol. 19, no. 11, p. 113 035, 2017.

[124] M. H. Steinecker, "Sub-Doppler Laser Cooling and Magnetic Trapping of SrF Molecules," PhD thesis, Yale University, 2019.

[125] M. Haw, N. Evetts, W. Gunton, J. Van Dongen, J. L. Booth, and K. W. Madison, "Magneto-optical trap loading rate dependence on trap depth and vapor density," *J. Opt. Soc. Am. B*, vol. 29, no. 3, pp. 475–483, 2012.

[126] V. S. Bagnato, L. G. Marcassa, S. Miranda, S. Muniz, and A. de Oliveira, "Measuring the capture velocity of atoms in a magneto-optical trap as a function of laser intensity," *Phys. Rev. A*, vol. 62, no. 1, p. 013 404, 2000.

[127] M. Anwar, D. V. Magalhães, S. T. Müller, M. Faisal, M. Nawaz, and M. Ahmed, "Revisiting the capture velocity of a cesium magneto-optical trap: Model, simulation and experiment," *Laser Phys.*, vol. 24, no. 12, p. 125 502, 2014.

[128] H. Williams, L Caldwell, N. Fitch, S Truppe, J Rodewald, E. Hinds, B. Sauer, and M. Tarbutt, "Magnetic trapping and coherent control of laser-cooled molecules," *Phys. Rev. Lett.*, vol. 120, no. 16, p. 163 201, 2018.

[129] L. Anderegg, B. L. Augenbraun, Y. Bao, S. Burchesky, L. W. Cheuk, W. Ketterle, and J. M. Doyle, "Laser cooling of optically trapped molecules," *Nat. Phys.*, vol. 14, no. 9, pp. 890–893, 2018.

[130] C. A. O'Hare, "Dark matter astrophysical uncertainties and the neutrino floor," *Physical Review D*, vol. 94, no. 6, p. 063 527, 2016.

[131] L. Barak, I. M. Bloch, M. Cababie, G. Cancelo, L. Chaplinsky, F. Chierchie, M. Crisler, A. Drlica-Wagner, R. Essig, J. Estrada, *et al.*, "Sensei: Direct-detection results on sub-gev dark matter from a new skipper ccd," *Physical Review Letters*, vol. 125, no. 17, p. 171 802, 2020.

[132] L Zhong, S Al Kenany, K. Backes, B. Brubaker, S. Cahn, G Carosi, Y. Gurevich, W. Kindel, S. Lamoreaux, K. Lehnert, *et al.*, "Results from phase 1 of the haystac microwave cavity axion experiment," *Physical Review D*, vol. 97, no. 9, p. 092 001, 2018.

[133] A. A. Geraci, C. Bradley, D. Gao, J. Weinstein, and A. Derevianko, "Searching for ultralight dark matter with optical cavities," *Physical review letters*, vol. 123, no. 3, p. 031 304, 2019.

[134] H Fosbinder-Elkins, C Lohmeyer, J Dargert, M Cunningham, M Harkness, E Levenson-Falk, S Mumford, A Kapitulnik, A Arvanitaki, I Lee, *et al.*, "Progress on the ariadne axion

experiment," in *Microwave Cavities and Detectors for Axion Research*, Springer, 2018, pp. 151–161.

[135] S. Hoedl, F Fleischer, E. Adelberger, and B. Heckel, "Improved constraints on an axion-mediated force," *Physical review letters*, vol. 106, no. 4, p. 041 801, 2011.

[136] P. Hamilton, M. Jaffe, P. Haslinger, Q. Simmons, H. Müller, and J. Khoury, "Atom-interferometry constraints on dark energy," *Science*, vol. 349, no. 6250, pp. 849–851, 2015.

[137] P. Pugnat, L. Duvillaret, R. Jost, G. Vitrant, D. Romanini, A. Siemko, R. Ballou, B. Barbara, M. Finger, M. Finger, *et al.*, "Results from the osqar photon-regeneration experiment: No light shining through a wall," *Physical Review D*, vol. 78, no. 9, p. 092 003, 2008.

[138] K. Ehret, M. Frede, S. Ghazaryan, M. Hildebrandt, E.-A. Knabbe, D. Kracht, A. Lindner, J. List, T. Meier, N. Meyer, *et al.*, "New alps results on hidden-sector lightweights," *Physics Letters B*, vol. 689, no. 4-5, pp. 149–155, 2010.

[139] D. Budker, V. V. Flambaum, X. Liang, and A. Zhitnitsky, "Axion quark nuggets and how a global network can discover them," *Physical Review D*, vol. 101, no. 4, p. 043 012, 2020.

[140] W. Hu, M. M. Lawson, D. Budker, N. L. Figueroa, D. F. J. Kimball, A. P. Mills, and C. Voigt, "A network of superconducting gravimeters as a detector of matter with feeble nongravitational coupling," *The European Physical Journal D*, vol. 74, no. 6, pp. 1–10, 2020.

[141] E. D. Hall, R. X. Adhikari, V. V. Frolov, H. Müller, and M. Pospelov, "Laser interferometers as dark matter detectors," *Physical Review D*, vol. 98, no. 8, p. 083 019, 2018.

[142] A. Derevianko and M. Pospelov, "Hunting for topological dark matter with atomic clocks," *Nature Physics*, vol. 10, no. 12, p. 933, 2014.

[143] P. Sikivie, "Experimental tests of the" invisible" axion," Tech. Rep. 16, 1983, p. 1415.

[144] P. W. Graham, I. G. Irastorza, S. K. Lamoreaux, A. Lindner, and K. A. van Bibber, "Experimental searches for the axion and axion-like particles," *Annual Review of Nuclear and Particle Science*, vol. 65, pp. 485–514, 2015.

[145] B. Roberts, P Delva, A Al-Masoudi, A Amy-Klein, C Baerentsen, C. Baynham, E Benkler, S Bilicki, W Bowden, E Cantin, *et al.*, "Search for transient variations of the fine structure constant and dark matter using fiber-linked optical atomic clocks," *arXiv preprint arXiv:1907.02661*, 2019.

[146] P Wcisło, P Morzyński, M Bober, A Cygan, D Lisak, R Ciuryło, and M Zawada, "Experimental constraint on dark matter detection with optical atomic clocks," *Nature Astronomy*, vol. 1, no. 1, pp. 1–6, 2016.

[147] B. M. Roberts, G. Blewitt, C. Dailey, M. Murphy, M. Pospelov, A. Rollings, J. Sherman, W. Williams, and A. Derevianko, “Search for domain wall dark matter with atomic clocks on board global positioning system satellites,” *Nature communications*, vol. 8, no. 1, p. 1195, 2017.

[148] A. Banerjee, D. Budker, J. Eby, H. Kim, and G. Perez, “Relaxion stars and their detection via atomic physics,” *arXiv preprint arXiv:1902.08212*, 2019.

[149] S Afach, D Budker, G DeCamp, V Dumont, Z. D. Grujić, H Guo, D. J. Kimball, T. Kornack, V. Lebedev, W Li, *et al.*, “Characterization of the global network of optical magnetometers to search for exotic physics (gnome),” *Physics of the Dark Universe*, vol. 22, pp. 162–180, 2018.

[150] D. J. Kimball, D Budker, J Eby, M Pospelov, S. Pustelny, T. Scholtes, Y. Stadnik, A. Weis, and A Wickenbrock, “Searching for axion stars and q-balls with a terrestrial magnetometer network,” *Physical Review D*, vol. 97, no. 4, p. 043 002, 2018.

[151] S Pustelny, D. Kimball, C Pankow, M. Ledbetter, P Wlodarczyk, P Wcislo, M Pospelov, J Smith, J Read, W Gawlik, *et al.*, “Global network of optical magnetometers for exotic (gnome): Physics novel scheme for exotic physics searches,” *arXiv preprint arXiv:1303.5524*, 2013.

[152] M Pospelov, S. Pustelny, M. Ledbetter, D. J. Kimball, W. Gawlik, and D Budker, “Detecting domain walls of axionlike models using terrestrial experiments,” *Physical review letters*, vol. 110, no. 2, p. 021 803, 2013.

[153] W. H. Press, B. S. Ryden, and D. N. Spergel, “Dynamical evolution of domain walls in an expanding universe,” *The Astrophysical Journal*, vol. 347, pp. 590–604, 1989.

[154] D. Antypas, D. Budker, V. V. Flambaum, M. G. Kozlov, G. Perez, and J. Ye, “Fast apparent oscillations of fundamental constants,” *Annalen der Physik*, vol. 532, no. 4, p. 1 900 566, 2020.

[155] H Grote and Y. Stadnik, “Novel signatures of dark matter in laser-interferometric gravitational-wave detectors,” *arXiv preprint arXiv:1906.06193*, 2019.

[156] P Wcisło, P Ablewski, K Beloy, S Bilicki, M Bober, R Brown, R Fasano, R Ciuryło, H Hachisu, T Ido, *et al.*, “New bounds on dark matter coupling from a global network of optical atomic clocks,” *Science Advances*, vol. 4, no. 12, eaau4869, 2018.

[157] R. A. Battye, M. Bucher, and D. Spergel, “Domain wall dominated universes,” *arXiv preprint astro-ph/9908047*, 1999.

[158] P Sikivie, “Axions, domain walls, and the early universe,” *Physical Review Letters*, vol. 48, no. 17, p. 1156, 1982.

[159] A. Friedland, H. Murayama, and M. Perelstein, "Domain walls as dark energy," *Physical Review D*, vol. 67, no. 4, p. 043 519, 2003.

[160] J.-P. Uzan, "The fundamental constants and their variation: Observational and theoretical status," *Reviews of modern physics*, vol. 75, no. 2, p. 403, 2003.

[161] K. Nordtvedt, "G/g and a cosmological acceleration of gravitationally compact bodies," *Physical review letters*, vol. 65, no. 8, p. 953, 1990.

[162] J. M. Goodkind, "The superconducting gravimeter," *Review of scientific instruments*, vol. 70, no. 11, pp. 4131–4152, 1999.

[163] H. Virtanen and A. Raja-Halli, "Parallel observations with three superconducting gravity sensors during 2014–2015 at metsähovi geodetic research station, finland," pp. 75–87, 2019.

[164] D. Banka and D. Crossley, "Noise levels of superconducting gravimeters at seismic frequencies," *Geophysical Journal International*, vol. 139, no. 1, pp. 87–97, 1999.

[165] J. Aasi, B. Abbott, R. Abbott, T. Abbott, M. Abernathy, K. Ackley, C. Adams, T. Adams, P. Addesso, R. Adhikari, *et al.*, "Advanced ligo," *Classical and quantum gravity*, vol. 32, no. 7, p. 074 001, 2015.

[166] W. A. Terrano, E. G. Adelberger, C. A. Hagedorn, and B. R. Heckel, "Constraints on axionlike dark matter with masses down to 10- 23 ev/c 2," *Physical Review Letters*, vol. 122, no. 23, p. 231 301, 2019.

[167] B. P. Abbott, R. Abbott, T. Abbott, M. Abernathy, F. Acernese, K. Ackley, C. Adams, T. Adams, P. Addesso, R. Adhikari, *et al.*, "Observation of gravitational waves from a binary black hole merger," *Physical review letters*, vol. 116, no. 6, p. 061 102, 2016.

[168] J. Aasi, B. Abbott, R. Abbott, T. Abbott, M. Abernathy, K. Ackley, C. Adams, T. Adams, P. Addesso, R. Adhikari, *et al.*, "Advanced ligo," *Classical and quantum gravity*, vol. 32, no. 7, p. 074 001, 2015.

[169] G. G. Raffelt, "Particle physics from stars," *Annual Review of Nuclear and Particle Science*, vol. 49, no. 1, pp. 163–216, 1999.

Appendix A: Tapered Amplifier Design

This tapered amplifier design is based on the idea that the more off-the-shelf components you can use, the faster the turn around time, and the higher stability it will have. This is because the design will not rely on the skill of the machinist making it, and instead relies on Thorlab components. There are only 3 parts that need any modification, the base plate to mount the TA to the table, the U-Bench requires you to mill a small groove, and custom mount for the chip itself. Drawings for each of these components are included at the end of this chapter, along with a parts list in Table A.1. Some of the parts will depend on the size of the asphere you select, and I will leave this general by specifying XX. You need to buy the correct side adapters so everything fits together, and that depends on the asphere selection. The extension from the EXXRMS adapter is taken off the black mounting ring, and fed through the S1TMXX and glued, leaving the S1TMXX free to screw in and out of the slip plate to set the focal length. In addition to the listed items a temperature controller, current controller, optical isolator, and the TA chip itself are needed. Given the large fluctuations in the prices of these items I will leave them off the parts list, instead focusing on what is unique to this design.

Name	**Part Number**	**Quantity**	**Unit Cost ($)**
U-Bench	CBB1	1	82
X-Y Slip Plate	SPT1	2	67
Asphere Objective	EXXRMS	2	35
Coated Apspheric Lens	Numerous	2	80
Adater to Mount Objective	S1TMXX	2	24
Cage Mount Post	ER1	8	5.2
Thermistor	TH10k	1	5
TEC Unit	TECD6	1	15
Thermistor	TH10k	1	5
		Total Cost ($)	560.6

Table A.1: Parts list for optics and mounting structure of this tapered amplifier design.

The design gets it stability from a Thorlabs U-bench (CBB1) that every other component mounts to. The angle between the aspheres which focus (collimate) the seed (output) of the amplifier are set by this design, and are not adjustable. This means the TA-Chip mount must be carefully aligned relative to the U-bench when it is first installed, but when everything is tightened the lack of freedom means this angle does not drift, and will not need to be adjusted. As always there is a trade-off between adjustability and stability. To adjust the height and lateral offset of the aspheres relative to the TA chip, a SPT1 slip-plate is used. To align this slip-plate image the spontaneous emission of the TA chip under low drive current without any seed light, looking at the the output of the chip and light sent backwards from the input. Adjust each slip-plate's position until both images are symmetric, an offset lens will cause an aberration that is easily visible on the camera. The distance between the lens's and the TA chip are controlled by for far the asphere mount is screwed into its holder. This can be very carefully controlled if the apply some Teflon tape to the threads, increasing the resistance when the asphere is adjusted. Imaging the spontaneous emission is also very helpful to ensure the input and output are both collimated, and the focal length and slip plate position will need to optimized a few times to get everything right. The TA is thermally stabilized by a TEC placed between the U-Bench and the TA chip mount, and the heat is dumped through the mounting structure into the table. To decrease the thermal resistance, and increase the stability of the system, some thermal paste connecting the system to the table was applied for each system. This system proved to be robust for daily operation, and requires minimal machining. The mount as shown is designed for DILAS DHP chip formats, but can be easily modified for C-Mount tapered amplifier chips. If possible, I would suggest the user avoid C-mount as it is much harder to align properly, and thermally anchor.

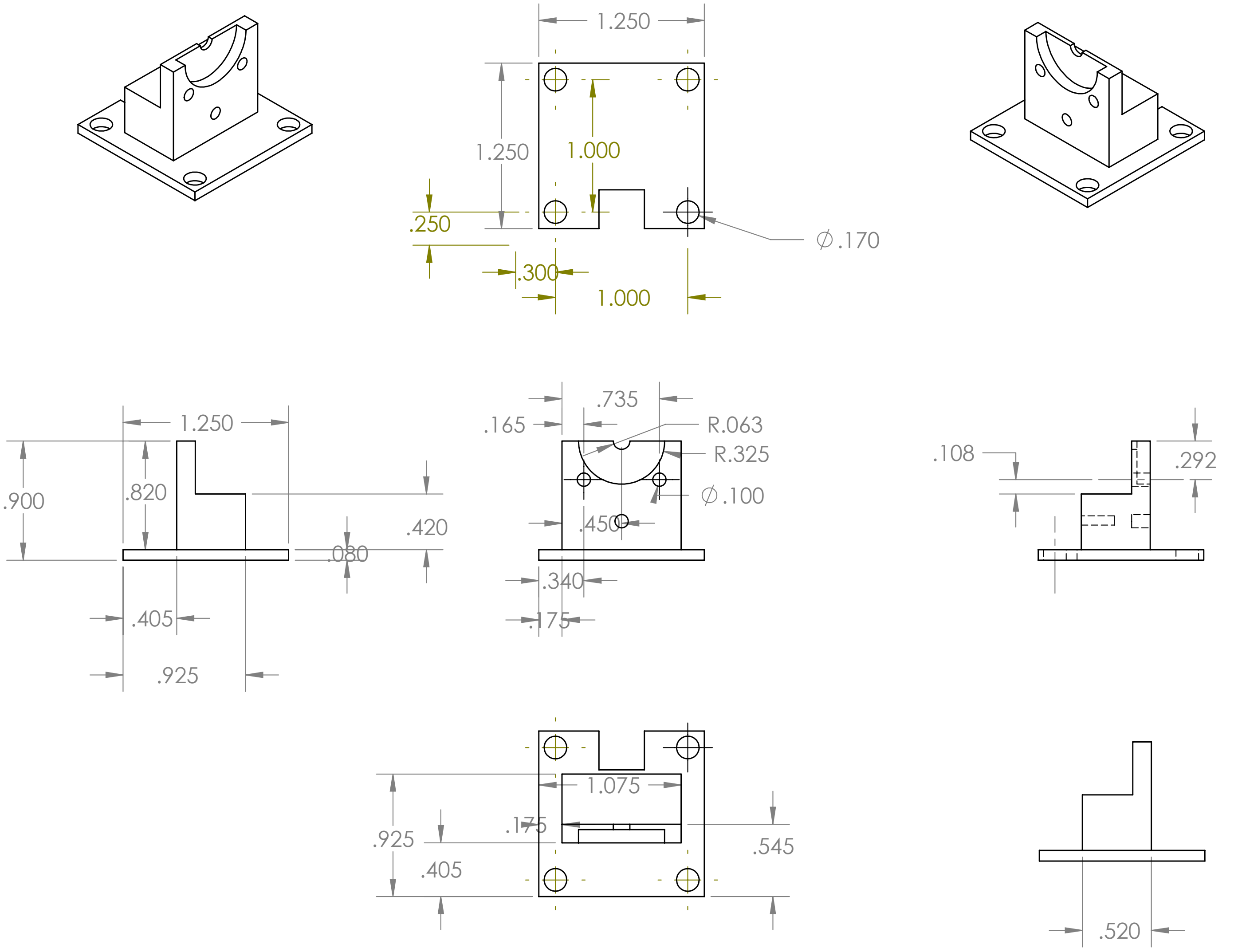
1.250
1.250
1.000
.250
.300
1.000
∅.170
1.250
.900
.820
.420
.080
.405
.925
.735
.165
R.063
R.325
∅.100
.450
.340
.175
.108
.292
1.075
.175
.925
.405
.545
.520

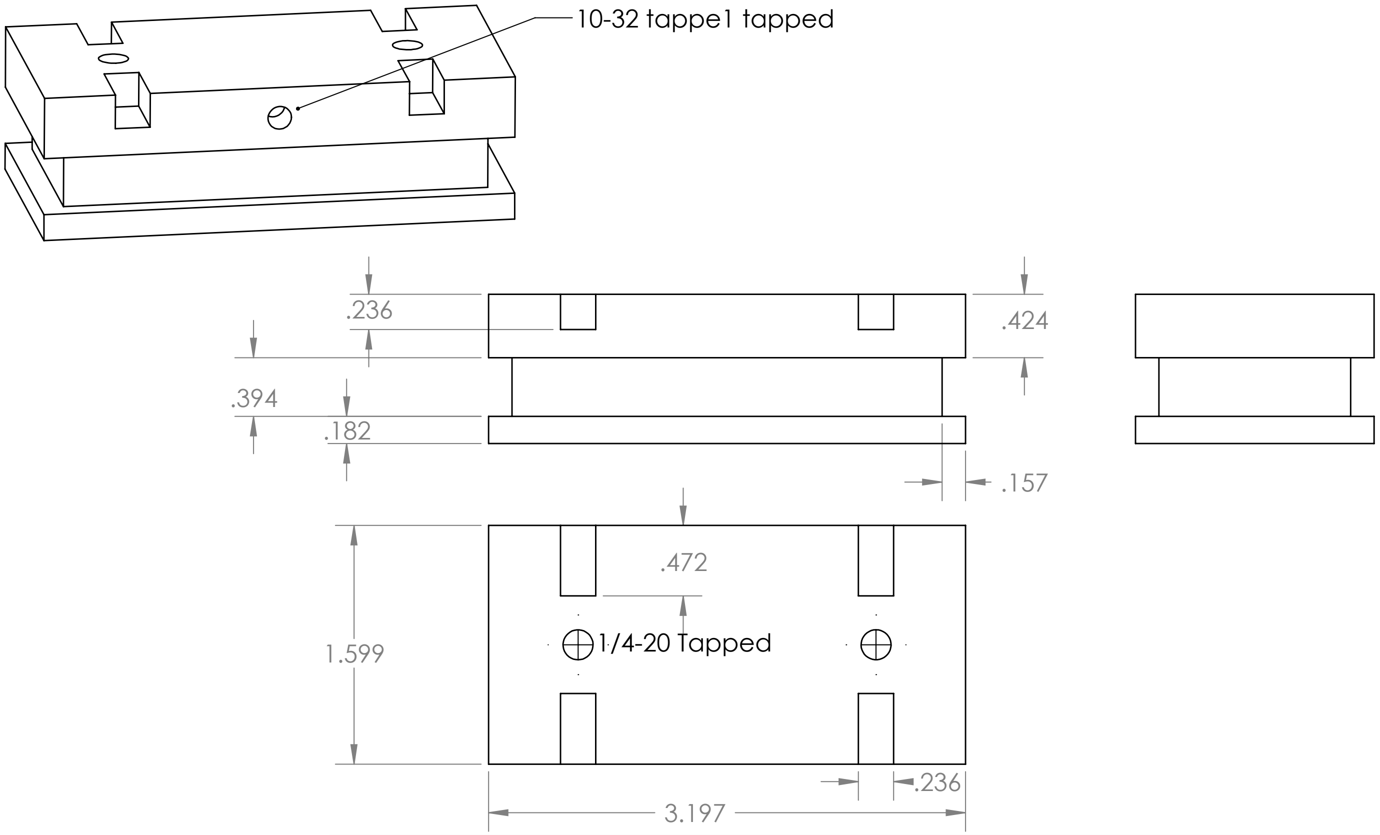

		UNLESS OTHERWISE SPECIFIED:		NAME	DATE	
		DIMENSIONS ARE IN INCHES TOLERANCES: FRACTIONAL ± ANGULAR: MACH ± BEND ± TWO PLACE DECIMAL ± THREE PLACE DECIMAL ±	DRAWN			
			CHECKED			TITLE:
			ENG APPR.			
			MFG APPR.			
		INTERPRET GEOMETRIC TOLERANCING PER:	Q.A.			
		MATERIAL	COMMENTS:			SIZE A DWG. NO. A_Table_Block REV
NEXT ASSY	USED ON	FINISH				
APPLICATION		DO NOT SCALE DRAWING				SCALE: 1:1 WEIGHT: SHEET 1 OF 1

PROPRIETARY AND CONFIDENTIAL

THE INFORMATION CONTAINED IN THIS DRAWING IS THE SOLE PROPERTY OF <INSERT COMPANY NAME HERE>. ANY REPRODUCTION IN PART OR AS A WHOLE WITHOUT THE WRITTEN PERMISSION OF <INSERT COMPANY NAME HERE> IS PROHIBITED.

5 4 3 2 1

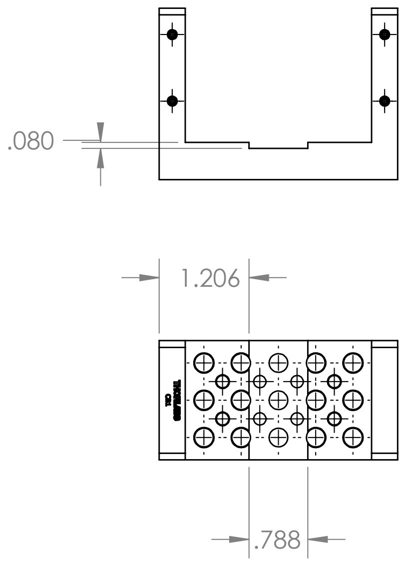

		UNLESS OTHERWISE SPECIFIED:		NAME	DATE	
		DIMENSIONS ARE IN INCHES TOLERANCES: FRACTIONAL ± ANGULAR: MACH ± BEND ± TWO PLACE DECIMAL ± THREE PLACE DECIMAL ±	DRAWN			
			CHECKED			TITLE:
			ENG APPR.			
			MFG APPR.			
		INTERPRET GEOMETRIC TOLERANCING PER:	Q.A.			
		MATERIAL	COMMENTS:			SIZE **A** DWG. NO. U-bench REV
NEXT ASSY	USED ON	FINISH				
APPLICATION		DO NOT SCALE DRAWING				SCALE: 1:2 WEIGHT: SHEET 1 OF 1

PROPRIETARY AND CONFIDENTIAL

THE INFORMATION CONTAINED IN THIS DRAWING IS THE SOLE PROPERTY OF <INSERT COMPANY NAME HERE>. ANY REPRODUCTION IN PART OR AS A WHOLE WITHOUT THE WRITTEN PERMISSION OF <INSERT COMPANY NAME HERE> IS PROHIBITED.

5 4 3 2 1

Appendix B: High NA Collection System

In order to maximize SNR for fluorescence detection it is important that you collect as much of the emitted light as possible from the molecules. For the majority of the experiments in this thesis, a two lens imaging system was used to collect the emission and focus it on the surface of the PMT. This is a very spatially selective way of collecting light, and it had good background subtraction because of this. However the limited size of the lens, means we were only able to collect around 5% of the light emitted the molecules. To improve this number we designed two elliptical collection mirrors that were both able to collect closer to 60% of the emitted fluorescence. The first design offers only 90 degree probe angles, and the second allows for 90 degree and 45 degree laser probes (relative to the molecular beam. Elliptical reflectors work by taking the light that is emitted at one special point inside the curve of the mirror, and focusing it on a second point a fixed distance away. These systems were design to have the molecular beam and the probe laser intersect at this point, and the PMT's surface was placed at the second point. Each collector is mounted in vacuum, and can give you an order of magnitude increase in the collected light. However in practice, they resulted in substantially higher background counts so the SNR actually decreased when they were installed for direct detection experiments. In order to be useful, a background free detection scheme such as two photon excitation would be needed. Both designs were manufactured by Optiforms, and the drawings/part numbers for the design are included below.

NOTES: UNLESS OTHERWISE SPECIFIED

1. ELECTROFORM REFLECTOR FROM MASTER TOOL WITH SPECULAR SURFACE QUALITY OF 80-50 SCRATCH-DIG PER MIL-PRF-13830B.
2. NOMINAL THICKNESS (T) MAY VARY ± T/4 WITHIN .25 OF EDGES.
3. REFLECTIVE SURFACE COATING: TBD

REVISIONS			
REV	DESCRIPTION	DATE	APPROVED
1	INITIAL PROPOSAL RELEASE	04/25/19	JPH
A	HOLES THRU ALL, WERE THRU ONE WALL	04/26/19	JPH

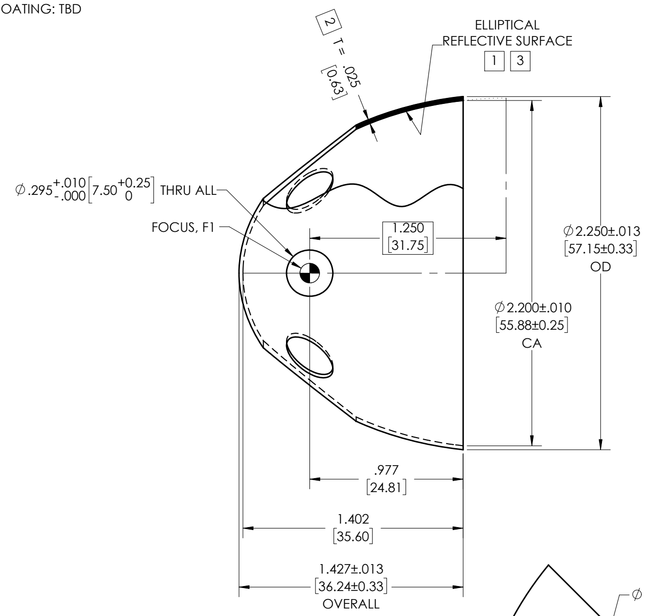

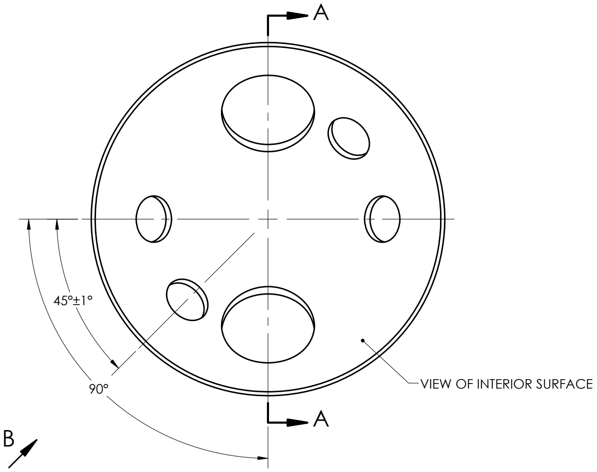

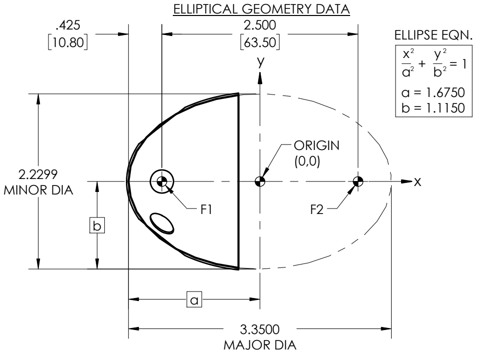

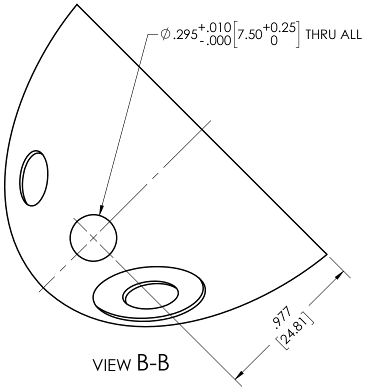

VIEW B-B

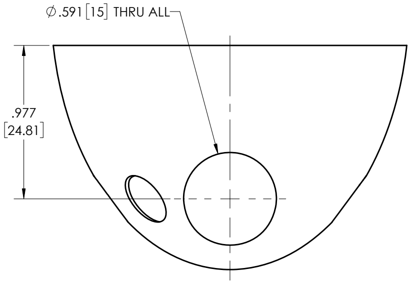

NEXT ASSY	USED ON
APPLICATION	

UNLESS OTHERWISE SPECIFIED
DIMENSIONS ARE IN INCHES [mm]
GD&T PER ASME Y14.5-2009
DO NOT SCALE DRAWING
TOLERANCES
FRACTIONS ± 1/16
DECIMALS .XX ± .02 .XXX ± .005
ANGLES ± 1/2°
SURFACE ROUGHNESS 63√
DEBURR SHARP EDGES & HOLE RIMS .015 MAX.
CHAMFER THREADS .01 PAST ROOT DIAMETER
THIRD ANGLE PROJECTION

CONTRACT NO.	19-PROPOSAL		
DRAWN	JPH	DATE	04/25/2019
CHECKED		DATE	
ENGR	RRS	DATE	04/25/2019
MATERIAL	ELECTROFORMED NICKEL - LSSN TYPE 1 (MAKE FROM E64NV-0100)		
FINISH	NONE (SEE NOTE 3)		

optiforms

42310 WINCHESTER RD.
TEMECULA, CA 92590
WWW.OPTIFORMS.COM

REFLECTOR, ELLIPTICAL, TBD
COLUMBIA UNIVERSITY

SIZE	CAGE CODE	DWG. NO.	REV
C	0Y1Y4	QSP-002717-2	A

SCALE	WT. (REF)	CAD NO.	SHEET
2:1	0.06 lbs.	QSP-002717	1 OF 1

REVISIONS			
REV	DESCRIPTION	DATE	APPROVED
1	INITIAL PROPOSAL RELEASE	12/14/17	JPH

NOTES: UNLESS OTHERWISE SPECIFIED

1. ELECTROFORM REFLECTOR FROM MASTER TOOL WITH SPECULAR SURFACE QUALITY OF 80-50 SCRATCH-DIG PER MIL-PRF-13830B.
2. NOMINAL THICKNESS (T) MAY VARY ± T/4 WITHIN .25 OF EDGES.
3. REFLECTIVE SURFACE COATING: TBD

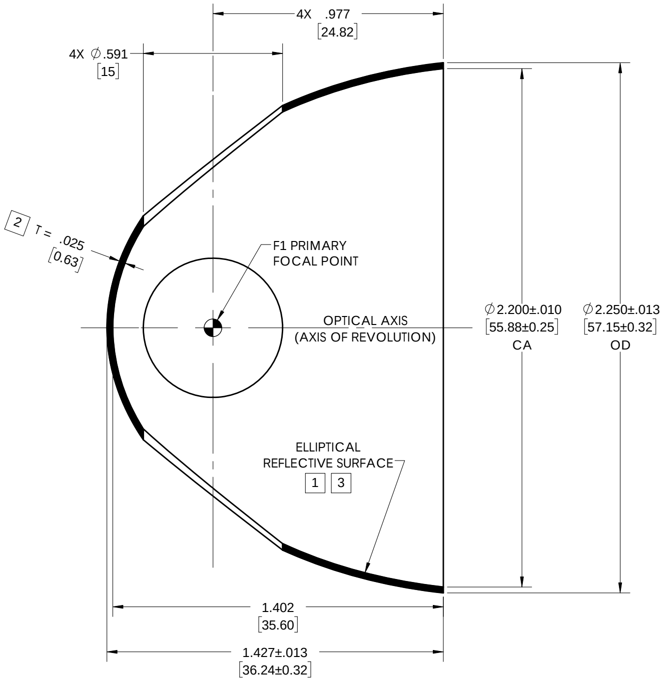

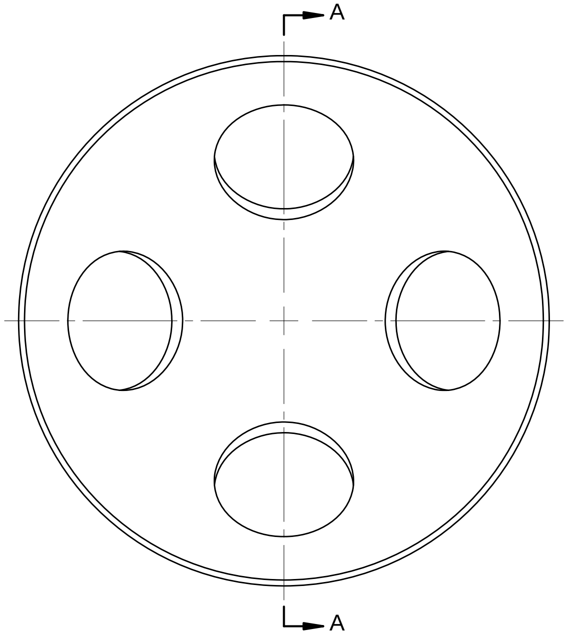

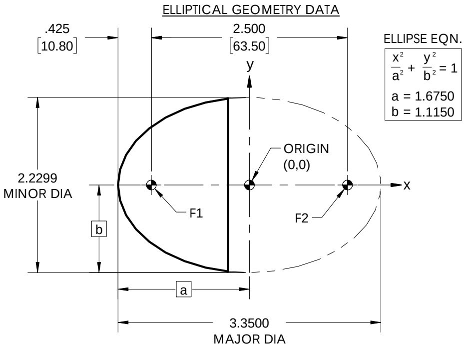

NEXT ASSY	USED ON
APPLICATION	

UNLESS OTHERWISE SPECIFIED
DIMENSIONS ARE IN INCHES [mm]
GD&T PER ASME Y14.5-2009
DO NOT SCALE DRAWING

TOLERANCES

FRACTIONS	DECIMALS	ANGLES
± 1/16	.XX ± .02 .XXX ± .005	± 1/2°

SURFACE ROUGHNESS $\sqrt{}^{63}$
DEBURR SHARP EDGES & HOLE RIMS .015 MAX.
CHAMFER THREADS .01 PAST ROOT DIAMETER

THIRD
ANGLE
PROJECTION

CONTRACT NO.	17-PROPOSAL		
DRAWN	*JPH*	DATE	*12/13/17*
CHECKED		DATE	
ENGR	**RRS**	DATE	**12/13/17**
MATERIAL	ELECTROFORMED NICKEL - LSSN TYPE 1 (MAKE FROM E64NV-0100)		
FINISH	VACUUM DEPOSITED TBD (SEE NOTE 3)		

42310 WINCHESTER RD.
TEMECULA, CA 92590
WWW.OPTIFORMS.COM

REFLECTOR, ELLIPTICAL, TBD
COLUMBIA UNIVERSITY

SIZE	CAGE CODE	DWG. NO.	REV
C	0Y1Y4	**QSP-2355**	1

SCALE	WT. (REF)	CAD NO.	SHEET
3:1	0.059 lbs.	QSP-2355	1 OF 1